GEOMECHANICS OF VOLCANO INSTABILITY AND THE EFFECTS OF

INTERNALLY ELEVATED PORE FLUID (GAS) PRESSURES

Mark Edward Thomas

A thesis submitted in partial fulfilment of the

requirements of Kingston University for

the degree of Doctor of Philosophy

August 15

GEOMECHANICS OF VOLCANO INSTABILITY AND THE EFFECTS OF INTERNALLY ELEVATED PORE FLUID PRESSURES

Mark E. Thomas

Abstract

Volcano flank collapse events affect volcanic edifices where a range of different processes are at work. However, there is at least one mechanism of generating instability that may be present at all volcano collapse locations: increases of edifice pore fluid pressures from internal sources.

The use of geomechanical classification schemes such as the Rock Mass Rating (RMR) show that a volcano can be considered mechanically weak and little more than a pile of granular material. Initial field work and laboratory testing demonstrated that it is possible to estimate volcanic rock-mass compressive (σ_{cm}), tensile (σ_{tm}) and cohesive (c) strength from the RMR using the power law relationships $\sigma_{cm} = 0.5161e^{(0.0581*RMR)}$, $\sigma_{tm} = 0.0055e^{(0.0744*RMR)}$ and $c = 0.0349e^{(0.0649*RMR)}$.

Simple analogue models using sand piles as scaled proxies for a volcano edifice demonstrate that internal gas pressure is a viable mechanism for promoting structural instability. Complementary two-dimensional limit equilibrium methods (LEM) confirm this effect, showing a clear reduction in edifice stability with increasing degrees of internal pressurisation. However, internal pressures in excess of 25 MPa are needed to reduce the Factor of Safety below unity, indicating this mechanism is unlikely to be the *solitary* contributor to sector collapse.

Three-dimensional numerical modelling of edifice stability using *FLAC^{3D}* provides a sophisticated means of undertaking a complex analysis of volcano instability caused by internal pressurisation. Five model geometries were examined over a pressure range of 0 to 20 MPa that allowed the sensitivity of gas pressure on structural stability to be assessed quantitatively. Significant reductions in stability were observed in all cases, with the most unstable modelled edifice possessing a combination of 'weak' foundations and shallow regional gradient. A key finding is that the instability observed in both the analogue and LEM results are replicated in the 3D numerical models, confirming for the first time the significance of internal (gas) pressurisation as a potential trigger mechanism for volcano flank failure.

Acknowledgements

Table of contents

Preface

Since the events at Mount St. Helens during May 1980, considerable attention has been focussed on the mechanisms and consequences of volcanic edifice collapse. As a result, volcano instability is increasingly recognised as a societal hazard, and is now considered as the precursor for some of the most devastating forms of natural disaster associated with volcanoes. There are now over 500 recognised cases of volcanic edifice collapse which have resulted in large volcanic debris flows (Siebert, 1992), and volcanic slope failures and associated explosive eruptions have resulted in more than 20000 fatalities in the past 400 years (Siebert *et al.* 1987). The research that has been conducted in this field has led to a better understanding of volcanic edifice collapse, but understanding and predicting volcanic collapse remains a complex and challenging task. With this improved, but far from complete knowledge and increased public awareness of the problem, comes an inherent risk. In discussing slope instability, Chen (2000) observed,

"In the early days, slope failure was always written off as an act of God. Today, attorneys can always find someone to blame and someone to pay for the damage – especially when the damage involves loss of life or property"

While not a direct comment on volcanic slope failure, this statement is as applicable to a volcanologist as to a civil engineer, and applies to all volcanic hazards, not just volcanic slope failures. In short, with the power of prediction comes the burden of liability. If an evacuation is ordered and nothing happens, then the liability is of the human and economic costs of a false alarm. Conversely, if there is no evacuation and there is then a major sector collapse, then there is the liability of loss of life. However, no level of 100% certainty can be made in any prediction or model for natural processes. The level of uncertainty in predicting any type of volcanic slope failure is much higher than in any other form of volcanic event, as slope failure can occur with the absence of any pre-cursory magmatic behaviour (Reid, 2004; Siebert *et al.* 1987). For example, the 1888 eruption at Bandai-san was strictly phreatic and no juvenile material was found in either the debris-avalanche or the air-fall tephra deposits, nor was the collapse followed by the eruption of magma (Siebert *et al.* 1987). The notion that a collapse event could occur at virtually any volcano, even one that has been deemed long inactive, has been suggested by many authors (e.g. van Wyk de Vries and Francis, 1997; Vidal and Merle, 2000). The apparent lack of dependence of large-scale

volcanic slope failures on magmatic or even volcanic behaviour makes predicting and understanding these events very difficult. There are many volcanoes that are not considered to pose a conventional (eruptive) volcanic threat to the surrounding inhabitants and therefore are not being monitored. If indeed there is no requirement for a volcano to be considered active for it to undergo sector collapse, then any one of these could pose a substantial threat and until the event occurred we would know nothing of it.

1. Introduction

1.1 Types of volcano and eruption style

Magma can generally be thought to have formed in two distinct ways, by decompression of hot material at divergent plate boundaries and hot spots and by melting at convergent plate boundaries caused by hydration of the mantle wedge (Grove, 2000). It is not too surprising then that the magma erupted at volcanic vents differs depending on the processes of magma generation. In turn, it should not be surprising that there are several types of volcano and eruption style, the nature of which depends on the type of magma which is erupted.

What exerts a primary control on these differences is the lithosphere; it acts as a filter, modifying the compositions of magmas from the time they are generated to eruption at the surface. The thicker and lower density the filter, the greater its effect at impeding the ascent of mantle-derived magmas, which at origin are largely basaltic in nature (Perfit and Davidson, 2000).

At divergent plate boundaries and hotspots the lithosphere is generally being stretched and therefore thinned, which allows for decompression melting and magma generation. However, in doing this the magma filter is also being thinned, as such the magmas erupted at the surface closely resemble the magma at source and are largely basaltic. Basaltic magmas compared to other magma types, typically have a relatively low viscosity ($<10^3$ Pa s, Murase and McBirney, 1973) and higher temperature ($\sim1250^oC$, Spera, 2000) which allows gas to separate from the magma (Simkin and Siebert, 2000). This leads to mainly effusive eruptions involving long lava flows and, ignoring the extremely voluminous eruptions of large igneous provinces, commonly leads to the creation of a shield volcano. Shield volcanoes are broad volcanic constructs consisting of multitudes of lava flows with flank slopes typically around 5°. The flanks are less than half the steepness of those that are found at volcanoes formed at well-developed convergent boundaries and shield volcanoes are also usually much larger.

Volcanism at convergent plate boundaries is much more complex and diverse. Early magmatism at convergent plate boundaries usually occurs at oceanic or continental arcs and is typically basaltic, while the later and more prolonged magmatism tends to be more evolved with a predominance of

more differentiated andesitic magmas. This broad trend may simply reflect the thickening of the arc crust and lithosphere through time as volcanism continues, essentially increasing the thickness of the magma filter, and giving a greater potential for differentiation. (Perfit and Davidson, 2000; Davidson *et al.*, 2007). The principal type of volcano in this setting is the composite cone or stratovolcano, composed of blocky lavas and lesser pyroclastic deposits. This is in part because the longer a magma has to differentiate (the larger the filter) the more viscous it becomes as it loses "liquid" melt through crystallisation of minerals, much like the progressive freezing of an ice cube. However, this process can also occur without the presence of a "filter" simply though significant crystallisation resulting from long residence periods within a crustal magma chamber (Marsh, 2000). If this magma is then erupted at the surface, the lava flows do not travel very far and break up, becoming very blocky. This type of volcanism also has the potential to be more explosive as the volatiles are concentrated in an increasingly viscous magma.

There are exceptions to what has been discussed in this section and it in no way suggests any hard and fast rules about the location of a particular type of volcano. Rather, it has purely been described how the geological setting of a volcano may influence its behaviour. This is an important concept, as given the geological setting of a volcano may have a bearing on its *form* and *activity*, these two factors play an important role in the potential a volcano has for collapse. This suggests that the geological setting of a volcano may indirectly dictate its susceptibility to undergo large-scale flank collapse.

1.2 Types of edifice failure and feedback mechanisms relating to failure

The details of collapse theory are discussed in more detail in Chapter two, and what is presented here is simply a brief outline of the types of edifice failure and what their implications are for the volcano as a whole. Failure of a volcanic flank can range from small volumes such as those associated with the 2002 collapse at Stromboli, Italy (Baldi *et al.*, 2005) to the enormous flank failures of the Hawaiian Islands (Iverson, 1995). Perhaps it is a rather obvious correlation, but none the less, the larger the volcano, the larger the flank failure that can occur. This is why the largest of the volcanic mass movements are restricted to the large intra-plate shield volcanoes that are associated with hotspots, while the composite cones found at convergent plate boundaries experience smaller mass wasting events. Flank collapse frequency also varies greatly between

individual volcanoes suggesting that some are more prone to flank failure than others. The largest of the composite volcanoes developed on continental crust being particularly at risk. Their structure of mechanically unsound materials compounded by the steep slopes of the flanks promotes the generation of flank instability. Consequently, they experience flank collapse, all be it on a relatively smaller scale (typically ranging from 0.5-10 km^3 in volume (Voight, 2000)), far more frequently than their more stable and essentially homogenous shield-like counterparts (McGuire, 1996) that can involve volumes in excess of 5,000 km^3 (Moore, 1994). Examples of such collapse events include the ~0.15 Ma 1-2 km^3 collapse of the Llullaillaco stratovolcano volcano, northwest Argentina (Richards and Villeneuve, 2001) and the several giant landslides that have occurred on the Hawaiian Ridge, that have removed volcano-flank sectors in excess of 1,000 km^3 (Iverson, 1995).

It is fairly obvious, that when a volcano loses a substantial part of its structure due to a flank collapse event, there are likely to be some associated changes in its behaviour, the most dramatic of which is an explosive eruption due to decompression. This is what happened in the 1980 eruption of Mount St. Helens. Failure and removal of the north flank rapidly decompressed the magma within the edifice, leading to the climactic explosive eruption (Voight *et al.*, 1983). However, not all collapse events end in such dramatic circumstances. Feedback mechanisms may simply take the form of creating a new, preferential site for magma emplacement due to a reorganisation of the stress field within the edifice (Tibaldi, 2004).

1.3 The dangers of volcano instability – Why is it important to understand?

Over 500 million people world-wide, a number increasing by over a million per annum, live in the hazard zone adjacent to active volcanoes (Siebert, 1992); this fact *demands* a better understanding of how, and under what circumstances, volcanic edifices may fail catastrophically. The process of volcanic edifice slope failure threatens all aspects of everyday life for those in the potential hazard zones. It should therefore follow that the first efforts of tackling the problem should be directed towards education and re-location, in an attempt to avoid any potential confrontations between the volcano and the surrounding population. Although this would undoubtedly be the most effective method of preventing loss of life and property, the practicalities of such action are not feasible. Even if a well-documented risk exists, there is a tendency for the lay person to overlook volcanic hazards as a once in a millennium occurrence that does not affect their day to day life. A prime
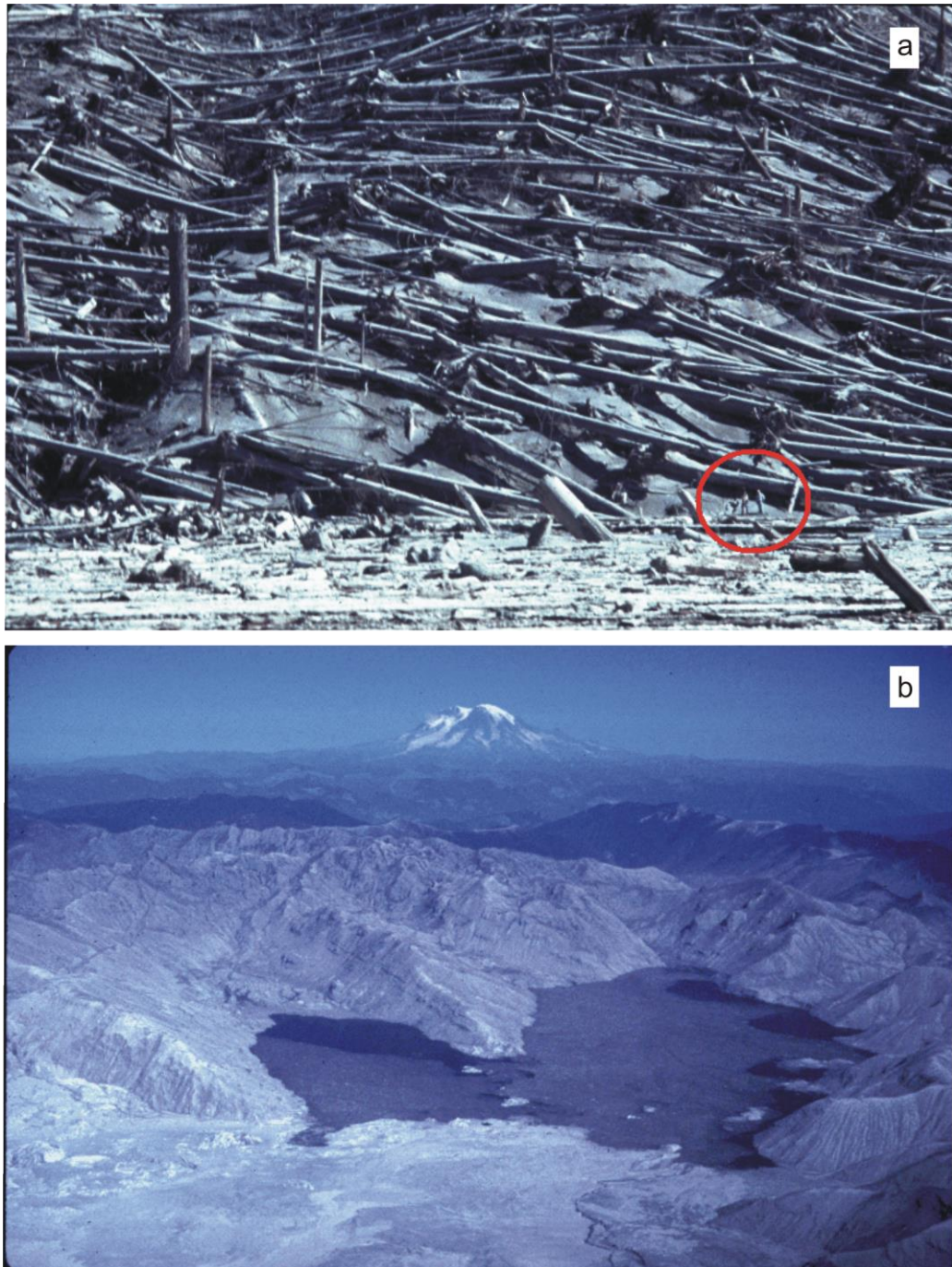
Figure 1.1: Photographs of the devastation taken in the aftermath of the 1980 eruption of Mount St. Helens. (a) Trees blown down by the force of the lateral blast released after the initial landslide following the failure of the North slope, note the scale, circled in red are two USGS scientists. (b) Arial view of Spirit Lake. The position of the lake shore line was greatly affected by the input of volcanic debris, and the lake was almost completely saturated with tree trunks as can be seen in the photograph. Also evident in both photographs is the blanket of grey volcanic debris that covers the landscape, and the apparent lack of vegetation on the slopes, which were once covered with the trees now floating in the lake (b). Photographs by Lyn Topinka (1980).

example of such behaviour occurred on the small Caribbean Island of Montserrat during the final two decades of the last century (Druitt and Kokelaar, 2002), where a study entitled *Volcanic Hazards from Soufriére Hills Volcano, Montserrat, West Indies,* (commissioned in 1986 and completed by Wadge and Isaacs in 1987) was all but ignored in the nine years prior to the 1995 eruption. On July 25th 1995, one week into the eruption, the then Governor of Montserrat and the leader of the scientific team from the Seismic Research Unit sent a telegram to the UK Foreign and Commonwealth office, expressing astonishment that recommendations in the report had not been noted and also that there had been no contingency plans drawn up. This case has only come to light due to the recent activity on Montserrat, and the truth may be that there are many more cases which would conform to this example if a volcanic centre was to become newly active. This is even more alarming considering that a large-scale volcanic collapse event may possibly occur even if a volcano is not labelled as active (e.g. those described at long-dormant volcanoes in Kamchatka, Melekestsev and Braitseva (1984)).

The 1980 eruption of Mount St. Helens is a well documented case of volcanic flank collapse (Voight, 1981; Voight et al., 1981, 1983; Vinciguerra et al., 2005a), and the events that occurred at Mount St. Helens are rightly associated with large areas of devastation (Fig. 1.1). However, the actual landslide event was relatively small in comparison to the volcanic landslides generated by some historical edifice collapses (Table 1.1). The volume of the Mount St. Helens volcanic debris avalanche (later to become a debris flow, see Section 1.3.1) was only estimated to be 2.5 km^3, a volume eleven times smaller than the 28 km^3 Pleistocene avalanche at Popocatepetl, central Mexico (Siebert *et al.*, 1987).

Debris avalanche deposits are poorly sorted mixtures of dominantly lithic material from the source volcano and its underlying basement (Seibert *et al.*, 1987). A debris avalanche is defined by McGuire (1995) as "having been formed by the large-scale collapse of a volcanic edifice, or part thereof, in the absence of significant amounts of water". They display a number of common morphological and fabric-related features. The surfaces of such deposits have typically irregular, hummocky topography consisting of many small hills and closed depressions (Glicken, 1982, Siebert *et al.*, 1987, McGuire, 1996). This common topography is thought to reflect the underlying presence of large boulders or mega blocks, which may have dimensions in excess of a kilometre,

Volcano	Deposit	Volume (km^3)	Run out (Km)
Popocatepetl		28	33
Shasta		26	50
Nevado de Colima		22-33	120
Socompa		17	35
Chimborazo	Riobamba	8.1	35
Mawenzi		7.1	60
Volcán de Colima		6-12	43
Akagi	Nashikizawa	4	19
Galunggung		2.9	25
Mount St. Helens	1980	2.5	24
Fuji	Gotenba	1.8	24
Shiveluch	1964	1.5	12
Bandai-san	1888	1.5	11
Asakusa	Migisawa	0.4	6.5
Egmont	Pungarehu	0.35	31
Unzen	1792	0.34	6.5

Table 1.1. Volumes and runout distances of selected subaerial volcanic debris avalanches (McGuire, 2003).

with the topographic lows coinciding with the more disrupted and finer-grained material (McGuire, 1996). The size of clasts within the deposit varies widely both within the deposit and within differing authors' descriptions of the same deposit. A grain-size distribution study on the Mount St. Helens Debris avalanche produced average values of 4%, 11% and 42% for clay (< 0.004 mm), silt and sand, respectively; with the remaining 43% comprising of particles >2 mm (Voight *et al.*, 1983). When it is considered that some blocks within the avalanche deposit were over 100 m long, it is apparent that this study focused on the fine fractions, but gives an idea of the variation of grain-size encountered, even in a limited grain-size study of a volcanic debris avalanche deposit. Debris avalanche deposits are considered as both the primary deposit and hazard from large-scale
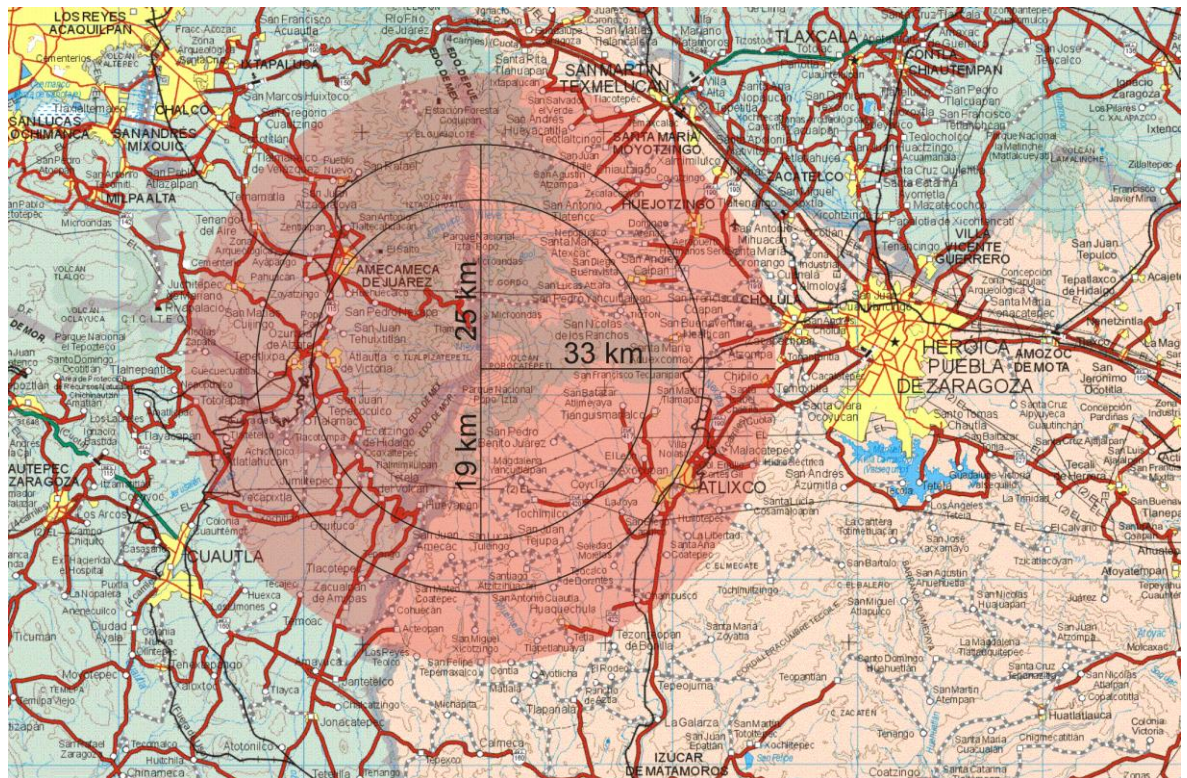
Figure 1.2: Popocatepetl and the surrounding area, the radius of Zone 1 (19 km) and Zone 2 (25 km) which represent the proposed zones of high and medium danger respectively (see text) are shown. The shaded area with a radius of 33 km represents the runout distance of the Pleistocene volcanic debris avalanche (Table 1.1), which was directional and not a blanket covering of the entire shaded area. (Map: Maps of Mexico)

volcanic collapse within this thesis, and although secondary hazards (e.g. lahars) are discussed briefly in Section 1.3.1 they are given no further consideration elsewhere in this thesis. The work presented in this thesis concerns solely the generation of structural instability. After failure has occurred, collapse deposits may take many forms, none of which relate directly to the research undertaken.

Whereas Mount St. Helens is situated in a relatively remote area of Washington State, USA, Popocatepetl is situated less than 70 km from the centre one of the world's largest cities. Mexico City, with a population of over 20 million and an area covering approximately 600 square miles, is probably one of the most densely populated areas on Earth, yet it is located within reach of one of the world's most active volcanoes. On the flanks of Popocatepetl CENAPRED (Centro Nacional de Prevencion de Desastres (2006)) consider 108,000 people in 30 towns within 12 miles (19 km) of the summit to be at high risk, and a further 386,000 in 98 towns up to 16 miles (25 km) from the summit at medium risk. In total, over 500,000 people live within the run out distance (33 km) of the

Pleistocene volcanic debris avalanche (Fig. 1.2) and in potential reach of any future similar large-scale volcanic debris avalanche. With the population centres surrounding such volcanic edifices growing every day, the understanding of the processes behind generating large-scale volcanic collapse becomes imperative.

1.3.1 Associated hazards resulting from large-scale volcano collapse

The hazards associated with large-scale volcanic collapse are significant in themselves, but the potential risk is heightened by the spectrum of phenomena that could possibly be triggered or sourced by a collapse event. This was a lesson learnt during and subsequent to the eruption of Mount St. Helens on May 18th 1980. Although a major event in its own right, the landslide and associated debris avalanche only contributed a small part of the destruction resulting from the eruption. The Mount St. Helens crisis demonstrated how the interactions of a large volcanic landslide and a shallow magma body can have multiple devastating effects, including lateral blasts, lahars, pyroclastic flows, and extensive ash fall (McGuire, 2003). The question of whether these events would have occurred, or had the same devastating effects without the large-scale rapid decompressive eruption triggered by the failure of the north flank remains unclear. Indeed, if there had been no large-scale flank failure the crisis may not have culminated in a voluminous eruption and a summit dome building eruption similar to the recent activity described by Dzurisin et al., (2005) may have occurred. Furthermore, the speed that these phenomena were unleashed meant that no mitigation procedures could be implemented once the sequence of events had been initiated.

Lateral blasts

Landsliding on a massive scale can quickly unload a hydrothermal or magmatic system, leading to major explosive activity. The term lateral blast refers to a volcanic explosion with a significant low-angle component, directed in a sector of less than 180° (Crandell and Hoblitt, 1986). Where structural failure triggers a decompressive lateral blast, pyroclastic flow formation closely follows the debris avalanche (McGuire, 1996). The blast can quickly overtake the avalanche and thus, the deposits of these often juvenile magma-rich events may be mixed with or overlie the more lithic-dominated avalanche material. The pyroclastic density currents produced by the lateral blasts of

Mount St. Helens and Bezymianny volcano devastated areas of 500 – 600 km^2 around each volcano (Siebert *et al.*, 1987).

Pyroclastic flows and extensive ash fall

Pyroclastic flows and air-fall deposits tend to pose a lesser threat to human life than other associated hazards, mainly because they occur late in the paroxysmal phase of a collapse driven eruption, following the removal of material overlying the central vent through debris avalanches and lateral blasts (Siebert *et al.*, 1987). The direction of emplacement is therefore likely to be constrained by the newly formed collapse scar and they flow over areas already devastated by the previous events. However, significant disruption to surrounding agriculture caused by extensive ash fall has been reported following such events (Blong, 1984).

Lahars/Debris Flows

In many cases, the debris avalanches formed during volcano flank collapse do not stay "dry" for long. Available water from saturated volcaniclastic sequences, snow and ice covering the volcano, or from surface water bodies becomes readily entrained into the avalanching mass (Janda et al., 1981; McGuire, 1996). It is at this point that they cease to be debris avalanches as described by McGuire (1995), and become debris flows or lahars. It is difficult to distinguish between the two types of flow, but Lahars are interpreted as being more mobile (Jakob, 2005) and tend to extend further beyond the margin of debris avalanche deposits (Siebert *et al.*, 1987). Lahars may also be formed several years after a collapse event due to break out of lakes that have been dammed by debris avalanches. As a debris avalanche travels further from the source region it loses energy, hence, typically the frequency and size of blocks falls with increasing distance from the source. This leads to a rise in the matrix proportion of the avalanche deposit. As a consequence, especially when water is involved, debris avalanche deposits often grade into debris flows as a natural progression (McGuire, 1996). Such a transition is observed at both Mount St. Helens and Mount Shasta (Crandell, 1989). Owing to the greater mobility of debris flows and lahars they can travel much further distances than debris avalanche deposits, and can impart extensive property damage and threat to human life in populated areas tens of kilometres from the original collapse event.

Tsunamis

The most potentially devastating hazard associated with large-scale volcanic edifice collapse is that of associated tsunamis. The catastrophic collapse of both ocean island and coastal volcanoes may produce large tsunamis, while volcanoes located near large inland lakes also present a similar risk (e.g. Mombacho, Nicaragua). Any large mass entering a body of water has the capability of generating a tsunami. Some 5% of all tsunamis are estimated to have been formed by volcanic activity, and at least one fifth of which are from volcanic landslides (Smith and Shepherd, 1996). Exemplified by the 1792 collapse of Mount Unzen (Japan), even small (0.34 km^3, Table 1.1) landslides can generate highly destructive waves. At Unzen, the debris avalanche, which was not accompanied by any recorded volcanic activity, entered Ariake Bay and triggered a tsunami which caused 14500 deaths (Siebert *et al.*, 1987). By far the largest proposed volcanogenic tsunamis have been associated with emplacement of the giant Hawaiian Island debris avalanches. A proposed wave-train associated with a collapse of Lanai volcano around 105 ka is reported to have crossed the Pacific and impacted energetically upon the coast of New South Wales in Australia, travelling some 8,200 km and still retaining a large destructive power (Young and Bryant, 1992). It is the large distances over which volcanogenic, landslide-induced tsunamis can have a destructive influence that makes them so potentially devastating.

The associated hazards discussed above all have the potential to impart far reaching effects, well beyond the primary volcanic debris avalanche. It should therefore be obvious why it is important to gain a better understanding of the processes that may lead to large-scale volcano flank collapse, and it should also be obvious that it is important to consider *all* forms of potential volcanic hazard at a volcano that has a history of sector collapse.

The development of instability and the conditions that favour structural failure of volcanic edifices is currently a major focus of volcanic research. The apparently common behaviour of many volcanoes to fail catastrophically is drawing attention to the frequency and the scale of the associated hazards, and in particular has highlighted the devastating consequences of a potential large volume failure occurring near a densely populated area. Perhaps the number one priority should be to implement hazard mitigation programs around all volcanoes with an identified risk. Unfortunately, without adequate monitoring and a comprehensive understanding of the processes

that drive edifice instability, such mitigation programs may be fatally flawed. For the time being, hazard mitigation programmes must evolve with the increasing knowledge that is being gained through research, and new programmes must be implemented as new areas at risk are discovered.

1.3.2 The difference between typical landsliding and large-scale volcano collapse

Large (>0.1 km^3) volcanic edifice collapses can deeply dissect volcano flanks, often creating distinctive, steep-walled amphitheatres with gently dipping floors (Siebert, 1984; Siebert *et al*., 1987). This morphology contrasts strongly with that produced through typical gravity-induced large rock avalanches, where failure tends to produce thinner collapse scars (Reid, 2004). The basal failure in typical landslides is structurally controlled and is usually congruent with the dip of the flank (Elsworth and Voight, 1996). The thinner scars produced by this type of collapse form relatively *shallow* rear scarps compared to the length of the collapse scar and these types of landslides are considered shallow within thesis. In contrast, the gently dipping basal failure in large volcanic edifice collapse events tends to be shallower than the flank angle, can cut across any structural controls, and may even dip in the opposite direction (Elsworth and Voight, 1996, Okubo, 2004). This produces relatively *deep* rear scarps compared to the length of the collapse scar and these types of landslides are considered deep within thesis. Examples of shallow collapse in volcanic terrains include the 1984 seismic induced flank collapse of Ontake, volcano, Japan (Reid, 2004) and the rainfall induced collapse of Casita, volcano, Nicaragua, (Kerle and van Wyk de Vries, 2000) while large-scale deep-seated collapse was typified by the 1980 eruption of Mount St. Helens (Voight, 1981; Voight et al., 1981, 1983).

The case of deep-seated large-scale volcano collapse is therefore problematic, as in the absence of internal pressures; failure of natural slopes only occurs if the slope angle exceeds the friction angle of the soil or rock. Deep failure has been defined by the shallow angle of the basal failure surface, which by virtue of being shallower than the flank angles will be less than the angle of friction of volcanic materials that make up the flank. Many of the giant Hawaiian landslides for example are assumed to slide over failure surfaces which have inclinations of 10° or less (Elsworth and Voight, 1995; Iverson, 1995; Voight and Elsworth, 1997). This indicates that the presence of significant additional forces are required to facilitate the collapse of these flanks. These additional forces are discussed in Chapter two.

The differences between shallow and deep landslides have profound implications for hazard assessment. Since shallow or deep failure is defined by the relative depth of the failure scarp compared to the length of the failure scar, either type can take place over a range of scales. However, for a slope of given dimensions the volume of debris avalanche produced from a deep collapse will be far greater than from a shallow collapse. It also follows that deep-seated collapse of a relatively small slope can produce more voluminous debris avalanche deposits than shallow collapse of a much larger slope. It should therefore be apparent that the scale of devastation caused by volcanic landslides depends on the processes that engender collapse, and that there is need for better understanding of the contributions that are required for the generation of deep-seated instability.

1.4 The internal gas pressure hypothesis

As will be outlined in Chapter two, there are many proposed mechanisms and triggers associated with volcanic edifice collapse. All these mechanisms and triggers are able to interact with and enhance each other, but none are omnipresent. All volcanoes that can be considered active have one thing in common: they all must have somewhere beneath or within them a magma body. As long as this magma remains molten it can provide a source of heat, differentiate and crystallise, and in the process generate excess volatiles within the magma body.

Through the heating (boiling) of ground water and the escape of the volatiles from the magma, it is possible to generate substantial amounts of pore fluids, in particular volcanic gases. While the emission of these gases has long been routinely monitored, little is known of the mechanical effects of the gas phase on the shear strength and structural integrity of the edifice. These volcanic gases are continually generated as long as the volcano remains active, and may lead to substantial pore pressure increases especially when combined with pore pressures generated hydrostatically, related to a ground water level within the slope. It is proposed that, in principle, internal gas (fluid) pressurisation can play a critical role in weakening a volcanic edifice, promoting structural instability on a large scale, resulting in rapid destabilisation and massive sector collapse.

1.4.1 Aims and objectives

Aims

The aim of this study is to investigate the role of internal gas pressure in promoting volcano instability, hence improving the insights into the causes of large volcanic landslides. The specific dynamics of pore fluid (gas) pressure generation and enhancement are not directly under investigation, and significantly elevated pore pressures generated by this method are assumed possible. Only the influence of such events are being investigated.

Objectives

Through the course of this thesis it will be demonstrated through the use of several techniques, that internal pore fluid (gas) pressurisation plays an important role in the generation of deep-seated volcanic instability.

Firstly it will be demonstrated through the use of geomechanical classification schemes that a volcanic edifice is not a strong and coherent mass of material and can be considered as an inherently weak structure that may be susceptible to regular slope failure.

The validity of the internal gas pressurisation hypothesis is then tested, initially through the use of simple, sand pile, scaled analogue models pressurised from a source of compressed air. This is followed by further more rigorous investigations undertaken using numerical methods.

Simple two-dimensional limit equilibrium calculations are used to exemplify the difference in stability between that of a volcanic edifice with no excess internal pore pressures derived from deep sources, and that of one with such conditions.

More detailed modelling is then conducted using $FLAC^{3D}$ in full three-dimensional form using finite-difference computation. This allows consideration of the interaction between internally elevated pore fluid pressures and other conditions that may influence stability. These conditions include the effect of a weak substratum, over-steepened slopes or regional gradients. Finally, the modelling approach highlights the potential of $FLAC^{3D}$, a readily available commercial geotechnics code, to contribute significant new knowledge in the quest to better understand the mechanics of volcano instability.

1.5 Thesis road map

The Introduction and Chapter two lay the foundations by outlining the current understanding of volcano edifice collapse. Despite many studies, theories regarding volcanic edifice collapse still involve large amounts of conjecture and it is clear we still have a lot to learn.

Chapter three introduces in detail, the concept at the heart of this thesis, namely a destabilising process involving the build up of internally sourced pore fluid (gas) pressures. Possible sources of deep generated gas pressurisation are identified, and the effects of a substantial gas phase on the structural integrity of a volcano are discussed.

Chapter four shows how the stability of a volcanic slope can be quantified by introducing the concept of the "rock mass". It is shown that a volcanic edifice can be considered an inherently weak structure, vulnerable to a range of internal or external triggers.

The following chapters (five and six) are the results sections. These chapters detail the range of analogue and numerical modelling experiments undertaken to investigate and quantify the role of internally sourced pore pressure increases in destabilising a volcanic edifice. Chapter five is concerned with the analogue modelling and Chapter six with the two-dimensional limit equilibrium modelling and full three-dimensional finite-difference modelling through the use of $FLAC^{3D}$. Finally, the last Chapter, seven, contains a discussion with concluding remarks.

2. Collapse theory

2.1 Pre-May 1980

Prior to the events at Mount St. Helens in May of 1980, very little information existed in the literature about the mechanisms and triggers of large-scale collapse events. Some consideration was given to the mapping and identification of the chaotic debris flow deposits that had been found surrounding several volcanoes (e.g. Gorshkov, 1959, 1963; Moore, 1964), but no real attempt was made to study the causes or consequences of these deposits. Thus, although the evidence existed to demonstrate the potential for volcanoes to undergo large-scale sector collapse, volcanologists were still mainly thinking '*upwards*' not '*outwards*'.

2.1.1 The first true recognition of volcanic landslides?

Arguably the first publication to address specifically the issue of volcanic landslides was the 1950 paper of R.W. Fairbridge "Landslide Patterns on Oceanic Volcanoes and Atolls". Drawing on aerial photography taken during the Pacific war, Fairbridge (1950), remarked that "*It appears that the concave "bights" in the normally convex outlines of both oceanic volcanoes and coral atolls may be engendered by big submarine landslides*". When discussing the oceanic volcano of Goenoeng Api (6° 41' S., 126° 41' E), it was noted that theoretically the shape of the island (which represents the top of a submerged cone) should be circular and indeed the submarine contours indicate that it is very nearly so at depth. But at sea-level its plan exhibits a number of deep arcuate gashes, or bights, interrupting the otherwise circular outline. Fairbridge rejected the concept of subaerial valley erosion and it was suggested that these concavities are giant landslide gashes. This theory was backed up by soundings, that not only clearly indicated the positions of the slides, but also the fans of debris at the foot of the old pile (Fig. 2.1). It was also noted that two of the three slides did not break the crater, thus the sliding was interpreted as independent of the eruptions with the steep slopes and stratified nature of a volcanic cone considered sufficient causes for producing large landslides. However, it was also suggested that associated seismic action may well be expected to operate as a trigger mechanism, and interestingly this is a mechanism that is still considered to operate in a primary role today (McGuire, 1996, Thomas *et al.*, 2004a). Fairbridge (1950) made no attempt to explain the processes or consequences involved with volcanic collapse other than the
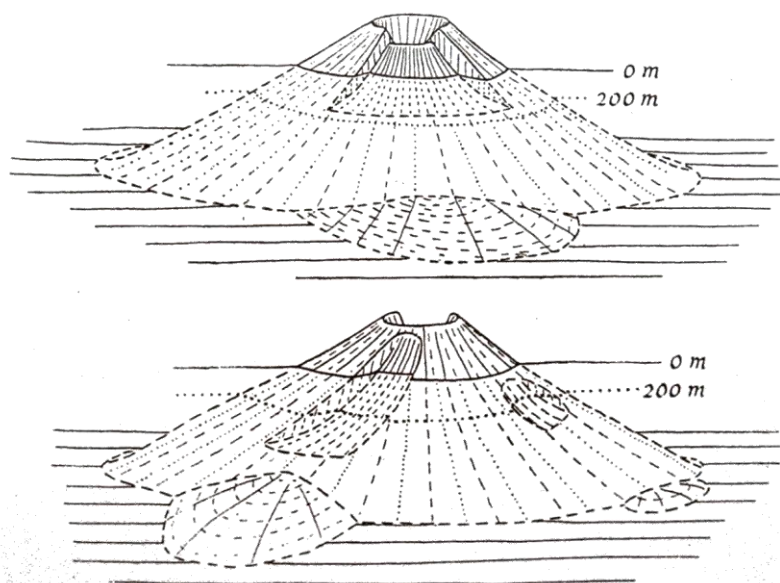
Figure 2.1: A sketch from Fairbridge (1950) of the oceanic volcano of Goenoeng Api (6° 41'
S., 126° 41' E), showing the positions of the slides, and also the fans of debris at the foot of
the old volcanic pile inferred form depth soundings.

brief mention of seismic action operating as a potential triggering mechanism but did comment that

"*it is remarkable that the gravitational collapse of such cones does not take place on a large scale*".

This statement must be assumed to refer to landslide processes encompassing whole volcanic

flanks, as he previously described the bights on Goenoeng Api as "*giant landslide gashes*". It is

now apparent that collapse of volcanic edifices on a grand scale is common-place during a

volcano's lifetime and it is this lack of comprehension of scale that appears to been the greatest

limiting factor on the understanding and recognition of giant volcanic landslides prior to the giant

landslide and explosive eruption of May 18th 1980 at Mount St. Helens.

2.1.2 Problems with recognising the scale of volcanic landslides

Few authors prior to May 1980 recognised the hazard potential of large-scale volcano instability,

but Moore (1964), reported on two large landslides on the slope of the Hawaiian ridge northeast of

Oahu. He described one of the slides as "*more than 150 km long and this largest slide extending

northeast is also marked by a blocky welt in the middle and the lower end*". The sole of the slide is

estimated at 6000 m below sea-level and averages 2,000 m in thickness (Fig. 2.2). The important

observation that the upper end of the slide was marked by a distinct concavity in the regional slope

was also made, and it was commented that this large amphitheatre was also typical of many
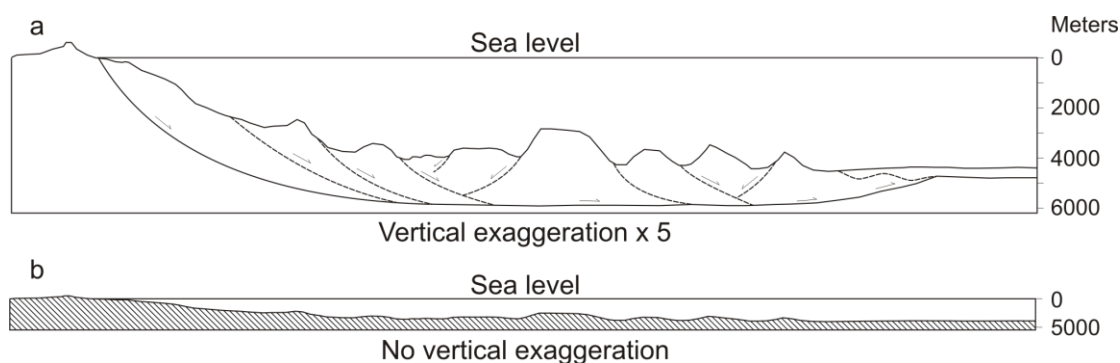
Figure 2.2: Schematic cross section adapted from Moore (1964), showing the submarine topography north-east of the island of Oahu, Hawaii. This possible landslide suggested by Moore (1964) has since been confirmed as the Nuuanu landslide, the world's largest recorded volcanic landslide covering an area of approximately 23,000 km^2.

smaller landslides. Source region amphitheatres are one of the major features used today for identifying possible sites of past mass movements in volcanic terrains. Much like Fairbridge (1950), Moore (1964) concluded that the position of the steep slopes of the Hawaiian volcanoes is favourable to landsliding adding that "*large structures have also been mapped on several of the volcanoes above sea-level, best seen on Hawaii in the south east*".

While only some authors recognised the signs of volcanic landslides, fewer still recognised their potential scale, and the majority of scientists working in the field of volcanology made little reference to the notion of volcanic flank collapse through the process of large-scale landsliding. The lack of understanding of the processes involved in large-scale volcanic flank instability and collapse is exemplified in Ridley (1971). Discussing the origin of collapse structures in the Canary Islands, he comments; "*Their size precludes landsliding as the dominant force in their formation, although it may have played a minor role in modifying the bounding walls*". Instead, it was thought that migration of magma away from a general area of the fissure zones towards the flanks caused collapse on a large scale by a trap-door mechanism, resulting in calderas considerably different from those of volcanoes with a central magma chamber. The Orotava and Güimar valleys are today uniformly recognised as two of the largest volcanic landslide scars on the planet (Hürlimann *et al.*, 1999; 2001, Ablay and Hürlimann, 2000). It may be said that, before first hand observation of the events at Mount St. Helens, the theory of *giant* volcanic landslides really was *too big to believe*. It is beyond doubt that the collapse of the North sector of Mount St. Helens identified and focussed attention on the possibility of large-scale volcanic edifice collapse. It is sobering to think that,

without the Mount St. Helens eruption, there may still today be little appreciation of the threat posed by giant volcanic landslides, particularly those in a continental setting.

2.2 Post-May 1980

An unexpected turn of events can quickly focus attention on what was once hardly noticed. That is exactly what happened in the aftermath of the 1980 Mount St. Helens eruption.

Within seven years of the Mount St. Helens eruption, 196 potential large scale volcanic debris avalanches had been identified globally within the Quaternary. Major slope failures and associated explosive eruptions had been attributed to more than 20 000 fatalities in the previous 400 years, with 17 historic events estimated to have occurred between 1628 and the 1980 Mount St. Helens event (Siebert *et al.*, 1987). This represents an unprecedented increase in the recognition of a geological hazard. While Siebert *et al.*, (1987) concurred that "*Detailed investigations (*referring to Mount St. Helens*) have provided new insights into a type of eruption that had previously received little attention*", concern was expressed about the influence that a single well-documented eruption would have on interpretations of similar events elsewhere. This was a valid concern, as no two flank collapses are likely to be identical in terms of precursors, triggering mechanism and eruption style, but similarities *are* to be expected.

There are now over of 500 recognised cases of volcano edifice collapse, which have resulted in large volcanic debris flows (Siebert, 1992). More importantly, the hazard potential posed by such events has now been identified. Siebert (1992) estimated that structural failure of volcanic edifices has occurred globally four times a century over the last 500 years, while McGuire (1996) infers that this may be an underestimate.

2.3 Types of eruption (Bezymianny - Bandai - Unzen - type)

When discussing large volcanic landslides in association with eruptions, there are now two widely accepted eruption types. The 1888 eruption of Bandai volcano, Japan, and the 1956 eruption of Bezymianny, Kamchatka, both produced large debris avalanches and formed morphologically similar horse-shoe shaped craters (Siebert *et al.*, 1987). It was suggested by Siebert *et al.*, (1987) that the terms Bezymianny - and Bandai - type eruptions be used to classify eruptions associated

with the formation of similar depressions, the former having a magmatic component, and the latter being solely phreatic. The characteristics of Bezymianny - and Bandai-type eruptions are summarised in Table 2.1. Ui (1985), introduced a third, less frequent type of eruption associated with formation of volcanic debris flows and horseshoe-shaped calderas; in this example the characteristic morphology of a volcanic edifice that has undergone flank collapse is produced, but without any accompanying eruption (magmatic or phreatic); although eruptions may have occurred at nearby volcanoes. Ui (1985) referred to these as Unzen-types events, after the 1792 "*eruptions*" at the Unzen volcanic complex, Japan. Collapse events of this type are often attributed to the effects of large-scale hydrothermal alteration (Lopez and Williams, 1993).

The frequent occurrence of lateral blasts with large volcanic landslide avalanches distinguishes these eruptions from other types of explosive activity. As discussed by Siebert (1987), the lateral blasts associated with landslides have often been interpreted as large-scale phreatic or hydrothermal explosions (e.g. Gorshkov, 1959). However, unlike steam blast explosions, large horseshoe-shaped craters or calderas are formed. These depressions have also been attributed to an explosive origin, but it can be shown that their volumes are equivalent to those of the associated debris avalanche deposits (Fig. 2.3). This demonstrates that slope failure dominates their formation (Siebert, 1984), and that the lateral blasts are almost certainly due to decompressive explosions

Bezymianny-type	Bandai-type
Pre-paroxysmal phreatic or magmatic eruptive activity	Typically sudden initiation of paroxysmal phase
Paroxysmal eruptions are magmatic and phreatomagmatic	Nonmagmatic paroxysmal eruptions
Lateral blast possible ($10^7 - 10^8$ m^3)	Lateral blast less likely
Debris Avalanche ($10^8 - 10^{10}$ m^3)	Debris Avalanche ($10^7 - 10^{10}$ m^3)
Pumiceous pyroclastic flows ($10^7 - 10^8$ m^3)	No pumiceous pyroclastic flows
Air-fall tephra ($10^7 - 10^9$ m^3), mostly juvenile material	Air-fall tephra (10^6-10^8 m^3) accessory material only
VEI 3 – 5	VEI 2 – 4
Construction of post-paroxysmal lava dome or central cone	Eruption typically ends with paroxysmal phase

Table 2.1: Characteristics of Bezymianny- and Bandai-type eruptions. Adapted from Siebert *et al.*, (1987). VEI is the Volcanic Explosivity Index (Newhall and Self, 1982)
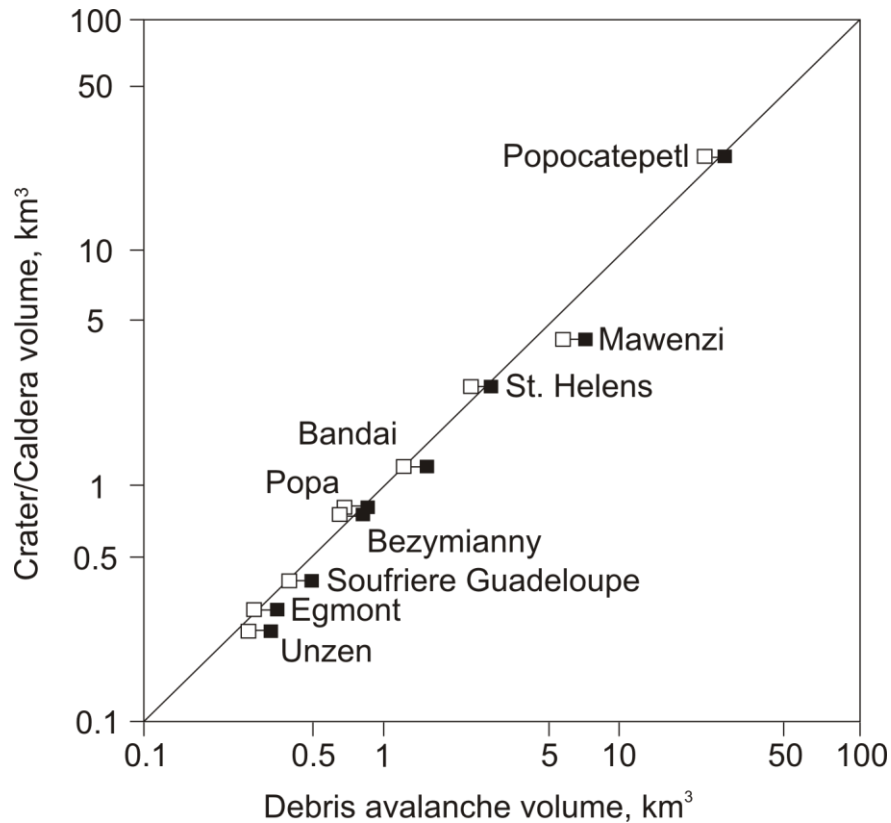
Figure 2.3: Volume of debris avalanche deposits compared with volume of missing sector of volcano (modified from Siebert, 1984). Black squares represent measured volumes of debris avalanche; open squares, in situ pre-avalanche volumes within the volcano, assuming 25% expansion during transport and deposition, except for the St. Helens in situ volume, which is a calculated volume.

caused by the unloading associated with the movement of the landslide mass. This is the case for all true occurrences of large-scale volcanic flank collapse, and in the case of some collapse events, no paroxysmal eruptions may have occurred without the onset of the movement of the landslide.

2.4 Processes and deposits of giant sector collapse

The processes of flank collapse may occur several times at a volcano (Ablay and Hürlimann, 2000), forming individual collapse scars or enlarging previously existing scars. Like collapse calderas, some of which form by incremental growth during successive eruptions (Walker, 1984), some avalanche calderas form in multiple episodes, with the orientation of subsequent slope failures being influenced by earlier failure scarps and deposits (Tibaldi, 2004). However, this incremental growth need not be over several events. For example, it is now accepted that the failure of the north flank of Mount St. Helens occurred in stages, as three retrogressive slide blocks
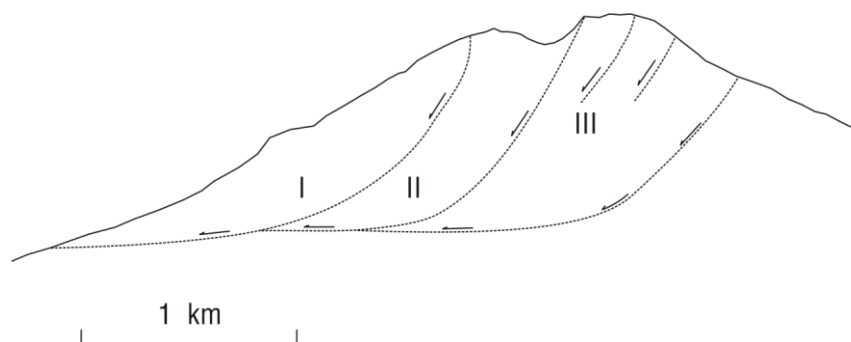
Figure 2.4: Cross-section of Mount St Helens volcano, 1980 (modified from Voight and Elsworth, 1997). The collapse was interpreted as retrogressive failure of three principal blocks, indicated by the Roman numerals.

(Fig. 2.4) (Voight and Elsworth, 1997). Each subsequent block failed in turn as the system tried to adjust to rapid changes in stress and pore pressure states due to the near instantaneous collapse and removal of the overriding failed mass.

The size of volcanic landslides varies greatly (Fig. 2.3), they are now recognised to range from small or moderate rock-slide avalanches with volumes of a few hundred to a few thousand cubic metres (e.g. Siebert *et al.*, 1987, McGuire *et al.*, 1991), to massive slope failures involving entire sectors of the edifice involving volumes in excess of 5,000 km^3 (e.g. Moore *el al.*, 1994). Ground failure in most volcanic terrains inevitably involves gravity-driven, down slope mass-transfer from the source to the deposit area. The great potential energy of large volumes of rock atop high standing volcanoes enables rapid movement of debris over long distances (Siebert *et al.*, 1987). In the case of minor rock-falls, the distances involved may only be of a few tens to hundreds of metres, but at the other end of the scale, the giant Hawaiian landslides have travelled distances of several hundred kilometres (Moore *et al.*, 1994). Summarised in Table 1.1 are some of the most influential recorded debris avalanches. No two collapse events form identical deposits or follow exactly the same path. Depending on factors, such as the nature of the failed material, the underlying terrain and the precise failure mechanism, the transported mass may continue to travel in a coherent block or become completely disrupted (McGuire, 1996).

Volcano collapse data from around the world show that horse-shoe calderas have lengths between 2 and 7 km and equal or less width. The manner of collapse causes large blocks of the edifice to mix with altered rock from any hydrothermal systems, with the amount of altered minerals in the resulting deposit ranging from 0.5 to 5 % (Lopez and Williams 1993). Many authors have linked the

mobility of volcanic debris avalanches to the presence of hydrothermally altered material within the avalanche (e.g. Siebert *et al.*, 1987, Lopez and Williams, 1993) and this may explain the excess travel distance of some volcanic debris avalanches. For historic examples of volcanic debris avalanches and many ancient deposits, the ratio of vertical drop to run out length is much lower than the ratio in non-volcanic debris avalanches of similar volume. The reason is that the majority of hydrothermal processes form large volumes of clay minerals, and it has been found that the presence of clay in volumes as low as 1% - 2% contributes greatly to the mobility of non-volcanic debris avalanches (Costa, 1984); thus, the same can expected for debris avalanches of a volcanic origin.

However, it is not necessary to have large-scale hydrothermal alteration to involve clay minerals in the process of volcanic flank collapse. The size of the failure generally dictates whether the failure is confined solely to the volcanic edifice or whether it involves the underlying basement, with the latter having profound effects on the composition and physical properties of the debris avalanche and deposit. Many volcanic edifices are built on clay-rich sediments (van Wyk de Vries and Borgia, 1996), and large failures, which incorporate a substantial volume of the sub-volcanic basement may enrich the debris avalanche with clay minerals in this way. At Socompa, in Northern Chile, a debris avalanche deposit containing up to 60% basement material has been documented (van Wyk de Vries and Francis, 1997), and at Mombacho, Nicaragua, a weak zone located in the sub-volcanic basement, which is formed of clay-rich old oceanic crust of the Cretaceous Nicoya complex, is about 20% of the total height of the edifice (van Wyk de Vries and Borgia, 1996, van Wyk de Vries and Francis, 1997). The presence of these weak and extensively altered materials, especially clays, producing low-angle detachment surfaces and accompanied by the boiling of supercritical hydrothermal fluids, is predicted to be a major factor in producing low-rigidity, perhaps partially fluidised avalanches (Voight *et al.*, 1983, Lopez and Williams, 1993, Day *et al.*, 1997).

2.5 Precursors

There may be few warning signs of an ensuing volcanic collapse event, and what warning signs exist may be missed. This is because any collapse event with a magmatic component will exhibit all the precursors of a normal magmatic eruption including significant seismic and volcanic activity, with the volcanic activity taking the form of either phreatic or magmatic eruptions. (Fig. 2.5).

Conversely, showing how important it is not to rely on signs of seismic and volcanic activity; deformation and small slope movements were all that immediately preceded the 1792 Unzen avalanche (Siebert *et al.*, 1987). Caution should be taken if basing any risk assessment on precursory event ... movements, that are precursory to both non-volcanic and volcanic slope failure alike, may be cut short by external triggers (Voight *et al.*, 1981; 1983).

Figure 2.5: Duration of precursory seismic and/or eruptive activity of post-paroxysmal eruptions (modified from Siebert et al., 1987). 1. precursory seismic activity; 2, phreatic eruptions; 3, magmatic eruptions.

Seismic activity

Prior to the 1980 Mount St. Helens eruption, earthquakes occurred repeatedly for nearly two months, although the number of smaller earthquakes decreased (Endo *et al.*, 1981). Over 10,000 earthquakes were recorded between 20 March and 18 May, 1980, and of these, 2400 were of local magnitudes greater than 2.4 (Endo *et al.*, 1981; Malone *et al.*, 1981). In addition, many phreatic eruptions were observed prior to the failure event (Voight *et al.*, 1983). The period of seismic activity prior to the 1980 Mount St. Helens eruption correlates directly with, and may result in part from, deformation (Okada, 1983). Precursory seismic and volcanic activity however, does not necessarily warn of the threat of large-scale volcanic flank collapse, as these are signs usually detectable at any erupting or active volcano.

Ground Deformation

Major deformation of the flanks of a volcano may cause oversteepening. In terms of a possible large-scale flank collapse, an oversteepened slope is a more worrying precursor than seismic or general volcanic activity, as it acts to fundamentally weaken the flank of the volcano. The unseen intrusion of a cryptodome at Mount St. Helens (Donnadieu and Merle, 1998) caused massive deformation of the north flank, with the average horizontal displacement reckoned from 25th March to 7th April being 4.7 m/day; the maximum rate was 9.7 m/day (Voight *et al.*, 1983). The volume increase associated with the oversteepening of the North slope and the formation of a bulge was estimated to be 0.12 km^3 (Jordan and Kieffer, 1981). Large scale deformation may also be expected to produce outward-dipping normal faults, leading to the formation of small grabens and flat shear zones may become visible (Donnadieu *et al.*, 2001).

2.6 Generating structural instability and triggering collapse

McGuire (1996) stated that, "*structural failure – the common outcome of edifice instability – may, like the attainment of instability itself, take place over a range of time-scales*". This statement suggested that there are many processes that may play a pivotal role in volcano flank failure, each of which may work on different timescales. It will be show in this Section that the causes of volcanic instability and ensuing failure are indeed numerous (Fig 2.6), and rarely if ever, confined to the effects of a single process or condition. These processes and conditions can be broadly separated

Process or Condition	Ability to Generate Instability	Ability to Trigger Collapse
Dyke Intrusion	✓	✓
Rifting	✓	
Volcanic Spreading	✓	
High level magma Intrusion (Not Dykes)	✓	✓
Pre-existing Basement Faults	✓	✓
Weak Core	✓	
Surface Loading	✓	✓
Seal-Level changes	✓	
Siesmogenic Ground Accelerations		✓

Table 2.2: Commonly accepted processes and conditions that can *generate* instability and/or that *trigger* collapse. For a full description of each process see the text.
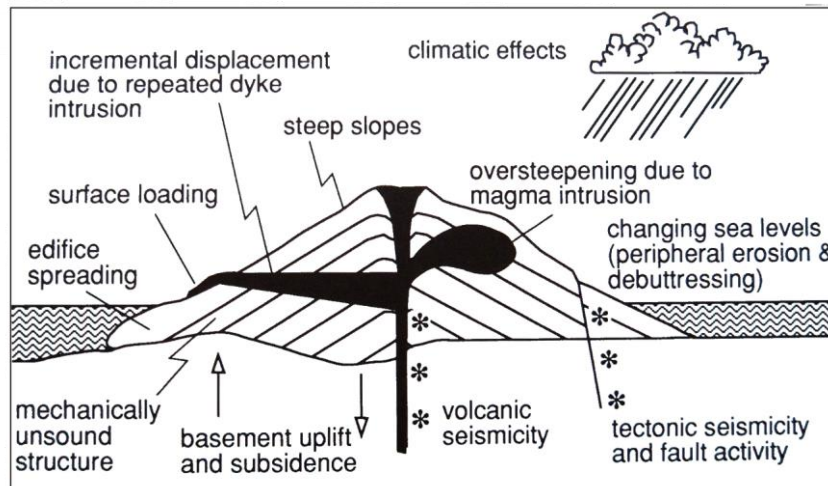
Figure 2.6: Factors contributing to the development of structural instability at active volcanoes (from McGuire, 1996).

into two categories; those that *generate* instability and those that *trigger* collapse (Table 2.2). In this thesis, a trigger is defined as *any event that initiates a rapid movement or complete failure of a volcanic flank*. It is important to note that using this definition some volcanic collapse events may have occurred without the effect of a "trigger" and these events represent failure of a volcano flank that has been sufficiently destabilised to fail solely under the effect of gravity. An example of such behaviour is suggested at Mount Rainier where massive amounts of hydrothermal alternation have significantly weakened large volumes of the rock mass (Reid *et al.*, 2001). Some processes may also facilitate both the underlying generation of instability and the instantaneous triggering of collapse. For example, the surface loading of a relatively stable slope may simply decrease its

notional stability, while the same event occurring on a slope that is already close to failure may be enough to directly trigger collapse.

The development of major structural failure (collapse volumes > 0.1 km^3) tends to be confined to the larger edifices (McGuire, 1996), a statement somewhat confirmed, as less than 10% of volcanoes < 500 m high compared to greater than 75% of volcanoes > 2,500 m high have experienced a major collapse event in the central Andes (Voight, 2000). It would appear that the generation of volcanic instability is, in some way, linked to the size of the volcanic edifice, with small monogenetic cones only experiencing small-scale slumping and sliding (McGuire, 1996), and the truly massive collapse events are only characteristic of major polygenetic volcanoes.

Dyke Intrusion

The intrusion of dykes, much like any other intrusion, gives rise to changes in pore fluid pressures. Any increase in pore pressures will act to decrease stability by reducing the effective stress (Terzaghi, 1943). For a detailed explanation of effective stress the reader is directed to Section 3.2, but for the purposes of this Chapter, the fluid pressurisation mechanisms associated with dyking and magmatism identified by Voight and Elsworth (1997) include:

- Those mechanically developed in porous elastic media around rapidly-intruded dykes

- Thermal expansion of aquifer pore fluids

- Pressurised volatile separation in high level intrusions

- Hydrothermal system overpressuration mechanisms

- Shaking-induced pore-pressure generation (from intrusion related siesmicity)

Thus, dyke intrusion is seen as a driving force in the initiation of instability by way of direct magma pressurisation, and by decreasing the resisting force by way of pore fluid pressure enhancement (Elsworth and Voight, 1996; Voight and Elsworth, 1997). Dyke intrusion can also be considered as a trigger. Iverson (1995) asked the question "*can magma-injection and ground water forces cause massive landslides on Hawaiian volcanoes?*". On the scale of the Hawaiian slides the answer appeared to be *no*; although Iverson concluded that a sector of a flank 3-4 km long could well be

displaced by dyke injection, the potential excess magma pressures were concluded not to be high enough to be the sole contributor toward the triggering of the massive Hawaiian volcanic landslides. Progressive weakening of slip-surfaces, which would result in anomalously low friction angles, was proposed as a potential method of allowing the large scale Hawaiian landslides to exist. In this case, the triggering mechanism (dyke injection) would essentially short cut the long-term generation of instability (weakening of the slip-surface), which, given time may have resulted in failure. Contrary to Iverson's findings, Voight and Elsworth, (1997) concluded that considering the site-specific structure and stratigraphy of individual volcanic flanks, the potential for failure appears feasible as a result of this triggering mechanism at *certain* locations. Frequent seismicity may also accompany dyke intrusions and seismicity is discussed as a separate triggering event.

Rifting

Rifting, while associated with persistent dyke emplacement, is considered separately as it acts on a scale and time span that precludes it being considered a trigger. Rifting constitutes a major contributory factor in the progressive development of instability (McGuire, 1996). Rifting can occur in a number of different ways. Incremental displacement of an entire flank due to repeated dyke intrusion leads to increases in dilatational stresses through dyke wedging, leading to substantial strain weakening. Where a preferred emplacement vector for radial dykes and parasitic cones parallel to the directions of maximum horizontal compression exists (i.e. a rift zone), the result is an elongation of the edifice, and development of an asymmetrical stress field. Unsurprisingly, flank failure often occurs normal to this direction (Voight and Elsworth, 1997). This behaviour has been identified at many volcanoes world-wide, (Siebert, 1984; Carracedo *et al.*, 1999; Tibaldi, 2004). Not only does the persistent intrusion of dykes influence the stress field and hence the failure locations, but repeated intrusion also decreases the strength of the volcanic rock-mass (see Chapter four for further information on the importance of rock-mass principles). For every repeated intrusion a new set of fractures are produced, or existing sets are modified. Consequently the peak strength of a fractured rock mass within an active rift zone is constantly reduced by the introduction of new discontinuities.

It is undoubtedly the case that instability is commonplace at rift zones. However, what remains unclear is whether outward movement of volcanic flanks leads to the passive rising of magma, or

whether intrusion, in the form of dykes, drives flank movement. Bonforte and Puglisi (2003) note that sliding of the east and south flanks of Mount Etna volcano has generally been interpreted as a passive effect of the dyke intrusion, but their work highlights that flank movements are observed without evidence of shallow intrusion and could even facilitate the magma ascent. This theory is supported by Tibaldi and Groppelli (2002), who suggested that magma can passively rise under the rift governed by the collapsing east flank of Mount Etna. It was also noted that many seismic ruptures occur without eruptions, and seismic creep does not usually correlate with eruptions, suggesting that gravity is the driving force and intrusion may only act as an accelerant. Rifting however, is more prominent at some volcanoes than others that have experienced massive flank collapse (e.g. Tenerife compared with Mount St. Helens), so is unlikely to be a common denominator of volcano collapse events.

Volcanic Spreading

All of the earth's largest volcanoes undergo structural adjustments in response to their increasing size and weight. Commonly, these adjustments originate from deep within the volcanoes' edifices and even their substrates. Although the deformations involve settling or collapse of upper slopes and summits of volcanoes, they ultimately produce horizontal motion along their distal slopes and even beyond (Borgia *et al.*, 2000). Therefore, the role of the sub-volcanic basement in the development of instability in volcanic terrains *cannot* be underestimated. The substrates upon which volcanoes rest may often be sediments lithified by no more than the weight of the volcanic edifice itself, the growth of a volcanic edifice on a weak substrate strongly promotes volcanic spreading (McGuire, 1996). The contact between the volcanic pile and the basement can be considered as a large discontinuity. Hydrothermal alteration along this pre-existing structural discontinuity may produce favourable conditions for volcanic spreading and the initiation of deep-seated failure surfaces (Donnadieu *et al.*, 2001). van Wyk de Vries and Francis (1997) suggested that Mombacho volcano in Nicaragua experienced failure caused predominantly by basement spreading, but the time scales involved in such a process can not account for collapse intervals such as those recorded at Augustine volcano, Alaska (Siebert et al., 1995).

High level magma intrusion

The large-scale endogenetic addition of magma can lead to rapid oversteepening (McGuire, 1996) (Fig. 2.6), and this type of behaviour was witnessed preceding the collapse of Mount St. Helens (Voight *et. al.,* 1983). Oversteepening is often accompanied by the upturning of strata, so that any planes with low shear strength that were created during the building of the edifice are rotated into a more vertical orientation. Other causes of instability during magmatic intrusion include the generation of major shear faults (Donnadieu and Merle, 1998) caused by the displacement of the volcanic slopes to accommodate the intrusion. It is possible that these major shear faults may act as guides for failure surfaces.

Large intruded magmatic bodies remain hot for a considerable period of time after emplacement and consequently remain less viscous and much more deformable than the surrounding country rock, being mechanically weaker than the pre-existing edifice rocks and act to generate a form of instability (Donnadieu and Merle, 1998). Intrusion at relatively high levels within an edifice not only creates bulging and oversteepening, but commonly produces a system of faults that can lead to the formation of summit grabens as observed at Bezymianny volcano and Mount St. Helens (Donnadieu and Merle, 1998; Donnadieu *et al.*, 2001). These large-scale structural changes would clearly have an adverse effect on the general stability of a volcano as any faulting or fracturing of the rock mass would decrease its strength. High level intrusions of this type can also cause increases in thermal and mechanical pore pressures as discussed in response to dyke intrusion, with similar destabilising effects. The processes associated with high-level intrusion can be considered separately as triggers in their own right because although an edifice may have experienced similar activity in the past without failure, it may have been weakened enough for any new intrusion to trigger an almost instantaneous collapse. A large non-volcanic fissure opened during the 1949 eruption of the Cumbre Vieja volcano, La Palma, Canary Islands, with vertical displacements of a maximum of 4m, and dipping at roughly 60°. Why was it showing signs of instability after this eruption? There had been previous eruptions. One possible reason for this is that the edifice may have been potentially unstable for a substantial part of its history, but it may have passed a critical point after which strain weakening set in (Day *et al.*, 1999).

In general magmatic intrusion (including dyke intrusion) is now considered as one of the primary triggers of large-scale collapse (Elsworth and Voight, 1995; Voight and Elsworth, 1997; Elsworth and Day, 1999). Magmatic intrusions can also play a role in generating what is considered an equally important trigger; seismogenic ground accelerations which are discussed as a separate mechanism in this Section.

Pre-existing basement faults

Vidal and Merle (2000) recently proposed a novel model of flank collapse involving reactivation of basement faults beneath a volcanic edifice. In the models, collapse is produced by the interaction of a normal (vertical) basement fault and the edifice, producing an upturning of layers, which develops a bulge within the deformed flank. This model has almost identical visual precursory activity to that of models concerning high-level magmatic intrusions, and although a different mechanism, instability is essentially generated in the same manner through oversteepening and weakening of the edifice flanks. The one major difference between the two models is that the reactivation of basement faults does not need to be accompanied by magmatic activity. Ultimately, through progressive weakening, the repetitive faulting model is capable of producing edifice collapse in the absence of volcanic activity (Vidal and Merle, 2000). Such behaviour is interpreted to have occurred at Cantal volcano, Massif Central, France (Vidal and Merle, 2000) Conversely a single reactivation of a basement fault could be enough to directly trigger flank collapse of an already unstable edifice. This implies that edifice failure should be of concern at long inactive volcanoes (Vidal and Merle, 2000). While the model of Vidal and Merle (2000) is concerned with normal faulting, both reverse and normal faulting (uplift or subsidence) have the potential to decrease edifice stability, as shown in Figure 2.6 (McGuire, 1996).

Weakened core

Although the sub-volcanic basement may offer the right conditions for volcanic spreading, this type of behaviour is not confined to within the basement. Hydrothermal activity within volcanic edifices often leads to development of weak cores as a result of alteration. This leads to a mechanically unstable edifice that is able to deform until potentially catastrophic collapse occurs, or a stable shape is regained (Cecchi *et al.*, 2005). Gravitational deformation, flank spreading and ultimately

flank bulging leading to collapse (Fig. 2.6) may be responses to a hydrothermally altered weak core. Once again, the formation of a flank bulge, similar to those created by magma intrusion (Donnadieu and Merle, 1998) and also by reactivation of basement faults (Vidal and Merle, 2000) may be seen as the final response to a weakened core. Although producing structures similar in appearance, a distinction between the processes that produce them should be possible, as each of the mechanisms would theoretically be accompanied by differing precursory activity. These include, but are not limited to, the occurrence of magmatic activity, large-scale seismicity and the speed of deformation. The presence of a weakened core is not ubiquitous however, and substantial debris avalanche deposits totalling 180 km^3 have been found surrounding Cantal volcano, Massif Central, France, which shows no signs of having an extensively altered core (Vidal and Merle, 2000).

Surface Loading

Placing additional weight on potentially unstable volcanic flanks (i.e. loading of an unstable surface through extrusion (Fig 2.6)) has the ability to further decrease stability or if the flank is sufficiently unstable trigger failure. This type of behaviour has been recorded at Llullaillaco volcano, northwest Argentina. Young dacite lavas have been interpreted as being erupted from a central vent on top of the older edifice. The viscous nature of these flows resulted in stacking of short stubby flows overloading the already steep and unstable older edifice, cumulating in a 1-2 km^3 collapse of its south eastern flank approximately 0.15 Ma (Richards and Villeneuve, 2001). Endogenic changes to a volcano have not been recorded at many sites of volcano flank collapse (Siebert *et al.*, 1987) so can therefore not be considered as a primary process in generating volcano instability and triggering collapse.

Sea-level changes

Sea-level changes may play a major role in destabilising oceanic volcanoes. Some coastal volcanoes may also be affected in a similar way, but to a much lesser extent (McGuire *et al.*, 1997). Oceanic volcanoes are massive structures, with much of their mass below sea-level. The force of the water surrounding the volcano acts as a support to the huge weight of the volcanic pile, buttressing the edifice and helping to stabilise any mobile sectors. Any fall in sea-level can reduce

the buttressing effect, consequently reducing the overall stability of the volcano flanks. Falls in sea-level will also sub-aerially expose new parts of the edifice, this leads to peripheral erosion which can lead to oversteepening and destabilisation of the volcanic flanks. Some tentative links have been made between falling sea-levels and collapse events in the Canary Islands (Fig. 2.7) (Carracedo *et al.*, 1999), but the age correlations are not entirely convincing. However, oceanic collapse events occurring in periods of low sea-level is consistent with the theory of Weaver *et al.*, (1992), that megaturbidites can also be shown to coincide with changing sea-level.

Seismogenic Ground Accelerations

Seismogenic ground accelerations (earthquakes), play a *significant* role in triggering volcanic edifice failure. The failure event at Mount St. Helens was an eye-opening example, within 10 seconds of the time of the initial earthquake disturbance (Voight, 1981) the north slope began to slide northwards along the recently formed fracture system, beginning the formation of the rapid moving debris avalanche (Voight *et al.*, 1983).

Triggers of a seismic nature can be either internal or external with respect to the edifice. Internal seismic triggers are related to magmatic movement within the edifice and thus can be termed volcanogenic earthquakes. Pore fluid pressure increases induced through magmatic intrusion have
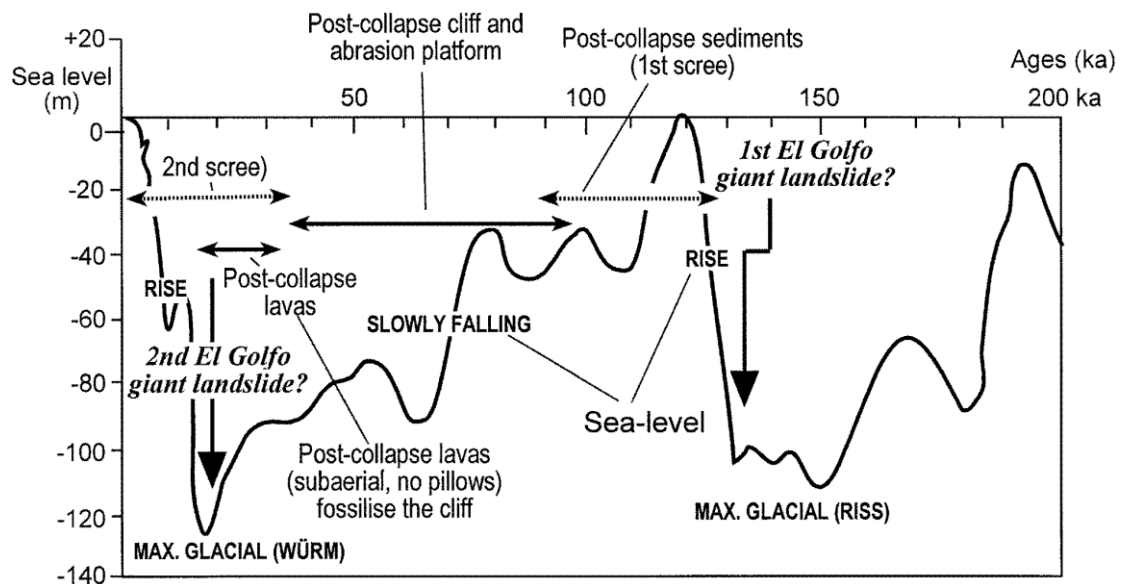
Figure 2.7: Sea level curve adapted by Carracedo *et al.,* (1999) showing that the age constraints of the two giant El Golfo landslides on El Hierro, Canary Islands, are consistent with both events occurring at low sea level stands.
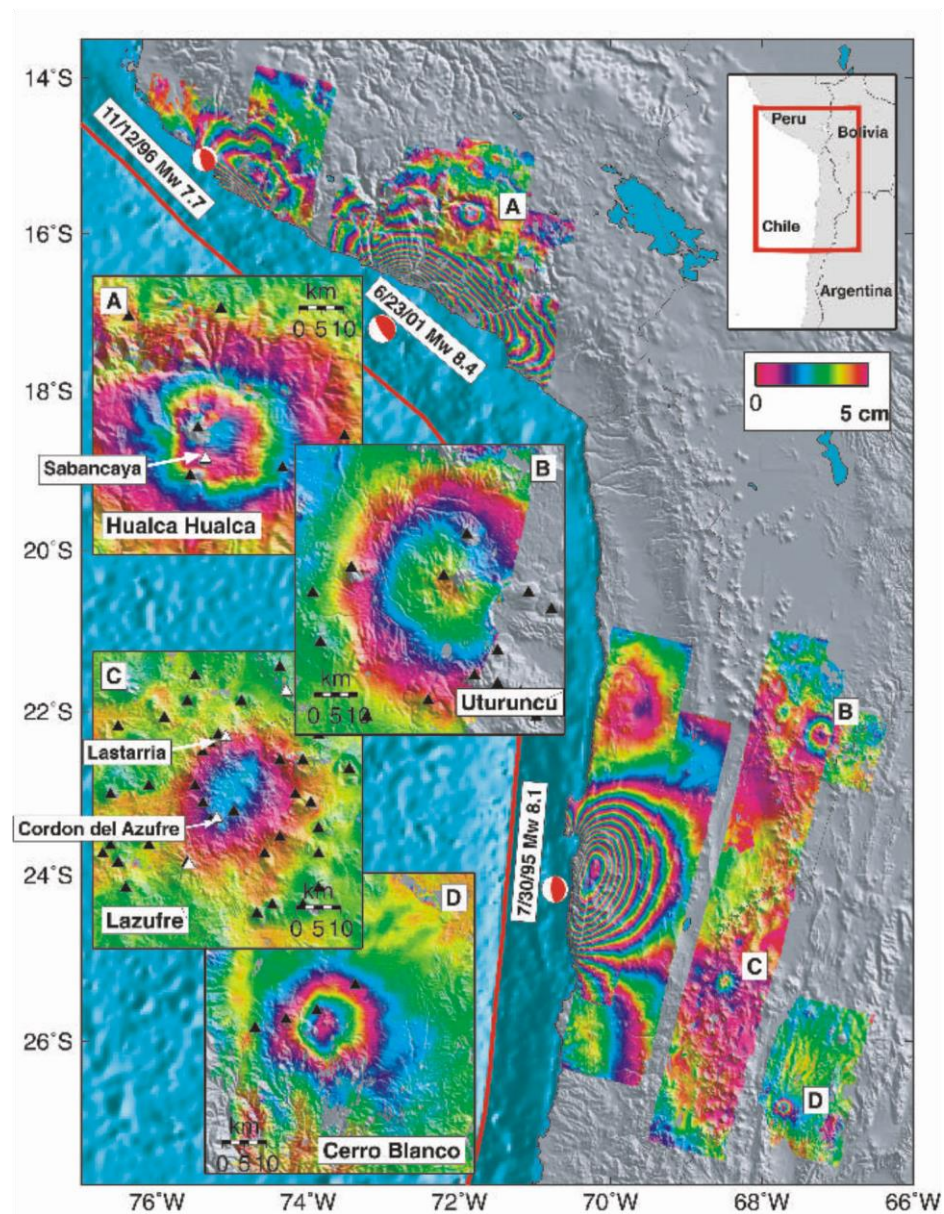
Figure 2.8: Colour contours of ground deformation draped over shaded relief from three subduction zone earthquakes along the South American coast (Pritchard and Simons, 2004). Each contour corresponds to 5 cm of deformation in the radar (satellite radar interferometry) line-of-sight direction. The amount of displacement recorded at great distances from the epicentres illustrates the potential for *remote* triggering events.

the potential to trigger large earthquakes as a result of both mechanical and thermal straining of the

rock fluid medium (Elsworth and Voight, 1995). In addition, the seismic energy released from an earthquake is much greater in a case where there are elevated pore fluid pressures present; hence the likelihood of failure in these cases is greatly increased (Voight and Elsworth, 1997). Volcanic explosions, magmatic or phreatic, can also generate significant dynamic loading through ground shaking that could trigger collapse.

External seismic triggers pose a greater threat as they have the potential to initiate failure at volcanoes that are not exhibiting major, or any, signs of activity. Regional or local tectonic earthquakes may dynamically load unstable volcanic edifices that are not active or indeed have not been considered active for many years. This may take many forms including reactivation of basement faults (van Wyk de Vries and Francis, 1997) or earthquakes originating in subduction zones (Pritchard and Simons, 2004). The fact that regional earthquakes may act as a trigger is an important one to grasp, as volcano flank collapse may be triggered from an event that occurred a substantial distance from the unstable edifice (Fig. 2.8). A collapse event itself may also act as a source of a seismic trigger for near volcanic edifices. Vibrations from adjacent, rapidly moving landslides can act in the same way as an earthquake, cause dynamic loading and in turn trigger further collapse (Voight and Elsworth, 1997).

2.6.1 The Missing Link?

The presence of weak substrates, hydrothermal systems, repetitive magmatic intrusions, eruptions and earthquakes in volcanic regions are more common than massive slope failures, and none of the processes or conditions discussed in Section 2.6 are common to all volcanoes. This suggests that stringent requirements involving contributions from multiple mechanisms and materials are required to produce failure (Voight and Elsworth, 1997).

The above may seem to suggest that there is no common link in terms of an eruptive trigger between collapse events at different locations. However, increasing pore fluid (specifically gas) pressures within an edifice from internal deep sources can in principle occur irrespective of the level and nature of volcanic activity providing there is some form of deep magmatic body. As will be shown in Chapters three to seven, large-scale internal pore fluid pressure increases can play a significant role in driving structural instability pushing an edifice towards a state of criticality where

is it susceptible to even the slightest triggering event. So, could this be the common link behind sector collapse?

2.6.2 Differences between ocean island and subaerial stratocone flank collapse

The largest volcanic slope failures of all occur on large oceanic, basaltic shield volcanoes, despite their low slope angles (typically less than 20°) and largely homogenous composition. A possible reason for this is that volcanoes of this type are inherently more stable than their polygenetic continental counterparts in their subaerial expression and their subaqueous portion is supported by the buttressing effect of the surrounding ocean. This means they that in order to generate sufficient destabilising forces to initiate collapse they have to grow to much larger sizes. The outcome of this is when ocean island volcanoes do collapse there is more volcanic mass available to fail.

The large oceanic, basaltic shield volcanoes can experience all the destabilising factors that affect every other type of volcano (Section 2.6), but are in addition substantially affected by changes in sea-level (McGuire *et al.*, 1997, Carracedo *et al.*, 1999). Volcanoes situated in a marine setting may also sit on very weak ocean sediments or haloclastite layers, which can provide ready locations for décollements and the initiation of volcanic spreading (McGuire, 1996, Walter & Troll, 2003, Oehler *et al.*, 2004). These substrata are comparatively weaker, being both '*wetter*' and younger than those situated in a continental setting, and the ease of which spreading can take place along these low strength layers leads to the development of well defined slumping (Oehler et al., 2004). These slumps can become extremely large e.g. the Hilina slump, Kilauea volcano, Hawaii which has been active and growing for approximately 43,000 years (Okubo, 2004). These features are far greater than any to be found on subaerial stratocones and may later evolve into debris avalanches (with or without the aid of a trigger) resulting in truly massive collapse events (Oehler *et al.*, 2004) such as the Nuuanu landslide off the north east cost of Oahu, Hawaii which covers an area of approximately 23,000 km^2.

2.6.3 Why volcanoes *must* fall down .. again and again

As a final word, when the problem of volcano edifice stability is looked at in its simplest form, structural instability seems unavoidable. Although most mountains grow by uplift and differential erosion of lithified rocks brought from depth, volcanoes grow by accumulation of new deposits that

are generally poorly lithified and may rest upon substrates that are similarly weak. As such they are built at the angle of repose. This means that a volcanic edifice will generally be built at the steepest angle that it is able to support itself. The ever-increasing height and weight of volcanic mountains is then made more precarious by poor consolidation of the constituent deposits, and enhanced by the hydrothermal alteration that further weakens the rock mass (Borgia *et al.*, 2000). Thus, much reorganisation of the edifice structure simply under the effect of gravity can be expected before a stable shape is produced. Any "external" forces such as elevated pore fluid (gas) pressures, seismic activity or magma intrusion simply accelerates the process.

If the appropriate conditions are maintained, then growth, destabilisation and collapse may be cyclic. The first ever collapse of a volcano will theoretically affect the largest edifice, both in terms of volume and height, as observed at Stromboli, Italy (Tibaldi, 2001; Apuani *et al.*, 2005). This is because at that time the edifice is at its strongest. Subsequent collapses usually involve smaller pre-collapse edifices, and occupy an inner position with respect to the previous failure. This behaviour seems to have a straight-forward explanation. The altered stress fields within a volcanic edifice following a collapse event can lead to the propagation of fractures, dykes and general magmatic intrusions in the circum-collapse zone, and hence increased production in that sector. The higher production results in more rapid accumulation of deposits without sufficient time for adequate compaction and erosion in order to stabilize the volcanic succession and the morphology of the cone flank (Tibaldi, 2004). In essence, a feedback effect occurs where decompression resulting from sector collapse deflects the rising magma into preferred directions until a critical mass of a new cone is reached and the same flank collapses again under the effect of gravity and/or any triggering forces. An example of such activity is observed at Stromboli, Italy where at least four sector collapse events have occurred in the last 13 kyr, all within the initial collapse scar (Tibaldi, 2004, Apuani *et al.*, 2005). A similar example may be forming at Tenerife where the current active summit complex it interpreted to have been constructed directly over the rear scarp of a previous collapse scar (Ablay and Hürlimann, 2000). In addition to this, conditions might occur where the time gap between collapse and the formation of a new young summit cone causes extensive alteration upon which the new cone lies (Frank, 1995). This may involve a considerable thickness of the old failure surface, upon which the new edifice lies being covered in weak, weathered, debris avalanche deposits, which have very high clay contents and may act as

preferential hydrothermal pathways. Either mechanism, the preferential location of rapid extrusion of material, or the alteration of what is to be the base of a new summit cone, are capable of decreasing the size that an edifice has to achieve to become unstable. If these two mechanisms are additional then the critical pre-collapse size is reduced further still.

Just as collapse mechanisms are variable, so is the apparent period of collapse cycles. For example, to date, Augustine volcano, Alaska, has an average collapse cycle of only 150-200 years (Siebert *et al.*, 1995). Other edifice-destabilisation cycles operate on a much longer time scale. At Colima, Mexico, collapse seem to occur every few thousand years (Komorowski *et al.*, 1994), while the giant collapses of the Hawaiian volcanoes occur on the order of every 20-100 ka (Lipman *et al.*, 1988). However, it is worth nothing that collapse cycles must be related to magma supply rate, which dictate how quickly the volcano can be re-built. If this rate drops so will the return period of collapse.

3. Theory of internal pressurisation

3.1 Internal or external pressurisation?

Although explosive eruptions and/or tsunamis are major consequences of volcano instability, *it is the processes that cause massive flank collapse that is the focus of this research*. Geotechnical engineers and geologists studying landslides are familiar with fluid pressurisation by water, and its modifying effects on the shear strength of soils and rocks (e.g. Voight, 1978; Bromhead, 1986). Ordinarily, this pressurisation is by groundwater of meteoric origin (external), and is rarely artesian, being hydrostatic and related to a ground water level within the slope. Groundwater bodies created by infiltration from the surface lead to shallow landsliding and thus slopes which are stable against deeper-seated modes of failure (e.g. Bromhead, 1995). Recently, Voight and Elsworth (2000), have proposed a novel, highly non-linear instability mechanism for the hazardous collapse of lava domes where dome failure is instigated by internal gas overpressure. Subsequent work in this area (Reid, 2004; Thomas *et al.*, 2004a; Vinciguerra *et al.*, 2005a) has confirmed that, in principle, internal gas (fluid) pressurisation can play a critical role in promoting structural instability on a much larger scale, resulting in rapid destabilisation and massive sector collapse. While increases in internal pore pressures may be generated by fluids (rain etc.) infiltrating from outside to produce surficial landslips, significant deep seated failure and large volume run-out lengths seem only likely to occur where the pressure source originates within the edifice (Reid, 2004; Thomas *et al.*, 2004a,).

As a first step towards understanding edifice failure at a basic level what has been modelled is a destabilising mechanism involving gas pressurisation (e.g. Gerlach *et al.*, 1996) that affects sections of, or the entire interior of the edifice, and whose external expression is a deep-seated failure mode (landslip) that might be the cause of catastrophic eruption. These models thus differ from many recent studies of volcano instability (e.g. Reid *et al.*, 2001; Acocella, 2005) where the effects of internal fluid (gas) pressures are not considered and collapse is driven purely by gravity aided perhaps by regions of weak (hydrothermally altered) rock or the mechanical forces associated with direct intrusion of magma into the edifice. The concept of edifice strength (Chapter four) becomes critical when considering internal fluid pressurisation, as the use of unrealistically
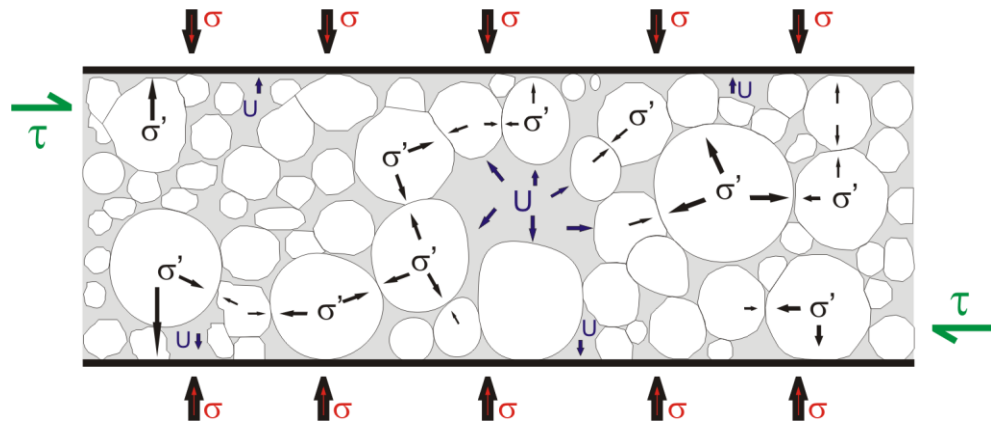
Figure 3.1: Diagrammatic representation of effective stress. The application of the stress σ compresses the pore fluid (grey) and induces a pore fluid pressure, u. This pore fluid pressure, u, is present throughout all the grey pore fluid and acts in all directions. Hence the effective stress σ' is equal to the force "pushing" the grains together, σ, minus the force "pushing" the grains apart, u, equation 4.1. The value of σ' is instantaneous, and will vary throughout the material (i.e. it is not a universal constant), as it is highly dependent on the degree of contact between individual grains. The lower the value of σ', the easier it is for the force τ to shear the material, as it is easier for the grains to move over each other.

high strength parameters raises the nonsensical idea of a 'floating' volcano, in which the rock mass making up the edifice is so strong that the internal pressure can counteract the weight of the overlying volcano without the edifice failing in any way. The structure then becomes neutrally buoyant and essentially would float, much like a hovercraft.

3.2 Effective stress

The response of any porous material to stress depends not only on the total stress state but also on the pore fluid pressure. In fact, within an edifice, the stress producing material deformation is exactly equal to the difference between the total stress and the pore pressure. This difference is known as the effective stress. Although this principle was clearly stated by Charles Lyell (1797-1875) in his *Elements of Geology* (Terzaghi, 1960), the concept of effective stress was not widely used until it was defined in soil mechanics by Terzaghi (1943).

If this concept is simplified into only the vertical plane, and a stress (σ) applied to a porous granular material is considered. This stress will be transmitted throughout the material from grain to grain. If we have a pore fluid pressure (u) also present within the pore spaces, it will act in an opposing

direction to σ . We thus have a stress (σ) pushing the grains together and a pore pressure (u) pushing the grains apart. This leaves an effective stress (σ') (Fig. 3.1). All measurable and visible effects of a change of stress, such as compression, distortion and a change of shearing resistance are due exclusively to changes in effective stress. The effective stress (σ') is related to total normal stress (σ) and pore pressure (u) by

$$\sigma' = \sigma - u \qquad\qquad \text{(Equation 3.1)}$$

Hence, it is the effective stress that causes changes in strength, volume and shape within the rock mass. It does not represent the exact contact stress between grains but the distribution of load carried by the medium over the area considered. Knowing this, it is now possible to equate σ' as the distributed force with which the grains within the material are being pushed together. If we now add a horizontal shear stress (τ) to a cohesionless material, in order to move the grains over one another (to shear the material), τ must be greater than or close to (if considering additional triggering methods) the value of σ' multiplied by a function of the angle of friction (see equation 4.14). Therefore, the lower the value of σ' the lower the value of τ required to shear the material (Fig. 3.1).

If this simple case is now applied to a volcano flank (Fig. 3.2), σ becomes the stress induced from the weight of the volcanic overburden, τ represents the stresses induced from the potential slide block wanting to move along the potential failure surface, and u and σ' are the same as in the earlier simple example (Fig. 3.1). It is thus clear that it will be easier for the flank to fail at lower values of σ'.

By far the easiest and most direct way of decreasing σ' is to increase u (equation 3.1). This is the basic theory of how increasing the pore fluid pressure can promote volcanic flank instability. There are two other ways in which it is possible to decrease σ'. One is to reduce σ by removing some of the volcanic overburden. If the release in stress caused by the removal of overburden is not matched by an immediate similar decrease in pore pressure (which barring the triggering of an eruption is unlikely, as the response to loading is faster than unloading), σ' can be decreased significantly. This could possibly explain why many slope failures, including those of volcanic flanks, are thought to occur in retrogressive stages. Rapid collapse of sections of volcano flanks
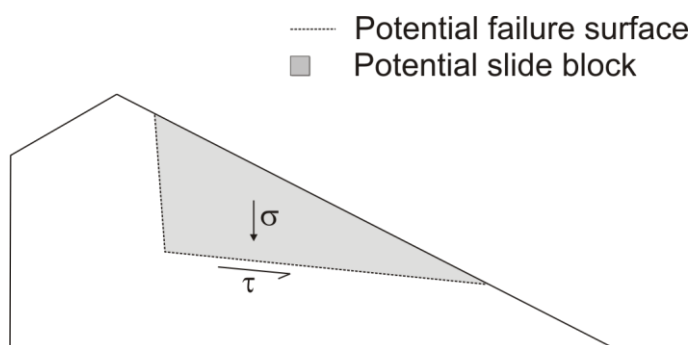
Figure 3.2: Schematic cross section of a volcanic flank, demonstrating the basic principle of effective stress promoting landsliding on a large scale. σ represents the stresses induced from the weight of the volcanic overburden and τ is the stress induced from the potential slide block wanting to move along the potential failure surface. u and σ' act at a smaller scale as in Figure 3.1 to promote destabilisation inside the edifice.

leave behind unstable steep scarps and the stress field within the edifice is not able to readjust on a similar time scale leading to secondary collapse. Such a retrogressive failure mechanism is now widely accepted to have occurred at Mount St. Helens (Voight and Elsworth, 1997) (Fig. 2.4). If the volcano is in a state such that the pore pressure is actively increasing (due to a deep source of increasing pore fluid pressure), reducing σ through small, relatively shallow mass wasting events may have catastrophic consequences. This is because u continues to increase as σ decreases, leading to rapidly decreasing values of σ' at depth.

The second and less effective additional method of reducing σ' is by increasing σ. While this appears at first glance counter-intuitive, the fluids that fill the pore spaces are less compressible that the rock that contains them. This means that if the weight of the overburden is increased, the grains within the rock are easier to compress than the pore fluids filling the spaces between the grains. This leads to an *apparent* increase in the pore fluid pressures, much like squashing a balloon increases the pressure exerted by the fluid within it (the air) until the balloon bursts. If this *apparent* increase in pore fluid pressure u is greater than the increase in σ, σ' decreases. Obviously, the absolute increase in u cannot directly exceed σ as this violates the principle of conservation of energy. However, while the increase in σ is usually brought about by a directional loading and is distributed in a non-uniform manner throughout a material, dependent on the nature grain to grain contacts, the increase in u is omnidirectional and equal throughout connected areas

of pore fluid. Hence local apparent decreases in σ' are possible as σ and *u can* act in different directions (Fig. 3.1).

In summary, any volcano that is passively de-gassing may act to decrease σ' through increases in pore fluid pressure. Hence, over time and given the right conditions, a volcano can become unstable. The situation is worse for actively erupting volcanoes. Not only is the internal gas flux higher during an eruption, existing pore fluid pressures may also experience a rapid increase due to thermal expansion caused by direct magma intrusion. Newly erupted products or newly emplaced magma high in the edifice both act to increase σ through increased loading. This increases *u* indirectly by compressing the pore fluid spaces. The addition of new material can cause shallow local instabilities leading to small volume failures, initiating rapid removal of small amounts of volcanic overburden. The stress response to unloading is much slower than that due to loading; hence *u,* already elevated through an increase in the gas flux, thermal expansion and pore space compression, is being contained by smaller values of σ. These factors combined can lead to dramatic decreases in the value of σ'. It is hard to overstate how important the concept of effective stress is to the mechanical conditions leading to failure, and how, when just considering this one variable, the potential for generating instability through increasing the pore fluid pressure exists at all volcanoes.

3.3 Sources of internal pore fluid (gas) pressure inside volcanoes

Major volcanic eruptions are frequently preceded by emissions of large quantities of volcanic gases via vigorous fumarolic activity (Gerlach *et al.*, 1996, Wallace, 2001, Oppenheimer *et al.*, 2003). However, while the emission of volcanic gases and their compositions are routinely monitored, the mechanical effects of the gas phase on the shear strength and structural integrity of the edifice have been mostly overlooked. It was first recognised in the mid 1990s that thermal expansion, hence, increased pressurisation caused by the expanding pore fluids could be linked to edifice collapse (Reid, 1994a; 1994b; 1995). Pore-fluid pressures generally exceed those generated by mechanical stresses due to magma intrusion (Voight and Elsworth, 1997, Elsworth and Day, 1999), underlining the potential importance of internally-driven gas pressurisation relative to other proposed modes of flank instability. Internal gas sources are numerous (Gerlach *et al.*, 1996);

sources include juvenile gas released from magma chambers and conduits (Jaupart, 1998) and the progressive dehydration of the volcano's hydrothermal system (Lopez and Williams, 1993, Reid, 2004). Prior to dehydration, hydrothermal activity can also play an important role by chemically weakening the rock mass, rendering it more susceptible to mechanically induced structural failure by whatever means (Borgia, 1994, Murray and Voight, 1996, Rust and Neri, 1996, Voight and Elsworth, 1997, Vidal and Merle, 2000, Reid *et al.*, 2000; 2001). The importance of the condition of the rock mass is discussed in detail in Chapter four.

Although the specific dynamics of magma degassing are not under investigation, it is noteworthy that significant advances have been made in this field recently (Sparks, 2003; Gonnermann *et al.*, 2007) and that the mode of failure proposed here is, in part a direct consequence of separation of gas from magma. Steady degassing by itself need not result in deep failure of the edifice as gas may simply dissipate via fumaroles. However, a long-term or sustained high flux gas emission from depth increases the chances of developing significantly elevated pore pressures. Both these situations are likely at stratocones and also oceanic islands, where massive landslides have taken place without significant precursor eruptions.

Wallace (2001) stated that typically, the concentrations of dissolved volatiles within *crustal* storage reservoirs are sufficient to cause saturation of the magma with a multi-component vapour phase. Exsolution of these dissolved volatiles can occur in response to crystallisation of the magma and reductions in the confining pressure surrounding the body. This exsolved vapour would presumably be present as bubbles dispersed throughout the magma reservoir. As a result, particularly eruptions of silicic magma can release large amounts of SO_2 derived from *pre-eruptive* exsolved vapour, despite the fact that such magmas generally have very low concentrations of dissolved sulphur. The amounts of volatiles implied by this are very large, suggesting that exsolved vapour (gas) may accumulate in the apical regions of magma bodies in near-surface storage reservoirs during repose periods between eruptions (Gerlach & Graeber, 1985; Hurwitz *et al.*, 2003; Gonnermann *et al.*, 2007). Interestingly, the volume fraction of exsolved gas at the top of many magma bodies may be about 30 vol. % (Wallace *et al.*, 1995; Wallace, 2001). This is the same value of porosity (30 vol. %) predicted by Candela (1991) to represent the percolation threshold at which spherical gas bubbles become sufficiently interconnected to allow permeable flow through a

network of bubbles (e.g. Rintoul and Torquato, 1997). Thus, once this volume fraction of exsolved gas is reached, if no eruption occurs, gas may be lost out of the top of the system by advection through a permeable bubble network. Gas may then be transferred into an overlying hydrothermal system and may get trapped below low permeability barriers above the magma body (Voight and Elsworth, 1997), or be leaked out towards the surface (Fig 3.3).
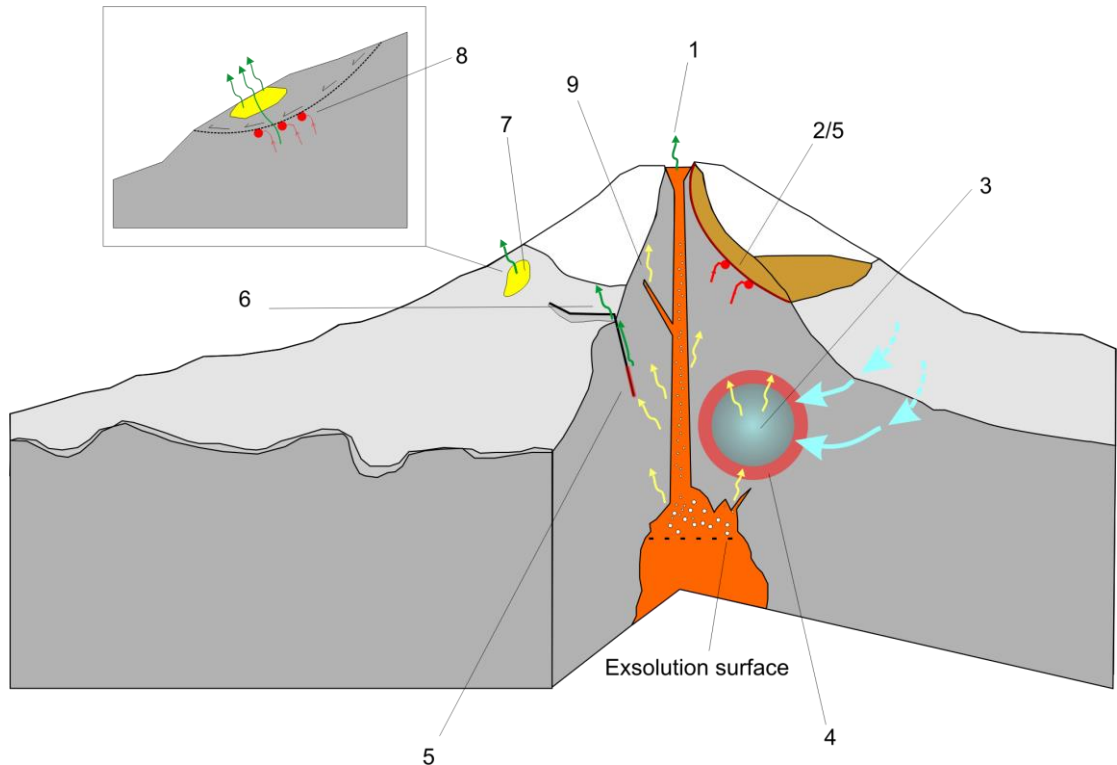
Figure 3.3: Schematic cut-away section of a volcano showing the major sources and pathways of internally generated pore fluids (gas) within a volcano. Yellow arrows denote sources of gas (mainly due to outgassing from the chamber and conduit above the exsolution surface), red arrows or areas shaded red represent pore fluid traps or areas of reduced permeability/porosity, and green arrows indicate where gas may be lost from the system. Areas of particular importance include: 1) Loss of gas through an open conduit (open-system degassing), either through buoyant/advective bubble rise (Hurwitz *et al.*, 2003), gas flow through porous and permeable magma (Edmonds *et al.*, 2003), or through fractures within the magma body caused by brittle deformation of the ascending magma (Rust *et al.*, 2004); 2) Barriers to fluid migration caused by breccia deposits lining old collapse scars; 3) Dehydration (boiling) of active hydrothermal systems (Reid, 2004); 4) Regions of hydrothermally altered rock mass, with a high proportion of clay minerals which act to reduce permeability and porosity; 5) Hydrothermal alteration (see 4) along preferred fluid pathways such as pervasive faults/old collapse scars; 6) Rapid, concentrated loss of gas along preferred fluid pathways to the surface such as pervasive faults/fracture; 7) Well developed fumarole fields; 8) Small mass movements acting to seal well developed fumarole pathways which may result in a rapid increase of pore fluid pressure; 9) Exsolution and outgassing from dykes and sills intruded within the edifice.

A mechanism by which volatiles may separate from the magma before a value of 30 vol. % of exsolved gases is reached is that of diffusion pumping (Chouet *et al.*, 2005). Diffusion of gas from a supersaturated magma generates bubble growth and increases the internal pressure of the bubble. Bubble expansion is resisted by the viscosity of the surrounding magma and the confining effect due to the finite yield strength of the overlying column of material. Elastic inflation therefore occurs as a result of bubble pressurisation and inflation proceeds until the yield strength of the magma is reached, at which point the magma begins to flow. Magma fragmentation by viscous shear near conduit or chamber walls wall may induce the coalescence and collapse of bubbles intersected by shear planes, thereby allowing gas escape through a transient network of fractures. This results in a pressure decrease in the magma body and the collapse and welding of the fracture network effectively sealing the gas escape route shut. Repeated cycles of shear fracture and welding of magma provide a ratchet mechanism by which the gas phase within the source region can be recharged and evacuated (Chouet *et al.*, 2005), again possibly accumulating in the apical regions of magma bodies or below hydrothermal caps.

Large quantities of gas may also accumulate at the apical regions of dykes. The pressure gradient near the tip of a dyke must always be very large in order to continue propagation through the narrow tip. As a result, the pressure in the tip of a dyke must be very small, theoretically even zero. It is the exsolution of magmatic volatiles that buffers the tip pressure (Lister, 1990; Lister and Kerr, 1991) and the tip space is normally occupied by a pocket of the most soluble volatile species (i.e. a gas). Immediately behind this is a foam of bubbles of gas, both the most soluble gas and other, less soluble species (Wilson and Head, 2003). Although the vertical length of the gas-dominated upper parts of dyke may be small, their lateral extent means large volumes of exsolved volatiles are involved. These scenarios all result in the potential for large amounts of "*free*" gas to exist within a volcano. "*Free*" gas being that which occupies pore space within the rock mass and is free to migrate.

Regardless of how the "*free*" gas originated, if the chamber or conduit walls are permeable and at a lower ambient pressure than the gas, gas may escape laterally and vertically into the wall rock (Jaupart and Allegre, 1991; Eichelberger, 1995; Gonnermann *et al.*, 2007). However, processes such as mineral precipitation due to hydrothermal activity, which acts to reduce permeability, raises

questions as to what extent degassing into wall rocks occurs (Gonnermann *et al.*, 2007). In partial answer to these questions, gas flow measurements at active silicic volcanoes (Wallace *et al.*, 2003) have been used to demonstrate that considerable vertical gas flow must take place over an area much larger than the estimated conduit width (Edmonds *et al.*, 2003). A summary demonstrating the most important potential sources and pathways of gas within a volcano is presented in Figure 3.3.

It has been identified above that depending on the porosity, permeability and therefore hydraulic diffusivity (equation 3.2) of the volcanic rock mass, the "*free*" gas may be able to significantly increase pore pressures in restricted pore spaces. The hydraulic diffusivity, *D* (Delaney, 1982), of fluid saturated rock masses can be defined as:

$$D = \frac{k}{n\mu\beta}$$
(Equation 3.2)

The two variables of importance here are *k,* the intrinsic permeability (10^{-21} - 10^{-10} m^2, Reid, 2004; Vinciguerra *et al.*, 2005b) and *n,* the porosity. The other variables involved are μ, the dynamic viscosity of the fluid and β, the isothermal compressibility for fluid mass in a fixed volume. Permeability and thus diffusivity can vary over several orders in volcanic rock masses primarily due to the many different types of volcanogenic rocks and continually differing degrees of hydrothermal alteration. Significantly elevated pore fluid pressures may only occur within a specific range of hydraulic properties and are unlikely both for very high and low values of hydraulic diffusivity (Reid, 2004). In higher-diffusivity rock masses, fluids expand, usually via a high permeability and dissipate elevated pressures; thus not propagating to an extent to destabilise the edifice. With very low diffusivity rock masses, expansion is retarded and extremely high pore pressures build near the pressure source. These high pressures may lead to hydrofracturing or brecciation of the rock mass, effectively increasing the rock mass permeability and dissipating fluid pressures (Reid, 2004).

3.4 Destabilising effects due to increasing pore fluid pressures

Hill *et al.* (2002) developed the idea that a volcanic edifice may be "primed", close to the point of failure. Internal fluid pressurisation would be an ideal driving mechanism, pushing an edifice

towards this point. As discussed in Section 3.2, by increasing the internal pore pressures, failure may be initiated without any physical changes occurring within the volcanic rock mass. This concept is discussed further in Chapter four. In this critical state, the structure is exposed to the threat of small internal or external perturbations that may trigger volcanic activity and/or massive collapse of the edifice. This may take place with little or even no pre-cursory signs. Examples of where large scale sector collapse has occurred in apparently dormant volcanoes include the 1888 eruptions of Bandi-San (Japan) and Ritter Island (Melanesia) (Siebert *et al.*, 1987). A critical question relates to how the internally-derived gas flux may become blocked or slowed, building up an overpressure that can lead to the onset of failure, independent of any specific relation to a new rising batch of magma and eruption. It is important to note that the pore fluids need not become completely trapped to cause significant destabilisation effects. Simply increasing the gas flux into a system with a fixed permeability and porosity will be sufficient to generate substantial decreases in effective stress, hence decreasing stability. In particular, the geometry and internal distribution of diffuse, low permeability pore fluid traps is important. For all numerical models considered within this thesis, it is assumed that degassing is pervasive throughout the edifice resulting in a symmetrical distribution of elevated pore fluid pressures around the source of the pressure increase. It is acknowledged that this may be a simplistic approach, and that the specific hydraulic properties of the volcanic material and distribution of pore fluid traps and vents are paramount to the development of significant internal pore fluid pressures. Unfortunately, the detailed mapping and lithology testing that would be required to achieve this for just one part of a volcano is far beyond the scope of this project. Therefore, all models referred to within this thesis are assumed to have the material properties and distribution of these properties concurrent with developing significant pore fluid pressures. A more in-depth discussion on the importance of the above factors can be found in Section 7.6 and a brief discussion follows here.

The most important pore fluid traps are volumes of material that have been extensively altered by hydrothermal alteration to large quantities of clay minerals. Possible scenarios that could arise from the trapping of gas include small mass movements of unstable edifice sections or further increases in pore fluid overpressure which can result in larger volume failures. Rapid pore pressure increases are then possible when strains associated with minor deep-seated instabilities act to seal surface-venting gaseous fumaroles (Fig 3.3). Of equal importance are the methods of gas dissipation within

the edifice, particularly rapid gas loss along linear discontinuities such as pervasively extensive faults (Fig. 3.3). This is because the levels of instability promoted through methods of internal gas pressurisation are very susceptible to even small changes in the edifice structure and properties.

This leads to a fundamental question:

Is deep seated volcanic instability generated by increases in internal pore pressures an ubiquitous occurrence at active volcanoes?

On the one hand, all active volcanoes de-gas, generating a potential increase in pore pressures. Most, if not all active volcanoes also posses vigorous hydrothermal systems. On the other hand, there are far more volcanoes than there are recognised large-scale sector collapse events. Therefore, all volcanoes may not have the internal structure and properties conducive to generating sustained high pore fluid pressures. So, under what simple conditions can pore pressure changes lead to large-scale destabilisation and ultimately edifice sector collapse? The remainder of this thesis will address this important question in detail.

4. Estimating volcano strength

4.1 The importance of rock mass strength

A volcanic edifice may be considered an immovable object, a towering mass of rock that on first glance appears extremely strong and coherent. However, at its most basic level, a volcanic edifice is made up from discrete layers of different rock types (a rock mass), cut through on a range of scales by pervasive and penetrative discontinuities including faults, fractures and contact surfaces (Fig. 4.1), making it difficult to assign an overall strength. Characterisation of the rock mass strength can be further hindered by long time gaps in volcanic activity that result in the development of residual soils (Hürlimann *et al.* 2001), or by hydrothermal alteration, where the rock is chemically altered primarily to clay minerals (Crowely & Zimbeman, 1997; Reid *et al.*, 2001). Both residual soils and most hydrothermally altered material will cause a decrease in the strength properties of an edifice relative to its unaltered state. However, even without these degrading effects, a volcanic rock mass, and by implication the volcano itself, is an inherently weak structure when compared to the intact strength of its constituent parts (Fig. 4.2). An exception to the weakening of the rock mass is the process of silicification, a type of hydrothermal process actually acts to strengthen the rock mass and increase its elasticity (Watters *et al.* 2000). This is an important point to note as there is a tendency to automatically associate areas with active hydrothermal activity with places where there is a reduction in rock mass strength.

The concept of studying and defining rock mass strength was developed for use in the mining industry after several fatal accidents that resulted from overestimates of strength characteristics (Bieniawski, 1973). A very simple relationship exists between the volume comprising the rock mass and its overall strength. The larger the volume of rock, the greater the number of fractures and discontinuities that must be considered. For volcanic rock masses such as massive lava flows where the spacing of discontinuities is on the scale of metres, the rock unit would not normally be regarded as a fractured rock mass for strength purposes as single blocks may be on the scale of several meters. However, upon inspection, the sample size affects overall strength and its strength behaviour, and when considering the entire rock mass there is a significant reduction in strength with increasing sample size (Fig. 4.2). This fact is well demonstrated by Schultz (1996), who
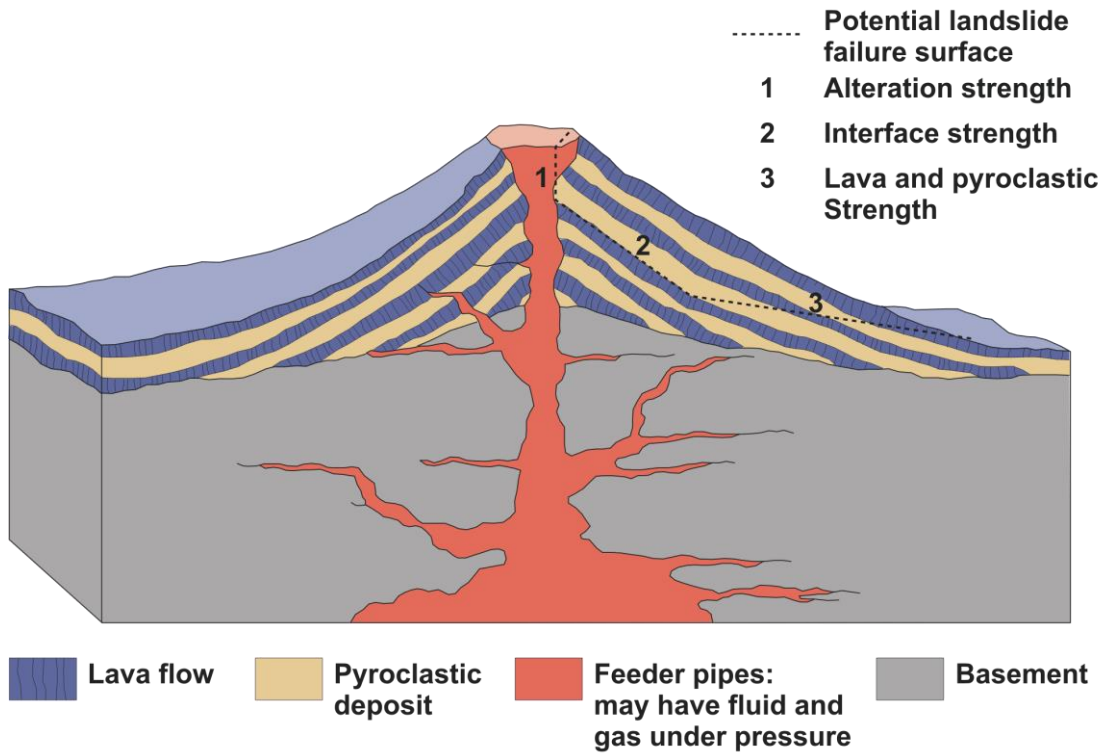
Figure 4.1: Schematic cross section through a volcanic edifice detailing the three main areas of strength within a volcanic edifice, modified from Watters *et al.*, (2000).
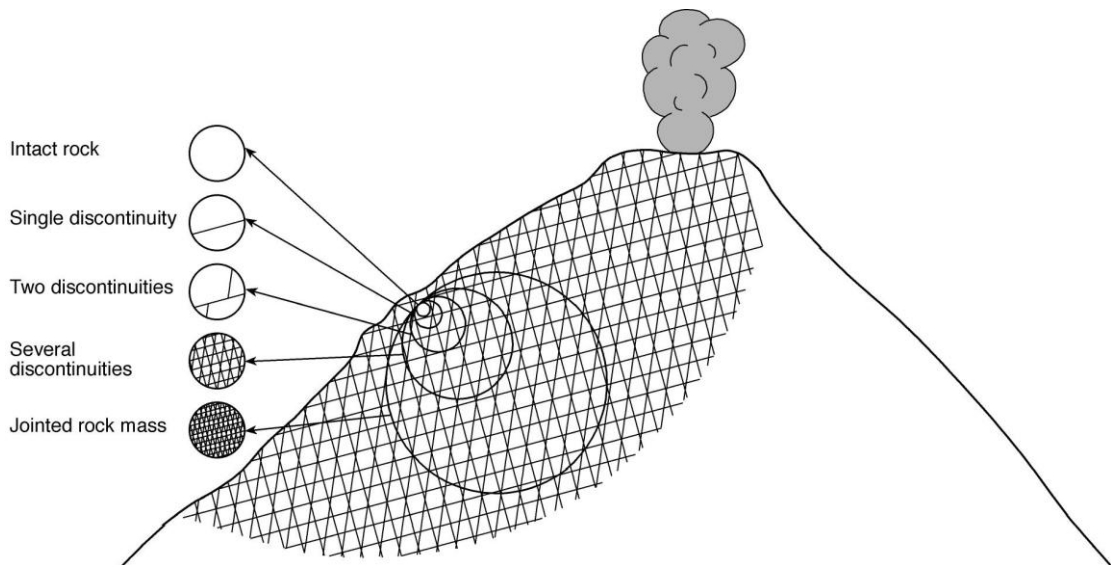
Figure 4.2: Diagrammatic representation of the effect sample size has on the rock mass strength. At a smaller scale the absolute strength of the rock is more important, but the larger the volume of rock, the greater the number of fractures and discontinuities that must be considered. Hence as the sample size increases, the strength of the overall mass decreases as discrete blocks can move along an increasing number of low strength discontinuities. (Modified from Voight, 2000)

showed basaltic rock masses on the meter scale are best described as intact material partially separated into irregular blocks by numerous discontinuities. However, at a scale much greater than the block size studied, the entire lava flow is best described as an equivalent continuum and a rock mass. Essentially, the strength of a rock mass depends on two attributes 1) the strength of the intact pieces and 2) their freedom of movement which, in turn, depends on the number, orientation, spacing and shear strength of the discontinuities. The strength of small samples determined in the laboratory has no bearing on the true strength of a volcano, as the compressive strength of an intact laboratory sample may be up to two orders of magnitude greater than that of the rock mass. It is thus important *not* to overestimate the strength of a volcano. In particular, when considering internal pressurisation of a volcanic edifice, the distinction between *intact* and *rock mass* strength becomes critically important. As discussed in Section 3.1, the limiting factor governing how much internally generated pressure can build up within an edifice is the strength of the edifice itself. If unrealistically large intact rock strengths are used for modelling purposes, the internal pressure may become great enough to counteract the weight of the volcanic pile, such that the structure becomes neutrally buoyant and may theoretically float.

4.2 Rock mass classification schemes

Rock mass classification schemes have been under development for over 100 years since Ritter's (1879) attempt to formalise an empirical approach to tunnel design (Bieniawski, 1978). Classification schemes such as the Rock Mass Rating (RMR) of Bieniawski (1976; 1989) form the basis of an empirical approach to estimating strength criteria and other rock mass properties. Widely used in engineering, they have found applications in the stability analysis of tunnels, slopes, foundations and mines, and most recently, volcanic systems (Voight, 2000; Thomas *et al.*, 2004b; Okoubo, 2004) At an outcrop scale, a rock mass is an aggregate material consisting of intact material, associated discontinuities such as bedding planes, faults, joints, solution surfaces, and any areas of alteration. The concepts of a rock mass and associated classification schemes are powerful tools for estimating strength criteria on a large (decimetre) scale. Although several rock mass classification schemes exist, the most widely used is the Rock Mass Rating System (RMR) of Bieniawski (1976; 1989), and is the major scheme used for this study. Other classification schemes include the Geological Strength Index (GSI) of Hoek *et al.*, (1992) and Hoek (1994), which is used

to a lesser extent within the scope of this study. The following two sub sections are a brief description of the two named classification schemes.

4.2.1 The RMR system

Bieniawski (1976) published the first comprehensive details of a rock mass classification called the Geomechanics Classification or the Rock Mass Rating (RMR), based upon case histories drawn from civil engineering. The RMR system uses five main parameters to classify the rock mass (Table 4.1), the strength of the intact rock, the Rock Quality Designation (RQD) of Deere (Deere & Deere, 1988), the spacing of discontinuities, the condition of the discontinuities and the groundwater conditions (Schultz 1995; 1996). In the years since its first use, this system has been refined successively as more case records have been examined and incorporated into the rating system. The current RMR ratings have changed significantly from the original 1976 criteria. A comprehensive summary of these modifications was compiled by Bieniawski (1989), which contains some rating adjustments that are specific to tunnel design and small-scale slope stability and not applicable for use in determining the strength of large-scale volcanic rock masses. These rating modifications (including modification for joint orientation) will not be included in any RMR ratings presented in this project, as the objective is to use the RMR in such a way to obtain a general idea of the overall rock mass strength, not the stability of individual slopes.

By their nature, all rock masses are discontinuous, and a volcanic edifice is no different. Descriptive classification schemes like the RMR can be used to make predictions about the mechanical properties of the rock mass if used in conjunction with relevant empirical expressions. A particularly powerful combination involves an integration of the RMR and the Hoek-Brown Criterion (Hoek & Brown 1980; Hoek, 1983) devised to assess rock mass strength (see Section 4.5). For example, Schultz (1995; 1996) used RMR data in this way to show that the rock mass compressive strength of basalt is up to 80% weaker than its intact compressive strength as measured under laboratory conditions. This result has important implications for volcano edifice strength, and is developed more fully in Section 4.5 using RMR data collected as part of this project.

Strength of intact rock	Uniaxial Compressive Strength, MPa	>250	100-250	50-100	25-50	5-25	1-5	<1
	Point-load Index, MPa	>10	4-10	2-4	1-2	For this low range UCS is preferred		
1.	Rating	15	12	7	4	2	1	0
	RQD, %	90-100		75-90	50-75	25-50	<25	
2.	Rating	20		17	13	8	3	
	Spacing of discontinuities, m	>2		0.6-2	0.2-0.6	0.06-0.2	<0.06	
3.	Rating	20		15	10	8	5	
	Condition of discontinuities	Very rough, Discontinuous, No separation, Unweathered		Rough walls, separation < 0.1 mm, Slightly weathered	Slightly rough, separation < 1 mm, Highly weathered	Slickensides or Gouge <5mm thick, or continuous separation 1 – 5 mm	Soft Gouge > 5mm thick Or Separation > 5mm continuous, decomposed wall rock	
4.	Rating	30		25	20	10	0	
Ground Water	General conditions	Completely dry		Damp	Wet	Dripping	Flowing	
5.	Rating	15		10	7	4	0	

Table 4.1: The RMR classification parameters and their ratings (shaded), modified from Bieniawski (1989). RMR = 1+2+3+4+5 and $\leq$ 100.

4.2.2 The GSI

The Geological Strength Index (GSI), introduced by Hoek (1994) and Hoek *et al*. (1995) provides a system for estimating the rock mass strength for different rock mass conditions. It is a similar system to the RMR, in being a descriptive rock mass classification scheme. The GSI can be considered as better representing poor rock masses (RMR < 25) as it relies much more on descriptive observations rather than observed physical measurements, which may be close to impossible to obtain in highly disrupted, very poor quality rock masses (Hoek, 1994). The full GSI rating system is presented in Tables 4.2 and 4.3, but experience has shown that Table 4.2 is sufficient for field observations using only the letter code to identify each rock mass category. These codes can then be used to estimate the GSI value from Table 4.3 (Hoek and Brown, 1997). For better quality rock masses (RMR/GSI >25), the GSI can be estimated directly from the RMR. If the 1989 version of Bieniawski's RMR classification is used, then the GSI = RMR -5 where RMR has the Ground Water rating set to 15 and the rating adjustment for the joint orientation set to zero. As explained in Section 4.2.1, for the purposes of this project, the joint orientation is not considered within the RMR, and is assigned a value of zero for all RMR values presented.

ROCK MASS CHARACTERISTICS FOR STRENGTH ESTIMATES	SURFACE CONDITIONS	VERY GOOD — Very rough, fresh unweathered surfaces	GOOD — Rough, slightly weathered, iron stained surfaces	FAIR — Smooth, moderately weathered or altered surfaces	POOR — Slickensided, highly weathered surfaces with compact coatings or fillings of angular fragments	VERY POOR — Slickensided, highly weathered surfaces with soft clay coatings or fillings
STRUCTURE		DECREASING SURFACE QUALITY ⟹				
BLOCKY - very well interlocked undisturbed rock mass consisting of cubical blocks formed by three orthogonal discontinuity sets		B/VG	B/G	B/F	B/P	B/VP
VERY BLOCKY - interlocked, partially disturbed rock mass with multifaceted angular blocks formed by four or more discontinuity sets	DECREASING INTERLOCKING OF ROCK PIECES	VB/VG	VB/G	VB/F	VB/P	VB/VP
BLOCKY/DISTURBED- folded and/or faulted with angular blocks formed by many intersecting discontinuity sets		BD/VG	BD/G	BD/F	BD/P	BD/VP
DISINTEGRATED - poorly inter-locked, heavily broken rock mass with a mixture or angular and rounded rock pieces		D/VG	D/G	D/F	D/P	D/VP

Table 4.2: Characterisation of rock masses on the basis of interlocking and joint alteration (Hoek 1994).
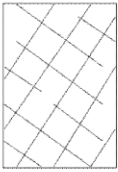
GEOLOGICAL STRENGTH INDEX From the letter codes describing the structure and surface conditions of the rock mass (from Table 5.2), pick the appropriate box in this chart. Estimate the average value of the GSI from the contours. Do not attempt to be too precise. Quoting a range is more realistic than stating a single GIS value STRUCTURE	SURFACE CONDITIONS	VERY GOOD Very rough, fresh unweathered surfaces	GOOD Rough, slightly weathered, iron stained surfaces	FAIR Smooth, moderately weathered or altered surfaces	POOR Slickensided, highly weathered surfaces with compact coatings or fillings of angular fragments	VERY POOR Slickensided, highly weathered surfaces with soft clay coatings or fillings
		DECREASING SURFACE QUALITY ⇨				
BLOCKY - very well interlocked undisturbed rock mass consisting of cubical blocks formed by three orthogonal discontinuity sets		80 70				
VERY BLOCKY - interlocked, partially disturbed rock mass with multifaceted angular blocks formed by four or more discontinuity sets	DECREASING INTERLOCKING OF ROCK PIECES		60 50			
BLOCKY/DISTURBED- folded and/or faulted with angular blocks formed by many intersecting discontinuity sets				40 30		
DISINTEGRATED - poorly inter-locked, heavily broken rock mass with a mixture or angular and rounded rock pieces	⇩				20 10	

Table 4.3: Estimate of Geological Strength Index, GSI, based on geological descriptions (Hoek 1994).

4.3 Field collection of rock mass geotechnical data

The RMR and GSI data collected for this study were obtained from two separate areas (Fig. 4.3) that have experienced extensive past volcanic activity. The first area, Snowdonia (North Wales, UK), was active during most of the Ordovician and early Silurian (Duff and Smith, 1992). The second area, Tenerife, Canary Islands, has experienced subaerial activity from 12 Ma to the present day (Carracedo, 1994). In total, 8 distinct rock types were examined from a total of 30 field locations, allowing 74 RMR and 19 GSI values to be determined (Tables 4.4 and 4.5). Lithotypes sampled range in composition from alkali basalt to rhyolite, and with the exception of several micro-granite samples from Snowdonia, the rock masses examined were exclusively volcanic in origin, comprising of a mixture of lava flows, dykes and air-fall tuffs. Although an intrusive granitic rock is unlikely to be found on most volcanic slopes it is included in this study to demonstrate the potential weakness inherent in all igneous rock masses. The Snowdon volcanic series is mainly Ordovician in age (Owen, 1979) whereas the units examined on Tenerife are generally < 4 Ma old and in some cases, the product of historic eruptions (Carracedo & Day 2002). The extensive time gap between the two field locations, one ancient and the other geologically young, allowed us to assess the degree to which the gross age of the rock mass (climatic influences excluded) may have influenced the rock mass strength. Studying rocks from two distinct types of volcanic system, one plume related (alkali basalt dominated) and the other characterised by back-arc volcanism (calc-alkaline silica dominated) also allowed us to examine how differing volcanic environments may produce differing qualities of rock mass. In terms of the size of outcrop examined, the volume of rock mass examined in each locality varied between each location, with observed surface areas ranging from 6 to 180 m^2 (Fig. 4.4). Tables 4.4 through 4.8 summarise all the rock mass data collected and calculated during the course of the project, with full details of the rock mass strength data (including locality information) able to be found in Appendix D.

4.3.1 Snowdonia

The area of Snowdonia is situated in North Wales, United Kingdom, (Fig. 4.3) and is largely composed of pyroclastic rocks and rhyolitic lavas belonging to the Snowdon Volcanic Series (Williams and Ramsay, 1968). At its centre lies the peak of Snowdon, 1,085 metres above sea-level, and it is the rocks from the Snowdon Volcanic Series that are studied in this project. The
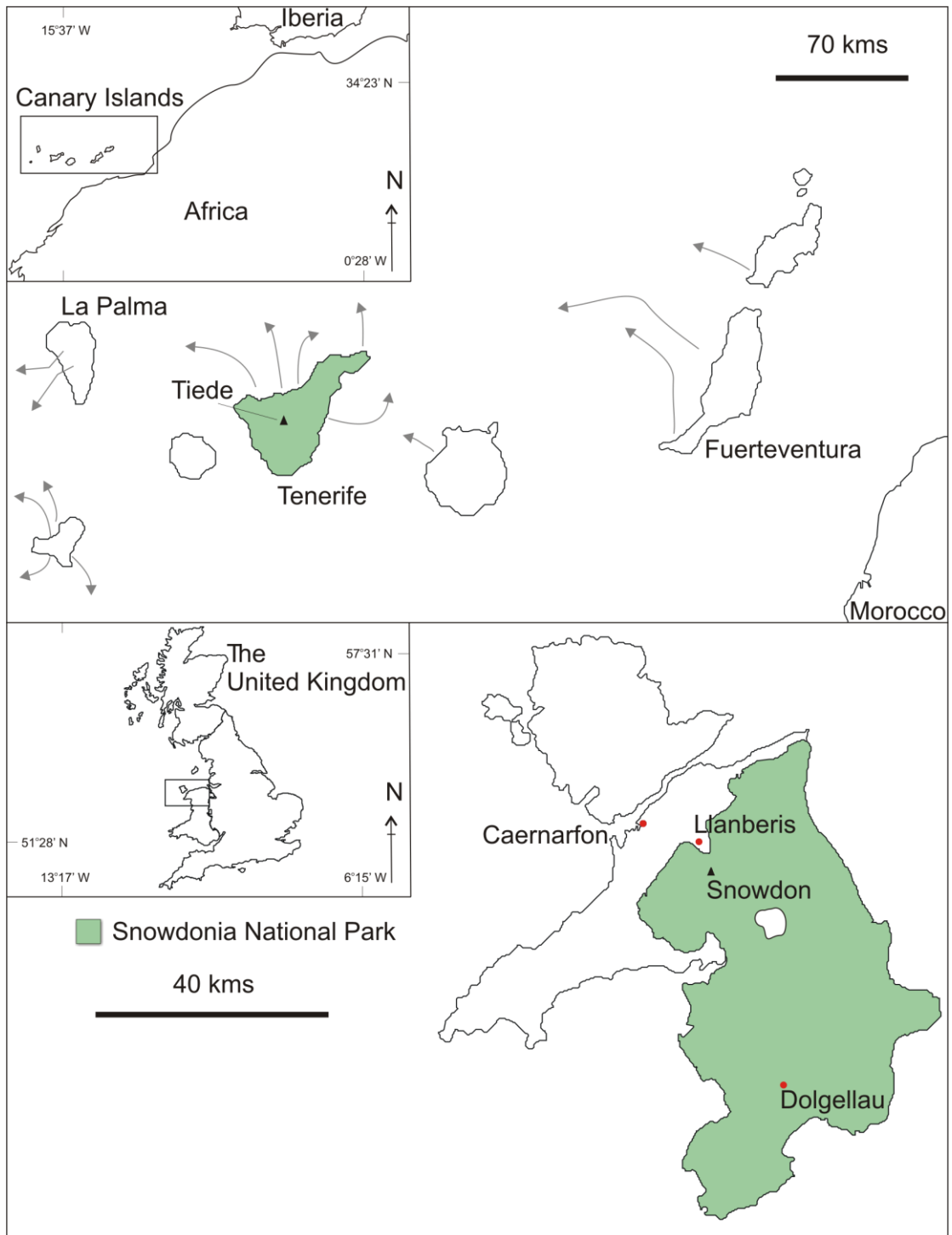
Figure 4.3: Location maps for Tenerife, Canary Islands and Snowdonia, United Kingdom. Also shown on the regional map of the Canary Islands as grey arrows, are the locations of interpreted lateral collapse events. The arrows also define the inferred path of the debris deposits, as depicted by Carracedo and Day (2002).
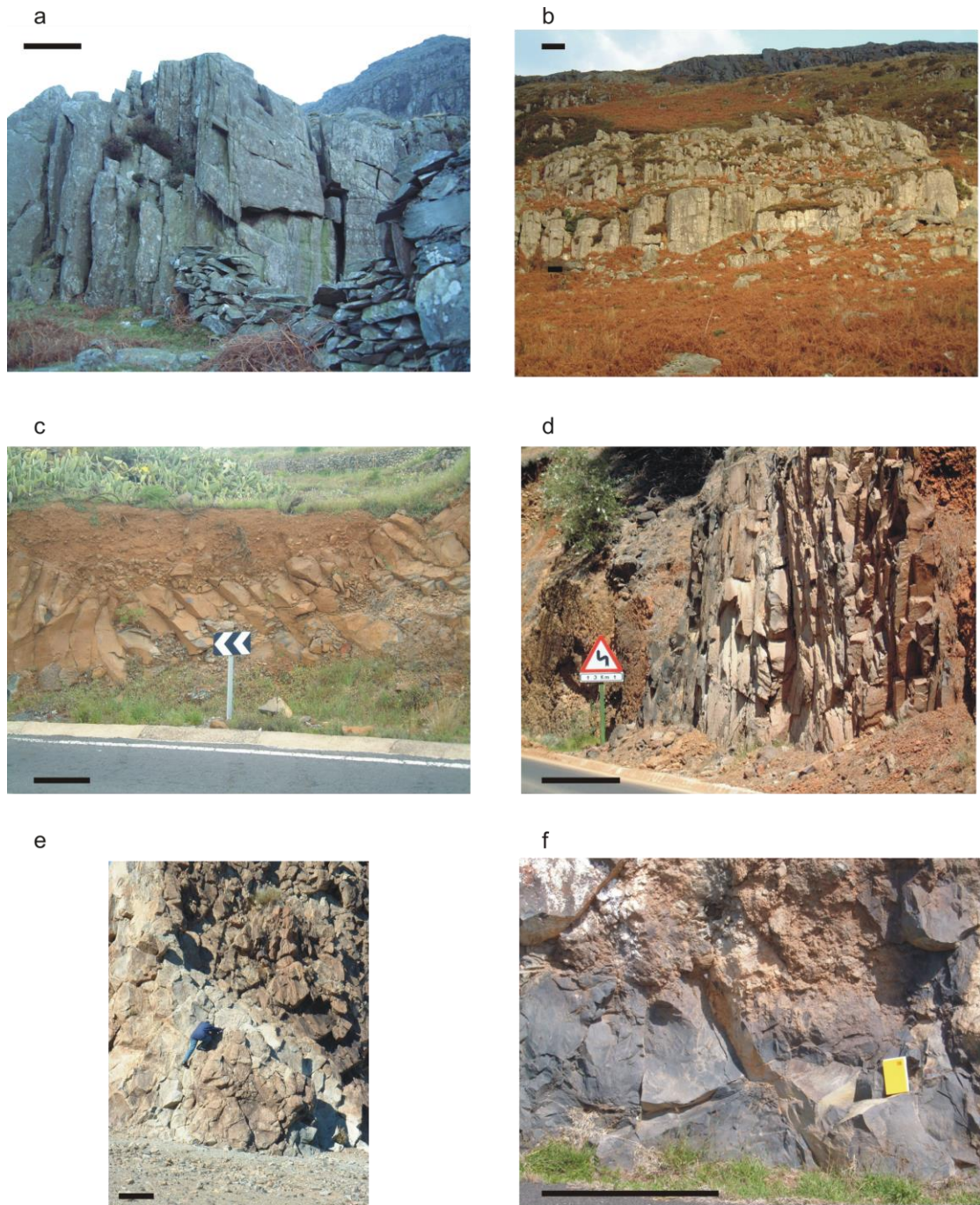
Figure 4.4: Photographs illustrating rock masses studied using the rock mass classification schemes outlined in Sections 5.2.1 and 5.2.2. Photographs **(a)** and **(b)** are rock masses from Snowdonia; photographs **(c)** to **(f)** are rock masses from Tenerife. In all photographs the black bar represents a horizontal distance of 1.0m. Locations of each photograph are as follows: (a) 53° 6'36.50"N   4° 6'22.66"W; (b) 53°6'10.50"N   3°55'54.89"W; (c) 28°5'20.81"N   16°41'28.51"W; (d) 28° 9'56.11"N 16°38'3.69"W; (e) 28°12'32.58"N 16°38'46.78"W and (f) 28°9'17.85"N   16° 30'43.60"W.

series is divisible into an Upper Rhyolitic, a Bedded Pyroclastic and a Lower Rhyolitic Series (Williams and Ramsay, 1968). As with most volcanism in North Wales, the Snowdon Volcanic Series is associated with the subduction of the Iapetus oceanic slab, and the ensuing arc and back-arc volcanism. Full ocean closure is considered to have occurred by ~450 Ma (Hutton, 1988), when subduction was replaced by sinistral strike slip tectonism (Thorpe *et al.*, 1993). In particular, the Snowdon Volcanic Series is related to late back-arc extension and volcanism (Woodcock and Strachan, 2000), which is thought to have utilised pre-existing deep-seated crustal lineaments to channelise large volumes of rhyolitic magmas to the surface (Kokelaar, 1988; Gibbons *et al.*, 1999).   In contrast to the majority of volcanism of similar age in the region, there is evidence that in central Snowdonia the volcanism had at least a temporary subaerial expression (Howells *et al.*, 1981), with these volcanoes forming islands in the otherwise marine Welsh Basin (Woodcock and Strachan, 2000), and indeed, all the rocks studied in this project have been interpreted to have be emplaced subaerially. Therefore, any specific conclusions drawn may not be applicable to sub-marine volcanism, as the products of such events would be rapidly quenched. This may lead to substantially different rock mass properties to those cooled relatively slowly, in a subaerial setting.

4.3.2 Tenerife (Canary Islands)

The Canary Islands are an archipelago of seven large islands in the Atlantic Ocean, just over 100 km east of Cape Juby on the African coast (Fig. 4.3). There are broad similarities between the Canaries and the Hawaiian Islands in the fact that they are both groups of intraplate oceanic-island volcanoes dominated by basaltic magmatism (Carracedo and Day, 2002). This similarity may suggest that the Canaries are also related to an upwelling mantle plume or hotspot. Tenerife is the largest of the Canary Islands (Fig. 4.3), with a total surface area of 2,057 km^2 and a total height of about 8,000 m starting at the sea floor 4,000 m.b.s.l. (Hürlimann *et al.*, 2001). Indeed, it is the third-highest ocean-island volcano in the world behind the Hawaiian volcanoes Mauna Loa and Mauna Kea. Determining volcanic rock mass strength data from Tenerife has particular relevance to this project as the island has a well documented history of lateral collapse, (Navarro and Coello, 1989; Cantagrel *et al.*, 1999; Ablay and Hürlimann, 2000; Hürlimann *et al.*, 1999; 2001) and is almost completely surrounded by complex debris aprons (Ablay and Hürlimann, 2000). The northern side of the island alone is postulated to have experienced at least six successive north-directed

avalanches (Cantagrel *et al.*, 1999), believed to be the source of the 1,000 to 1,200 km^3 of volcanic debris imaged by Watts and Masson (1995), which is spread widely across the sea floor north of Tenerife.

It has previously been assumed that activity has been continuous in Tenerife since emplacement of the oldest subaerial lavas some 12 Ma (Carracedo and Day, 2002). This would suggest that Tenerife is still in its shield building stage. However, recent work indicates that a break in volcanic activity on Tenerife may have occurred from about 4 Ma (Ancochea *et al.*, 1990; Carracedo and Day, 2002). This implies that the Las Cañadas volcano which has been active in the central and southern parts of the island since about 3 Ma, is in fact a very large and vigorous post-erosional (post-shield) volcano (Ablay and Hürlimann, 2000; Carracedo and Day, 2002). The Las Cañadas edifice developed upon the basaltic shield series, comprising of the Teno, Anaga and Roque del Conde massifs (Cantagrel *et al.*, 1999). The Teno and Anaga massifs form the western and eastern extremities of the island respectively, and the Roque del Conde massif forms an inlier in the southern part of the island (Ablay and Hürlimann, 2000). However, the Las Cañadas edifice is not thought to be the first expression of post-shield volcanism. The oldest post-shield volcanics belong to the Boca Tauce volcano, which is now buried beneath the Las Cañadas edifice and has been identified from gravity and magnetic anomalies (Ablay and Kearey, 2000). The Las Cañadas edifice grew in three main destructive cycles during the past 3.5 Ma, each culminating in what has been interpreted as either caldera collapse or large-scale flank collapse (Cantagrel *et al.*, 1999; Hürlimann *et al.*, 1999). Evidence for either mechanism exists is the form of extensive breccias (Cantagrel *et al.*, 1999) and marine geophysical data (Watts and Masson, 1995) to the north of the island, and extensive pyroclastic deposits to the south (Bryan *et al.*, 1998; 2002). The current Las Cañadas caldera depression is occupied by two large, active stratovolcanoes, Teide and Pico Viejo, which give Tenerife its present relief (Fig 4.5).

Tenerife can be considered an ideal location to sample rock mass strength data for use with modelling volcanic collapse, as there is a wealth of recent volcanic rocks of varying chemistry, lithology and strength and also a large amount of evidence to support the occurrence of several large-scale collapse events associated with the island. However, in this study, there is no attempt to model the physical processes involved with these precise collapse events. This is because,
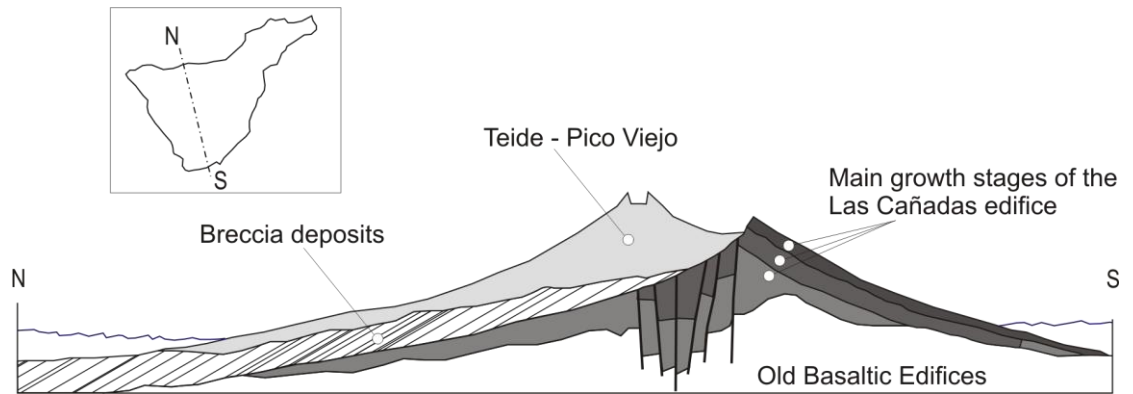
Figure 4.5: Schematic cross section of Tenerife adapted from Cantagrell *et al.* (1999). The three main phases of growth of the Las Cañadas edifice can still be seen to the south, which include voluminous pyroclastic rocks interpreted as caldera collapse products (Bryan *et al.*, 1998). The north side of the island is largely lacking in pyroclastic material, but several extensive breccias have been identified, which are interpreted as the products of successive northward directed lateral collapse (Cantagrell *et al.*, 1999).

although several of the factors discussed in Chapter two may have played a pivotal role in the generation and triggering of Tenerifian collapse events, there are too many unknown parameters that were not ascertainable with the resources available to this project to model a specific volcano accurately. It is for this reason that the models conducted during this project are generic examples, and it is also for this reason that no critical examination of a single volcano has been conducted, as this may lead the reader to consider that there has been an attempt to model a particular edifice.

4.3.3 Rock Mass Rating data collection method

At each locality, the RMR was calculated according to the rating system detailed in Table 4.1. No cores were taken during the course of the data collection and all RMR values were obtained from scan lines run across the outcrop face. To apply the RMR system, the rock mass is divided into a number of structural regions according to Table 4.1, such that certain features are more or less uniform within each region. Although rock masses are discontinuous in nature, they may, nevertheless, be uniform in regions when, for example, the type of rock or discontinuity spacing are the same throughout that region (Bieniawski, 1993). To gain a comprehensive overview of the rock mass condition and characteristics, the RMR was calculated both horizontally and vertically for each segment of the examined rock mass. The horizontal and vertical RMR values were then averaged to give one RMR value for that region. This was done with the aim of producing an

A. Snowdonia	Rock Type	Total Number of Ratings	RMR
	Rhyolite	16	52-74
	Tuff	20	47-74
	Micro Granite	8	57-79
B. Tenerife			
	Basalt	14	48-92
	Phonolite	11	38-89
	Welded Ignimbrite (Phonolitic)	1	70
	Rhyolite/Obsidian	2	77
	Phonolitic	2	59-71

Table 4.4: Summary of the RMR data collected from the two field areas studied. For full details (including locality information) see Appendix D.

Tenerife	Rock Type	Total Number of Ratings	GSI
	Basalt	11	22-67
	Phonolite	3	22-35
	Phonolitic	5	35-53

Table 4.5: Summary of the GSI data collected from the two field areas studied. For full details (including locality information) see Appendix D.

overall estimate of rock mass strength rather than an estimate that may favour one particular orientation.

All but one of the constituent parts of the RMR can be determined reliably in the field. The strength of the intact rock however, requires some laboratory testing of samples. The RMR system incorporates two representations of strength, the point load strength index and the Uniaxial Compressive Strength (UCS), either one of which can be used in the determination of the RMR. The details of sample strength testing as discussed in detail in Section 4.4.

A summary of the RMR values calculated for each particular rock type can be found in Table 4.4. For simplicity, an averaged RMR determined for each area of rock mass examined in this study is used in any stability modelling. However, we accept that it may not be realistic to assign a single value to a volume of rock mass, and that a range of RMR values may be more appropriate. It is

further cautioned that any stability analysis carried out with strength estimates determined by following the method outlined above should use the corresponding range of rock mass strength estimates in all calculations.
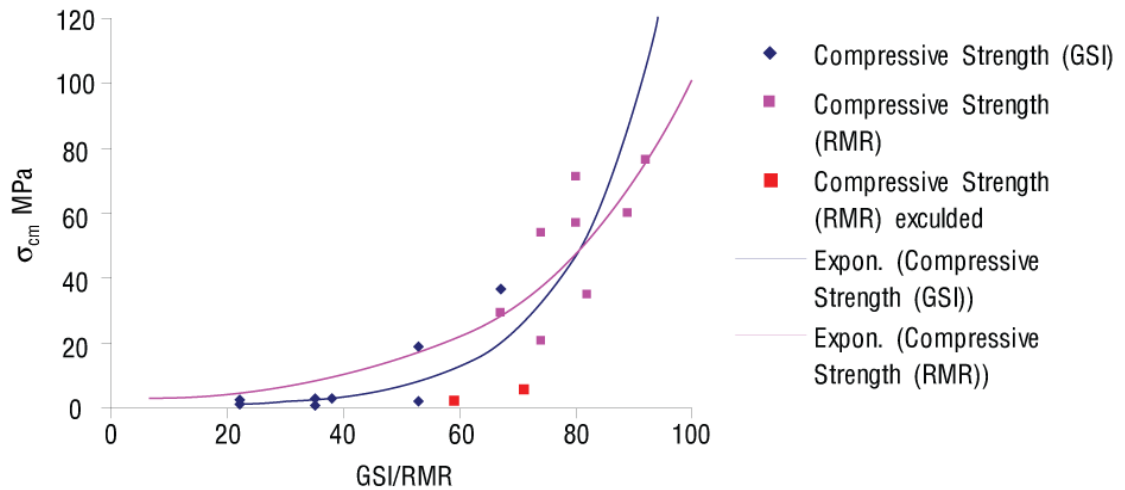
Figure 4.6: Comparison of rock mass compressive strength, σ_{cm}, calculated using RMR (squares) and GSI (diamonds) values from four localities on Tenerife. The value of σ_{cm} was calculated using the method outlined in Section 5.5. The first thing to note with the exception of the two red squares is that the GSI generally produces lower values of σ_{cm}. The two red squares were excluded for being anomalously weak (see the end of section 5.6 and figure 5.14). This is attributed to the less structured method of calculating the GSI. However, since the σ_{cm} data plots in the lower part of the y axis for the GSI, when a curve is fitted for prediction purposes it has too steep a gradient and predicts rock masses that are too strong at high values of GSI. An exponential fit was used (the curves labelled Expon.) as it proves the best sensible statistical fit to the larger data set interrogated fully in section 4.5.

4.3.4 GSI data collection method

Unlike the RMR, the GSI requires no physical field measurements, and is based purely on field *observations* (Tables 4.2 and 4.3). It does however have some similarities with the RMR. Like the RMR, when considering the GSI, the rock mass is divided into a number of structural regions that can be classified by Tables 4.2 and 4.3 and assigned an appropriate GSI value. This is a much quicker process than calculating a RMR, as it is purely observational. Indeed, with a good quality digital camera and some simple field notes, it would be feasible to estimate the GSI remotely from photographs.

Table 4.5 contains a summary of the GSI data collected during this project. Estimating the GSI proved inconsistent, with the range of GSI values recorded being much greater that than those of

the RMR for the same outcrop, and also usually indicating poorer quality rock masses than the corresponding RMR value for the same location (Fig. 4.6). However, all of the rock mass data collected from the field areas are from rock masses that would be considered *good quality* (RMR >25). Because of this, and the fact that above an RMR of 25 there is theoretically little difference between the two classification schemes, GSI data were considered, in this cases, unreliable and not used in any model inputs.

4.4 Sample strength testing

Intact rock strength data for many rock types including most volcanic rocks are readily available from published sources (e.g. Hoek 1983; Hoek & Brown, 1988; Okubo, 2004) and can be considered reasonably well-constrained. However, to ensure the suitability of these *estimated* intact strength values, limited strength testing of field samples was conducted. All samples on which strength testing was carried out were collected at field locations in Tenerife with relevant data given in Table 4.6. The types of outcrops from which samples were collected included fresh lava flows exposed in road cuts at locations 2-1, 3-1 and 3-2, and more weathered samples from the upper regions of lava flows naturally exposed on the surface at locations 3-3 and 4-1. Samples from locations 3-2, 3-3 and 4-1 relate to volcanics associated with Teide and Pico Viejo complex; and are < 0.2 Ma (Hürlimann *et al.*, 2004). Samples from the other locations relate to products of the Las Cañadas volcano; making then younger than 4 Ma but older than 0.2 Ma (Hürlimann *et al.*, 2004).

The Point Load Strength test (Anon, 1985) is an index test for the strength classification of rock materials. The test measures the Point Load Strength *Index*, as such the results should be used *as* an index, not an actual physical measurement of strength. However, it may also be used to quantify other strength parameters with which the Point Load Strength test is correlated. For example, the uniaxial compressive and tensile strength (Franklin *et al.*, 1972; Anon, 1985). As shown in Table 4.1 for the calculation of the RMR, either the Point Load Strength/Index or the UCS can be used. So, to calculate the RMR, it is not necessary to determine the intact rock UCS of the lithology that makes up the rock mass. However, for the direct estimates of the rock mass strength which are discussed in Section 4.5, a value or more realistically a suite of values for the UCS is needed. These data are presented in Table 4.6 and with the exception of location 4-1, all the samples

tested produced UCS values comparable to the estimated intact strength values used for all field localities for which strength testing was not undertaken. These estimated values can be seen in Tables 4.8 and 4.9. An explanation for the anomalously low strength of samples tested at location 4-1 is given at the end of Section 4.5. Full details of the Point Load Strength test method are found in Appendix C and the complete data set is given in Appendix D.

Location	Rock Type	Number of Samples	Is(50), MPa	UCS, MPa	Tensile Strength, MPa
Tenerife 05, 2-1. 20°09'17.77" N 016° 30'43.68" W	Basalt	10	8.67	173.4 - 216.8	-6.9
Tenerife 05, 3-1. 28° 5'17.12"N 16°41'29.84"W	Basalt	6	9.13	182.7 - 228.4	-7.31
Tenerife 05, 3-2. 28°13'11.1 N 016°40'53.4 W	Phonolite	10	4.42	88.5 - 110.6	-3.54
Tenerife 05, 3-3. 28°13'7.23"N 16°40'52.01"W	Basalt	10	4.77	95.4 – 119.2	-3.81
Tenerife 05, 4-1. 28°15'13.46"N 16°37'31.29"W	Phonolitic	10	1.21	24.3 – 30.4	-0.97

Table 4.6: Summary of the conducted point load strength testing calculated following the method outlined in the text. Full details can be found in Appendix D.3. All the samples used in strength testing listed in the table were obtained from lava flows.

Property	Symbol
Major principle stress	σ_1
Minor principle stress	σ_3
Hoek-Brown parameter	m
Hoek-Brown parameter	s
Unconfined compressive strength (UCS)	σ_c
Unconfined compressive rock mass strength	σ_{cm}
Tensile rock mass strength	σ_{tm}
Shear Strength	τ
Instantaneous friction angle	ϕ_i
Cohesive strength	c
Coefficient of friction	μ
Instantaneous cohesive strength	c_i
Normal stress	σ_n
Effective stress	σ'

Table 4.7: Rock mass equation variables.

4.5 Field results and application of rock mass properties to volcanic edifices

As introduced in Section 4.2, Hoek and Brown (1980; 1988) proposed a novel method for estimating rock mass strength that makes use of the RMR classification. The Hoek-Brown method, now widely used by geotechnical engineers to predict rock-fracture behaviour at the outcrop scale, has recently found application in the strength assessment of volcanic rock masses (Voight, 2000, Thomas *et al.*, 2004b). The following is a detailed analysis of the method for estimating volcanic rock mass strength published by Thomas *et al.* (2004b). This paper is also presented in Appendix A. Table 4.7 details the variables that are used in this process.

The general empirical criterion (Hoek-Brown criterion) for rock mass strength proposed by Hoek & Brown (1980) is defined by the relationship between the principal stresses at failure:

$$\sigma_1 = \sigma_3 + (m\sigma_c\sigma_3 + s\sigma_c^{2})^{1/2} \qquad \text{(Equation 4.1)}$$

where σ_1 and σ_3 are the major and minor principle stresses respectively at failure, σ_c is the unconfined (uniaxial) compressive strength of the intact rock; and m and s are empirical constants dependent on rock type and available from published sources (e.g. Hoek, 1983; Hoek & Brown, 1988). Standard values of σ_c determined from laboratory studies were mainly taken from the reference library within the *Rocscience* program *RocLab*, but can also be obtained from numerous published sources (e.g. Brown, 1981). These published data were constrained by the limited in-house strength testing described in Section 4.4, from which an averaged UCS specific to the tested rock mass was used. For a given rock mass (Hoek & Brown, 1988), the constants m and s are related to the RMR as follows:

$$m = m_i \exp\left[(RMR - 100)/28\right] \qquad \text{(Equation 4.2)}$$

and

$$s = \exp\left[(RMR - 100)/9\right] \qquad \text{(Equation 4.3)}$$

where m_i is the value of m for the *intact* rock. The same calculations can also be carried out replacing the RMR with the GSI. The special cases of unconfined compressive strength σ_{cm} and uniaxial tensile strength σ_{tm} for a rock mass can be found by putting $\sigma_3 = 0$ and $\sigma_1 = 0$ respectively into equation (4.1). Thus:

$$\sigma_{cm} = \left(s\sigma_c^2\right)^{1/2}$$ (Equation 4.4)

and

$$\sigma_{tm} = \frac{\sigma_c}{2}\left[m - \left(m^2 + 4s\right)^{1/2}\right]$$ (Equation 4.5)

Using the Hoek–Brown criterion to estimate the strength characteristics of rock masses from the two studied field areas discussed in Section 4.3, compressive strength reductions in the rock mass (σ_{cm}) of up to 96% relative to intact laboratory tested samples (σ_c) are observed (Table 4.8). Table 4.8 also lists rock mass tensile strength obtained directly from the Hoek-Brown Equations. Fig. 4.7 shows plots of rock mass compressive and tensile strength against RMR for rock masses from the two field localities studied in this project and also published rock mass strength data from Hawaii (Okubo, 2004). From Fig. 4.7a, it can be seen that the compressive strength of the rock-masses tested increases exponentially with RMR according to:

$$\sigma_{cm} = 0.5161e^{(0.0581*RMR)}$$ (Equation 4.6)

and appears largely insensitive to both the initial magma composition (basaltic or rhyolitic), and relative ages of the rock masses tested. An exponential relationship was chosen because it proved the best sensible statistical fit to the data. This is exemplified by its R^2 value of 0.8315 (Fig. 4.7a), compared to R^2 values of 0.4066 and 0.8029 for linear and power relationships respectively. A marginally increased R^2 value of 0.8392 is observed from a second order polynomial relationship, but this relationship has a complicated expression, which out weighs any potential benefits of a marginally better fit to the data. This apparent exponential increase suggests that relatively small changes in rock mass quality will impact significantly on edifice strength. This insensitivity to both rock composition and age suggests that these exponential relationships may be useful in providing

Rock Type	RMR	UCS[#], MPa	Rock-mass Compressive Strength, MPa	Rock-mass Tensile Strength, MPa
A. Snowdonia				
Rhyolite	52 – 74	~ 175	12 - 41	(-0.29) - (-1.5)
Tuff	47 – 74	~ 150	7 - 35	(-0.18) - (-1.4)
Micro Granite	57 – 79	~ 250	23 - 78	(-0.3) - (-1.55)
B. Tenerife				
Basalt	48-92	~ 150	8 - 73	(-0.2) - (-3.8)
Phonolite	38-89	~ 175	5 - 73	(-0.1) - (-2.6)
Welded Ignimbrite	70	~ 125	24	-0.9
Rhyolite/Obsidian	77	~ 200	56	-2
Phonolitic	59-71	~ 150	2 - 6	(0) - (-0.2)

Table 4.8: Rock mass strength data detailing the range of compressive and tensile strengths determined from the two field areas, [#]values estimated from Brown (1981).

quick and relatively accurate estimates of rock mass strength directly from the RMR recorded in the field. In Fig. 4.7a where the data for (σ_{cm}) is plotted alongside the fitted exponential curve, the mean error between the actual value and that predicted by the exponential fit is 21.4 % with a standard deviation of 23.0. However, if the imprecision of the RMR classification scheme is taken into account, this error falls to within an acceptable range, and provides a valid method of estimating, to a first approximation, rock mass strength directly from the RMR. It is also apparent from Fig. 4.7b that this exponential relationship also holds for the tensile rock mass strengths obtained through the use of the Hoek-Brown criterion, and:

$$\sigma_{tm} = 0.0055e^{(0.0744*RMR)}$$
(Equation 4.7)

As with the rock mass compressive strength an exponential relationship was chosen as it proves the best sensible statistical fit to the data. Since it is the aim to use the estimated rock mass strength properties in edifice stability studies, and most geotechnical software is still written in terms of Mohr-Coulomb criterion, it is necessary to determine an estimated angle of friction and cohesive strength for the rock mass. A graphical means of representing stress relationships was discovered by Culmann (1866) and later developed in detail by Mohr (1882), which led to the implementation of a graphical method (the Mohr stress circle). Uniaxial tension, unconfined axial (uniaxial) compression, or confined (triaxial) compression may affect failure of intact cylindrical rock specimens. Typical examples of effective stress circles for these types of failure are shown in
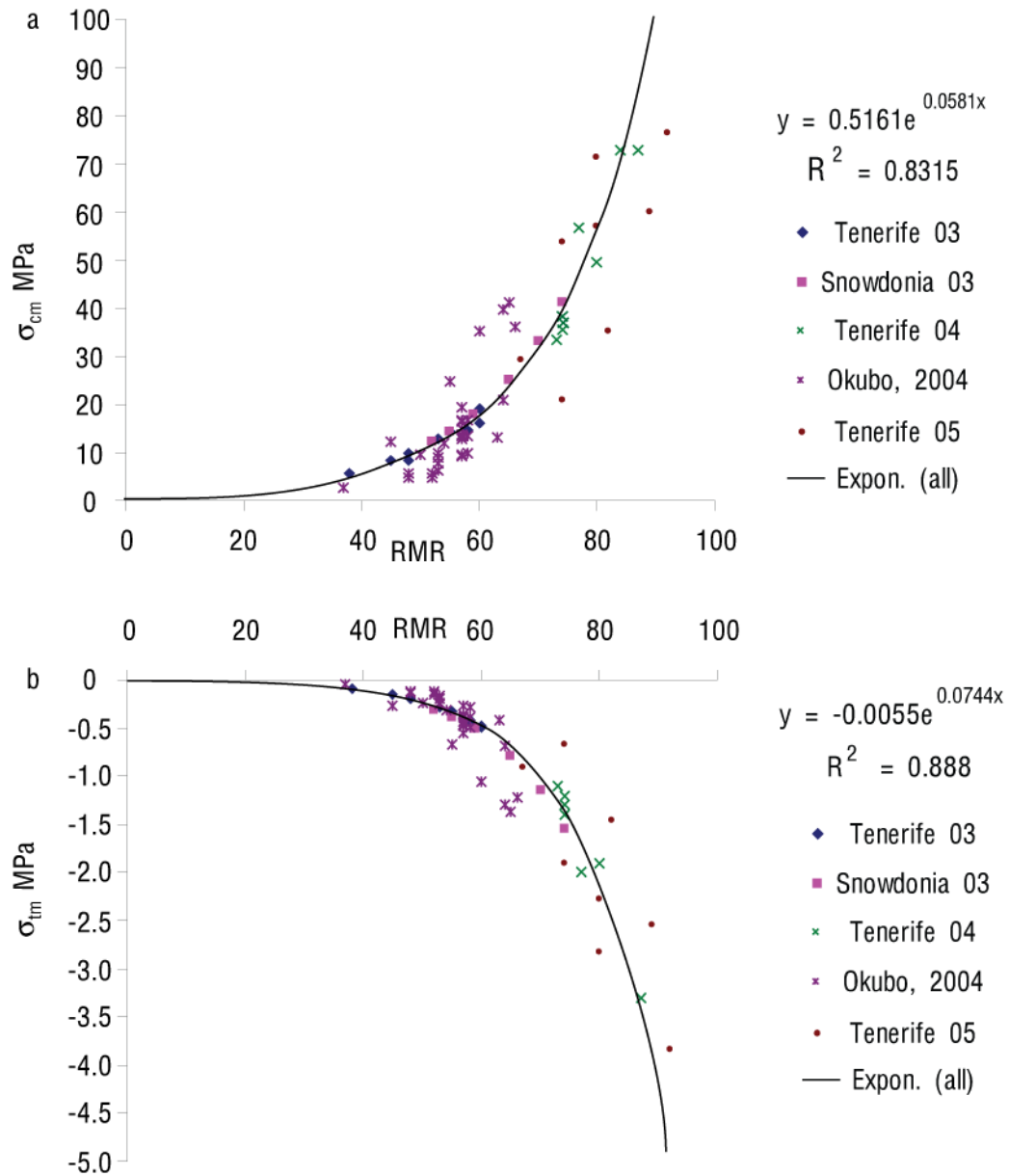
Figure 4.7: Plots of rock mass compressive (a) and tensile (b) strength verses RMR for field localities studied in this project and from Hawaiian rock mass data published by Okubo (2004).The curve labelled Expon. (all) is the best fit exponential relationship to the entire data set.

Figure 4.8. The envelope to the stress circles at failure (Mohr Failure Envelope) corresponding to the empirical failure criterion defined in Equation 4.8 was derived by Bray (Hoek, 1983) and is given by:

$$\tau = \left(Cot\phi_i - Cos\phi_i\right)\frac{m\sigma_c}{8}$$ (Equation 4.8)

where τ is the shear stress at failure (i.e. the shear strength) and ϕ_i is the instantaneous friction angle at given values of τ and normal stress (σ_n), this can be visualised as the inclination of the tangent to the Mohr failure envelope at the point (σ_n, τ), as shown in Figure 4.8. The value of the instantaneous friction angle ϕ_i is given by:

$$\phi_i = \tan^{-1}\left[4h\cos^2\left(30^o + \tfrac{1}{3}\sin^{-1} h^{-3/2}\right) - 1\right]^{-1/2}$$ (Equation 4.9)

where

$$h = 1 + \frac{16\left(m\sigma_n + s\right)}{3m^2}$$ (Equation 4.10)

at any given value of σ_n. Mohr failure envelopes for an assumed intact rhyolite and a rhyolitic rock mass from Snowdonia are compared in Figure 4.9. As expected, intact material is stronger than the jointed rock mass.
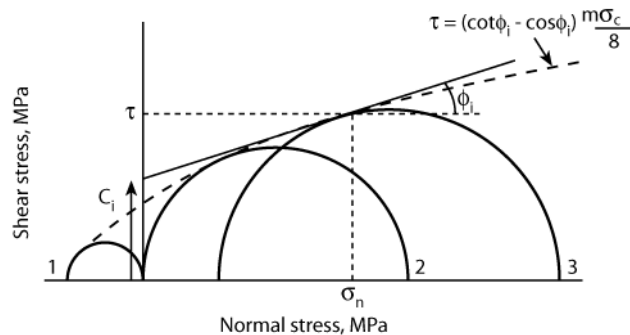

Figure 4.8: Typical failure circles for rock and the Bray strength envelope (Hoek, 1983): 1, uniaxial tension; 2, unconfined axial (uniaxial) compression; 3, confined (triaxial) compression. Also shown are the instantaneous values of friction angle (ϕ_i) and cohesion (c_i)
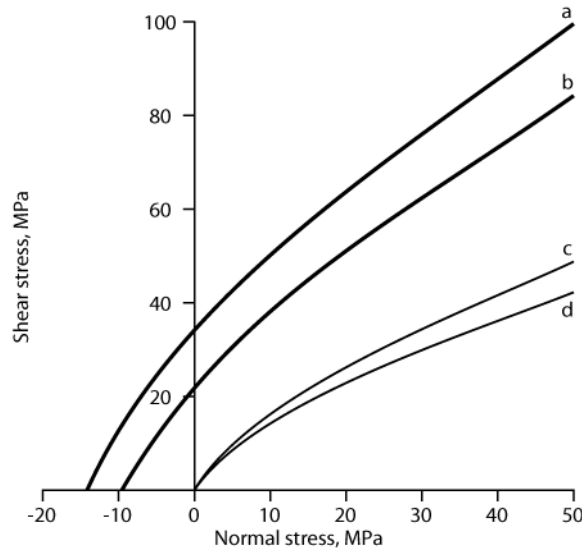
Figure 4.9: Mohr failure envelopes for a typical intact rhyolite and a rhyolitic rock mass. Intact: m_i = 16, s = 1, σ_c = 225 MPa (curve a); curve b is as curve a, but σ_c = 150 MPa. Rock mass: m = 2.68, s = 0.0039, σ_c = 225 MPa (curve c); curve d as curve c, but σ_c = 150 MPa. The Hoek-Brown constants m and s were calculated from equations 4.6 and 4.7 using an RMR of 50.

Shear stress tending to cause failure across a plane is resisted by the cohesion of the material (c) and a constant (μ) times the normal stress (σ_n) (pressure) across the failure plane. This is expressed in the Mohr-Coulomb equation for shear strength:

$$\tau = c + \mu\sigma_n \qquad \text{(Equation 4.11)}$$

where the constant μ is the coefficient of friction:

$$\mu = \tan\phi \qquad \text{(Equation 4.12)}$$

However, rather than being constants for jointed rock masses, c and ϕ both vary with stress level (Hoek & Brown, 1980). It is thus convenient to calculate the instantaneous values for cohesion (c_i) using the instantaneous friction angle defined in Equation 4.9. Thus, Equation 4.11 can be re-written as:

$$c_i = \tau - \sigma_n \tan\phi_i \qquad \text{(Equation 4.13)}$$

In Section 3.2, the concept of effective stress (σ') was explained. The effective stress represents the portion of the total stress acting on the soil or rock. Hence it becomes apparent that it is actually

the effective stress that determines the frictional strength, and Equation 4.11 should be revised to the form:

$$\tau = c + \mu\sigma'$$ (Equation 4.14)

i.e. the normal "*pressure*" is the effective stress, not the total stress. In a two dimensional case represented as a Mohr Failure Envelope, the effect is to move the whole circle towards lower values, without changing its size (Fig. 4.10). Because decreasing the effective stress through increasing the pore pressure moves the Mohr circle to the left, it can lead to intersection of the failure envelope, hence physical failure even though the principle stresses remain the same.

Figure 4.11 shows a Mohr Failure envelope (Equation 4.8) for a rhyolitic rock mass from Snowdonia, along with a plot showing the instantaneous friction angle (Equation 4.9) and instantaneous cohesion (Equation 4.13). It can be seen that, at low values of normal stress, the angle of friction is high and the cohesion is low. As the normal stress increases, this relationship is reversed, suggesting an increase in cohesion but a decreasing angle of friction at progressively deeper parts of the edifice interior. This may be an important factor in determining the shape of a failure surface within a volcanic edifice, and could be a simple explanation for why non-volcanic slope failures tend to be shallow and steep. As they lack the additional thermal and mechanical pore fluid pressure increases that most likely precede volcanic slope failures, hence not allowing them to overcome this increase in cohesion with depth. Although c and ϕ will vary with stress level, it is useful to fit a straight line Mohr-Coulomb relationship to the failure envelope, as it gives a good
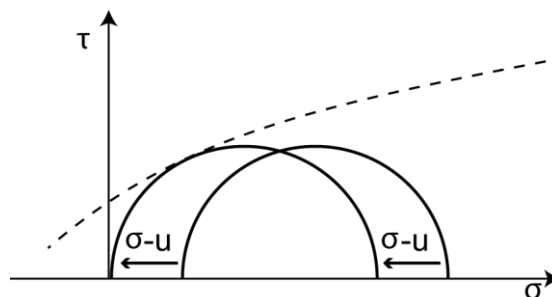
Figure 4.10: Graphical representation of how pore pressure affects the Mohr circle. Because decreasing the effective stress through increasing the pore pressure moves the Mohr circle to the left without any physical change in state, it can lead to intersection of the failure envelope (dotted line), hence physical failure even though the principle stresses remain the same (as represented by the fact the two Mohr circles are the same size).
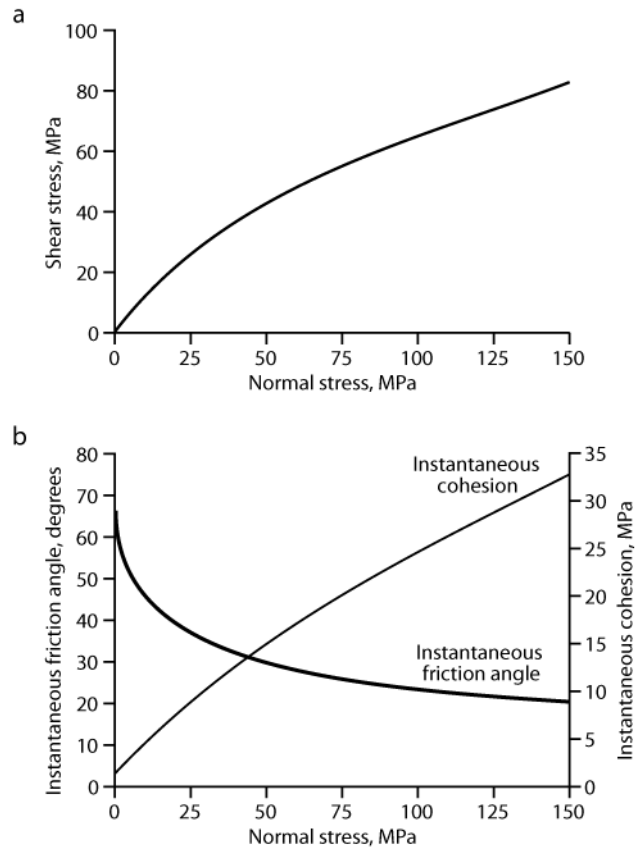
Figure 4.11: (a) Mohr failure envelope for a rhyolitic rock mass from Snowdonia; **(b)** plot showing the instantaneous angle of friction and instantaneous cohesion.

approximation of the rock mass angle of friction and provides an upper limit of cohesive strength (Hoek *et al.*, 2002). This is done *not* by fitting the 'best-fit' tangent to the Mohr failure envelope, which can lead to an overestimate of the cohesive strength, but by fitting a linear Mohr-Coulomb relationship (Equation 4.1) by a least squares method (Fig. 4.12) (Hoek *et al.* 2002). As previously stated, the value of cohesive strength produced from this method provides an upper limit, and it is prudent to reduce it to 75% of this value to serve any practical purpose.

A more convenient way to gain an estimate of the cohesive strength of the rock mass is to set $\sigma_n = 0$ in Equation 4.11. Thus, the cohesion becomes equal to the shear stress, and it can be read directly from the Mohr failure envelope as the intercept on the shear strength axis (Fig. 4.8). While this method may be statistically less accurate, it provides a much more realistic value of cohesion, and is much closer to a minimum rather than maximum value. For the purposes of stability analysis, this minimum approximation is preferable to the value obtained using the least squares method, and was the method used to obtain all calculated values of cohesion.   The angle of

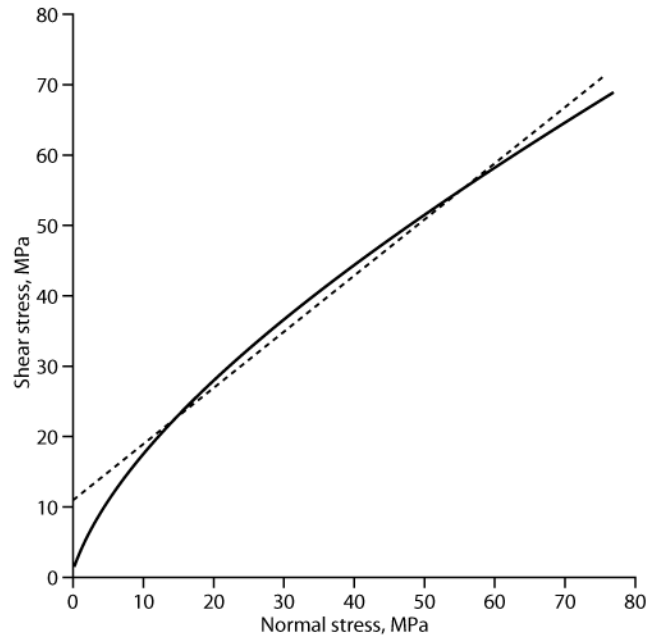**Figure 4.12:** Example of a straight-line Mohr-Coulomb fit to a Mohr failure envelope obtained using least-squares method. In this plot the cohesion can be read off the y-axis as the intercept of the straight line, although, in practice it is prudent to reduce this value by up to 75% for a realistic working estimate of cohesion (Hoek *et al.*, 2002).

Rock Type	RMR	UCS[#], MPa	Rock-mass Cohesive Strength, MPa	Rock-mass angle of friction, degrees
A. Snowdonia				
Rhyolite	52 - 74	~ 175	1.2 - 4.8	31.3 - 38.1
Tuff	47 - 74	~ 150	0.7 - 4.3	27.8 - 36.1
Micro Granite	57 - 79	~ 250	1.2 - 6.8	41.2 - 49.4
B. Tenerife				
Basalt	48-92	~ 150	0.8 - 8.6	28.1 - 42
Phonolite	38-89	~ 175	0.4 - 7.5	28 - 40
Welded Ignimbrite	70	~ 125	2.8	33.3
Rhyolite/Obsidian	77	~ 200	N/A	N/A
Phonolitic	59-71	~ 150	0.2 - 0.7	18.3 - 23.1

Table 4.9: Rock mass strength data detailing the range of cohesive strengths and internal angles of friction determined from the two field locations, [#]values estimated from Brown (1981).

friction and cohesive strength of rock masses determined for the visited field localities in Snowdonia and Tenerife are listed in Table 4.9. The values of cohesion are also plotted verses RMR in Figure 4.13, again, with published rock mass strength data from Hawaii (Okubo, 2004). The same exponential relationship identified between σ_{cm} and σ_{tm} and the RMR is also evident between values of rock-mass cohesive strengths and RMR, in the form:

$$c = 0.0349e^{(0.0649*RMR)} \qquad \text{(Equation 4.15)}$$

Again, an exponential relationship was chosen as it proves the best sensible statistical fit to the data.

Although the majority of data used in the determination of the exponential relationships shown in Equations 4.6, 4.7 and 4.15 were calculated using published values of intact strength, the samples listed in Table 4.6, on which strength testing was carried out as part of this project are also included in the data plotted in Figures 4.7 and 4.13 (identified in the key as Tenerife 05). These values fit the relationship and integrate well with the data set derived from purely published values. This suggests that estimating intact strength from published data regarding rock type, grain/crystal size and the condition of the rock is a valid method. The one exception is that of location 4-1.

The lava flow tested at location 4-1 lies within the current Las Cañadas caldera and can be traced onto the upper slopes of Teide. Therefore, these samples were interpreted as alkali rocks produced by late stage volcanism. Their location (Table 4.6) lead to these samples being inferred as originating from the most recent phonolitic lava flows (Carracedo and Day, 2002). However, their physical appearance differed significantly from phonolite samples collected at other locations (Fig.
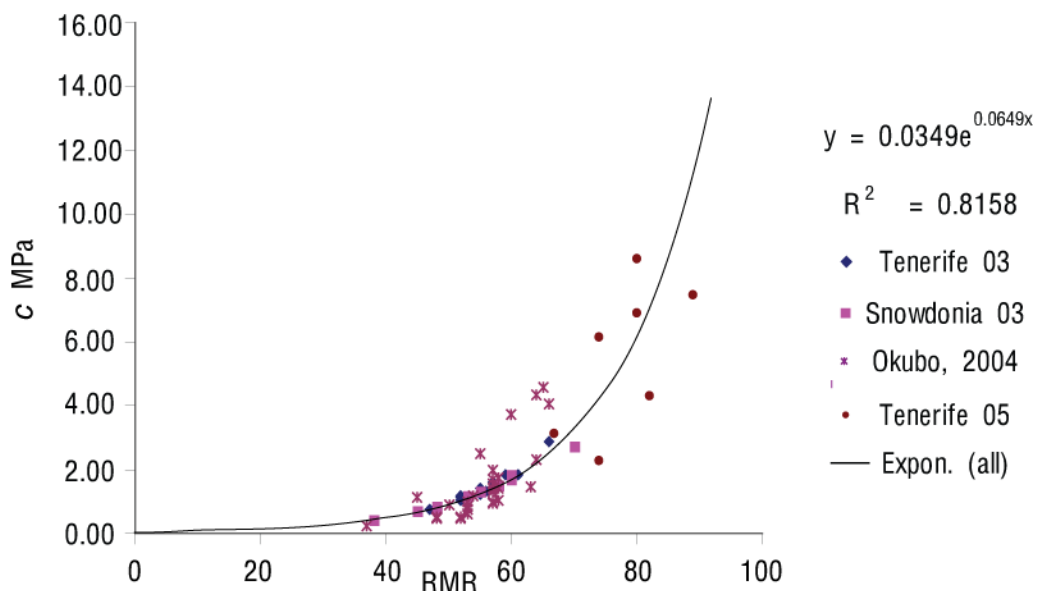

Figure 4.13: Plot of rock mass cohesive strength verses RMR for field localities studied in this project and from Hawaiian rock mass data published by Okubo (2004). The curve labelled Expon. (all) is the best fit exponential relationship to the entire data set.

C1, Appendix C), because of this, these samples are referred to as phonolitic in the tables presented in Chapter four. However, no geochemistry has been undertaken as part of this project which would confirm this interpretation. The samples tested at location 4-1 were omitted form the data set due to anomalously low calculated values of UCS. While the strongest sample from location 4-1 yielded an UCS of ~ 185 MPa, 60% of the samples collected for testing were found to be considerably weaker, with the lowest calculated UCS in the region of 8 MPa. These samples were highly vesiculated (Fig. 4.14), although they did not appear so from the outside and probably formed part of a thin crust that formed on top of individual flow lobes, or may represent volcanic rubble that has been re-incorporated into the flow. As a result of this, these samples were not applicable for use with the RMR in the calculation of the rock mass strength. This is because the categories of the RMR e.g. the spacing of discontinuities are dependent on the bulk rock mass properties. The anomalously weak samples from location 4-1 did not appear representative of the whole rock mass but constituted the majority of the samples collected. This resulted in a gross
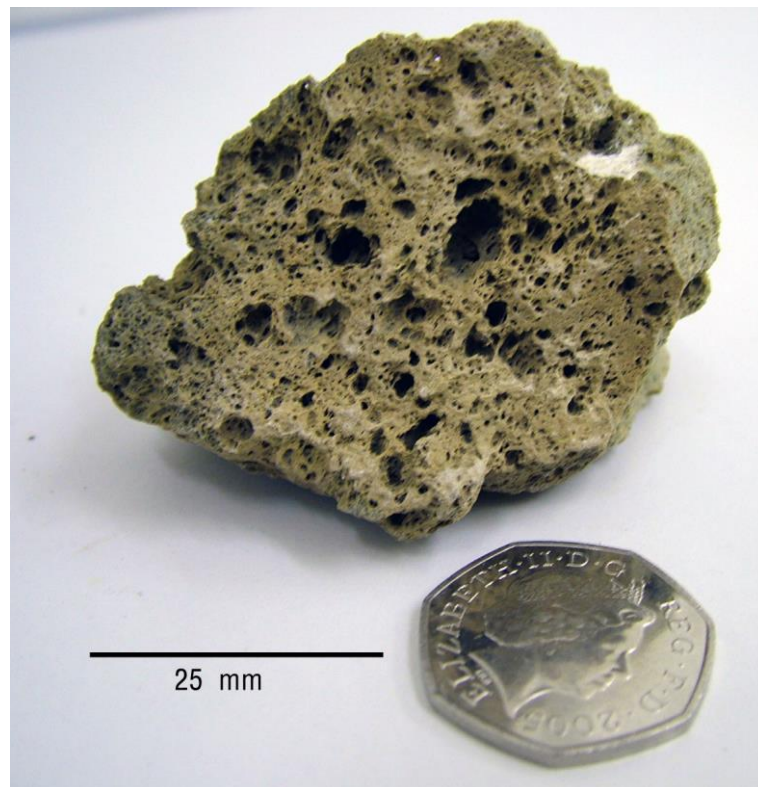

Figure 4.14: Photograph showing a highly vesiculated fragment of the phonolitic sample (location 4-1) created during the strength testing, which demonstrates why these samples produced such anomalously low rock mass strengths.

underestimate of the rock mass strength. This suggests that for volcanic rock masses; the minimum number of samples (10) suggested by Anon (1985) should be greater. All other locations with calculated UCS agree well with the previous data calculated using estimated UCS values as represented by the R^2 values of 0.83 and 0.89 for the σ_{cm} and σ_{tm} (Fig. 4.7), and 0.82 for c (Fig. 4.13).

4.6 Concluding remarks on estimating volcano strength

In order to quickly asses the overall strength of large areas of a volcanic rock mass the combined use of geomechanical rock mass classification schemes and the Hoek-Brown criterion allows a direct estimate of strength to be made. This method appears to hold true regardless of the types or ages of the volcanic rocks studied. Provided that the intact strength of the rock mass examined is reasonably constrained, either through published data or laboratory testing, the rock mass compressive, tensile and cohesive strengths can be estimated through a simple exponential relationship of the form $y = Ae^{(B*RMR)}$. Where A and B are constants defined in equations 4.6, 4.7 and 4.15, and the RMR can be substituted for the GSI. While the data calculated using actual measured intact strengths integrated well with the data calculated using published values, it does produce broadly higher values of rock mass strength. This can be seen from the plotted data labelled Tenerife 05 in Figures 4.7 and 4.13. It may therefore by prudent to always carry out a limited testing program to confirm the validity of published values when applied to the site under investigation, as unless the published values are for the exact rock mass being examined, there are almost certain to be slight discrepancies.

Of the two classification schemes used in this study the RMR produced more consistent results leading to the abandonment of the GSI at an early stage. However, this does not mean that the GSI has no application in this method of estimating physical values of rock mass strength. As discussed in Section 4.2.2 the GSI was designed to account for the failings of the RMR in assessing poor quality rock masses. This is because practical measurements, as required by the RMR, of discontinuity spacing etc. may not be possible in a completely disorganised rock mass such as a breccia. None of the rock masses examined in this study were considered poor quality (RMR <25); therefore the usefulness of the GSI in this situation was not assessed. It may be the

case, that where the strength of poor quality volcanic rock masses needs to be examined the two classifications need to be used side by side.

5. Analogue modelling

The use of scaled sand pile models in simulating volcanic flank collapse has been used to test an array of theories. The most common use of scaled analogue sand pile models has been to assess the effects of volcanic spreading, whether in response to volumes of a volcanic edifice weakened due to hydrothermal activity (van Wyk de Vries *et al.*, 2000), or to significant areas of weak and/or dipping substrata (Merle and Borgia, 1996; Wooller *et al.*, 2004), or some combination of both (Merle and Lénat, 2003; Oehler *et al.*, 2004; Cecchi *et al.*, 2005). Analogue sand pile models have also been used to simulate collapse induced by direct magmatic intrusion within the upper edifice (Donnadieu and Merle, 1998; 2001) and the reactivation of basement faults (Vidal and Merle, 2000). While the majority of studies concentrate on a single mode of collapse, others attempt to compare and contrast several different possible collapse scenarios (e.g. Acocella, 2005), and the technique is not limited to the modelling of volcanic collapse. For example, scaled analogue sand models have been used to investigate the sub-surface structures and collapse mechanisms of volcano summit pit craters (Roche *et al.*, 2001). It is therefore evident that the use of scaled sand pile models is well established and accepted within the scientific community, hence to first test the validity of the internal gas pressure hypothesis, a series of simple analogue experiments were conducted. The use of the analogue models allowed a relatively rapid creation of laboratory scale natural systems, permitting the rudimentary principals of the hypothesis to be tested before the undertaking of more time and resource intensive numerical modelling. This Chapter presents results of these initial analogue models.

5.1 Scaling of analogue models

Initial experiments were carried out with a simple uniform cone constructed of air dried angular (sharp) sand. Angular sand was used due to its higher internal angle of friction and repose compared to other types of granular material. Using scaling arguments following the Buckingham Π theorem (Middleton and Wilcock, 1994), the controlling parameters for a conical heap of sand are defined in Table 5.1. From Table 5.1 it can be seen that there are 5 variables with a total of 3 dimensions, which is equal to 2 independent dimensionless products (5 variables minus 3 dimensions), the stability number *N* and a non-named group Φ:

$$N = \frac{c}{\gamma H} \quad \text{and} \quad \Phi = \frac{\tan \phi}{\tan \alpha}$$

(Equations 5.1 and 5.2)

A model perfectly represents its prototype if the dimensionless products N and Φ are the same for both. The Φ parameter is matched if the ratio of the friction angles and the slope angles are the same. Estimates of the angle of friction for a volcanic pile as suggested by other authors (Jaeger and Cook, 1979; Voight *et al.*, 1983; Watters and Delahaut, 1995) matches closely the ~ 30° - 38° friction angle of the sand used. Thus, to satisfy the scaling arguments a model volcanic edifice needs the same slopes as its prototype, this will generally be the case since the angle of repose is approximately the same in both cases, as it is defined by the angle of friction.

For a 2000 m high volcanic cone, averaging the values presented in Table 4.9 for the strength properties of a volcanic rock mass, gives a value of c of 1.98 MPa (1980 kNm^{-2}), and taking γ to be 24 kNm^{-3} (Voight *et al.*, 1983) equation 5.1 gives a stability number (N) of 0.04. To achieve this stability number for a 0.2 m high pile of sand ($\gamma = 20$ kNm^{-3}) substituting these values again into Equation 5.1, c = 0.16 kNm^{-2} (160 Pa), a value which is too small to be practically measurable in most laboratories. Capillary tensions in air-dried sand would be very close to this value and possibly exceed it, with the cohesion of sand being ~ 145 Pa at nominal values of normal stress, which are generated from the overlying sand (Schellart, 2000). Other published estimates of sand cohesion range from 85 Pa (Cobold and Castro, 1999) to 250 – 300 Pa (Krantz, 1991). The value for the cohesion of sand required to satisfy our scaling arguments (160 Pa) lies within the range of the majority of published estimates. Hard though it may be to believe, a heap of sand on the laboratory workbench *does* truly represent an accurately scaled model of a large volcanic edifice in terms of material cohesion.

The fluid pressures scale on the basis of the maximum pressure (u), H, and γ through the pore pressure ratio r_u. By introducing this additional parameter, u, a further dimensionless scaling term is generated:

$$r = \frac{u}{\gamma H}$$

(Equation 5.3)

Variable	Definition	Dimensions
c	cohesion	kNm^{-2}
ϕ	friction angle	degrees
H	height	m
α	slope angle	degrees
γ	unit weight	kNm^{-3}

Table 5.1: List of the 5 variables and 3 dimensions (degrees are dimensionless) governing a conical heap of sand for scaling arguments following the Buckingham Π theorem.

This is also a linear scaling, so the reduced size of the physical model is realistic. What does not scale linearly is the rate dependency of the collapse mechanism, and the propagation of fluid pressures throughout the edifice. These effects must be scaled on the basis of a time factor, which depends on rock mass permeability, fluid-rock relative compressibility, the unit weight of the pore fluid, and some critical size parameter termed fluid flow path length, raised to power two. As with determining accurate hydraulic properties of the volcanic rock masses, modelling rate effects is outside the scope of this thesis, except for a qualitative assessment.

5.2 Building and failing sand 'volcanoes'

The models described in this study are made entirely of air dried angular (sharp) sand as discussed in Section 5.1, which differs from other studies where a mixture of varying quantities of sand and plaster are used (e.g. Acocella, 2005 and Cecchi *et al.*, 2005). The reason for our choice is that, as discussed in Section 5.1, the estimated values of cohesion for air dried sand agrees with our required model cohesion of ~160 Pa. Models in which a sand and plaster mixture is used are often scaled to a cohesion of 10^7 Pa (10 MPa) in nature (e.g. Oehler *et al.*, 2004, Acocella, 2005). As shown in Chapter four, assuming a cohesion of 10 MPa for volcanic rocks is far from realistic, so using a sand plaster mix is arguably too strong for analogue models. The draw back of using a weaker material is in the visual clarity of the model. The use of plaster allows fracture propagation and failure surfaces to be viewed easily due to increased cohesion. To overcome this limitation in the sand pile models, the experiments were filmed using a digital camcorder at a rate of 25 frames

per second. This allowed us to pause the recording at the point of failure and view precisely the geometry of the failure surface.

In this study, as with others previously cited (e.g. Merle and Borgia, 1996, Donnadieu and Merle, 1998, van Wyk de Vries *et al.*, 2000, Acocella, 2005 and Cecchi *et al.*, 2005) the cone was created by raining particles from above until the desired size was achieved. For dry sand the porosity and other bulk physical properties depend on the size, shape and packing of the grains. Even if an experiment tries to prepare several sand models in exactly the same way, some variation in properties will almost certainly ensue, because of involuntary fluctuations in packing (Krantz, 1991). With this in mind, and since the aim of the analogue model was to test the broad theory of internal gas pressurisation, not to accurately model a specific pile geometry, the sand was poured directly from a scoop onto the surface of the model base and no consistent height of pouring was used between model runs. This is interpreted as being the primary reason for the differing slope angles of the sand pile as identified in Table 5.2. While this limits the repeatability of individual experiments, it allowed the assessment of different size and shape sand piles that would not have been possible through using more controlled methods of constructing the model. This is more representative of real volcanoes, which do not observe perfect symmetry or constant slope angles, and are constructed in a some what *random* manner. Once a model run had been conducted the sand from that run was discarded and not used again. The pile rested upon a stiff substrate of variable angle, with provision for internal pressurisation by gas (compressed air) at a controlled rate pumped through the base (Fig. 5.1). The models were run with substrate angles of between 1° and 23° (Table 5.2).

Twenty four experiments were run with different sand pile sizes and substrate slope angles. The start of the experiment was defined as the time the compressed air line was turned on and the end of the experiment was defined as the time that the compressed air was visibly seen to eject particles of sand away form the model, termed the "destructive degassing" phase of the model runs. The compressed air line supplied the sand model at a constant rate of 0.5 litres per minute. Assuming a representative sand pile height of 0.06m and a pile slope angle of 30° (Table 5.2), it is possible to estimate the time it would take to completely fill the pore space of a representative sand pile at a flow rate of 0.5 litres per minute. The calculated volume of a cone with this height and

Figure 5.1: (Main) Diagrammatic sketch of the apparatus used to conduct the analogue modelling, Note the ability to increase or decrease the slope angle through the adjustment of the base support. The hose leads from the source of pressure (a compressed air line) to the hole in the base; this provided the means of simulating deep sourced pore fluid pressure increases in the models. (Inset) The actual apparatus, note that in this case the model is set up to use a head of water as a source of pore fluid pressure increase, however all models discussed within the thesis used compressed air.

slope angle is $9.42 \times 10^{-4} m^3$. Assuming that the sand has a porosity of approximately 40% (Cobold

and Castro, 1999) the volume of pore space is approximately $3.8 \times 10^{-4} m^3$. As 1 litre equals 1×10^{-3} m^3 exactly, the air is supplied to the base of the model at an equivalent rate of $8.33 \times 10^{-6} m^3 s^{-1}$. This would result in the pore space within the representative model being completely filled in approximately 45 seconds, a time consistent with those recorded as the end of the model run in Table 5.2.

5.3 Results of the analogue modelling

Of the 24 sand pile models that were completed only 14 of the models resulted in a flank collapse event (Table 5.2), and of these only 5 were deep-seated (these events are donated by an asterisk in Table 5.2). A form of instability was however, recorded in 16 of the 24 models run. Of these 16 cases, taking the 2 models where there was no accompanying failure, potential instability is interpreted through the propagation of radial fractures across the surface of the sand cone prior to any destructive degassing (Fig. 5.2). While this may be interpreted purely as a response to inflation of the sand pile, simply the generation of the fracture system acts to decrease the overall strength of the pile, hence reduce its overall stability. In the 8 cases where no instability was recorded the destructive degassing phase commenced before any visible signs of instability were recorded. There were three general outcomes of the analogue sand pile models and these are discussed in Sections 5.3.1 to 5.3.3

5.3.1 Passive degassing

The analogue sand pile models suggest that internally sourced generation of pore fluid pressure relies on very specific circumstances. As shown in the three models where no deformation was observed (Table 5.2) it can be the case that gas entering the pile from a deep source can escape passively with no physical disturbance to the pile. This is the simplest and least energetic of all the possible experimental outcomes. This behaviour results from a connected permeability network and allows gas entering the pile to escape quickly without causing any visible deformation. The implication is that for deep seated failure to occur, the permeability is a critical controlling factor.

5.3.2 Destructive degassing

By far the most common result of the sand pile models was that of destructive degassing (Table 5.2) occurring in 18 of the 24 models. It is very unlikely that any granular material which contains pore spaces will have a completely connected permeability network. Instead it may contain several small connected networks, but none in turn are connected to the other. In these cases, when the pore pressures were increased through pumping in the compressed air at the base of the pile, for the gas to escape the pile needed to deform to connect these networks. As the pile deforms,

Experiment Number	Angle of Substrate (degrees)	Angle of Sand Pile slope (degrees)	Height of Sand Pile (meters)	Time to collapse (c) and/or destructive degassing (dg) (seconds)	Comments
1	13	30	0.13	4.6 (dg)	No failure, just small eruption
2	13	17	0.04	8(c) 21 (dg)	At 8 seconds a continuous linear crack appeared across the surface on the pile and remained until the eruption
3	13	30	0.045	5 (dg)	No failure, just small eruption
4	5	30	0.05	10(dg) 15(c/dg)	At 10 seconds a small eruption in the summit area was observed. This eruption ceased and the pile re -pressurised, until at 15 seconds there was a small summit collapse followed immediately by an eruption
5	10	30	0.05	12 (dg)	No failure, just small eruption
6	16	30	0.06	12 (dg)	No f ailure, just small eruption. However, prior to the eruption radial fractures were observed across the surface of the pile (Fig 6. 2)
7	16	30	0.06	11(c) 24(dg)	Small rapid moving shallow failure at 11 seconds followed at 24 seconds by an eruption
8*	16	25	0.05	10 (c) 15(dg)	Development of radial fractures immediately preceded a collapse at 10 seconds followed at 15 seconds by a large eruption
9	16	35	0.07	N/A	Model run for longer than 600 seconds with no observed changes to the pile's structure
10	16	30	0.1	45 (c/dg)	Small summit slump at 45 seconds followed immediately by an eruption with rapid quarrying of the vent area and the pile interior
11*	23	30	0.045	19 (c/dg)	Large incremental collapse with two apparent slide blocks, followed immediately by large eruption
12	23	33	0.06	13 (c)	Small horse -shoe shape failure of upper slope, model then run to 600 seconds with no further observed changes
13*	23	28	0.05	47 (c)	Large horse -shoe shape failure of a complete flank model then run to 600 seconds with no further observed changes
14	15	30	0.03	57 (dg)	No failure, just large eruption, positioned directly in the centre of the pile

Experiment Number	Angle of Substrate (degrees)	Angle of Sand Pile slope (degrees)	Height of Sand Pile (meters)	Time to collapse (c) and/or destructive degassing (dg) (seconds)	Comments
15	9	30	0.06	10 (dg)	No failure, just small eruption. However, prior to the eruption a few small radial fractures were observed across the surface of the pile
16	5	20	0.12	121 (c/ dg)	Very small shallow failure followed immediately by large eruption
17^	5	30	0.13	249 (c?/dg)	Immediately prior to eruption large horse -shoe shaped fractures were observed, but no movement of the flank was recorded.
18	15	40	0.3	N/A	Model run for 600 seconds with no o bserved changes to the pile's structure
19	8	30	0.15	27 (c/ dg)	Small shallow failure followed immediately by an eruption
20	8	28	0.18	22 (c/ dg)	Small shallow failure followed immediately by an eruption
21	10	30	0.17	N/A	Model run for 600 seconds with no observed changes to the pile's structure
22*	10	30	0.27	20 (c) 39 (dg)	After 20 seconds radial fractures were observed and small incremental continual down slope movement of a whole flank occurred until an eruption at 39 seconds, with no well defined collapse.
23*	10	25	0.18	167 (c)	No observed structural changes until at 167 seconds energy was introduced into the model in the form of a sharp tap on the model substrate. Immediately a large horse -shoe shape failure of an entire flank then occurred. The Model run for 600 seconds with no observed changes to the pile's structure
24	10	30	0.27	190 (c/ dg)	Small summit failure followed immediately by an eruption

Table 5.2: Results of the analogue sand pile modelling. * Denotes an event interpreted as a deep seated collapse. ^ Denotes an event interpreted as a possible deep seated collapse.

Figure 5.2: Digital video still detailing the typical form of the fracture network that propagated on the surface of several of the sand pile models. This type of fracture network typically only appeared if there was no following large-scale collapse event.

fractures open connecting each network and the pore pressures keep these fractures open. Once a complete network was established and a fracture reached the surface, this became the preferential pathway for the escape of the gas, and further deformation stopped with the exception of the enlargement of the escape pathway as the pile continued to de-gas. This therefore reduced the pore pressures within the pile and also reduced if not nullified the potential for collapse. In some of the sand piles, this network subsequently became blocked and further deformation was then observed until a new escape pathway was established.

5.3.3 Collapse

Two types of collapse event were observed in the analogue models: 1) A shallow collapse of the summit area, involving typically less than one third of the pile height (Fig. 5.3) and 2) a deep-seated failure, which affected two thirds or greater of the height of the pile (Fig. 5.4). For a collapse event to occur, the permeability network must be sufficiently connected to allow gas migration, but with no

Figure 5.3: Digital video still detailing the typical surface expression observed in the sand pile models for a shallow failure.
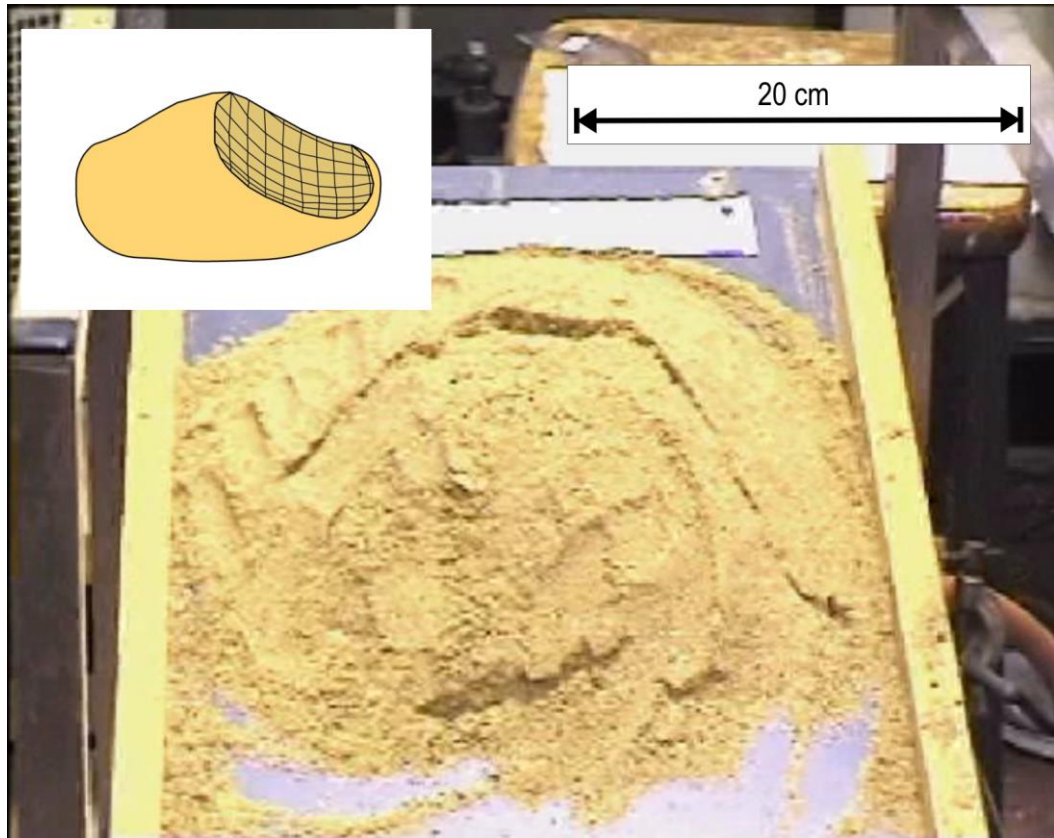
Figure 5.4: (main) Surface expression of a deep-seated failure of the sand pile, (**inset**) diagrammatic representation of the failure surface, with the overlying material removed.

clear pathway to the surface. Under these conditions pore pressures increase rapidly due to the continued influx of compressed air. Now, through the concept of effective stress outlined in Chapter three the overlying portion of the pile may become destabilised. If this destabilising effect can reach a sufficient magnitude before a channelised pathway to the surface is created (leading to destructive de-gassing) and the pore pressures drop, a collapse event will occur.

By far the most common type of collapse observed in the analogue models was the shallow event. For failure to only affect the upper third of the sand pile, gas must have already reached this level or above, along interconnected permeability networks without causing major instability. Due to the shape of a cone, reduced volumes of pore space occur towards its apex. As a consequence, pore pressures will be more easily elevated as more gas migrates into the upper third of the cone. If no pathway to the surface is established, reducing the increasing pore pressure, destabilisation and shallow collapse of the remaining overlying pile will occur.

For deep-seated failure to occur, the upwards migration of gas into the pile must be halted and pore pressures must increase close to the base. At deeper levels, there is more pore space within the pile for the volume of gas to occupy so it is much harder to significantly increase the pore pressures unless the migration of gas is tightly confined. At deep levels the weight of the remaining overlying pile is also much greater since there is more of it, resultantly, higher pore pressures are needed to destabilise the overlying pile. At these greater pore pressures, the opening of new fractures may well be preferential to the movement of the entire flank of the pile. The opening of new fractures within the pile results in new pathways for the gas to follow and may result in a complete pathway to the surface, a fact demonstrated by the observation that for each sand pile which experienced deep-seated failure there were approximately four that did not.

In ten of the fourteen models that experienced any collapse event, the collapse signified or brought about via destructive degassing, the end of the modelling process. Once a pile experienced failure, the failure surface in its simplest form then became another fracture which bisected the permeability network and was utilised by the gas to reach the surface, resulting in destructive degassing. Interestingly, two of the three models that showed no further deformation after the collapse also exhibited the deepest and largest failures. These failure surfaces are interpreted to have a much larger surface area and bisect the permeability network at a deeper level. The gas can then escape along this much larger fracture much more efficiently causing no destructive degassing. It follows then that although experiment 17 (Table 5.2) had the appearance of a shallow failure, with little observed movement and what appeared to be only large surface cracks prior to the destructive degassing phase. The size of the observed fractures indicates failure may well have been pervasive through the entire model, without the accompanying displacement, and it is noted as a possible deep-seated failure in Table 5.2.

5.4 Discussion and Interpretation of Analogue Modelling Results

The fact that deep seated failure was not observed in all models raises the question posed in Chapter three: "is volcanic instability generated by increases in internal pore pressures an ubiquitous occurrence at active volcanoes?"

From the results of the analogue models the answer to the question would appear to be somewhat unclear. As shown in Figure 5.4, deep seated failure *can* be caused by internal pressurisation. However, not all models exhibited such behaviour. In all 24 models, the only variables changed were the size of the cone, the angle of the cone slope and the angle of substrate slope that the cone was resting on. Table 5.2 shows however, no apparent relationship between these variables and the occurrence of failure, either deep-seated or shallow. Increasing the substrate slope angle between 5° to 23° appeared to have little to no effect except at the very top of this range, with all three models resting on a substrate with an angle of 23° suffering some form of collapse. However, a substrate angle of 23° is very steep and unlikely to occur under the entire area of a volcanic edifice in nature. A substrate angle of this magnitude was only included for comparative purposes to determine if a trend existed. This is contrary to what was expected, as steeper substrate slope angles were expected to generate greater instability, hence, more frequent deep seated collapse events. At the very least increasing the slope angle was expected to induce distinct changes to the deformation pattern (e.g. Wooller *et al.*, 2004.) The reasons for this may be two-fold:

1. As stated in Section 5.1 the rate dependency of the collapse mechanism, and the propagation of fluid pressures throughout the sand pile are not accurately scaled and the time scales involved to failure once the compressed air line has been activated are very short. This short time scale may override the increase in instability to the point that the effects of increased fluid pressures are observed before the effects of increased slope angle, with exception to those models resting on a substrate angled at 23°.

2. The materials used (i.e. sharp sand) within the analogue sand pile models exhibit entirely frictional plastic behaviour and fail in a brittle manner according to Mohr Coulomb behaviour (Schellart, 2000), and although the substrate slope angle can be varied, it was a fixed surface (Fig. 5.1). In nature, volcanic edifices also consist of materials that follow plastic behaviour such as hydrothermally altered clays, previous analogue modelling that has shown distinct changes in deformation patterns with changing substrate slope angle have been constructed partially of Newtonian materials that can "*flow*" (e.g. silicon) (Wooller *et al.*, 2004). The absence of these material types

from the models may mean that the effect of increasing the substrate slope angle is greatly reduced.

If the only three measurable variables within the models did not control the generation of deep-seated failure, and such behaviour does indeed occur in some models, the conclusion may be that the occurrence of deep-seated failure within the sand piles is indiscriminate. This is very similar to the situation as it appears in nature. The analogue modelling results indicated that internally sourced pore fluid pressure increases can cause deep-seated collapse of the sand piles, but not in every experiment. It is also known that volcanoes contain active hydrothermal systems and that all active volcanoes de-gas (both examples of generating pore fluids, hence internally sourced pore fluid pressure increases). But just as in the analogue models, collapse does not occur at every active volcano. Assuming therefore that internally sourced pore pressure increases are indeed instrumental in generating deep-seated instability at active volcanoes; it would appear that deep-seated flank failure within volcanic edifices is not controlled by the generation of elevated pore fluid pressures alone.

Although the simple sand pile models were not designed to simulate any real world volcano, it is interesting to compare the model features with those of known collapse events. Undoubtedly the most well-known and documented collapse is that of the 1980 Mount St. Helens eruption (Voight *et al.*, 1983). The observed model failure geometry was compared with that seen Mount St. Helens. The first and most striking resemblance is the shape of the failure scars (Fig. 5.5). Even though the collapse scar at Mount St. Helens was extensively modified by excavation resulting from the associated explosive eruption, this arcuate or horse-shoe shaped scarp is now commonly recognised in volcanic landscapes and is widely attributed to past volcanic lateral collapse events (Reid *et al.*, 2000; van Wyk de Vries *et al.*, 2000; Richards and Villeneuve, 2001). However, it is not only the failure scar of Mount St. Helens that bears a resemblance to those observed in the analogue models. The scar seen in the model shown in Figure 5.5 arguably resembles more closely the topography observed at Socompa, northern Chile (Fig. 5.5), the site of a very large (600 km^2) debris-avalanche deposit (van Wyk de Vries and Francis, 1997). The rapid initiation of a 1.5 km long fracture system across the bulge on the north slope of Mount St. Helens was observed seconds before the onset of failure (Voight *et al.*, 1983). Similar behaviour is observed in many of

Figure 5.5: Morphological similarities of the sand pile models **(top)** to the Mt St. Helens **(bottom left)** and Socompa **(bottom right)** collapse scars. Note the almost identical shape of the collapse scar in the model (white dashed line) and at Socompa (red dashed line). The collapse scar at Mount St. Helens has been modified after the initial collapse event by explosive activity and does not match the scar seen in the model as closely.

the sand pile models (Table 5.2 and Fig. 5.2). A further tentative comparison is that of the mechanical behaviour after slope failure.

At Mount St. Helens, the mass movement triggered a devastating volcanic eruption (Voight *et al.*, 1983). In the majority of the sand pile models, a collapse event also triggered an analogue eruptive

phase (destructive degassing). Clearly, the sand pile models examined here are a vast simplification of events at Mount St. Helens and factors other than internally-sourced pore pressure increases may have been at work. The models are also not scaled directly to Mount St. Helens so any comparisons are strictly qualitative. However, the geometrical similarities *do* suggest that that internal pore fluid pressurisation may have played an important role in the collapse of the north flank of Mount St. Helens, an idea further enhanced by recent work of Vinciguerra *et al.*, (2005a).

5.5 Analogue Modelling Conclusions

The simple models presented here show that by increasing the pore fluid pressures from a deep internal source, instability can develop, which may lead to the initiation of deep-seated collapse. In addition, the resulting failure geometries arising from internal pressurisation of the scaled models appear similar to some natural examples of sector collapse and although detailed morphological comparisons have not been conducted, the similarities are purely in physical appearance.

However, the lack of commonality in the outcome of the sand pile models suggests that although internally-driven increases in pore fluid pressure may be important, it is not the single controlling factor. The indiscriminate response of the sand piles to internally elevated pore pressures also indicates that even if identical materials are used to construct a cone, it is the small-scale, possibly even microscopic properties that ultimately determine the observed response. Although each sand pile was constructed using the same method (outlined in Section 5.2), there are variables within this method that may have given rise to small perturbations in the physical properties of the pile. The height from which the sand was poured from to form the pile was not consistent between experiments, possibly resulting in a difference in grain packing in each experiment, which may have directly affected the overall porosity and permeability of the sand pile. Also, while all the sand used in the modelling process was from a single source and air dried for the same amount of time, it is feasible that the un-dried sand did not have homogeneous moisture content values. This may have resulted in the air dried sand used in each experiment also having slightly variable moisture contents, hence, slightly variable values of cohesion. Despite the fact that these variations would be small from a mechanical perspective, they may have had an effect on the outcome of the analogue modelling, which possibly explains the range of results presented in Table 5.2. It may therefore be reasonable to assume a similar relationship exists within real volcanic edifices. While

two individual volcanoes may appear almost identical in appearance and construction, small differences in the porosity, and permeability of the whole volcanic system, may have a marked effect on role which internal pore fluid pressure increases play in generating volcanic flank collapse.

6. Numerical modelling

6.1 Numerical modelling and why it is important

Why use numerical modelling? The answer is that with the computing power available today, we can create and analyse much more detailed numerical models than we can ever hope to through the process of analogue modelling. The gulf in the ability between the two model types to replicate all known aspects of a real world system will only widen as computing power grows.

It is impossible to re-create full scale physical models of a volcano in the laboratory. When considering physical models of volcanoes it is always necessary to reduce the scale of the model and while the properties of the model can also be scaled accordingly it is never a completely true representation of the natural case. Numerical modelling allows us to create full-scale models using the properties that the actual volcanic material would have in nature.

The variation of properties is also something that is much more achievable in a numerical rather than a physical model. Firstly, the scale at which the properties can be varied is much greater in a numerical model and secondly, the number of variables we can introduce to a model is much larger when using numerical methods. For example, if a 2,500 m high volcanic edifice was underlain by a continuous 10 m thick clay lithology, this clay lithology may be expected to have a substantial effect on the rates of volcanic spreading and, in turn, slope stability. Most physical volcanic models vary in height from 0.1 to 0.3 m (e.g. Merle and Borgia, 1996; Donnadieu and Merle, 1998; van Wyk de Vries *et al.*, 2000; Acocella, 2005 and Cecchi *et al.*, 2005). If a 2,500 m high volcanic edifice is scaled to be 0.1 m high, the 10 m clay lithology underlying it would have a corresponding thickness of $4x10^{-4}$ m, or four tenths of a millimetre in the physical model. This level of detail is simply not possible in most physical models, and as a consequence many important variables have to be ignored in the use of analogue experiments.

Although sand pile models of volcanic edifices are easy and quick to construct (Cecchi *et al.*, 2005), once the model has run to completion and been observed it is practically impossible to re-create exactly the same experimental conditions. While a similar model may easily be constructed,

if it is the intention to examine the effects of small or even large changes to the model, the starting point will never be exactly the same. This of course is not true of numerical models; once a numerical model is created it can be restored to exactly the same conditions present upon its creation as many times as is required. This allows the effect of changes to the model to be observed at a level of detail not available with physical models.

As a result of the mentioned limitations with physical models, it is often the case that only one or two variables can be modelled at any one time within a physical model. As with other limitations of physical modelling, this can be overcome through the application of numerical techniques. Numerical models can be stopped at any point during the solution process and they may contain as many variables as the programmer wishes to include (allowing for limitations of the particular modelling code in use). This allows the programmer to examine the effects of many different variables at any point during the model solution. The use of numerical, computer-based modelling codes will continue to increase as the demand for more accurate and complicated modelling scenarios continues likewise.

6.1.1 Previous uses of numerical methods in modelling volcanic instability

Numerical modelling techniques have been used to asses the role of various processes in the failure of volcano slopes, and Voight (2000) identifies two general procedures that are used to evaluate volcanic slope stability. The first and most popular procedure is limit equilibrium analyses of stability.

While limit equilibrium analyses are the most popular form of stability assessment, their application has most frequently occurred in the modelling of intrusion (specifically dykes) as a trigger for the failure of volcanic flanks (e.g. Elsworth and Voight, 1995; Iverson, 1995; Elsworth and Voight, 1996; Voight and Elsworth, 1997; Elsworth and Day, 1999). These analyses assess stability in terms of limit equilibrium behaviour and assume that failure occurs as motion of a rigid, simple wedge, resulting from a static balance of driving and resistant forces along the potential failure surface. While this geometry is a vast over simplification, Iverson (1995) claims that if all other factors are constant, driving forces that are too small to displace an ideal, rigid wedge are also too small to displace a deforming flank. While this analysis is best suited to two-dimensional modelling,

a pseudo three-dimensional approach is applied by Elsworth and Voight (1995; 1996) and Elsworth and Day (1999). Although a 3D geometry was examined, it was constructed merely by extruding a 2D section, and provided little additional insight over 2D modelling other than the observation that the lateral restraints acting on the wedge became less significant for wider wedges. These numerical simulations of intrusion triggered failure are of particular relevance to this project as they model elevated pore fluid pressures related to intrusion as a destabilising method. However, there are fundamental differences which are discussed in Section 6.1.2.

Given the numerous studies concerned with instability generated by dyke intrusion, it is interesting, that most, if not all simulations concerning this topic are conducted in 2D, using limit equilibrium methods (LEM). Similar methods are used to model the destabilising effect of all types of intrusions, for example, volcanic edifice stability during cryptodome emplacement (Donnadieu and Merle, 2001). This is likely due to the complicated geometry of magmatic intrusions which would make 3D numerical modelling very time consuming.

The uses of LEM however, are not only confined to modelling instability generated through intrusion. This fact is demonstrated by Okubo (2004) who used LEM to asses the general stability of the Hilina slump, Kilauea volcano, Hawaii. Where the approach of Okubo (2004) differs from those before is the full integration of rock mass strength data into the stability analysis. This method demonstrated that the relatively quick procedure of ascertaining geomechanical properties using rock mass classification schemes in combination with well developed 2D numerical methods can produce detailed and rapid stability estimates.

The second principal method of evaluating volcanic slope stability as identified by Voight (2000) is deformation analyses, in which, numerical analyses employing finite-difference (FD) or finite-element (FE) procedures are used. Such analyses are less common than those employing LEM and include those conducted by Russo *et al.*, (1996); Hürlimann *et al.*, (1999) and Firth *et al.*, (2000). While the application of deformation analyses ranges, they are all mainly concerned with one thing; the effects of stress changes within the volcanic edifice (something not possible with limit equilibrium analysis). Such changes may be related, but not limited to, the magmatic plumbing system (Russo *et al.*, 1996; Hürlimann *et al.*, 1999), changes in topography brought about by additional loading or movement of existing flanks (Apuani *et. al.*, 2005) or heating of pore fluids

(Reid, 2004). The majority of deformation analyses (e.g. Russo *et al.*, 1996; Hürlimann *et al.*, 1999) do not attempt to assign a numerical value to stability, such as a factor of safety, which is common in LEM (see Section 6.2). Rather, the likelihood of failure is interpreted from the stress state of the model. This does not mean that it is not possible to assign such a value through deformation analyses, and indeed a factor of safety (Section 6.2) can be calculated from all FE and FD methods. This is usually achieved by reducing material strength in stages until failure of the model occurs. This strength-reduction technique has some advantages over the traditional LEM in that the critical failure surface is found automatically without the need to specify its shape or size (Voight, 2000). However, the speed of the strength-reduction technique is highly dependent on computing power (especially for larger models) and this has been a limiting factor in its usage.

With the exception of the pseudo-3D approach of Elsworth and Voight (1995; 1996) and Elsworth and Day (1999) previously mentioned, the majority of numerical modelling concerned with volcanic instability is conducted explicitly in 2D. Exceptions are rare, but Reid *et al.*, (2000) and Reid *et al.*, (2001) demonstrated the usefulness of full 3D stability analysis. Using a 3D extension of LEM and the inclusion of real world volcano topography, Reid *et al.*, (2000) and Reid *et al.*, (2001) were able to not only calculate a numerical value of stability, but predict which region of a volcano was most unstable. Unfortunately, being limit equilibrium models, these analyses were limited in their usefulness as they were concerned only with gravitational instability, and were unable to model any alteration in the stress-field. While these simulations established the usefulness of three-dimensional modelling in hazard prediction, the restricted nature of the LEM meant that any hazard prediction would be at best incomplete using this method.

6.1.2 The numerical approach used within this project

The numerical approach applied within this project is similar to that of Apuani *et al.*, (2005) in the way that firstly, simplified limit equilibrium stability analyses were preformed, in this case to establish the feasibility of the hypothesis introduced in Chapter three. This was then followed by more detailed deformation analyses. A major difference however, was the use of full 3D rather than 2D deformation analysis methods. This is a major step forward in the assessment of volcanic slope stability as Voight (2000) notes that the use of numerical codes allows the possibility of extending the approach into complex and changing geometries, which is not possible with LEM. While the

volcanic models examined through numerical methods in this thesis still exhibit simplified geometries they provide a basis from which more detailed models can be constructed and demonstrate that it is possible to model the stability of a volcanic edifice in full 3D as a result of stress-field modifications, specifically, reduction in the effective stress due to increased pore fluid pressures.

The effect on flank stability of elevated pore fluid pressures resulting from the heating of pre-existing pore fluids from high level intrusions has been examined in the past (Elsworth and Voight, 1995; Elsworth and Voight, 1996; Voight and Elsworth, 1997; Elsworth and Day, 1999). However, these studies vary significantly from the methods employed within this thesis. The previous studies (as discussed at the beginning of the Section) utilise LEM. As a result of this, any pore fluid pressures are estimated and then applied as a fixed vector force to the rear or underside of a rigid wedge. This is a poor method of assessing the effect of elevated pore fluid pressures as there is no ability to account for alteration of the stress field. The 3D deformation analyses performed as part of this thesis allow the prediction of stress-field alteration and therefore offer a much improved method for the modelling of pore fluid pressures increases.

6.2 Limit equilibrium analysis

Numerical analysis of the effects of gas pressurisation was carried out initially using two-dimensional LEM. LEM use the most widely-expressed index of stability, the Factor of Safety, (Fs), which for a potential failure surface is defined as the ratio of shear strength to shear stress:

$$Fs = \int_L s \Big/ \int_L \tau \qquad \text{(Equation 6.1)}$$

where s is the shear strength, τ is the shear stress, and the integration takes place along the length (L) of the failure surface. Numerical calculations were conducted using an in-house slope stability analysis package following the simplified iterative method of Bishop (1954). This form of stability analysis is commonplace in geotechnical engineering and merits no further discussion, if further information is required the reader is directed to Bishop (1954). Factors of safety of 1 or less imply instability, and ordinarily, analysis is conducted on a plane section through a slope about a centre of rotation. These two-dimensional methods of analysis usually give satisfactory results for simple
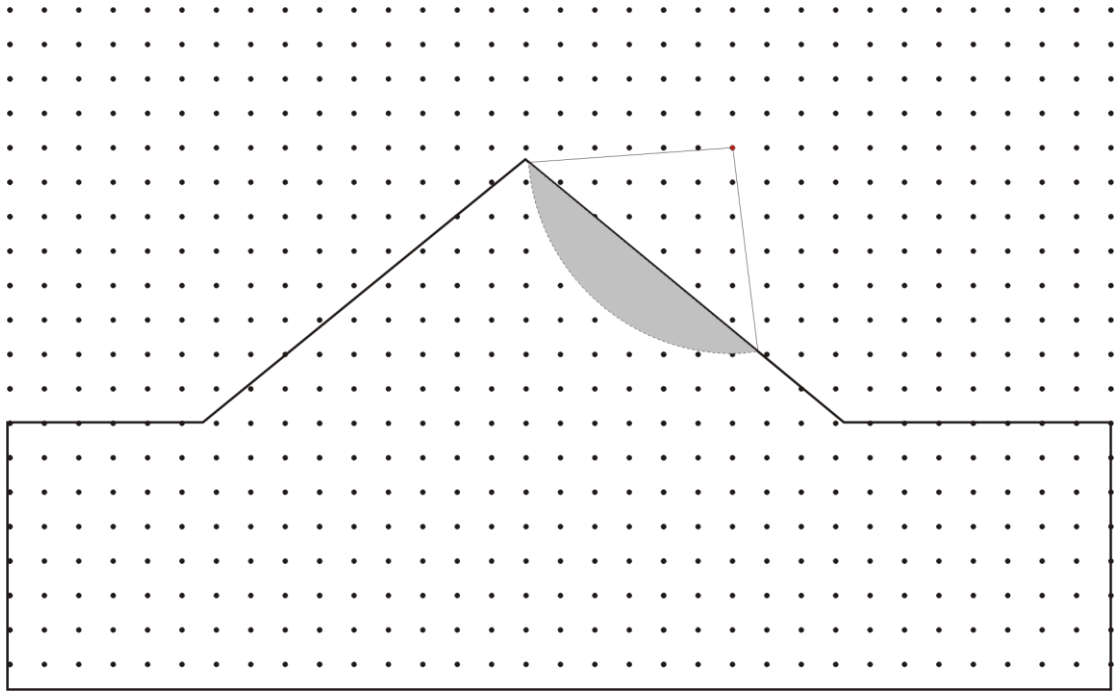
Figure 6.1: Example of the search grid method used in the LEM modelling. The grid is first generated, then, at every point on the grid, a number of trial failure surfaces with differing radii are examined resulting in a factor of safety for that surface. Mass from a trial failure surface has been shaded to illustrate the location of the failure surface and the material that would be liberated if the slope were to fail along this plane. The radius of the trial surface can be considered analogous to depth. Note the grid spacing is for visual clarity only, details of the search grids used in the LEM modelling can be found in Section 6.2.1.

cases. This approach was used by Voight and Elsworth (2000) as a general geometry for their limit equilibrium analysis of shallow flank and deep-seated edifice failure. Although our particular LEM analysis is restricted to two-dimensions, three-dimensional methods have been developed and applied to, inter-alia, non-uniform surface topography and loading, which arguably is closer to the case represented by an unstable volcanic edifice. However, as LEM were only initially used to validate the general project hypothesis and are not the main tool of stability analysis utilised, two-dimensional analysis for this purpose was deemed more than adequate.

The physical values used in the LEM calculations are those defined previously by Voight *et al.*, (1983) for the Mount St. Helens edifice where cohesion (*c*), 1,000 kPa (1MPa), angle of friction (ϕ), 40° and unit weight (*W*), 24 kNm^{-3}, with a pore pressure ratio (r$_u$) of 0.3. These values are also in good agreement with the range of physical properties of volcanic rocks presented by Schultz (1995; 1996) and Watters *et al.*, (2000). It should be noted that these values are also in good agreement with the strength data presented in Section 4.5, which includes data published by

Thomas *et al.*, (2004b), plus the data from additional more recent in house testing which is discussed in Chapter four.

6.2.1 The limit equilibrium models

A total of 42,500 possible failure surfaces were analysed during each calculation using a grid search pattern (Fig. 6.1). However, the number of viable potential failure surfaces in each calculation varied depending on the model geometry, as not all trial surfaces bisected the model topography (See Figure 6.1). For all three scenarios, two model geometries were used (Fig. 6.2) to represent the volcanic edifice with the physical properties discussed in Section 6.2 (above). These geometries were a uniform cone, and (Fig 6.2a) a more realistic geometry with topography similar to the pre-1980 eruption of Mount St. Helens (Fig 6.2b). No attempt has been made to model the Mount St. Helens collapse/eruption; it is only a similar topography that was used in the numerical models in order to examine the effects of a model geometry exhibiting non-symmetry. Results of both models are summarised in Table 6.1. Unlike the analogue sand pile models, the build-up of pore pressures is controlled and pore pressures are introduced to the models at the start of the calculations. The internally pressurised area was defined as 75% of the volume of the defined edifice and the value of pressurisation was set to 100% of the applied pressure at the pressure boundary as defined in Figure 6.2 and 0 at the 75% volume limit. The pressure was varied with a linear gradient between the two boundaries (Fig. 6.3).

It must be noted that the LEM modelling was conducted primarily as a method of partially validating the theory of internal pressurisation prior to more detailed three-dimensional work. As a result, no in-depth analysis was conducted using this method. The volume of space subject to high pore pressures within the LEM models is arbitrary, constructed purely to see if decreasing flank stability was possible through this method. For the model of the uniform cone shown in Figure 6.2a the area defined as the pressure boundary is large and simply mirrors the model topography. This was deliberate, as if the increased pore pressures resulted in no observable enhancement of instability within this LEM model, the underlying theory of this thesis would have needed to be re-assessed. The results of this simple model then allowed the construction of the more realistic test geometry shown in Figure 6.2b. In this geometry, the defined pressure boundary has a diameter of 1.2 km, which lies within typical ranges of magma chamber diameters of 0.5 – 5 km (Marsh, 2000). No

a

1 km

1 km

b

1 km

1 km
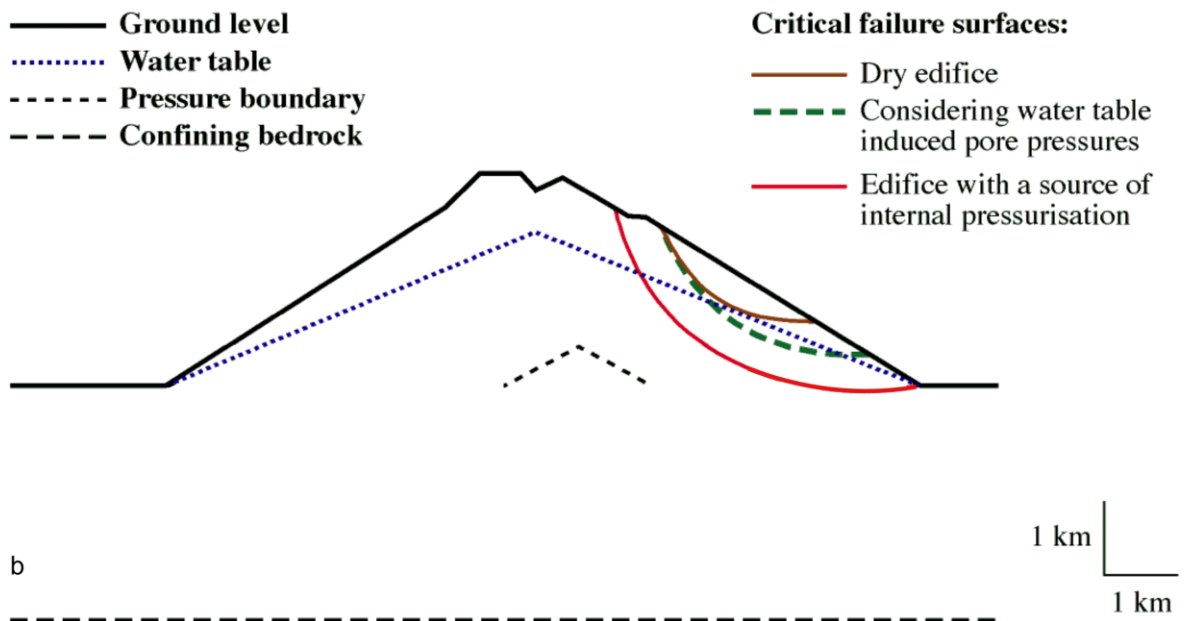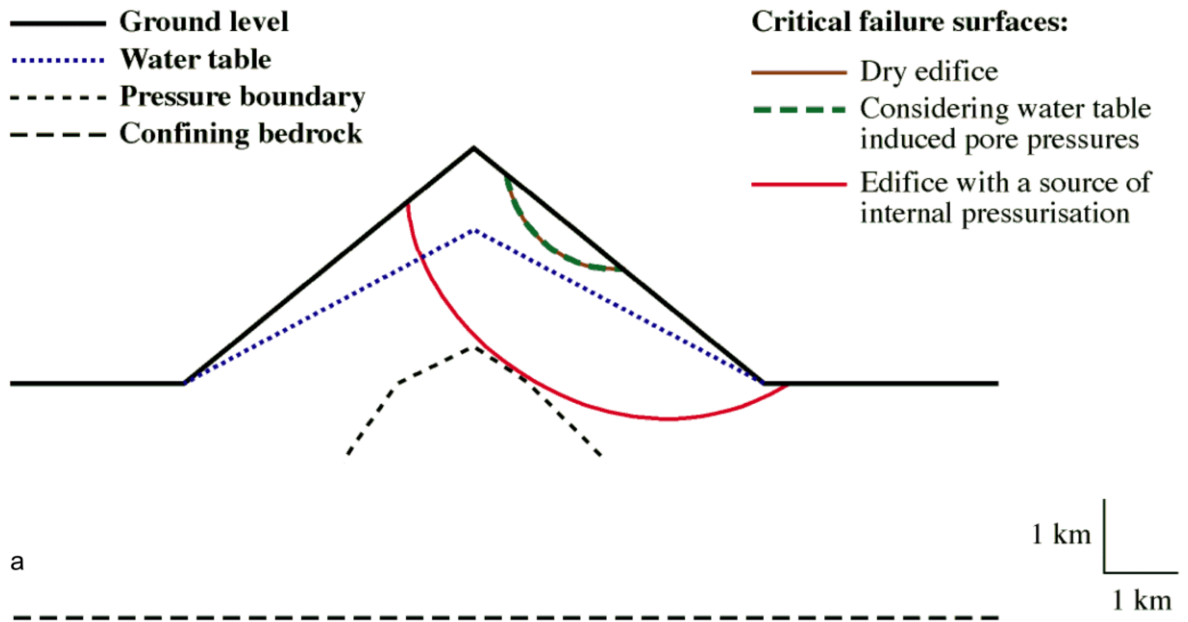
attempt is made to model a change in the nature or shape of the pressure field, and although specific conclusions are drawn from these models, few of the assumptions made are fully testable and the conclusions may be model-dependent.
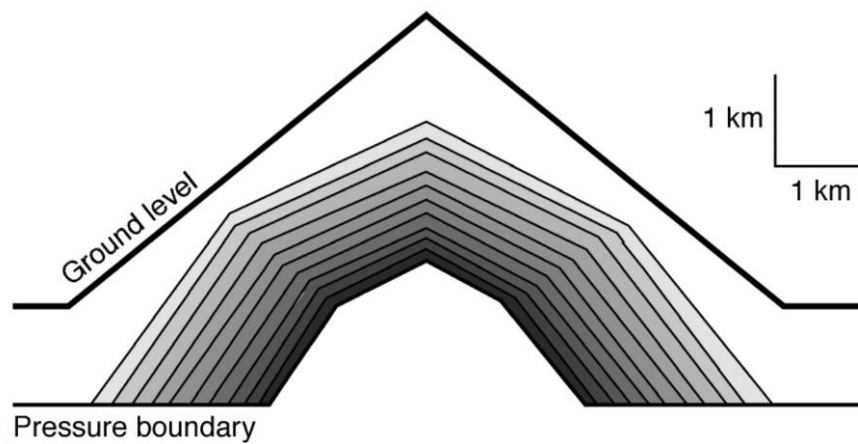
Figure 6.3: Example of how the internal pressure was distributed within the LEM models. The model geometry is that shown in Figure 6.2a, but the principal is the same for both models. The internally pressurised area was defined as 75% of the volume of the total defined edifice topography. The value of pressurisation was set to 100% (black) of the applied pressure at the pressure boundary as defined in Fig. 6.2, and 0% (white) at the 75% volume limit.

Figure 6.2: Potential critical failure surfaces for a uniform cone (a), and an edifice with pre-1980 Mt. St. Helens like topography (b); potential critical failure surfaces for a 'dry' edifice, and a 'wet' edifice are shown in addition to the potential deep failure surface for a 'wet' edifice plus internal gas pressurisation. Results are summarised in Section 6.2.2 and Table 6.1, and for details of how the pressure was distributed within the models see Figure 6.3.

6.2.2 Results of the limit equilibrium modelling

Factors of Safety for the Two Models in Fig. 6.2					
	Uniform Cone			St. Helens Topography	
1	*Dry*	1.73	1	*Dry*	1.99
2	*Wet*	1.32	2	*Wet*	1.53
3	*Wet plus Internal*	1.64 (16.3%)	3	*Wet plus Internal*	1.57 (67.6%)

Table 6.1: Summary of the two dimensional LEM modelling. For the *Dry* and *Wet* scenarios the *Fs* relates to the potential failure surface with the actual lowest *Fs (the potential critical failure* surface). For the *wet plus Internal*, the *Fs* relates to the *potential deep failure* surface, i.e. the potential failure surface with the greatest reduction in *Fs* compared with the dry scenario at 10 MPa pressure. The value in brackets represents the reduction in *Fs* of the *potential deep failure* surface.

Numerical results obtained from limit equilibrium modelling (LEM) are discussed in this section. LEM calculations were designed to examine the effects of three scenarios:

1.   No source of internal fluid pressurisation (*dry*)

2.   Internal fluid pressurisation produced by normal ground water infiltration only (*wet*)

3.   An edifice with a source of internal fluid (gas) pressurisation plus ground water infiltration (*wet plus internal*).

Figure 6.4a shows a plot of factor of safety (*Fs*) against slip circle radius (km) (which is used as an analogue for depth), calculated for the simple uniform cone shown in Figure 6.2a, for both the *dry* (no internal pressure) and *wet plus internal* scenarios. For the *wet plus internal* scenario, a range of internal pressures varying from 5 to 35 MPa is plotted. For both scenarios and at all pressures, a potential shallow instability is always present at the same location in the search grid at a slip circle radius of approximately 1.35 km (Fig. 6.4a). This is shown by the fact that for all pressures the upper part of the *Fs* curve always follows that of *no* internal pressure, and this shallow instability is found in this location due to the geometry of the model. This is to be expected as the internal pressure effects are not applied outside the 75% volume boundary, above which the pressure is set to 0 MPa (Fig 6.3). More significant then, is the deviation away from the no internal pressure line at depth with increasing values of pressure (Fig. 6.4a). As the pressure is increased it can be seen that the effect is two-fold:

1. To generate a potential deep failure surface within the interior of the edifice

2. To decrease the factor of safety for that potential failure surface.

Interestingly, for all pressures, the potential deep failure surface was found, via the grid search, to be centred at the same point in the grid (Fig. 6.4b), which is interpreted to be a function of the shape of the cone. While increasing the pressure did not move the location of this failure surface within the grid, it did deepen it, and substantially decrease the *Fs* associated with it. This is compatible with the results of the analogue sand pile models that indicated a deep (internal) source of pore fluid pressure increase can generate deep-seated volcanic flank instability. It can be seen from Figure 6.4a, that in the case of a simple uniform cone, an internal pressure of 35 MPa is theoretically enough to reduce the factor of safety for the entire flank below unity.
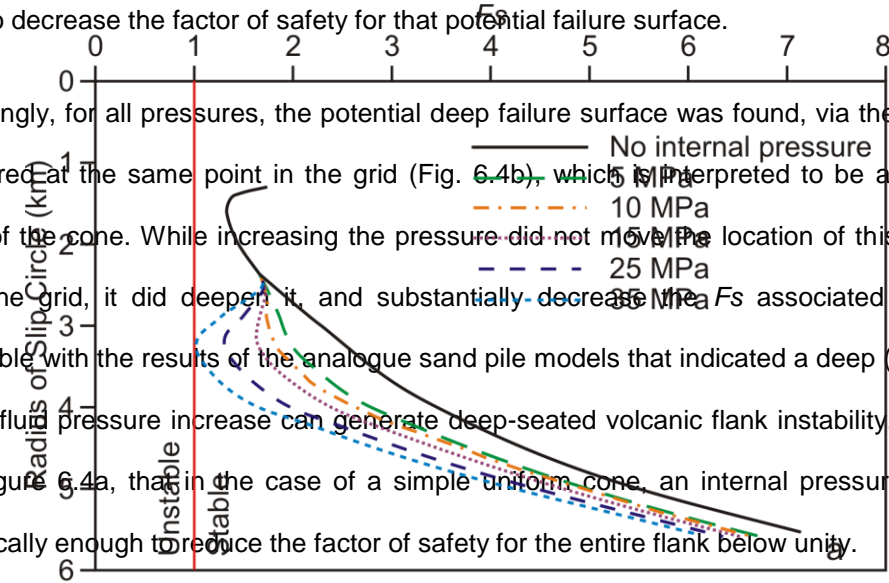
A similar relationship is also true for the model geometry shown in Figure 6.2b. Superimposed on Figures 6.2a and 6.2b are the *potential critical failure* surfaces (the slip circle surface closest to failing) for the *dry* and *wet* scenarios, in addition to the *potential deep failure* surface (the slip circle with the largest reduction in *Fs* compared to the dry scenario) for the *wet plus internal* scenario at a pressure of 10 MPa. The reasons for this value are discussed in Section 6.2.3. For the *wet plus internal* scenario at 10 MPa the *potential critical failure* surface (i.e. the slip circle with the lowest *Fs*) is still that of one at a shallow depth, and is the same potential surface as the *dry* and *wet* scenarios (Fig. 6.4a). However, the *potential deep failure* surface, which is associated with a source of internal pressurisation (Table 6.1 and Figure 6.2b) can be seen to be much deeper. Since it appears that increasing the pressure in the LEM models has no effect on the position of the *potential deep failure* surface (Fig. 6.4a), this potential deep failure surface can thus be considered the potential critical failure surface for higher internal pore pressures.

Figure 6.4: Plot of factor of safety (F_S) against depth for the uniform cone in figure 6.2a (a), calculated at increasing internal pressure. Note that at shallow levels the lowest of F_S is always in the same place (~1.35 km), as identified in the text. However, instead of steadily increasing with depth as in the curve at no internal pressurisation, the F_S starts to decreases at depth when considering increasing internal pressure, until at an internal pressure of 25 MPa, the Critical failure surface is no longer shallow, but is located at 3.2 km depth. All depths are taken from the slip circle to centre of rotation (b) and are not measurements below ground level.

The results plotted in Figure 6.2 and summarised in Table 6.1 clearly show that a deep (internal) source of pore fluid pressure increase can generate significant decreases in deep-seated volcanic flank stability. In addition, it has been shown that it is theoretically possible to completely destabilise an entire volcano flank through pore fluid increases alone. However, these theoretically large pressures are unlikely to be achieved in nature (see Section 6.4).

6.2.3 Interpretation of the limit equilibrium modelling results

Applying an internal pressure of 25 MPa, a value close to the estimates of magmastatic overpressure of Sparks, (1994) and Robertson *et al.*, (1998), displaces the potential critical failure surface with the lowest F_s from a shallow potential instability to a depth of 3.2 km from the centre of slip circle rotation (Fig. 6.4b). Further increasing the pressure to 35 MPa, a value within Sparks' (1994) suggested maximum theoretical overpressure of $\sim$ 50 MPa, lowers the F_s to below unity, making the slope unstable without any additional factors such as seismic loading or rock mass weakening. However, some caution should be exercised with these pressure estimates. The over-pressures of Sparks (1994) and Robertson *et al.*, (1998) are concerned with explosive lava dome eruptions and as such, should be considered as extreme maxima and may not be applicable to non dome forming volcanoes. These values are total fluid (*gas-bubble*) pressures within the conduit system and not from the build up of fluid (gas) that has completely separated from the magma. More realistic values of fluid (gas) overpressure are those suggested by Voight and Elsworth, (2000) for pressurised diffusive volatiles. While these values are also associated with lava domes as opposed to an entire edifice, Voight and Elsworth (2000) estimate gas pressures of 5 to 12 MPa within a cavity at the base of the dome and above the active conduit. This appears a reliable estimate for fluid (gas) overpressures. In this study, a value of 10 MPa was therefore used to look more closely at the positioning of potential critical failure surfaces within the two LEM model geometries.

Ultimately, the effect of increasing the pore fluid pressures is interpreted to drive the potential failure surface deeper within the edifice, so that the volume above any potential failure surface is increased substantially relative to external pressurisation by ground water infiltration alone (Fig. 6.2). Should the volcanic edifice fail in response to the effect of internally elevated pore fluid pressures then the potential volume of material liberated during failure will be far greater than

without the '*deep*' source of pressurisation, having profound implications for hazard assessment and mitigation.

6.3 *FLAC^{3D}* – Three-dimensional numerical modelling

FLAC^{3D} (Fast Lagrangian Analysis of Continua^{3D}) is a three-dimensional explicit finite-difference program for engineering mechanics computation. While *FLAC^{3D}* is itself now a well-established numerical modelling tool, the basis for this program is the long-serving numerical formulation used by the Itasca Consulting Group's two-dimensional program, *FLAC (Version 3.3, 1995)*. While *FLAC* has been shown to be a useful tool for modelling the complex system of volcanic collapse (Apuani *et al.*, 2005), *FLAC^{3D}* extends the analytical capability of *FLAC* into three dimensions, simulating the behaviour in three-dimensions of soil and rock or any other materials that undergo plastic flow when their yield limits are reached. Materials are represented by polyhedral elements within a three-dimensional grid that is adjusted by the user to fit the shape of the object to be modelled. Itasca Consulting (1998) stated that the explicit, Lagrangian, calculation scheme and mixed-discretization zoning technique of Marti and Cundall (1982) used in *FLAC^{3D}* ensure that any physical failure is modelled very accurately, and because no matrices are formed, large three-dimensional calculations can be performed without excessive memory requirements. *FLAC^{3D}* also contains a powerful in-built programming language, *FISH*, which enables the definition of user specific variables and functions as well as the ability to create fully customizable grid structures. *FISH* offers the unique capability for the tailoring of a commercial geomechanical modelling code to user's specific needs.

6.3.1 The *FLAC^{3D}* method

The three-dimensional numerical modelling in this project was performed specifically by *FLAC^{3D}* 2.00-2.122 (1998), while the specific details of each model are discussed in Section 6.3.2;   models typically consisted of approximately 1,200 grid points and 1,000 zones, and model solutions are achieved though iteration in time, where deformation can be monitored and failure can be identified. When in large-strain mode, the grid can deform and move with the material that is represented ensuring that any collapse mechanisms are modelled accurately. The deformation analysis followed standard numerical modelling procedure:

1. The geometry of the system is represented by a user defined finite-difference grid.

2. The model is divided into regions of differing material properties, a constitutive model is chosen, and the material properties are then assigned to each region. For all models discussed in this thesis, firstly an elastic constitutive model was used to set up the initial stresses. An elastic model was used to avoid brittle failure while reaching the initial equilibrium point. Then a Mohr-Coulomb constitutive model was used throughout the remainder of the modelling process.

3. The initial and boundary conditions are set. Initial stress gradients were applied corresponding to the effect of gravity acting in the negative Z axis direction at 9.81 ms^{-2}. The boundary conditions are specified as artificial boundary truncations since the model, not including the cone, can be considered infinite. These boundaries are defined using the FIX command. As such the initial stresses across this boundary are in equilibrium automatically.

4. The model is then stepped to equilibrium (if failure does not occur) before any subsequent alterations to the model are made. This step is repeated until all the required perturbations have been considered or failure occurs. The Equilibrium state is defined by the net nodal force-vector of the individual grid points within the model. The maximum unbalanced force represents the maximum recorded net nodal force-vector at any step. To be in equilibrium the maximum unbalanced force was required to be equal to or less than 0.5 N. For perfect equilibrium, the maximum unbalanced force would be 0, but for numerical analysis, the maximum unbalanced force will never reach this value. Therefore it is sufficient to say the model is in equilibrium when the maximum unbalanced force is small compared to the *initial* unbalanced force (typically < 0.1%). The *initial* unbalanced force for the models examined within this thesis was typically in the order of x10^{13} N, so a target maximum unbalanced force of 0.5 N represents approximately 0.5x10^{-11} % of the initial value.

5. The results are assessed.

The models can be translated, rotated and magnified, and with graphics facilities built into *FLAC^{3D}*, it is easy to generate high-resolution, colour-rendered plots. These colour-rendered plots of

surfaces showing contours or vectors are made in full 3D, and a 2D plane can be generated and located at any orientation within the model for the purpose of viewing contour or vector output on that plane.

The construction of the general grid geometry was achieved by primarily using two primitive shapes available in *FLAC³D*, the radcylinder (a radial graded mesh around a cylinder) and the cylinder (a cylindrical mesh). While these are arbitrary shapes (Fig. 6.5a), they are able to be distorted to fit complicated volumetric regions (Fig. 6.5b). Once these primitive shapes have been generated and modified, they are connected to form the general shape of a volcanic edifice used in all the models. Model specific changes to this general grid are discussed in Section 6.3.2. Initially, only a quarter of the grid is generated as the general model exhibits quarter-symmetry. The rest of the model is then generated using a reflect command to generate the grid structure across lines of symmetry (Fig. 6.5c). A useful feature of the grid generation is the ratio keyword as this allowed for an accurate solution without an excessive amount of zones. This is because the ratio keyword allows fine zoning around the base of the edifice to allow for detailed stress calculations, but a much coarser zoning on the periphery of the model. Within the generation of the general model a ratio of 1.15 was used, meaning that each successive zone is 1.15 times larger than the previous, moving from the base of the edifice to the model periphery in a horizontal direction.

All but one of the outputs discussed in Section 6.3.3, which are analysed from modelling within *FLAC³D,* are inbuilt variables calculated simply by stepping the model (e.g. stress, strain and displacement magnitude). However, since it is the aim to examine instability of volcanic slopes it is useful to be able to generate some form of a *Factor of Safety*. The factor of safety defined previously as a ratio of strength to stress (Section 6.2) can be calculated and plotted for all the zones in any Mohr-Coulomb *FLAC³D* model through the use of *FISH* functions. These can then be stored in an extra grid variable, for plotting or printing. It should be noted that any definition of a safety factor may be employed by writing an appropriate *FISH* function, not just the one outlined below. All *FISH* functions can be found in Appendix F.

The state of stress within any zone can be expressed in terms of principal stresses σ_1 and σ_3. This stress, in general, will plot as a circle, "a" with a radius r_a, on a Mohr diagram (Fig. 6.6). Failure

Figure 6.5: (a) The two simple primitives used in building the models, left to right the radcylinder and cylinder. **(b)** The modified cylinder primitive attached to the radcylinder base this forms a ¼ of the finished model. **(c)** The completed model, generated by reflecting along lines of symmetry present in **(b)**
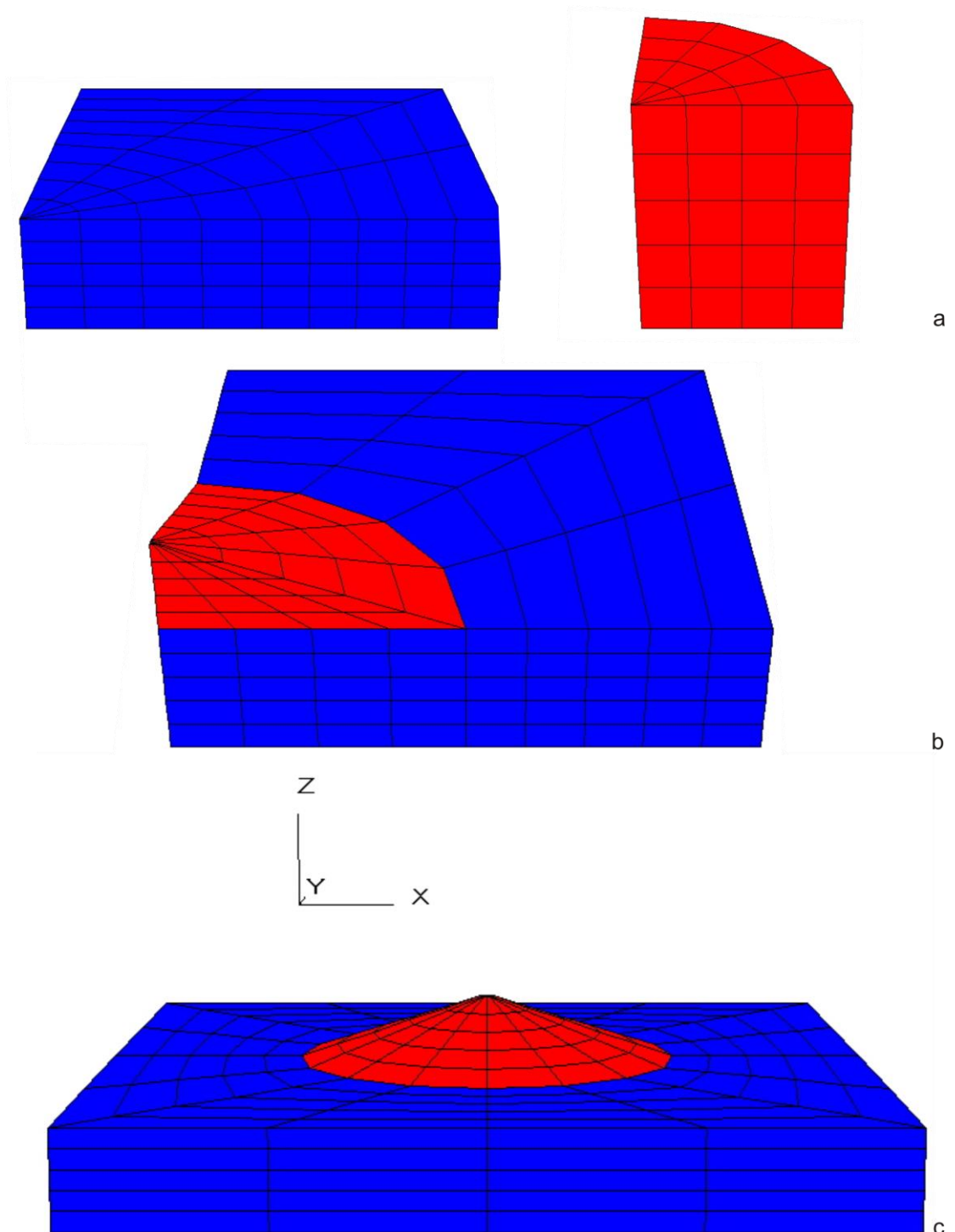
Bulk Modulus, Pa	Shear Modulus, Pa	Cohesion, Pa	Tensile strength, Pa	Angle of friction, degrees	Density, kgm^{-3}
24.0e3	12.4e3	1.35	0.7	37	2400

Table 6.2: List of the elastic and Mohr-Coulomb properties formatted as required for use in *FLAC^{3D}* (10.0eA is equal to 10.0x10^{A}) which were used in the simple slope model shown in Figure 6.7. This model was used to validate the definition of the factor of safety outlined in Equation 6.2.

occurs if this circle touches the failure envelope. The strength for the stress state represented by circle "a" is determined by holding σ_3 constant while increasing σ_1 until circle "b", with radius r_b touches the envelope (Fig. 6.6). The ratio of the radii of the two circles (*Fs= r_b/r_a*) is the strength/stress ratio. *Fs* is also known as the *failure index* or the *factor of safety.* The ratio r_b/r_a *(F)* which corresponds to the *factor of safety* can be defined as:

$$Fs = {r_b}\Big/{r_a} = \frac{\sigma_{3-}\sigma_{1f}}{\sigma_3 - \sigma_1}$$

(Equation 6.2)

where

$$\sigma_{1f} = \left(\frac{1+\sin\phi}{1-\sin\phi}\right)\cdot\sigma_3 - 2c\sqrt{\frac{1+\sin\phi}{1-\sin\phi}}$$

(Equation 6.3)

It is this definition of the factor of safety that is used for all *FLAC^{3D}* models analysed in this thesis.
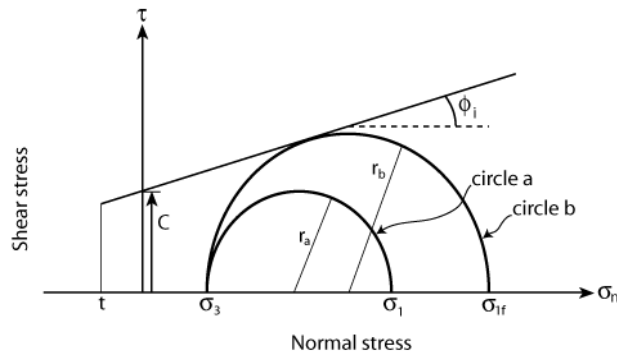

Figure 6.6: Strength/stress ratio for Mohr-Coulomb failure criterion. Circle b is touching the failure envelope, so we know the conditions at failure. By examining the ratio of r_b to r_a as outlined in the text, it is possible to determine the strength/stress ratio and hence a factor of safety for the stress state that is represented by circle a.
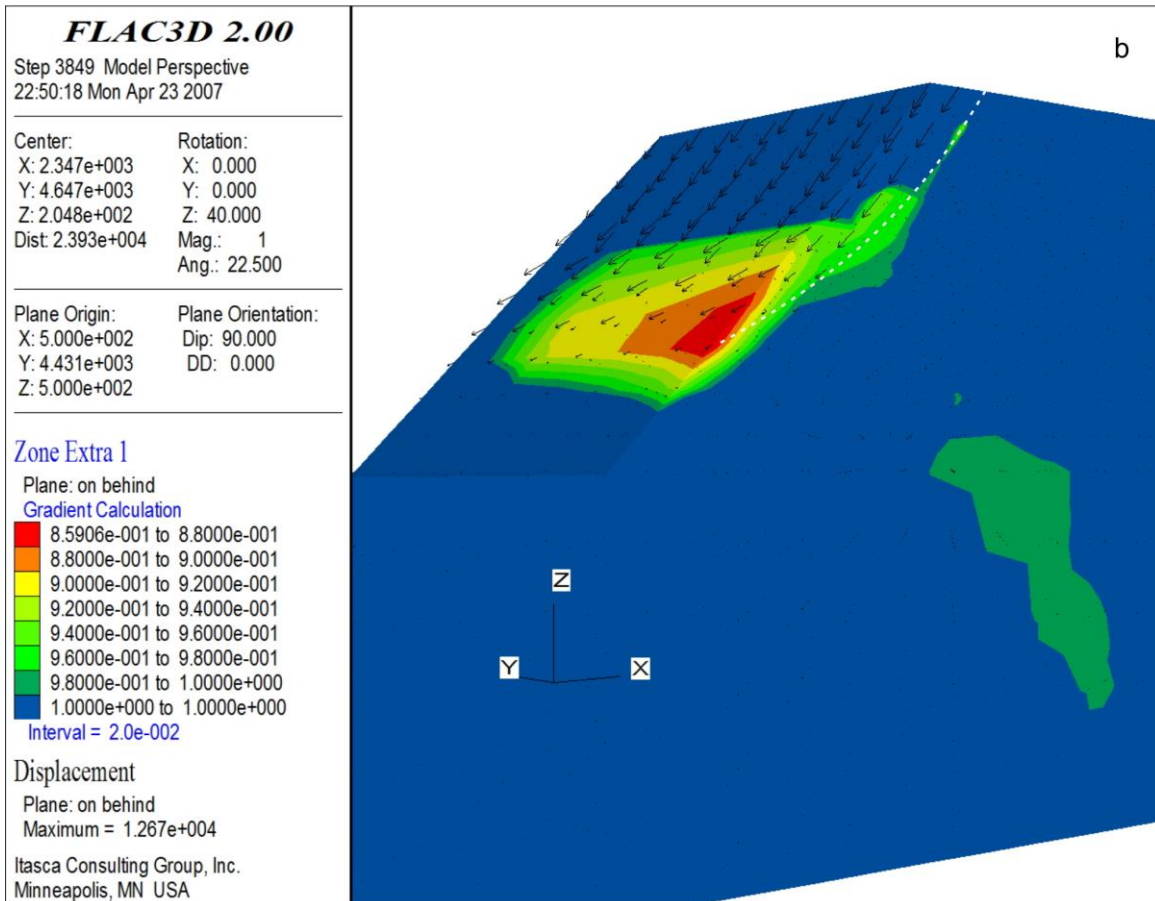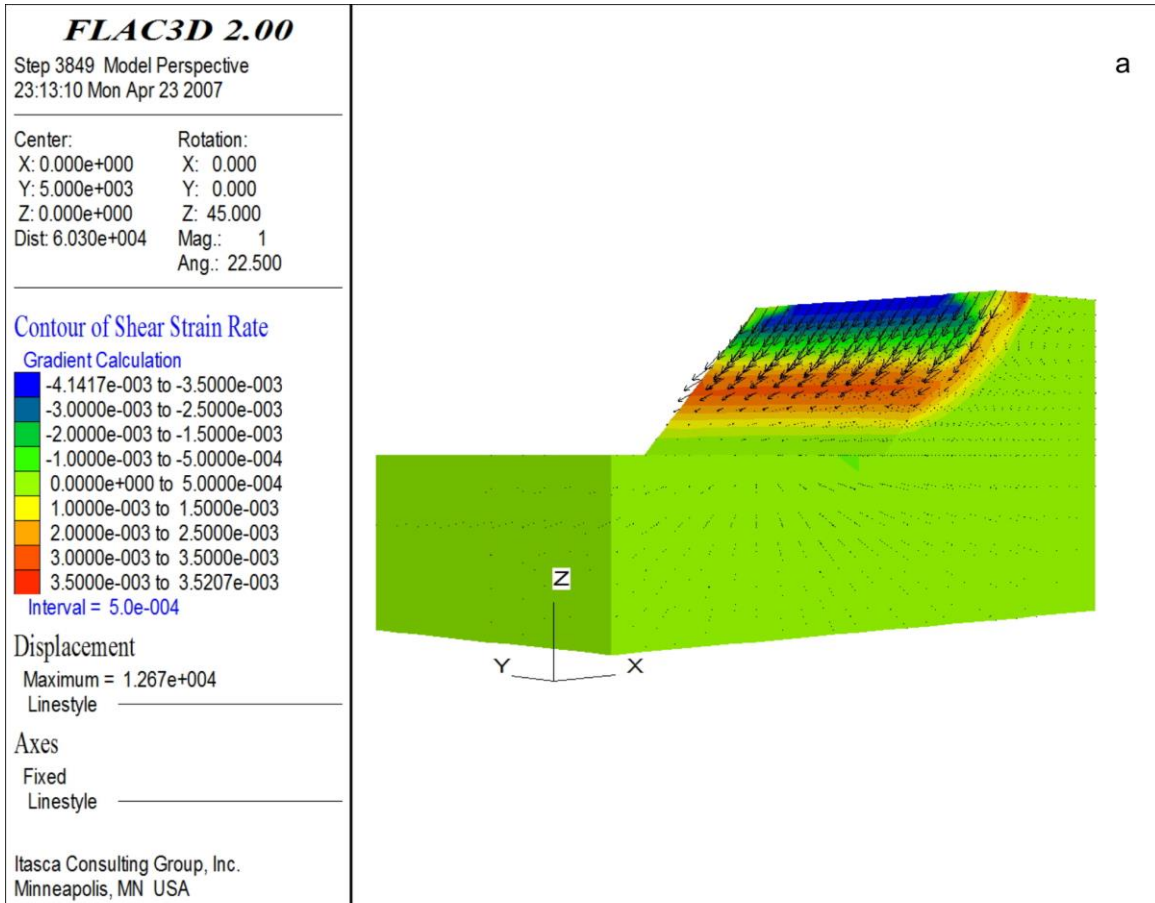
Figure 6.7: Continued on next page

FLAC3D 2.00

Step 4190 Model Perspective
15:56:01 Fri Dec 2 2005

Center: Rotation:
X: 7.660e+002   X: 0.000
Y: 4.357e+003   Y: 0.000
Z: 9.845e+002   Z: 40.000
Dist: 2.570e+004   Mag.:   1
                         Ang.: 22.500

Plane Origin: Plane Orientation:
X: 0.000e+000   Dip: 90.000
Y: 5.000e+003   DD: 0.000
Z: 1.416e-012

Axes
 Pos: (-6.000000e+003,0.000000e+000,2.000
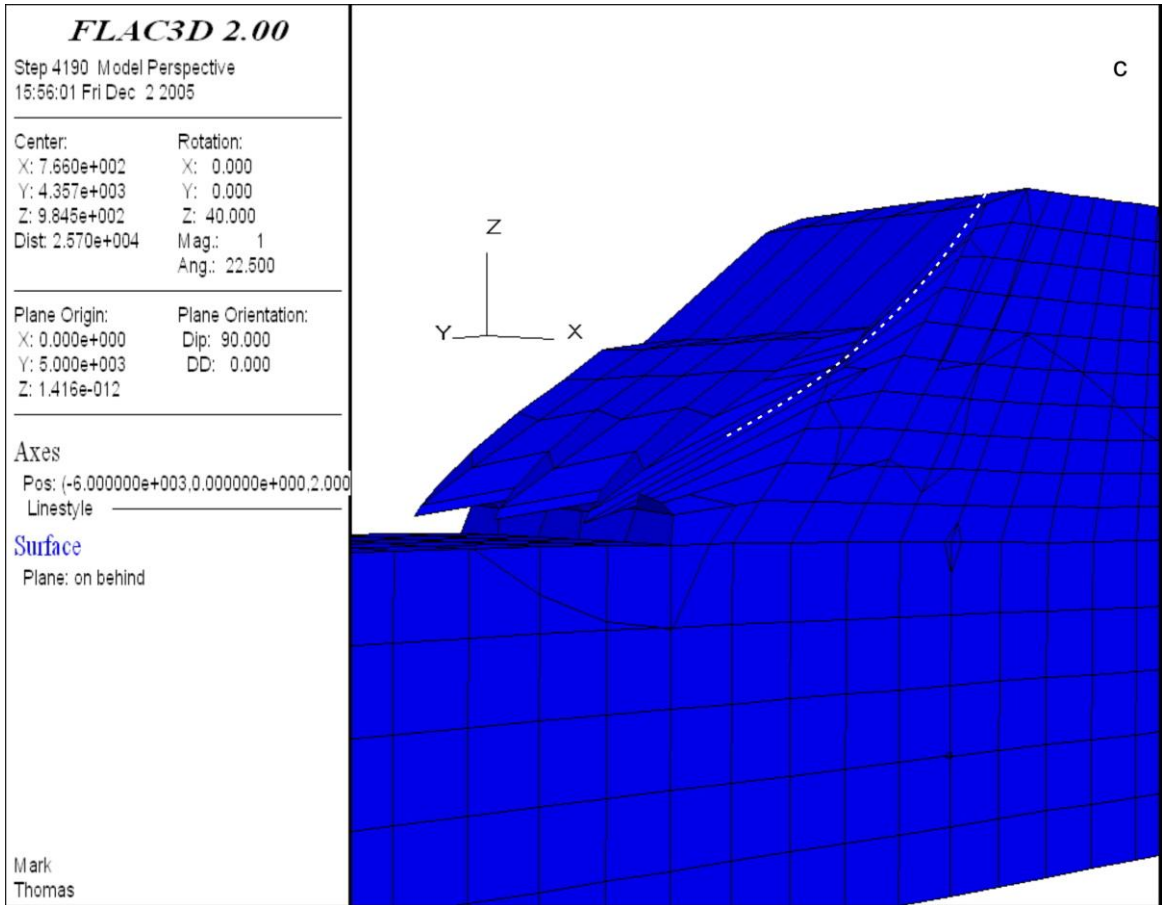 Linestyle

Surface
 Plane: on behind

Mark
Thomas

Figure 6.7 details a simple model which tests the definition of the factor of safety described in Equation 6.2. This test model was constructed with a slope angle of 8° more than the assigned angle of friction for the model material, and given a nominal cohesive strength (Table 6.2). These factors, in theory, should lead to an unstable slope, producing a *Fs* < 1 from the implementation of Equation 6.2 within *FLAC^{3D}*. The observed results in Figure 6.7 confirm this, hence proving its validity.

Since it is the intention of this thesis to examine the effect of pore pressures on volcanic edifice stability, it is necessary to introduce pore pressures into our three-dimensional models. Very little is known about the permeability and porosity fields inside a volcano. Because of this uncertainty, internal pressurisation is treated in a simplistic manner, with a uniform pressure applied across a boundary volume (this volume is defined as the pressure source) and allowed to dissipate linearly away from this volume, in the same way as the 2-D *LEM* models

This was achieved firstly by defining the volume of the pressure source and then removing this part of the finite-difference grid from the model. Removing parts of the model was achieved by

Figure 6.7: Simple *FLAC^{3D}* model of a uniform slope used to demonstrate the calculation of the factor of safety, *Fs*. **(a)** Plot showing shear strain rate and displacement vectors, **(b)** plot showing the calculated factor of safety and displacement vectors, **(c)** plot of the model at failure run in large strain mode. From (a), the areas of the slope experiencing the highest shear strain rates can be identified. In theory, areas of the slope experiencing high amounts of shear, as indicated by the shear strain rate, would be prime locations for slope failure to develop. Viewing the model in section (b), areas of the slope identified to have a *Fs* < 1 (green to red) are coincident with the areas of highest shear strain rate (a). This indicates that the *Fs* calculation detailed in Section 6.3.1 gives realistic results, and a white dashed line in (b) represents the best fit failure plane derived from the *Fs* values. If the model is run in large strain mode, the grid is able to deform and failure can be visualised (c). The model run stops when a zone takes on an impossible geometry (i.e. the zone has failed). The best fit failure plane identified in (b) is also superimposed on the large strain model (c), and the actual failure observed in (c) can be seen to lie exactly on this predicted failure plane, further validating the *Fs* calculation outlined in Section 6.3.1.

assigning a null constitutive model, which essentially removes all trace of the "nulled" volume from the active model; although the associated zones remain in place. The pressure is then applied as an equivalent uniform normal stress across the surface of the nulled volume. In order for the

created void not to collapse, firstly the normal stress is applied equal and opposite to any stresses already acting across the boundary. There is then a uniform addition to this normal stress equal to the desired pressure increase.

6.3.2 *FLAC*^{3D} model geometries

The three-dimensional modelling provides an examination of much more realistic (but still simplified) geometries than the two-dimensional LEM modelling. As such, the three-dimensional finite-difference modelling is vastly more sophisticated. The full code and data files for all the *FLAC*^{3D} modes are given in Appendix F, with important information about the model configuration summarised here. Five full three-dimensional geometries were examined using the properties identified in Table 6.3, and are summarised in Figure 6.8:

1. A simple uniform cone on a horizontal substrate. This geometry is referred to as "normal". In this geometry the cone has a radius of 6 km, a height of 2 km and a summit radius of 400 m, giving a slope angle of 19°.

2. As per geometry 1 but with the addition of a weak foundation underlying the cone (Table 6.3). This geometry is referred to as "weak"

3. As per geometry 1 but the whole mode is superimposed on a regional slope of 1.5^{o}. This geometry is referred to as "tilted"

4. A composite geometry consisting of two separate cones. Firstly, a broad shallow cone with a radius of 6 km, a height of 1 km and a slope length of 4.268 km giving a lower slope angle of 13.2^{o}. Resting on this lower cone is a much steeper upper cone with a radius of 1.732 km, a height of 1 km, and a summit radius of 200 m, giving an upper slope angle of 33.1^{o}. This geometry is referred to as "steep" although it is only the upper of the two cones that may be considered such.

5. The fifth geometry can be considered as the worst case scenario of the models. It combines all the elements of geometries 1 to 4 (i.e. an edifice with a steep upper cone on a wide base built on a 1.5^{o} regional slope and underlain by a weak foundation). This geometry is referred to as "tilted, weak and steep".

Although no attempt is made to model any real world volcano for the reasons discussed in Section 6.3.2 it is still necessary to validate the use of the five model geometries listed above, as if they show *no* resemblance to natural analogues, any conclusions drawn from the modelling processes
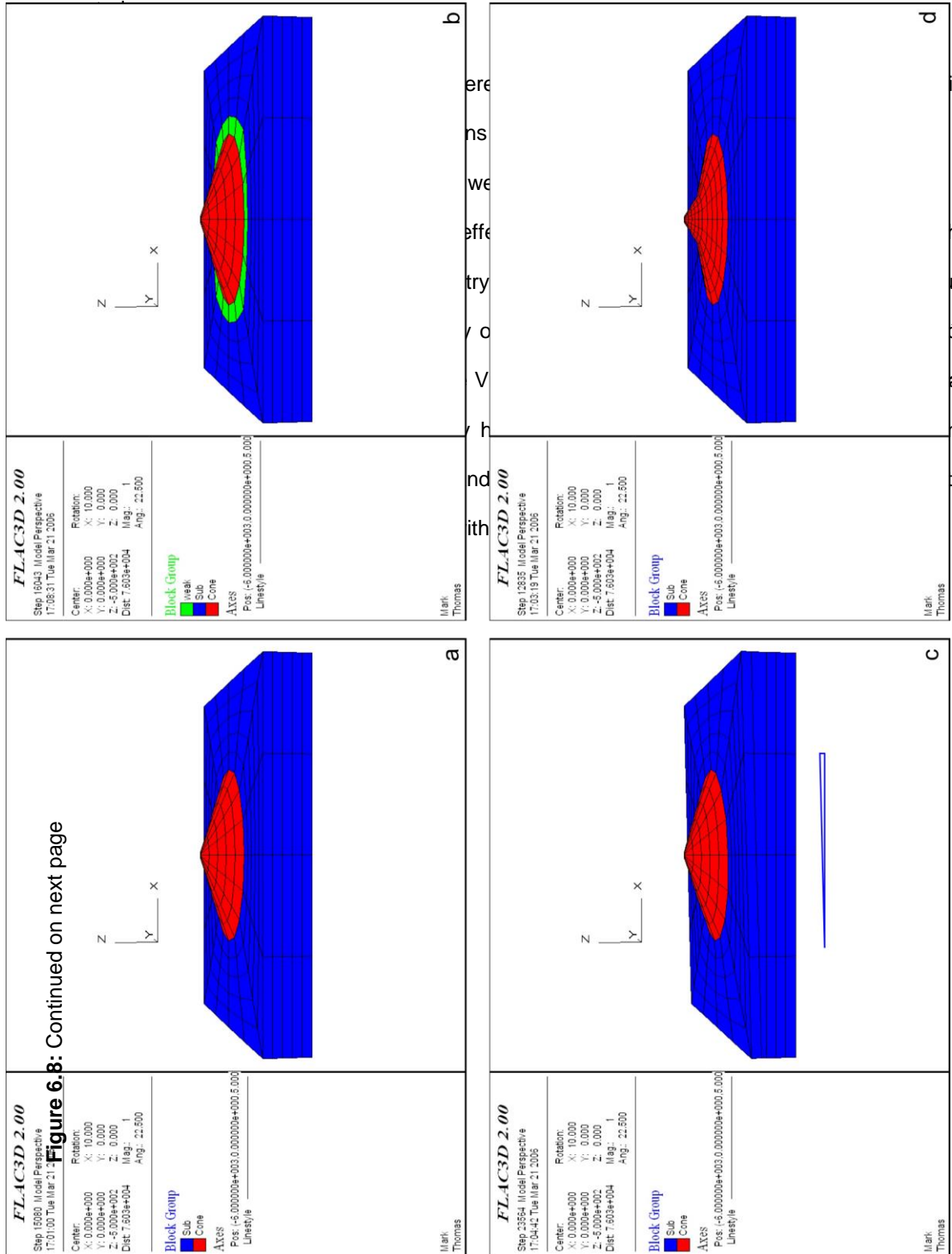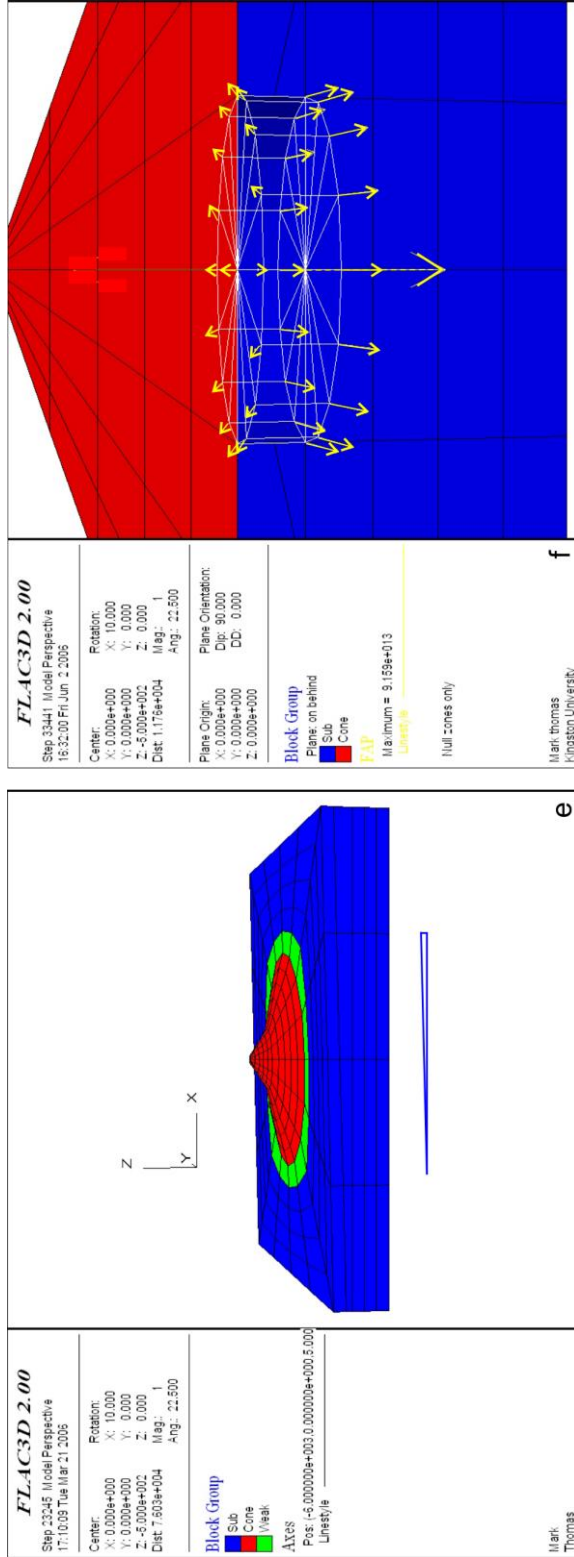

Figure 6.8: Continued on next page

Figure 6.8: The five model geometries used in the *FLAC³D* modelling. **(a)** normal, **(b)** weak, **(c)** tilted, **(d)** steep and **(e)** Tilted, weak and steep. The blue triangle below the models in (c) and (e) represents the imposed regional gradient. For a detailed description of each of the model geometries see section 7.3 and table 7.3. **(f)** Close up view of the volume defined in the text as the pressure source. The volume of the pressure source is defined by the white grid seen in (e), it has the same form in all the models. The yellow arrows represent the normal stress (pressure) applied across the boundary. Note the arrows on the bottom of the white grid are larger, this is because the pressure is applied is addition to any stresses acting across the boundary, they are larger to account for the greater natural stresses at depth. In (b) and (e) the green area represents the extent of the weak substrate, which has a depth extent of one zone.

Model name/ constituent part	Bulk Modulus, Pa	Shear Modulus, Pa	Cohesion, Pa	Tensile strength, Pa	Angle of friction, degrees	Density, kgm^{-3}
Normal						
Substrate	60.3e9	38.7e9	16.6e6	0.8e6	35	2700
Cone	10.0e9	10.5e9	1.98e6	0.76e6	37	2400
Weak						
Substrate	60.3e9	38.7e9	16.6e6	0.8e6	35	2700
Cone	10.0e9	10.5e9	1.98e6	0.76e6	37	2400
Weak area	30.0e9	10.5e9	0.18e6	0	28	2300
Tilted	As Normal					
Steep	As Normal					
Tilted, weak and steep	As Weak					

Table 6.3: List of the elastic and Mohr-Coulomb properties, formatted as required for use in *FLAC^{3D}* (10.0eA is equal to 10.0x10^{A}). These properties apply to the five model geometries discussed in the text. Mohr-Coulomb properties (cohesion, tensile strength and angle of friction) from field data (see Chapter four). Substrate properties taken from Kurz *et al.*, (2003).

regional gradient, a scenario that is present throughout much of the Central Andean volcanic province (Wooller *et. al.*, 2004).

The steep geometry, while smaller in overall size, can be considered analogue to the volcanic island of Tenerife. The model slope angles of ~ 30° and 13° are representative (in a worst case) of the current active volcanoes (Teide and Pico Viejo) and the old volcanic edifices upon which they are built respectively. Tenerife also has a well documented history of flank collapse (Navarro and Coello, 1989; Cantagrel *et al.*, 1999; Ablay and Hürlimann, 2000; Hürlimann *et al.*, 1999; 2001), making this an excellent choice of model geometry.

It is more difficult to locate a natural analogue for the worst case scenario presented in the tilted, weak and steep geometry. However, there is a potential similarity with Mombacho, Nicaragua. Mombacho, a stratovolcano on the shore of lake Nicaragua has undergone three previous episodes of collapse related to spreading on dipping substrata (van Wyk de Vries and Borgia, 1996, Cecchi *et. al.*, 2005) and a new, steep cone has now grown on the north-east part of the edifice (Cecchi *et. al.*, 2005). If this new cone were to grow any larger, Mombacho would exhibit all of the features of the tilted, weak and steep geometry, and its proximity to large population centres advocates the examination of type of model geometry. For all five model geometries, the ultimate

goal was to calculate the factor of safety (*Fs*) using the techniques outlined in Section 7.3.1. This was done for five pore pressurisation regimes, 0 MPa, 1 MPa, 5 MPa, 10 MPa and 20 MPa, for each model geometry. As detailed in Section 6.3.1, the calculation of the *Fs* in *FLAC*^{3D} differs for that of the LEM. The *Fs* is calculated for each individual zone of the model. Therefore unlike the LEM, no overall *Fs* for any particular potential failure plane is calculated. This makes the results obtained more open to interpretation. The pressure source in all models was defined as a cylindrical volume in the substrate immediately below the cone base with a fixed radius of 1500 m and being 600 m in height (Fig. 6.8f). Each pressurisation stage was applied consecutively to the model with no other changes after the previous stage had reached equilibrium (Fig. 6.9).

6.3.3 Results of the *FLAC*^{3D} modelling

As with the LEM for similar pressures, although the *Fs* was reduced in all cases as internal pressure increased, at no point did complete failure of a slope occur. This is a key result, indicating that collapse triggered only by internally-sourced pore pressure increases is unlikely unless pressures exceed 20 MPa. However, numerical deformation analyses allow more than just the *Fs* to be assessed.

Through the use of *FLAC*^{3D} it was possible to examine much more than just the factor of safety. The following sections detail the critical model outcomes and summarise the potential of deep sourced pore fluid pressure increases in generating volcano instability. The five models are described with the aid of Figures 6.9 to 6.15. The models are assessed through four major criteria, the number of steps that the model takes to solve (Fig. 6.9); maximum recorded displacement for the entire simulation (Fig. 6.10); maximum unbalanced force (Fig 6.9) and the calculated *Fs* (Figs 6.11 to 6.15). The maximum unbalanced force (Section 6.3.1) is analysed because this gives an indication of at what point in the model history the model is experiencing the greatest destabilising forces.
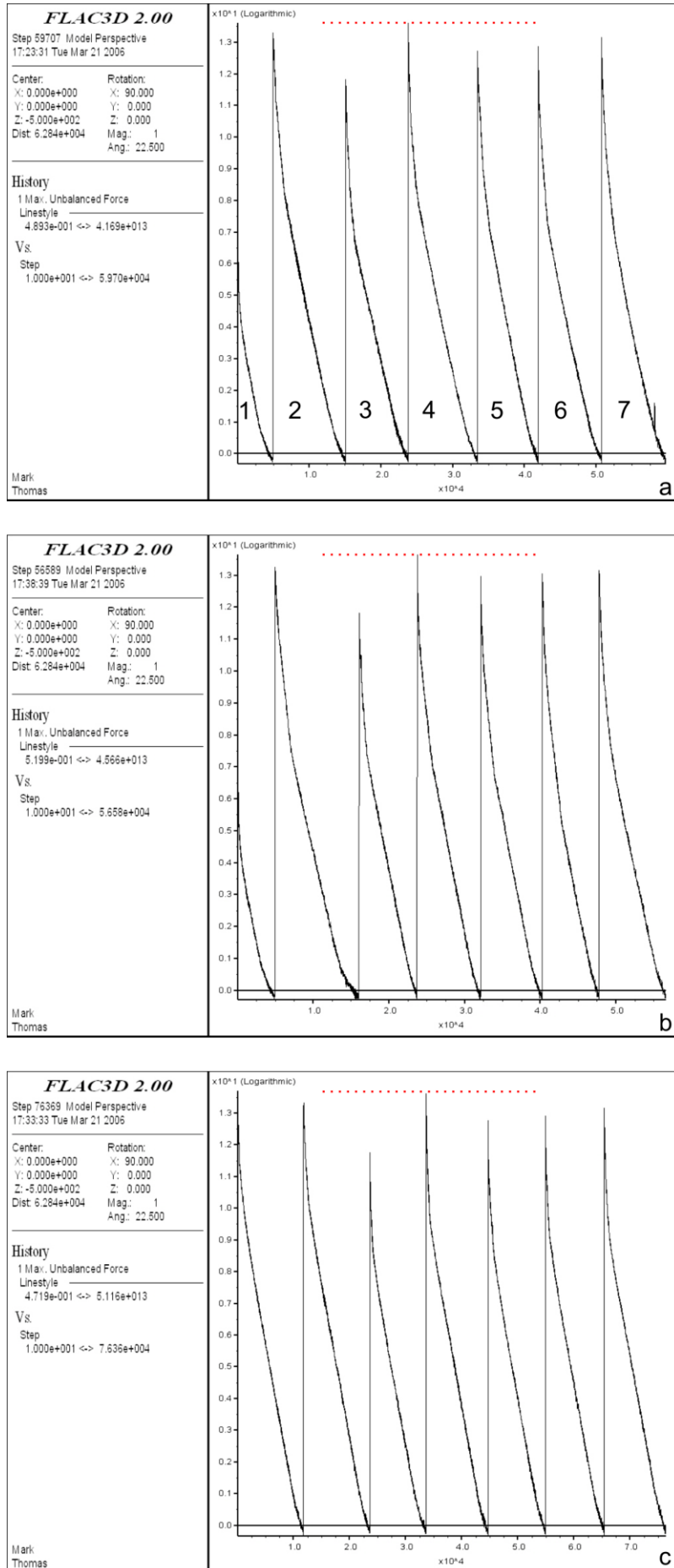
Figure 6.9: History plots of the maximum unbalanced force (*N*) (y-axis) verses number of steps x10^4 (x-axis) for each of the five model geometries. **(a)** normal, **(b)** weak, **(c)** tilted, **(d)** steep and **(e)** tilted, weak and steep. Each model has 7 distinct parts as shown in (a). Each one of these parts relates to the model solving to equilibrium at the end of a particular stage of the solution. (1) base and cone solved in elastic mode (2), Base and cone solved in Mohr-Coulomb mode, (3) Pressure source introduced and solved at 0 MPa overpressure, (4) 1MPa, (5) 5MPa, (6) 10 MPa and (7) 20 MPa (end of model). Note the log scale of the y-axis. The dashed red line represents the largest magnitude of maximum unbalanced force with in the models, which in all cases relates to stage 4. *Figure continued on the next page*.
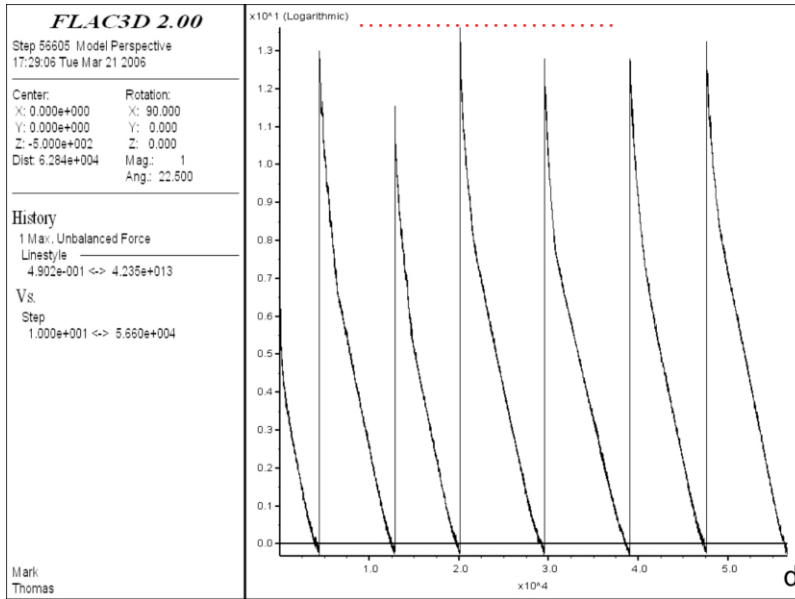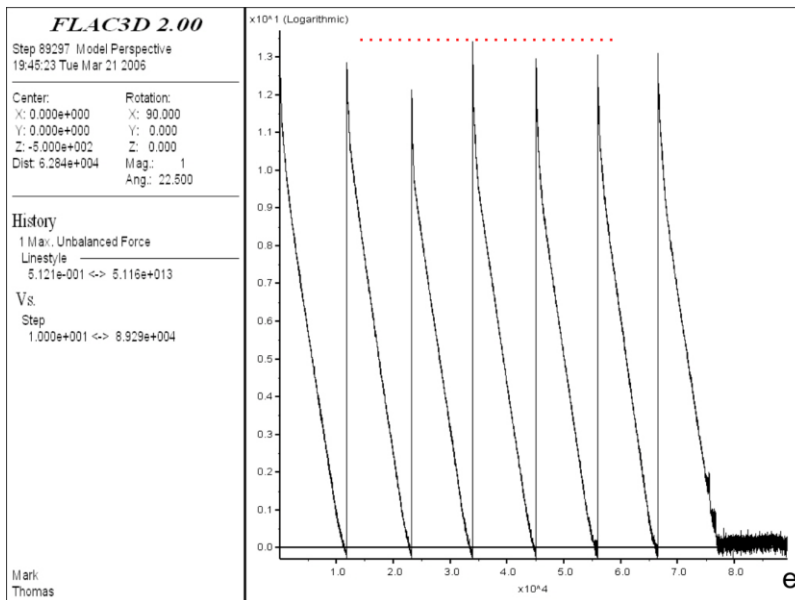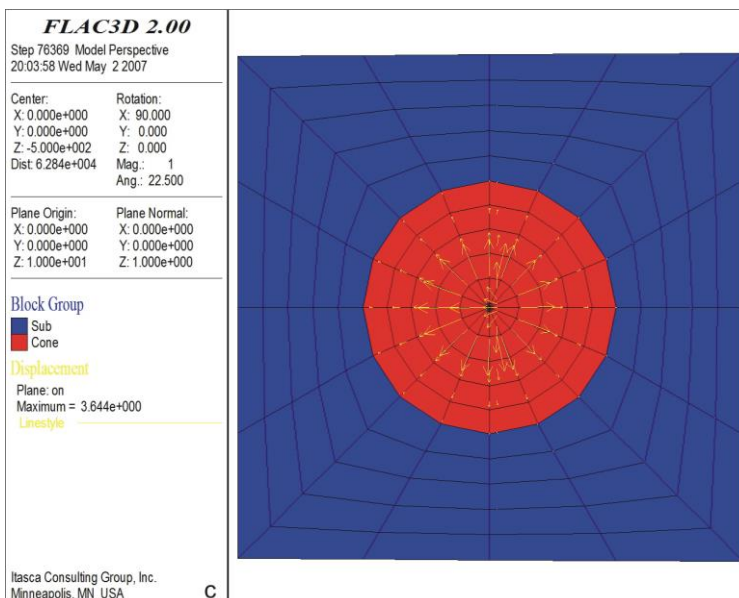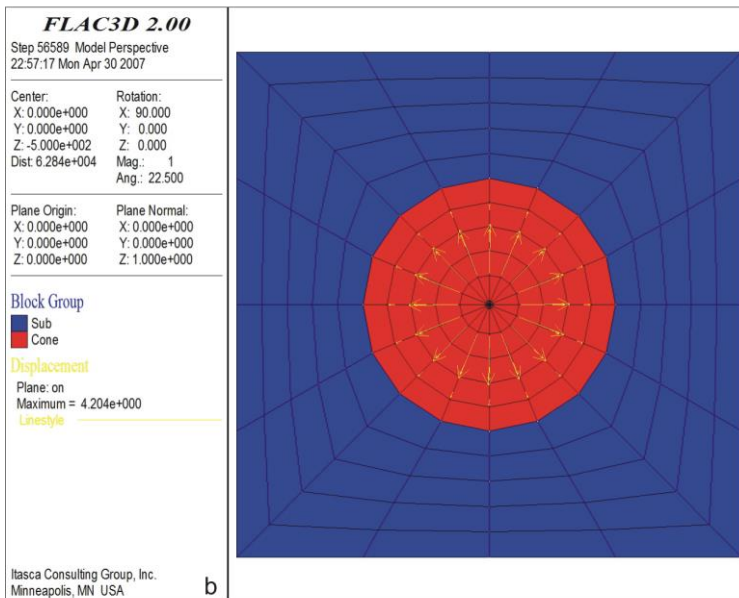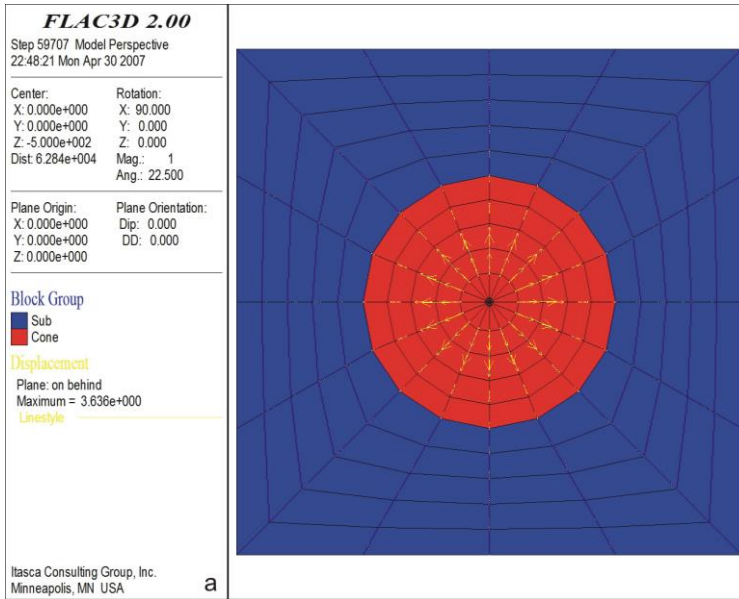
Figure 6.10: Vectors of maximum horizontal displacement (yellow arrow) for the five model geometries, **(a)** normal, **(b)** weak, **(c)** tilted, **(d)** steep and **(e)** tilted, weak and steep. Figures show the total displacement for the entire model run, i.e. the images represent the state at 20 MPa, but maximum displacement may have occurred before this point. The length of the yellow arrow represents the amount of displacement, with the maximum displacement recorded detailed din the key. Note the symmetry of displacement except for **(c)** and **(e)** which both exhibit regional gradients where the down slope direction is negative x as seen in Figure 6.8. *Figure continued on the next page*.
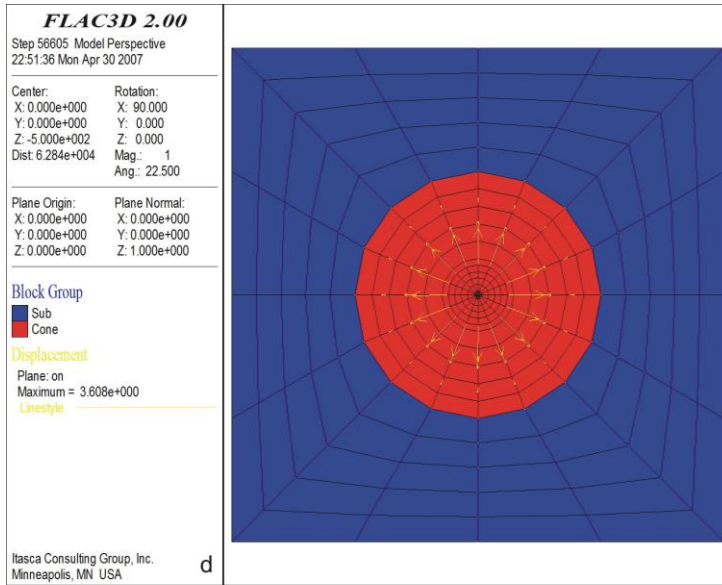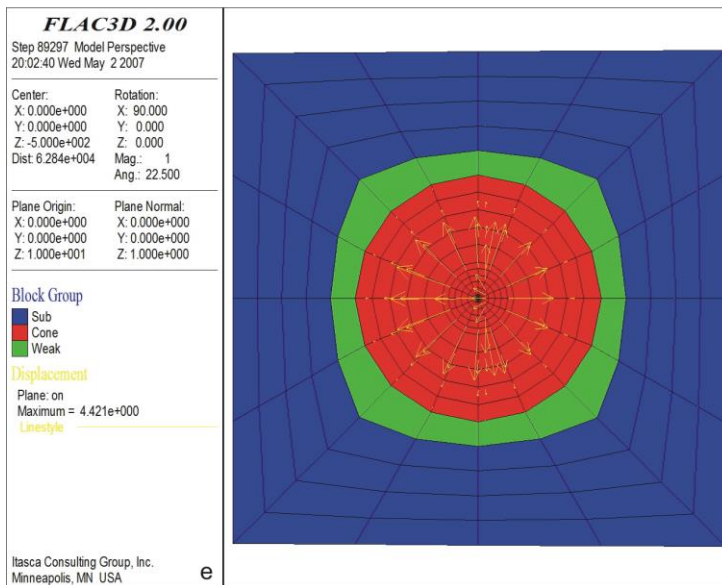
In general, increasing the applied pore fluid pressures over the four stages from 0 MPa to 20 MPa caused, as detailed at the start of this Section, a reduction in the *Fs* as internal pressure increased in all models. For each model geometry, the regions of reduced stability caused by the increase in pressure from 0 MPa to 1 MPa observe individual shapes. These regions are defined by the lower values of *Fs* (greens and yellows) in Figure 6.12. This is consistent with what would be expected, as the overall stability of the cone is controlled by the distribution of stresses within it. For each model the initial stresses will be slightly to markedly different as the model edifices possess varying shapes and properties. The simulated increase in pore fluid pressure acts to modify this existing stress field and decrease stability through the concept of effective stress (Section 3.2). Thus, the shape of the region of reduced stability is dictated, up to a point, by the shape of the initial stress field within the

edifice. Further increases in pressure (5 MPa and 10 MPa) do not act to greatly change the overall shape of the region of reduced stability. Rather, they simply increase its size (Figs. 6.12 to 6.14). This holds true until the final stage of simulated pressure increase. By the time the pressure is increased to 20 MPa the region of reduced stability encompasses most if not all of the edifice, it is at this point that the effect of the simulated pore fluid pressure increase is dominant and the region of reduced stability no longer maintains the same shape (Fig 6.15).

For all of the model geometries in the case of no internal pressurisation (Fig 6.11) a potential instability is present at the summit of the model cone. This can be seen from the yellow green and orange colours visible in the submit regions of Figures 6.11a-e This is the representation of the potential gravitational instability inherent in all slopes, and can be seen in section to only effect a relatively shallow potion of the cone. The key observations from each individual geometry are presented separately in the remainder of this section:

Normal geometry

Initial observations of the model geometries suggest that the normal geometry model should be the most stable. However, when studied in detail the results suggest this may not be the case. This model geometry was not the quickest to solve (reach an equilibrium state after the application of all four pressure increases) as might have been expected, (Fig. 6.9) taking a total of 59,707 steps (slightly more than both the weak and steep geometries). Neither did it show the smallest amount

Model Geometry	Total Maximum Displacement (meters)				
	Normal	Weak	Tilted	Steep	Tilted, Weak and Steep
Pressure					
0 MPa	N/A	N/A	N/A	N/A	N/A
1 MPa	0.86	0.89	0.84	0.81	0.87
5 MPa	1.33	1.43	1.36	1.28	1.41
10 MPa	1.98	2.20	2.0	1.94	2.18
20 MPa	3.64	4.20	3.67	3.61	4.45

Table 6.4: Summary of the maximum displacement recorded during the *FLAC^{3D}* modelling process for all five model geometries. The total maximum displacement is recorded continually from the start of the model through all model pressure states, and is representative of the maximum displacement experienced at any time in the models entire history. The displacement is not recorded in any particular direction and can be in the horizontal, vertical or any inclined plane.

of total recorded displacement (Table 6.4), although this is misleading. Whereas the largest model displacements were recorded in the vertical plane for all models (caused by inflation), examining the horizontal displacements (Fig. 6.10), the normal geometry did produce the smallest horizontal displacements. As expected, displacement directions were symmetrical about the centre of the cone.

The normal model geometry behaved in a similar manner to all the other geometries in the fact that, the biggest "shock" to the system occurred with the introduction of the smallest modelled pore pressure increase. This can be seen from the fact that the largest maximum unbalanced force (red dashed line) occurred during the modelling of a 1 MPa increase in pressure (Fig 6.9). Subsequent increases in pore pressure all induced a smaller maximum unbalanced force. Conversely, cone stability, as indicated by the calculated Fs decreased with each increase in pore pressure (Figs 6.11a to 6.15a). This would suggest that in response to pore pressure increases the system is not at its most unstable when it is experiencing the largest unbalancing forces. Rather, weakening of the edifice through progressive internal pore pressure increases plays a more pivotal role in generating instability than rapid, highly energetic events cause by almost instantaneous pore pressure increases in an otherwise stable system.

From examination of Figures 6.11a to 6.15a, it is apparent that the increase in pore pressure significantly destabilises the edifice. However, this destabilising effect is only evident on the surface of the cone at 20 MPa. The destabilising effect takes place deep within the edifice imparting the greatest effect close to and vertically above the pressure source, which suggests that, although the deep interior may be destabilised, there is little chance of failure and the edifice as a whole can be considered stable. However, the slight destabilising effect that does exist is visible over a large volume of the edifice (Fig. 6.156a). As with the recorded displacements the destabilising effect acts in a symmetrical manner indicating no preferential direction of potential collapse.

Weak geometry (weak substrate)

Given that this particular model was constructed with an inherent instability in the form of weak foundations (Fig. 6.8, Table 6.3), it is reasonable to assume this model would be less stable than that of the normal geometry. It may then seem surprising that it solved in the quickest time, taking

just 56,589 steps (Fig. 6.9). This most likely represents the efficiency of spreading due to the presence of a weak substrate, resulting in a stable form being reached in a relatively short time. This assumption is reinforced by the amount of displacement recorded. For the entire model run the weak geometry is second only to the tilted, weak and steep geometry in the amount of maximum recorded displacement (Table 6.4). This indicates that substantial lateral movement (spreading) of the model cone has indeed occurred. As would be expected with a symmetrical cone, the displacement directions were symmetrical about its centre.

The weak substrate has a profound effect on the stability of the edifice, with this geometry generating the largest volume of destabilisation observed in all the models run (Figs. 6.11-6.15). A significant area with a relatively low calculated Fs exists at the base of the edifice just above the weak foundation layer, even before any increased pore pressures are introduced (Fig. 6.11b). This instability is enhanced by each pore pressure increase introduced to the model. In terms of surface expression of the decrease in stability, the weak model geometry ultimately produces the largest area of observed relative surface instability (Fig. 6.15b). However, this region of instability is not visible until a pore pressure of 20 MPa is applied, and at this value, the maximum applied pore pressure increase, the model has observed Fs values within the cone (Fig. 6.15b) similar to the normal model geometry. A significant difference though, is that the lower values of Fs are present at deeper levels in the cone, placing the potential failure surface (see Section 6.3.4 and Figure 6.16) at a deeper level. This makes the edifice less likely to fail (See Section 6.4.2), and suggests that at 20 MPa, the weak geometry (as a result of efficient volcanic spreading) is more stable than the other models considered.

Tilted geometry

The two geometries identified as having a regional gradient of 1.5° in Section 6.3.2 have the greatest solve times (Fig. 6.9), with this, the tilted geometry having the second longest solve time, taking 76369 steps. Although only resting on a very gentle slope of 1.5°, the effect on the direction of displacement and the location of the greatest generated instability is profound. The preferred direction of horizontal displacement is observably down slope, with a smaller degree of spreading in the up slope direction (Fig. 6.10c). The total amount of recorded displacement is also large considering that there is no weak foundation (Table 6.4). The combination of these observations

reflects the additional down slope (gravity-driven) displacement of the destabilised cone in addition to that observed in the models with no regional gradient.

In comparison to the other model geometries examined, a similar sized region of instability is generated within the edifice at all pressure stages (Fig. 6.11-6.15), which is shown by the lower *Fs* values of greens, yellows and reds. There is however, a marked asymmetry, with a larger region of instability occurring in the down slope direction. This asymmetry is subtle at simulated pore fluid pressures of 1MPa and 5 MPa (Figs. 6.12c and 6.13c), but is clearly visible at pressures of 10 MPa and 20 MPa (Figs. 6.14c and 6.15c), particularly when viewing the surface plot. Looking at the surface instability generated when modelling a pore fluid pressure of 20 MPa (Fig 6.15c), a clear preferred orientation of potential failure is seen, although with a minimum *Fs* of 1.4 observed on the surface of the cone the modelled edifice is still relatively stable.

Steep geometry

Taking a total of 56,605 steps to reach equilibrium at a modelled pore pressure of 20 MPa (Fig. 6.9d), only the Weak geometry model solved in a shorter time. This was surprising considering the apparent increased instability of steep-sided composite cones compared with the broad shield volcanoes that is apparent in nature. What may also appear surprising is the fact that this model geometry produced the smallest total maximum recorded displacement. However, this is thought to be the case for two reasons:

1. A large portion of the maximum recorded displacement for the models that do not possess a weak foundation (which enables more efficient spreading) occurs in the vertical direction. This vertical displacement is detailing the effect of inflation of the edifice in response to the simulated pore fluid pressure increases. The presence of the steep upper cone places more mass directly on top of the position of the pressure source (Fig. 6.8d). This effectively limits the amount of vertical inflation in response to simulated deep-seated pore fluid pressure increases and hence, reduced the total recorded displacement.

2. Even though the upper cone is much steeper, a greater amount of spreading takes place in the lower shield-like cone base (Fig. 6.10d). This reflects the smaller area that the upper cone has to spread into before failure must occur. Essentially the area that the upper cone

has to spread into is limited by the area encompassed by the break of slope with the lower cone. For the upper cone to spread beyond this limit it must experience some form of failure. The assigned strength of the upper cone is such that failure is resisted and spreading is halted. While the lower, shallower cone does experience a greater degree of spreading compared to the steep upper cone, when it is compared to the other model geometries, the amount of spreading is also relatively low. This is a factor of the lower cone having the most shallow slope angle of all the slopes modelled. This slope is therefore inherently more stable, and a lesser degree if spreading is the result.

The combination of (1) and (2) results in the observed small magnitude of total displacement. As there is no regional slope or non-symmetrical distribution of material properties the displacement vectors are symmetrical about the centre of the cone.

The apparent reduced spreading of the upper cone appears to decrease its stability. Even without any induced pore pressures, there is a pronounced near surface region of relatively low stability within the upper cone (Fig. 6.11d). This is a result of the upper cone not being restricted and not being able to deform into its most stable shape. Although considered as a shallow potential failure in this thesis (as it is concerned with only gravitational instability and topography), the relatively unstable model area effects ~ 600 m of the upper cone to a depth of up to ~ 75 m. In engineering terms this would constitute a substantial failure, and be potentially destructive. It would appear then that despite the relatively rapid solve time and maximum displacements, the steep geometry is inherently the most vulnerable and potentially most hazardous geometry when *no* internal pore pressures are considered.

This instability is enhanced by increasing the pore pressure. Even at a pressure of 1 MPa most of the upper cone is plotted in green and yellow colours, representing a relatively low *Fs* (Fig. 6.12d), while at a pore pressure of 20 MPa this model exhibits the smallest surface area expression and internal volume of decreased stability, with almost the *entire* interior of the upper cone significantly destabilised, displaying a *Fs* of 1.2 or less (Fig. 6.15d). Only the tilted, weak and steep geometry exhibits a greater degree of instability. While the simulated pore pressure increases *do* have a direct remote effect on the upper cone, it is unlikely that they would have such an effect at this distance from the source as to destabilise the entire cone to the observed degree. A combination of
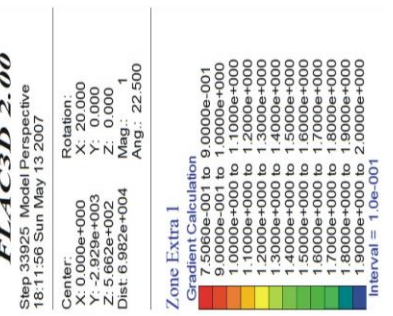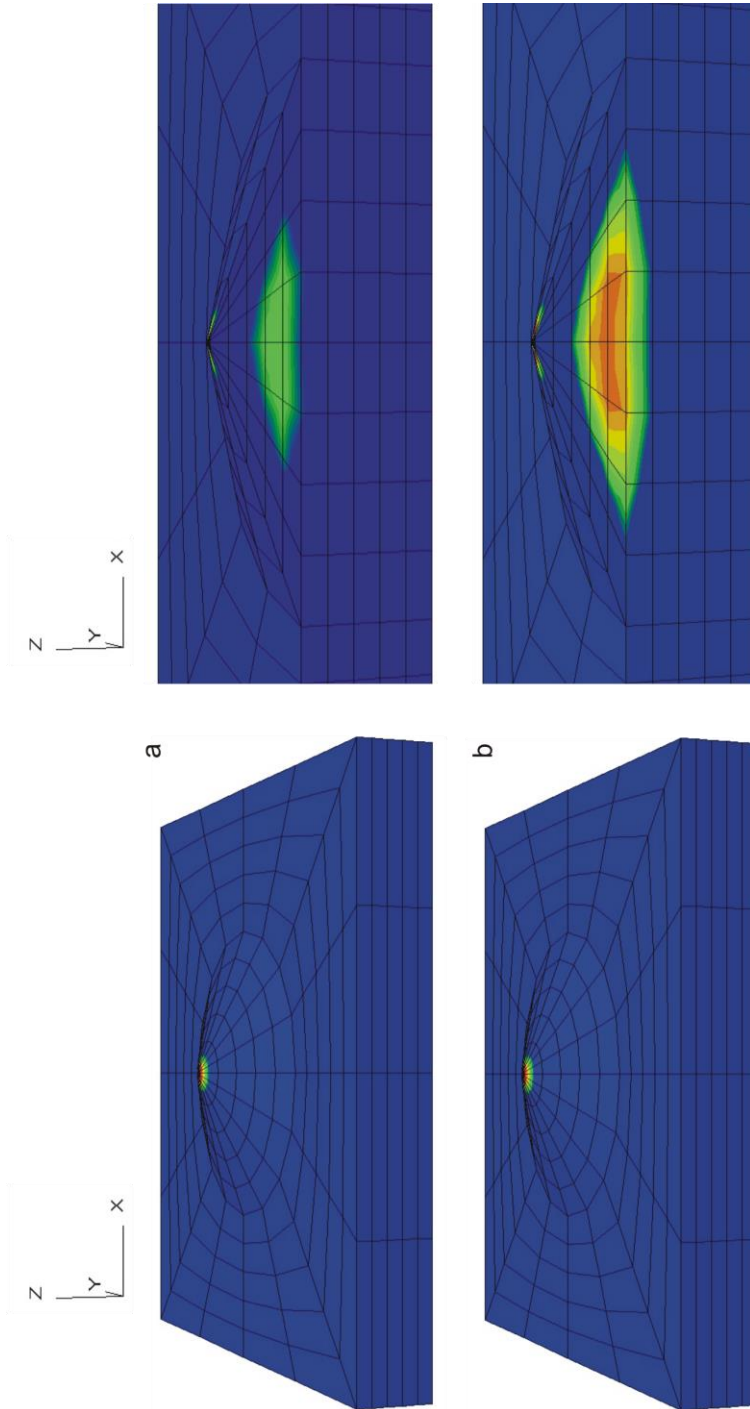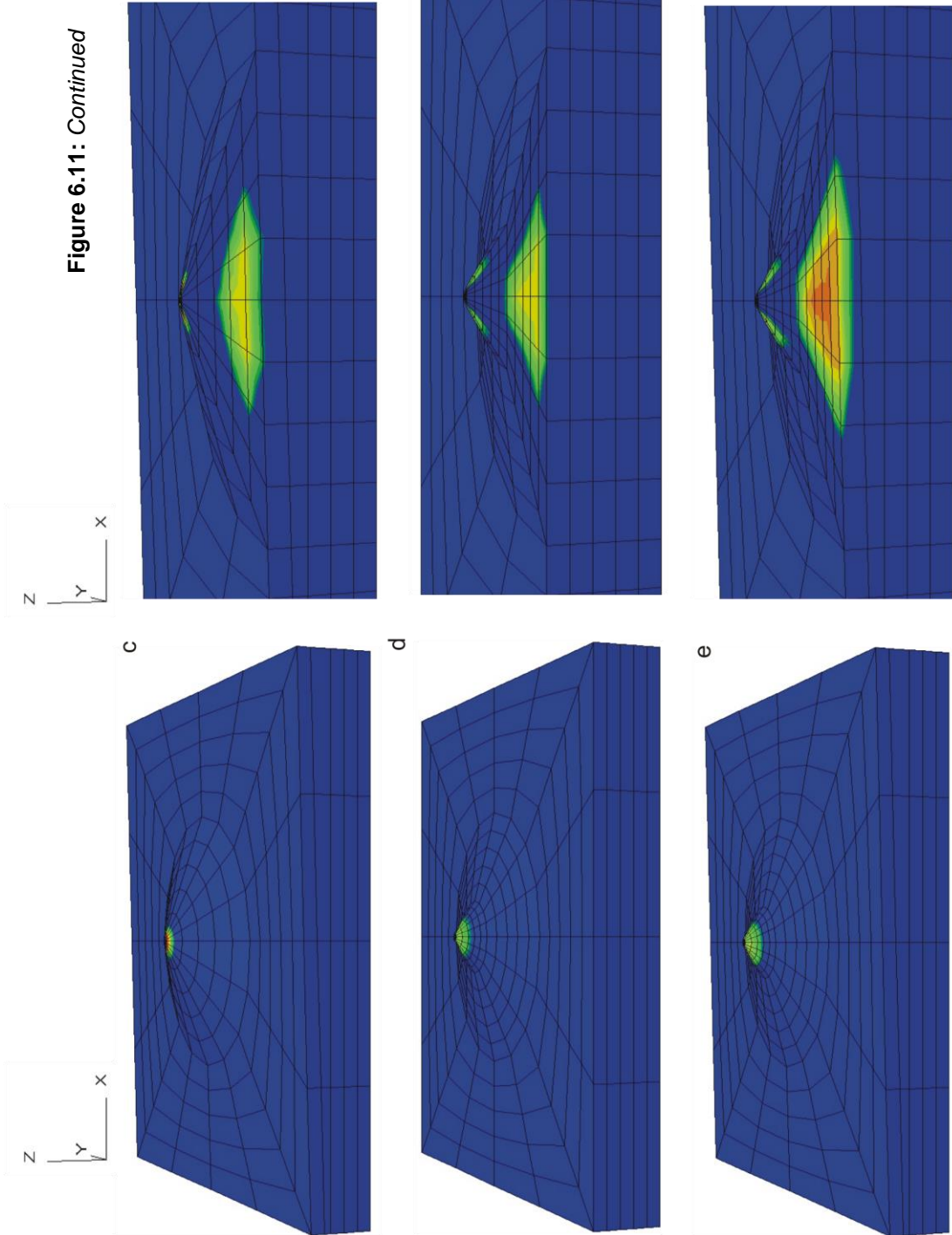
Figure 6.11: Plots of factor of safety for the five model geometries with no increases in pore pressure. **(a)** normal, **(b)** weak, **(c)** tilted, **(d)** steep and **(e)** tilted, weak and steep. From the key blue colours can be seen to have relatively high Fs therefore can be considered stable, while yellow and red colours represent lower values of Fs, therefore can be considered more unstable. For each model the plot on the left shows a surface plot, with the plot of the right showing a slice through the model at a dip of 90°. The factor of safety plots suggest that there is little risk of a deep seated failure, as there is no contiguous line or band of low Fs zones connected to the surface, and only relatively small volumes of the outer slopes are destabilised, with these areas localised at the top of the cones. The large volumes of destabilised material in the centre of the edifices in **(b)** and **(e)** are almost certainly due to the presence of the weak substratum increasing the tendency of the edifice to spread, destabilising its interior. *Figure continued on the next page.*

Figure 6.11: *Continued*

Figure 6.12: Plots of factor of safety for the five model geometries with a 1MPa increase in pore fluid pressure, refer to Fig 6.11 for description of figure layout. The most obvious difference to note when the pore pressures are introduced is a decrease in the F_s. This is observable from the key when comparing Fig 6.12 to 6.11. Interestingly, at this low value of pore pressure increase, the surface instability appears to reduce, possibly due to inflation and spreading in response to the increased pore pressures, hence a slight shallowing of the edifice slope angles. *Figure continued on the next page.*

Figure 6.12: *Continued*

Figure 6.13: Plots of factor of safety for the five model geometries with a 5 MPa increase in pore fluid pressure, refer to Fig 6.11 for description of figure layout. At a pore pressure increase of 5 MPa, the yellow colours representing F_s values less than 1, begin to join together rather than exist as individual areas, this is particularly visible by comparing 6.13a to 6.12a. This suggests that a 5 MPa increase in pore fluid pressures is enough to significantly destabilise the interior of a volcanic edifice. In **(e)** there is also the fist appearance of a strong directional surface instability, representing the effect of a regional gradient. This directional surface instability is enhanced further by additional increases in pore fluid pressure (Figs 6.14e – 6.15e). *Figure continued on the next page.*
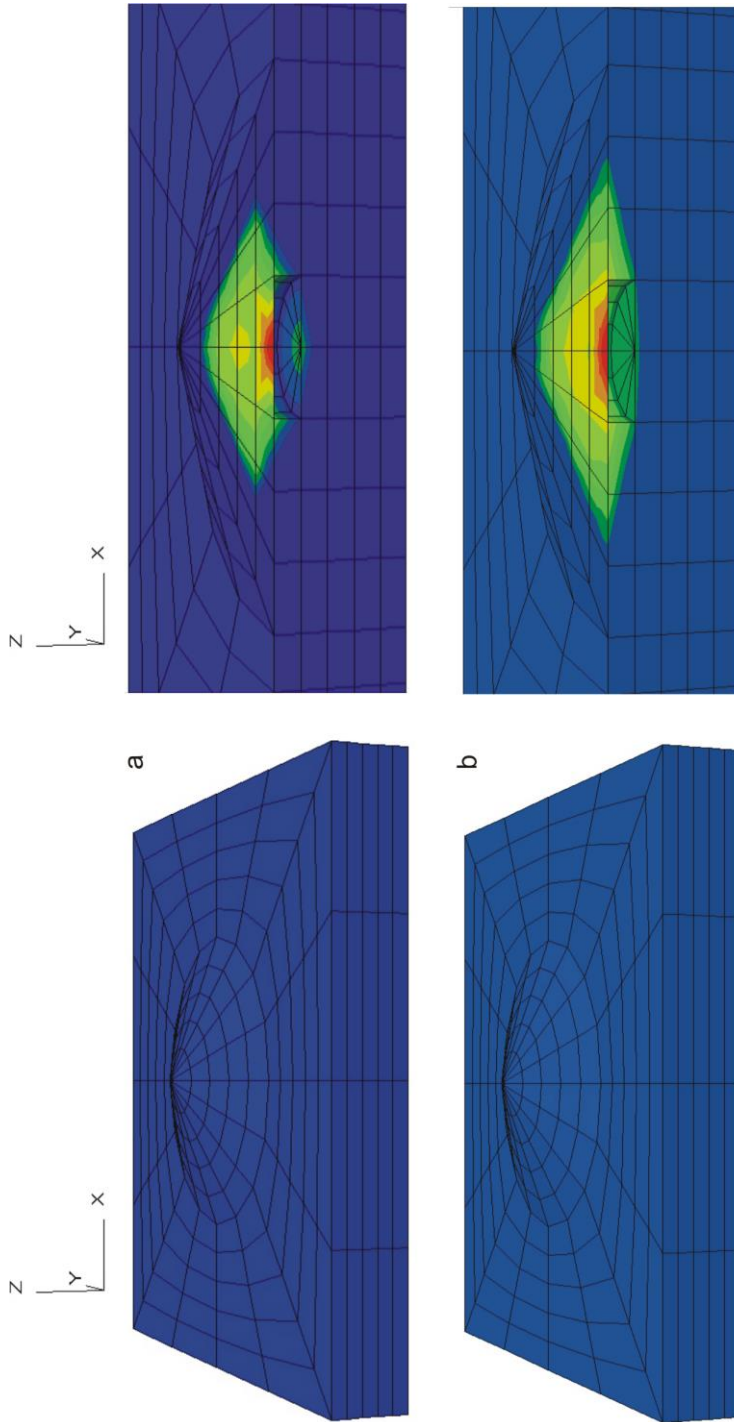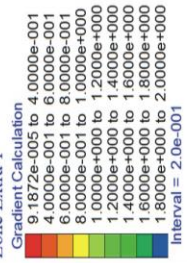
Figure 6.13: *Continued*
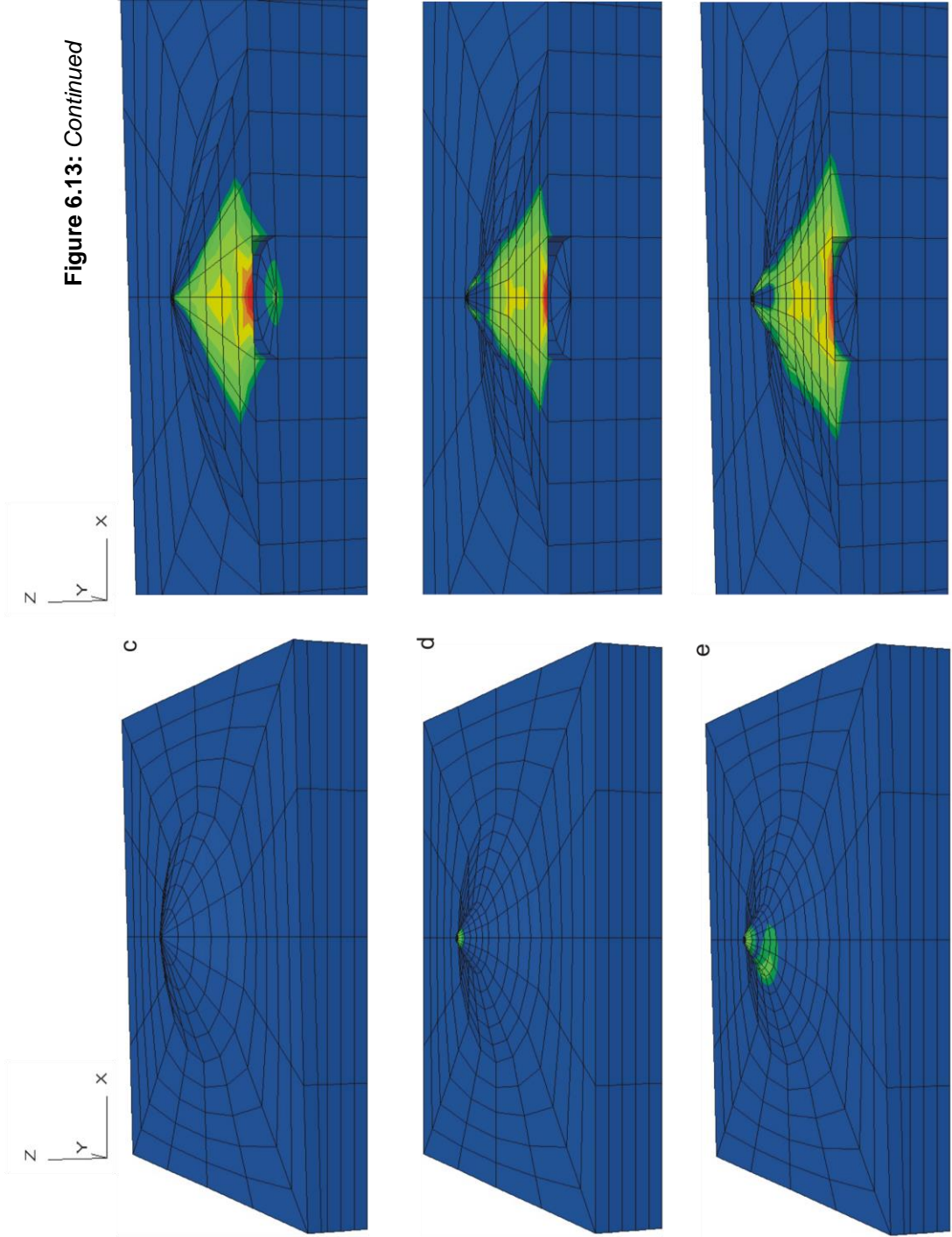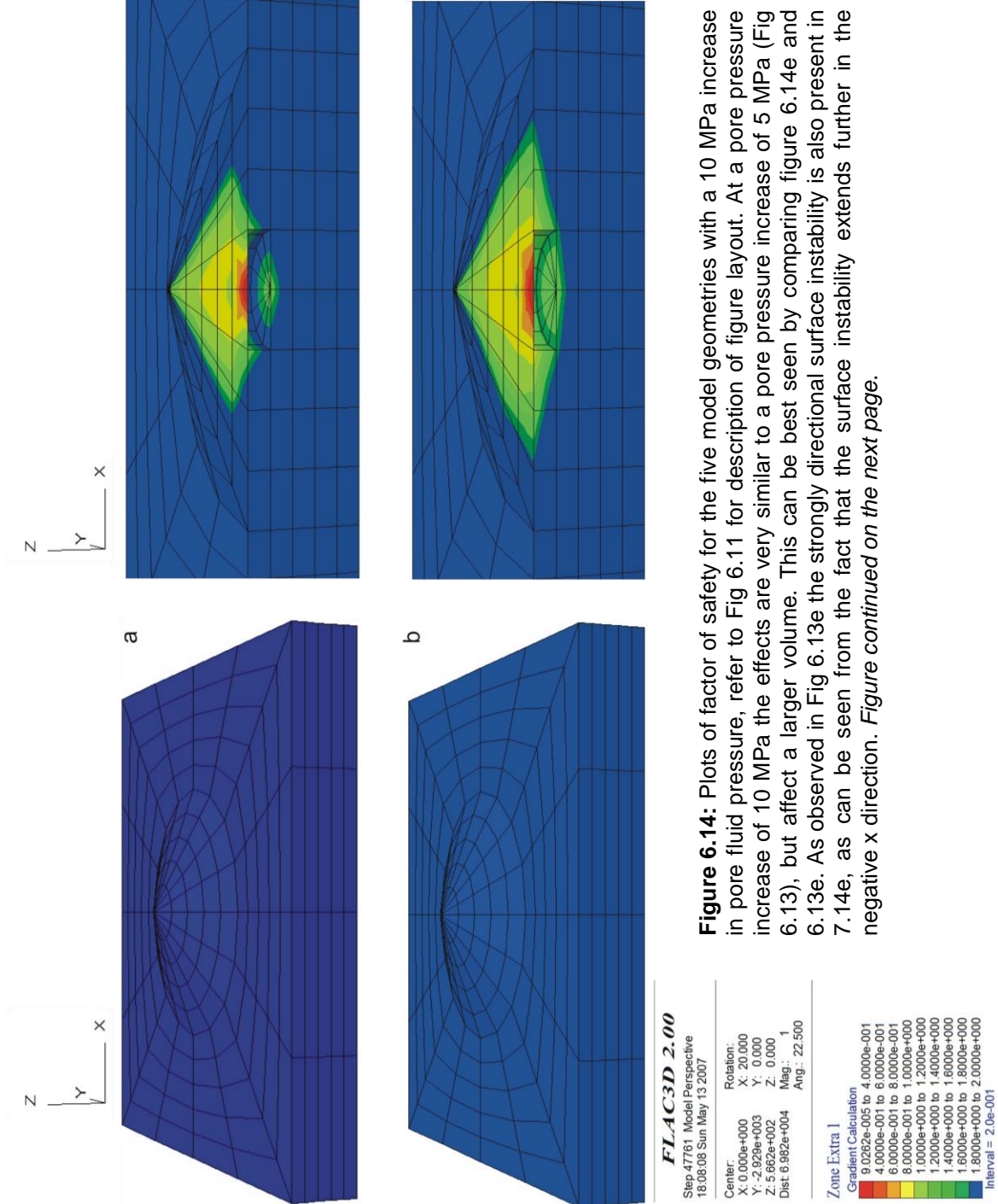
Figure 6.14: Plots of factor of safety for the five model geometries with a 10 MPa increase in pore fluid pressure, refer to Fig 6.11 for description of figure layout. At a pore pressure increase of 10 MPa the effects are very similar to a pore pressure increase of 5 MPa (Fig 6.13), but affect a larger volume. This can be best seen by comparing figure 6.14e and 6.13e. As observed in Fig 6.13e the strongly directional surface instability is also present in 7.14e, as can be seen from the fact that the surface instability extends further in the negative x direction. *Figure continued on the next page.*
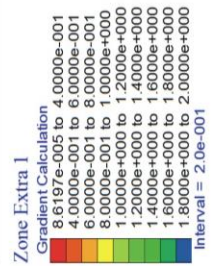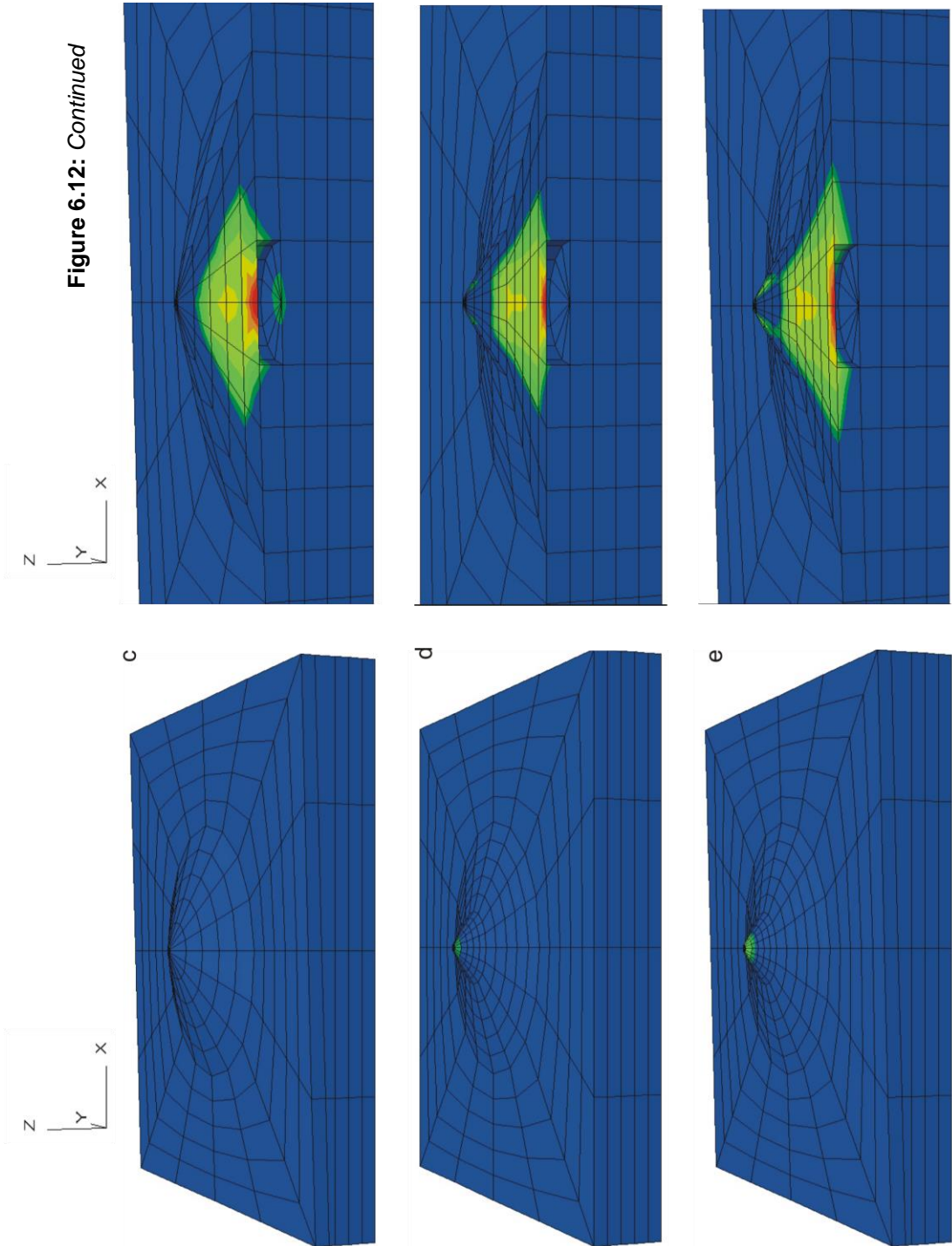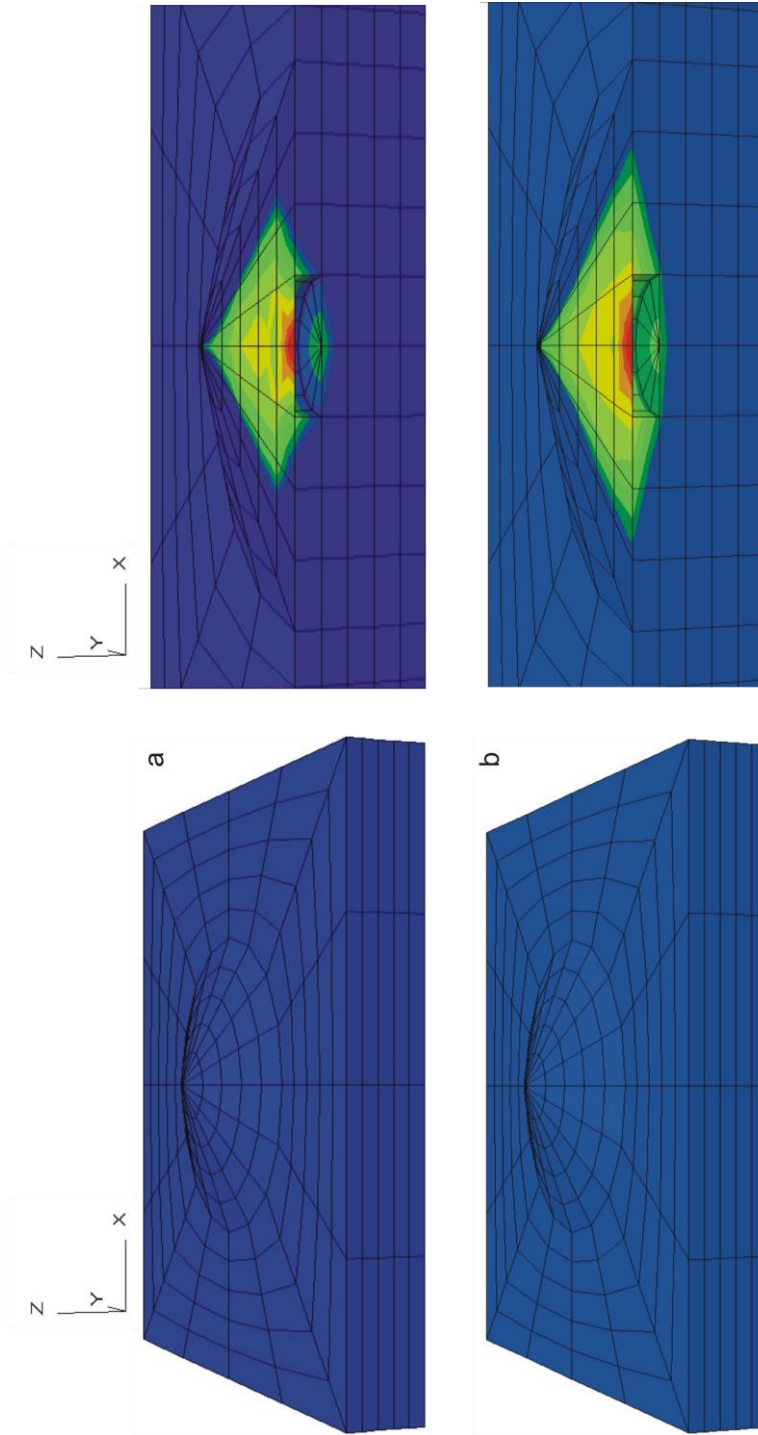
Figure 6.14: *Continued*
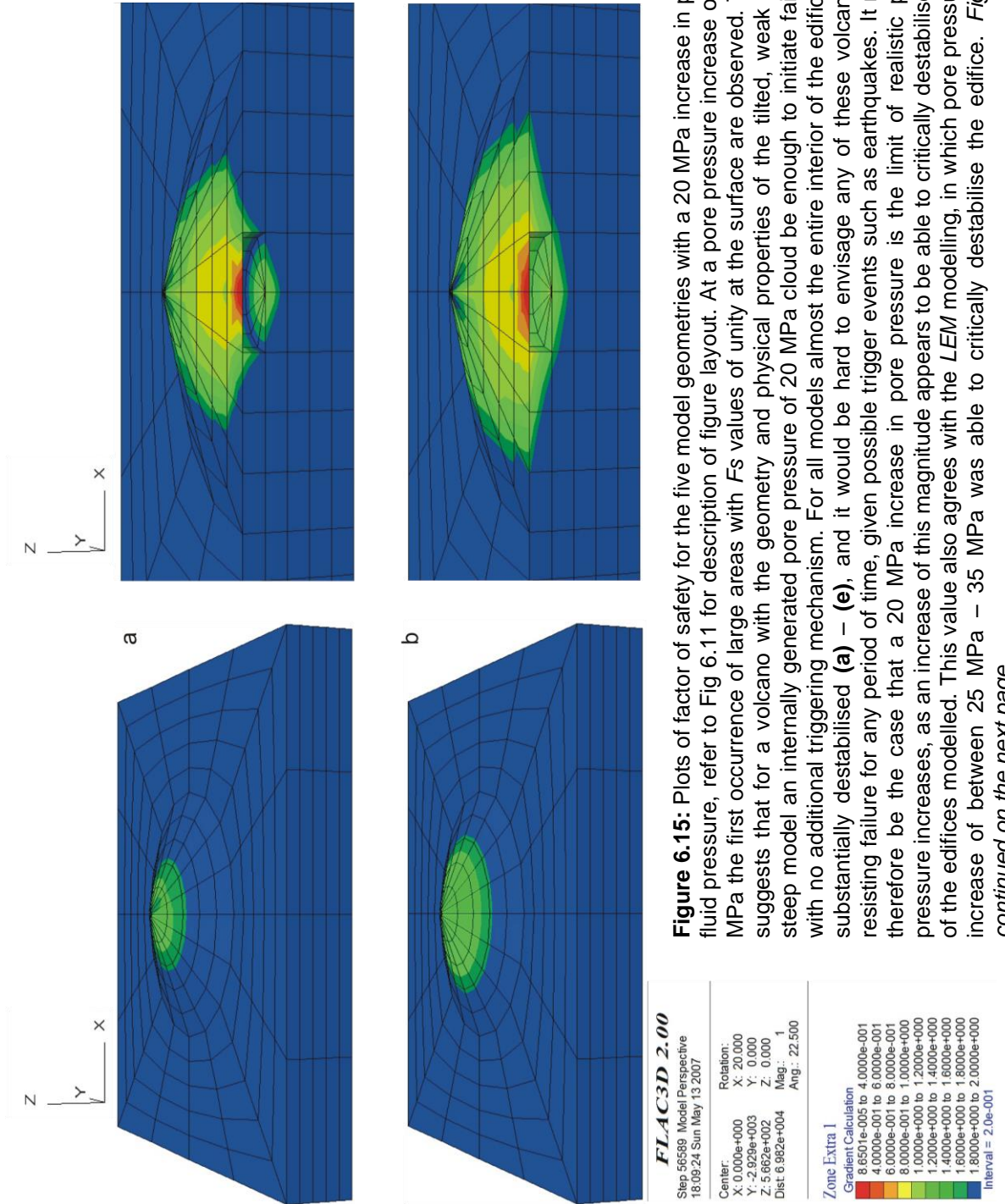
Figure 6.15: Plots of factor of safety for the five model geometries with a 20 MPa increase in pore fluid pressure, refer to Fig 6.11 for description of figure layout. At a pore pressure increase of 20 MPa the first occurrence of large areas with *Fs* values of unity at the surface are observed. This suggests that for a volcano with the geometry and physical properties of the tilted, weak and steep model an internally generated pore pressure of 20 MPa cloud be enough to initiate failure with no additional triggering mechanism. For all models almost the entire interior of the edifice is substantially destabilised **(a)** – **(e)**, and it would be hard to envisage any of these volcanoes resisting failure for any period of time, given possible trigger events such as earthquakes. It may therefore be the case that a 20 MPa increase in pore pressure is the limit of realistic pore pressure increases, as an increase of this magnitude appears to be able to critically destabilise all of the edifices modelled. This value also agrees with the *LEM* modelling, in which pore pressures increase of between 25 MPa – 35 MPa was able to critically destabilise the edifice. *Figure continued on the next page.*

Figure 6.15: *Continued*
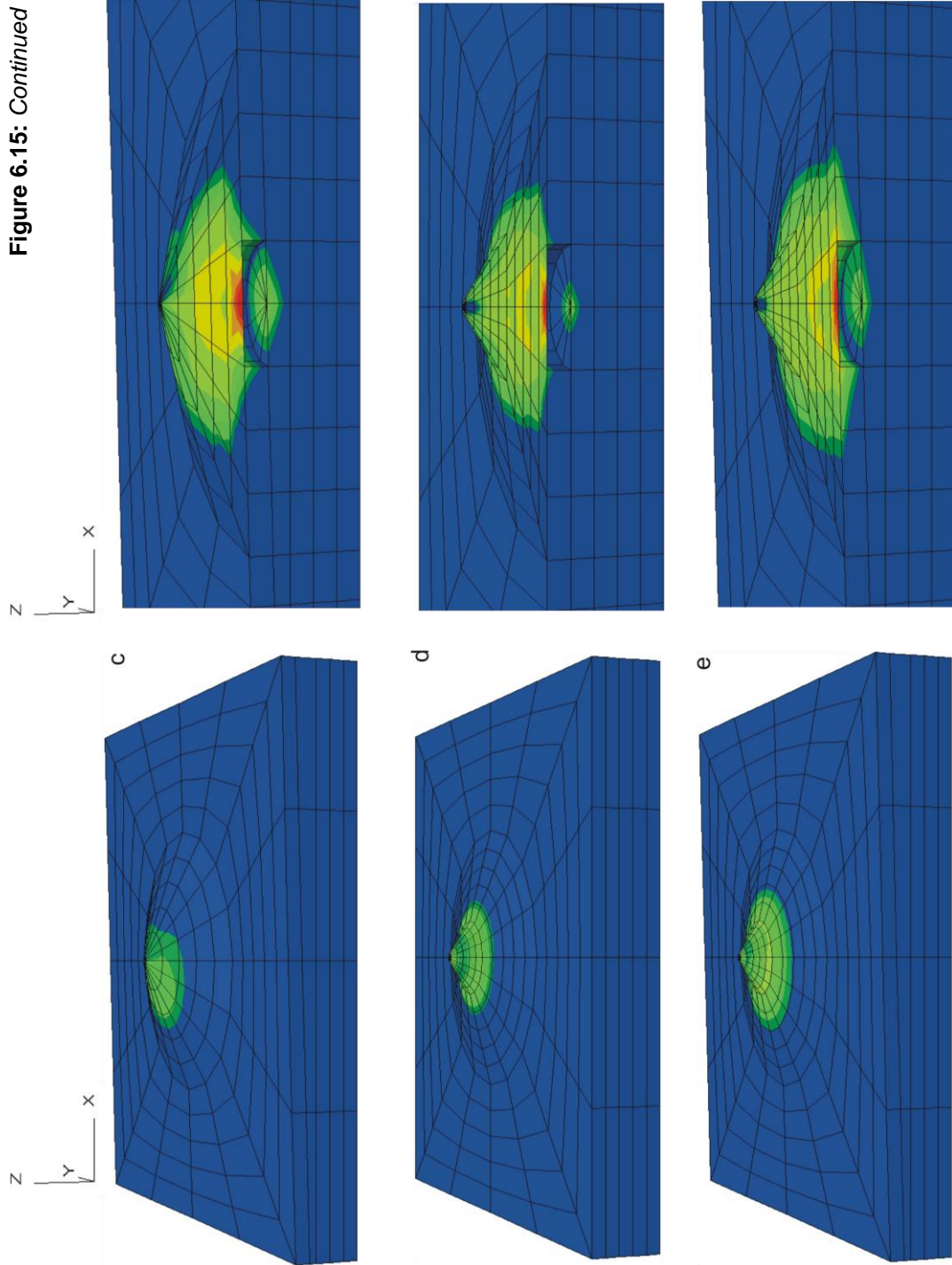
both this direct effect and the simulated pore pressure increases acting to destabilise the lower cone upon which the steep cone lies is the reason for the scale of generated instability.

Tilted, weak and steep geometry

As predicted in the model descriptions (Section 6.3.2), this geometry proved to be the most unstable, and with *Fs* values of between 1 and 1.2 observable on the surface of the cone at internal pore pressures of 20 MPa (Fig. 6.15e), it is the closest to failing. This high degree of model instability is reflected in a solve time of 89,297 steps, the longest of all the models. For the final pore pressure increase the model was barley able to reach equilibrium, and the erratic maximum unbalanced force curve shown in Figure 6.9e suggests that the model was experiencing slow failure at the very end of the model run. The maximum recorded displacement is also by far the greatest of all model geometries (Table 6.4), with a pronounced preferential direction of spreading observed in the down slope direction (Fig. 6.10e) in tandem with the largest observed horizontal displacements.

The three modelled elements of a weak substrate, steep upper cone and regional gradient all manifest in a similar fashion to when they are considered in isolation, but their combined effect is to substantially reduce edifice stability beyond that of any singularly modelled element. As with the weak geometry model, the addition of a weak substrate has a pronounced effect on the stability of this geometry such that a significant, deep-seated instability was present *without* any pore pressure effects (Fig. 6.11e). Also, reminiscent of the steep model geometry, the presence of the steeper upper cone causes a pronounced near surface region of relatively low stability within this upper cone, even when no excess pore fluid pressures are applied (Fig. 6.11e). Add in the influence of a regional gradient and this model geometry is affected quite dramatically by relatively small increases in pore pressure. At a simulated pore fluid pressure of 5 MPa a pronounced region of reduced stability is clearly visible at the model surface (Fig. 6.13e). This effect is enhanced with each further pressure increase and the stability of the upper cone reduced to a *Fs* approaching 1 at the surface, with much of the entire edifice being significantly destabilised at a simulated pore fluid pressure of 20 MPa (Fig 6.15e). As shown by the surface plots (Fig 6.11e to 6.15e), the regional slope has a marked effect on the preferred direction of potential collapse, with the *Fs* values lower in the down slope direction.

6.3.4 Interpretation of the *FLAC*^{3D} modelling results

Since *FLAC*^{3D} models a nonlinear system as it evolves in *model* time (the number of solution steps), the interpretation of results may be more difficult than with conventional numerical methods that produce a "solution" at the end of the calculation phase. There are however, two key indicators that were used to assess the state of the *FLAC*^{3D} models:

Unbalanced Force

The unbalanced force as discussed in Section 6.3.1 is a useful tool for defining an equilibrium state, but a low ratio of current maximum unbalanced force to initial unbalanced force only indicates that forces balance at each gridpoint. Steady state plastic flow may still be occurring, without acceleration. In order to distinguish between this condition and "true" equilibrium other indicators should also be examined.

Gridpoint Velocities

Although not discussed within the results, maximum gridpoint velocities were recorded at the end of each calculation and all found to be of the order of $x10^{-8}$ meters per step. As with gridpoint forces, velocities never decrease precisely to zero within a numerical simulation, so like gridpoint forces they are assessed in the form of a ratio. Maximum recorded displacements within the model were of the order of a few meters (Table 6.4), a further 1,000 steps at the end of the model run would produce an addition displacement of 10^{-5} m or approximately 0.0005 % of the current displacements. The value of this ratio is in agreement with the unbalanced force plots (Fig. 6.9) in suggesting that *all* models reached an equilibrium state.

Since all models are considered to have reached equilibrium the calculated *Fs* was used to further aid interpretation of the results. The method for calculating the Fs is discussed in Section 6.3.1. The *Fs* is calculated for each individual zone in the model rather than predicting a discrete failure plane. This has both positive and negative implications. On the negative side, unlike the results from LEM, it is hard to visualise the internal location of a complete potential failure surface. In contrast, the LEM calculates a discrete *Fs* for one surface only. Calculating a zone specific *Fs,* as done within the *FLAC*^{3D} modelling, gives a much more accurate picture of the complete stability of

the cone as the combined effect of every surrounding zone is used when the calculation is performed. Since the *Fs* is calculated from the stresses within the individual zones it is therefore possible to have a calculated *Fs* below unity for a zone within the models interior even though the model is in no danger of failing. This in most clearly seen within the weak model geometry with no induced pore fluid pressures (Fig 6.11b). At the initial equilibrium state there are very low values of *Fs* at the base of the cone (Fig 6.11b). These values are the result of relatively large amounts of spreading because of the weak foundations. The stress state within the zones which have experienced the most amount of displacement as a result of the spreading have been altered such, that when the *Fs* of these zones are calculated using the method outlined in Section 7.3.1 a low *Fs* value is the result. This is despite the fact that, as observed in Section 6.3.3 the spreading has acted to overall stabilise the edifice. While it is useful to observe all the zones with low values of *Fs* as this gives a general picture on where the strength of the edifice is being reduced, a potential failure surface is only indicated if there is a contiguous line of relatively low *Fs* values that may connect to the surface at either end. The results were examined so that any contiguous zones of relatively low Fs were identified and a best fit potential critical failure surface was positioned through aligned *Fs* minima. To demonstrate this, Figure 6.16 shows such potential critical failure surfaces for all five model geometries at a pore pressure of 20 MPa. The alignment of these *Fs* minima is most clearly seen in Figure 6.16b. For clarity, the same illustration without the potential failure surfaces is presented in Figure 6.15b.

Figures 6.15b and 6.16b both relate to the weak model geometry and two (four, if symmetry is considered, but unless stated otherwise only one direction of symmetry is discussed from this point forward) clear potential failure surfaces can be seen at a simulated pore fluid pressure of 20 MPa (Fig. 6.16b). In fact, at lease two potential failure surfaces are identified in all but the normal model geometry (Fig 6.16a–e). These two potential failure surfaces all take the form of a deep potential failure plane and one which is relatively shallower. The deeper potential failure surface is interpreted to exist entirely as an effect of the increase in pore fluid pressure. The shallower potential failure surface is the expression of an inherent instability instigated by the weak substrate, steep slopes, regional gradient or a combination of the three, and further enhanced by the pore fluid pressure increases. It is for this reason that only one potential failure surface is observed within the edifice of the normal geometry. This suggests that while increases in pore fluid pressures
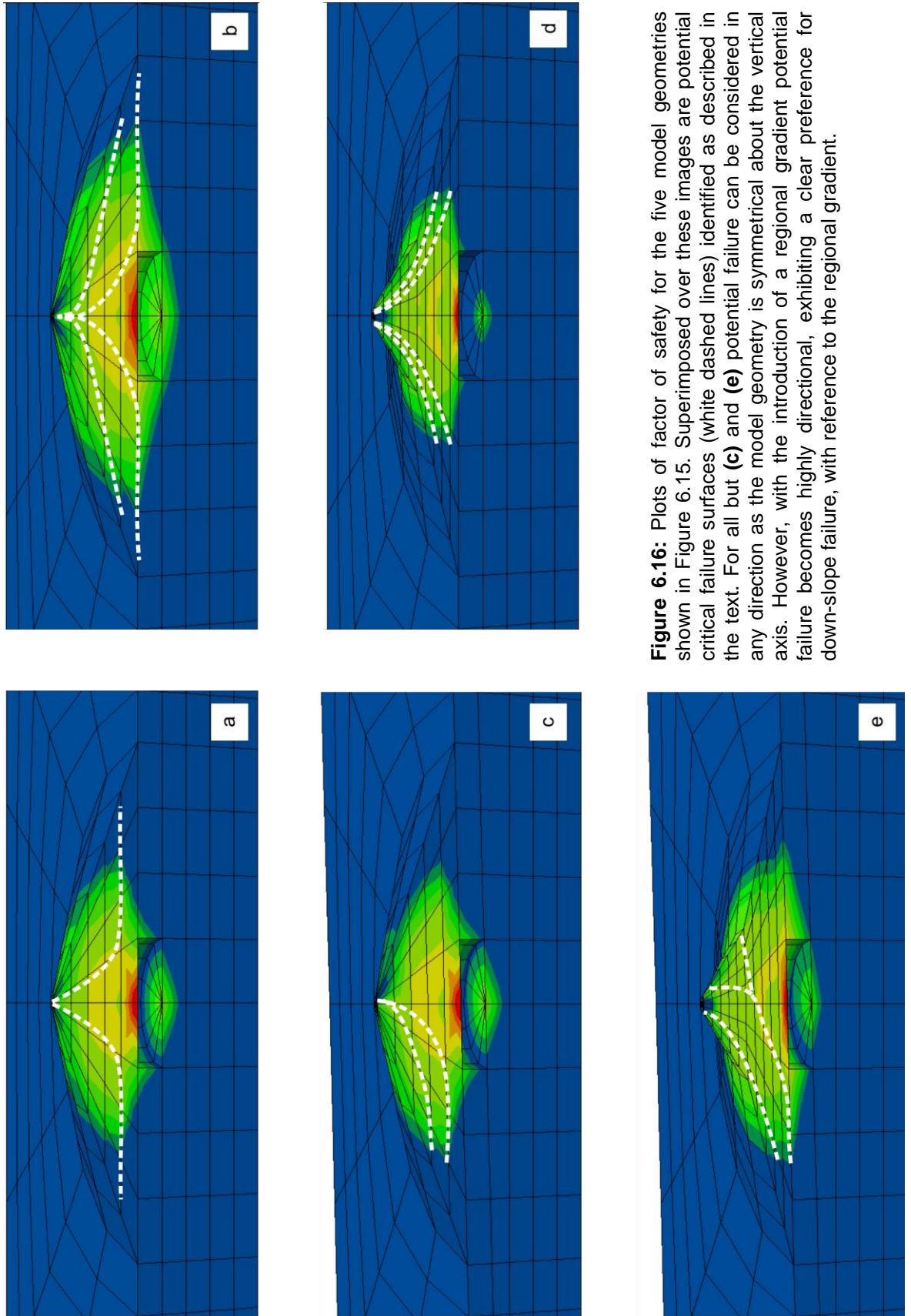
Figure 6.16: Plots of factor of safety for the five model geometries shown in Figure 6.15. Superimposed over these images are potential critical failure surfaces (white dashed lines) identified as described in the text. For all but **(c)** and **(e)** potential failure can be considered in any direction as the model geometry is symmetrical about the vertical axis. However, with the introduction of a regional gradient potential failure becomes highly directional, exhibiting a clear preference for down-slope failure, with reference to the regional gradient.

significantly lower the stability of volcanic flanks, the edifice geometry and foundations (even without considering internal architecture) play a pivotal role in how the destabilisation manifests within the edifice. To what extent individual factors affect the role of pore fluid pressure increases is discussed in more detail within Section 6.4.2.

6.4 Discussion of Numerical Modelling Results

6.4.1 Comparison of three-dimensional and two-dimensional methods

Both 2D and 3D numerical modelling methods were used during the course of the project. The 2D methods were utilised to a lesser extent and while some interesting comparisons between the 2D and 3D methods can be drawn, the primary role of the 2D methods was to validate the hypothesis presented in Section 1.4 prior to more detailed 3D modelling being undertaken. The emphasis on three dimensional modelling is not simply an excuse to produce colourful graphics that provide little new insight. Volcanoes *are* 3D structures, not 2D conic sections. Edifice stresses due to internal pressure dissipate *radially.* This means that 2D models, no matter how accurate, can only ever capture an upper stress bound, and are thus incomplete. The only way to gain a complete understating of stress evolution to the point of failure is to, as has been done within this thesis, model the processes in all three spatial dimensions.

So, what were the observed differences between the two methods? It is difficult to make a quantitative comparison, as the 2D LEM provides an explicit solution while the $FLAC^{3D}$ numerical method does not. However, with the exception of the extremely low calculated Fs values in $FLAC^{3D}$ which are explained in Section 6.3.4, there is a general agreement in the values between the two methods. For the uniform cone and more realistic topography examined with the LEM Fs values of 1.64 and 1.57 respectively were determined for the case of a simulated internal pore fluid pressure of 10 MPa (Table 6.1). If these values are compared with the Fs values within the edifice calculated in $FLAC^{3D}$ at the same pressure (Fig. 6.14) they are seen to be similar. The Fs values within the edifice calculated in $FLAC^{3D}$ vary between 0.8 and 2.0, and since there in no explicit solution it is reasonable to assume a discreet Fs value would lay between this upper and lower bound, which agrees with the values from the explicit LEM solutions. If the general shape of the potential critical failure surfaces from the two methods is compared there is also a general agreement (Fig. 6.17).
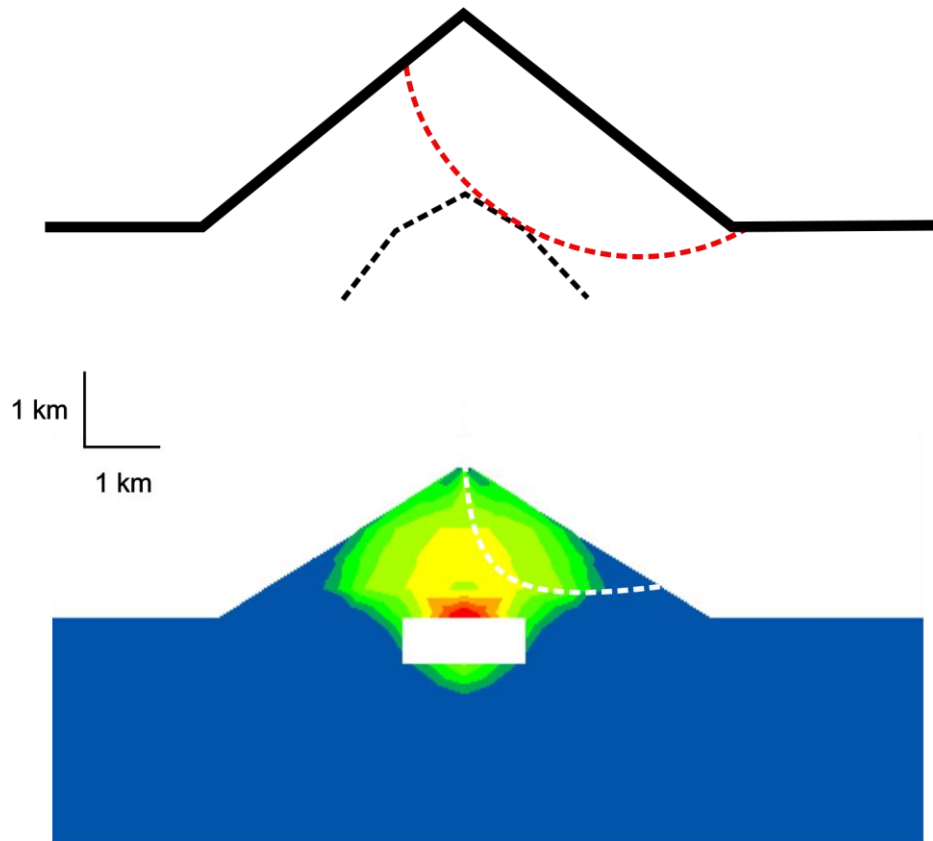
Figure 6.17: Comparison of potential critical failure surfaces (dashed lines) for a uniform cone determined from 2D LEM (top) and *FLAC^{3D}* numerical modelling (bottom). The LEM model show is that detailed in Figure 6.2a and the FLAC3D model shown in a simplified 2D section of the model presented in Figure 6.14a where the coloured contours refer to the *Fs* using the same key presented in Figure 6.14. The pressure source is defined by the dashed black line in the LEM model and the white rectangle in the *FLAC^{3D}* model. Although the overall size of the potential critical failure surface is smaller in the *FLAC^{3D}* model (partially because the modelled edifice is slightly smaller) the general shape is very similar to that identified by LEM. Both exhibit a deep, arcuate profile in section with the arc exhibiting a shallower, almost flat bottom in the *FLAC^{3D}* model. Both potential failure surfaces are also slightly "up-hill" (dipping the opposite direction to the slope) where the surface daylights near the foot of the edifice slope.

Both exhibit a deep, arcuate profile in section, exemplifying the ability of deep internally sourced increases in pore fluid pressures on generating deep-seated instability. However, the arc exhibits a shallower, almost flat bottom in the *FLAC^{3D}* model. Both also demonstrate a slightly "up-hill" section (dipping the opposite direction to the slope) where the potential failure surface daylights near the foot of the edifice slope. While this has to be the case for the LEM as stability is assessed for a number of pre-defined circular trial surfaces (Fig. 6.1), this is not so for the *FLAC^{3D}* modelling, and is a true representation of the potential critical failure surface. In fact, the flat bottomed arc

observed in the $FLAC^{3D}$ models is symptomatic of circular failure (Okubo, 2004). This shape is indicative of a deep-seated failure surface where structural control (gravity, topography, internal structure) is weak to non-existent (Okubo, 2004), suggesting that simulated pore fluid pressure increases are indeed the cause of the generated instability.

Even though the two model geometries presented in Figure 6.17 are of different size, with the LEM model being slightly larger, there is a marked difference in the sectional area above the potential critical failure surface, with that determined from the $FLAC^{3D}$ modelling being smaller. This is interpreted as the effect of lateral restraint on the potentially unstable edifice flank. As noted at the start of this section volcanoes *are* 3D structures. This means that there are forces resisting failure acting in all three spatial dimensions. The LEM only considers resistant forces along the 2D potential failure surface and does not take into account the forces acting on the sides of the 2D section. This is not the case with the $FLAC^{3D}$ modelling. When calculating the Fs in $FLAC^{3D}$, forces from all three spatial dimensions are accounted for. When considering a 3D cone there is more physical mass at its base than its apex, this means that greater forces are required to mobilise (fail) the base than the apex of the cone. In addition, for the same reasons as above, when considering the substrate below the cone, with no inherent weaknesses such as extensive slip-prone clays, there is at least an order of magnitude difference in the forces required to promote movement along a potential failure plane when comparing the 2D and 3D methods. It is for these reasons that the potential critical failure surfaces for the $FLAC^{3D}$ model is both relatively shallower and flatter at its base when compared to the potential critical failure surface identified in the LEM (Fig. 6.17). This shape of failure surface is much more realistic and has been observed at several volcanoes that have experienced massive sector collapse e.g. Bandai, Japan, Bezymianny and Mount St. Helens (Voight and Elsworth, 1997).

The most obvious difference and advantage of the $FLAC^{3D}$ modelling over the LEM is the ability to predict accurate possible collapse volumes. Estimated volumes of collapse, regardless of how detailed a 2D simulation is, will always be missing, and even within the 2D plane, slightly off due to lateral forces, as observed in Figure 6.17. By interrogating a series of sections dissecting the edifice, in conjunction with surface plots like those seen in Figures 6.11 to 6.15, it is possible to make reliable (depending on the accuracy of the input parameters) estimates of collapse volume.

More importantly from a hazard implication, because the full 3D geometry is modelled it is also possible to determine in which direction failure, if likely, would occur. An example of this can be seen in Figure 6.13e, where a clear preferred direction of failure can be seen in both the section and surface plots. Because the models which exhibit a preferred direction of failure examined in this thesis are, with the exception of the regional gradients, axisymmetrical, the preferred direction of failure would also have been identified through 2D LEM. However, the ability to model more complex, real world topography (that may vary along strike) in $FLAC^{3D}$ means that the ability to predict failure direction is significantly enhanced using this modelling method.

Interestingly, given the differences in the two modelling techniques they both impose a uniform upper boundary on what pore fluid pressures can be considered realistic, and whether it may be possible for increases internal pore fluid pressures alone to cause flank failure. For both the 2D LEM and $FLAC^{3D}$ modelling, failure is only predicted to occur as a sole result of increases in pore fluid pressure at a simulated pressure in excess of 20 MPa. This can be seen from Figures 6.4 and 6.15e. Figure 6.4 shows that for the case of the simple uniform cone modelled with LEM, a pressure of 35 MPa is required to decrease the Fs below unity. Figure 6.15e shows the only $FLAC^{3D}$ model geometry to exhibit Fs values of 1 – 1.2 on the surface of the model, which suggests that failure is possible. This geometry is the tilted, weak and steep geometry, and it only reaches this state of instability at a simulated pore fluid pressure of 20 MPa. This geometry is interpreted as the most unstable of all the geometries (Section 6.3.3) and it is therefore evident that pore fluid pressures greater than 20 MPa are required to completely destabilise the more stable geometries. This observation agrees well with the required value of 35 MPa predicted by the LEM. This value in the range of 20-35 MPa is approximately equally to lithostatic stress at a depth of 1 km (assuming a bulk rock density of 2500 kgm^{-3}) and is almost certainly a value which represents the point where pore fluid pressures become the dominant force rather than the pre-existing regional stress field. This is very unlikely to happen in nature as it raises the possibility of the 'floating' volcano discussed in Section 3.1. Rather, at these values of pore fluid pressure the tensile strength of the surrounding rock would certainly be exceeded, leading to fracturing and brecciation of the rock mass, an increase in the volume of pore space and decreases in pore fluid pressures. Therefore, the results of both the LEM and $FLAC^{3D}$ numerical modelling suggest that the role of internal pore fluid pressurisation is one of enhancing instability rather than the singular cause of collapse.

6.4.2 Comparison of the *FLAC^{3D}* models

While all the *FLAC^{3D}* models demonstrate the ability of increases in pore fluid pressure to promote edifice instability, there is a distinct variation between all the model geometries. The differences range from the degree of destabilisation to the area of the edifice affected. These differences are best observed in Figures 6.15 (Fs plots for a pressure of 20 MPa) and 7.16 (interpreted potential critical failure surfaces).

By comparing the location of the potential critical failure surface for the models at a simulated pore pressure of 20 MPa (Fig 6.16), several important inferences can be made about volcanic flank instability. The weak model geometry experienced greater horizontal displacement than either the normal geometry (where the only difference between these two models is the presence of the low strength foundation) or the steep geometry (Table 6.4). This was true even in the initial equilibrium state before any pore pressures were applied. This greater degree of spreading at the base of the cone acted to reduce the potential energy of the edifice slopes generally increasing the overall stability. This can be seen from the fact that the lower values of *Fs* are present at deeper levels within the edifice (Figure 6.15). However, the region of easily deformed substrate is also a very prominent structural weakness. When the pore fluid pressures are increased, this ready-formed structural weakness is utilised to dissipate the stresses building up inside the edifice. This is apparent from the fact that the potential deep failure surface lies at the very bottom of the cone, along the cone-substrate interface (Fig 6.16b), deeper than in either the normal or steep model geometries. Since the failure surface is so deep it has to pass through more of the edifice before it intersects the surface than in either the normal or steep geometries. As the overall *Fs* value for this failure surface will be a function of all the *Fs* values along the complete surface, a relatively high *Fs* value is predicted compared with either the normal or steep model geometries (Section 6.3.4). This is because the potential failure surfaces in these geometries pass through less of the edifice before they intersect the surface meaning that the low values of *Fs* impart more of an influence on these surfaces

In contrast, as discussed in Section 6.3.3, the ability of the steep upper cone present in the steep model geometry to undergo volcanic spreading is severely reduced. This means that the upper

cone is relatively more unstable as it is not able to achieve a shape which is as gravitationally stable as in the weak or normal models. The potential mode of failure observed in the steep model geometry reflects this. The quickest and easiest way for a steep cone to achieve a more stable shape is through small, relatively shallow landsliding, as this is a relatively rapid process. This behaviour is predicted by the *FLAC³ᴰ* modelling. The shallow areas of instability present with no simulated pore fluid pressures in the steep model geometry (Fig 6.11d) are enhanced and enlarged by successive increases in pore fluid pressure. At a simulated pore fluid pressure of 20 MPa the entire steep upper cone exhibits relatively low values of *Fs* with values in the range of 1.0 to 1.2 close to the surface (Fig 6.15d). This results in two relatively shallow potential failure surfaces, either of which encompass a much smaller volume of the edifice than either the normal or weak geometries (Fig 6.16d). Both of these potential failure surfaces pass almost exclusively through regions with *Fs* values of 1 to 1.2, making the steep model potentially much more unstable than either the normal or weak model geometries.

The normal model geometry falls in-between the two extremes of the weak and steep model geometry. There is no weak foundation so the potential failure surface does not lie as deep as in the weak model geometry. Nor is there as much a restriction to volcanic spreading as in the steep model geometry, meaning the edifice is able to achieve a more stable shape prior to applying the pore pressures. Consequently the potential failure surface is not as shallow as in the steep model geometry.

The assessment of the raw results suggested that the normal geometry model (which possessed no inherent structural weaknesses) could not be clearly considered the most stable. This was because in response to simulated pore fluid pressures it took longer to return to an equilibrium state than the weak model geometry, and exhibited both larger displacements and a larger volume of relatively reduced stability than the steep model geometry. However, from a hazard perspective a more detailed comparison would suggest that it is indeed the best of the three geometries, if not ultimately the most stable. This is because:

1. Although there is a lesser region of reduced stability recorded within the steep model, the *Fs* values advocate that actual failure is *far* more likely on these model slopes than in the normal geometry.

2. While the *Fs* value for the potential critical failure surface of the weak model geometry appears to be higher than that for the normal model geometry, it is not by a significant margin. This slight increase in stability is from an assessment of risk, outweighed by the additional volume of material that lies above the potential failure surface.

If the model geometries with regional gradients are considered the effect of the gradient is straightforward to observe. The additional gravity-driven instability caused by the edifice resting on a slight incline acts to further destabilise the volcanic edifice, adding a strong directionality (down the regional gradient) to the likely failure surfaces (Figs 6.11c/e to 7.15c/e). This additional destabilising effect may well be enough to result in a failure that would not have happened if the edifice was not resting on an inclination. However, it is worth bearing in mind that it is probably very difficult to find a real world volcanic edifice that does not lie upon some form of topography. It is therefore the case that nearly every volcanic edifice will have a preferred direction of failure. This is a point that can only be adequately addressed by full three-dimensional modelling. It is also interesting that the results of the *FLAC*^{3D} numerical modelling mirror the collapse models of real world volcanoes. The steep-sided upper cone of the steep model geometry appears prone to relatively shallow, multiple collapse events. This is similar to the collapse history of Augustine volcano, Alaska, a 1252 m high steep-sided anedsitic-dacitic stratovolcano (Siebert *et al.*, 1995) that has collapsed at least eleven times in the past 2000 years (Beget and Kienle, 1992). The results of the weak model geometry suggest that preferential movement along the weak layer leads to extremely deep-seated slow failure that may then cumulate in catastrophic collapse of huge volumes of volcanic flanks. A similar process is proposed for the east flank of Piton de la Fournaise, Reunion Island (Oehler *et al.*, 2004) where deep-level low strength layers are though to constitute a preparing factor in the generation of large scale flank collapse events.

It appears then that unfavourable effects on the overall stability of a volcanic edifice brought about by pre-existing structural weaknesses are enhanced by the effects of internal pore fluid pressure increases. It is therefore important to ensure that all the information regarding the structure of the volcanic edifice has been considered before any meaningful conclusions can be drawn as to the possible effects of internally elevated pore fluid pressures. It should also be pointed out that none of the listed models are specifically tailored to an oceanic island volcano setting. However, the

results are as applicable to this type of volcano as they are to any of the geometries examined. This is because the increases in pore fluid pressure appear to affect the volcano by altering the initial stress state of the edifice. While the initial stress field within an oceanic shield volcano may differ from those studied, due to the buttressing effect of the surrounding water and generally shallower slopes, the overall effect will ultimately be to reduce its stability.

6.5 Numerical Modelling Conclusions

The results of both the LEM and *FLAC*^{3D} numerical modelling undoubtedly show that given the right conditions, internal pore fluid pressurisation is able to generate significant decreases in volcanic flank stability. However, the results of both methods indicate that deep-sourced internal pore pressure increases are unlikely to be the sole contributor to massive volcanic flank collapse. This is because the pressure increases predicted for this to happen are unrealistically high, and would cause substantial degradation of the surrounding rock mass, ultimately reducing the pore fluid pressures through increasing pore space volume (porosity) and hence negating the effect of the increased pressure all together.

While the two methods were in agreement on the points discussed above, the geometries of the potential failure surface were slightly different for the two methods. The prescribed, circular nature of the potential failure surfaces analysed in the LEM almost certainly precludes the exact location and geometry of a potential failure surface being identified. The finite-difference method employed in the *FLAC*^{3D} modelling does not suffer this limitation and identifies the potential failure surface automatically, without any input as to its location from the user. This results in a more realistic shape of the potential failure surface (Fig 6.17), which, rather than exhibiting the shape of a perfect arc in profile, has a flatter bottom section (Okubo, 2004). This is an important difference from a hazard mitigation perspective as potential discrepancies in the geometry of a potential failure surface determined using 2D LEM would lead to miss-estimations of collapse volumes.

The results of the *FLAC*^{3D} modelling highlight that while deep-seated internal pore fluid pressures can act to destabilise entire volcanic flanks, it is the structural setting of the volcano that dictates how this effect manifests. Tibaldi (2004) clearly links the stress field within a volcano, and

specifically changes in the stress field to sector collapse. This link is also evident within the results of the *FLAC^{3D}* modelling. Increases in pore fluid pressures alter the stress field within a volcano by reducing the effective stress. Since the model geometries examined in *FLAC^{3D}* were slightly different the stress field in each model was also slightly different and the response to decreasing the effective stress varied for each geometry. A critical process which determines how pore fluid pressure increases affect the stability of an edifice appears to be volcanic spreading. Model geometries that were able to spread efficiently (i.e. the weak model geometry) achieved a more stable shape, hence reducing the gravitational forces acting to shear the slope. Model geometries that were unable to do this (e.g. the steep model geometry) did not reduce the shear stresses acting on the slope to the same degree and were considerably more affected by simulated increases in pore fluid pressure, leading to a much greater risk of failure.

7. Summary and conclusions

7.1 How strong is a volcano?

In Chapter four it was shown that the answer to the above question is "not very". Rock mass strengths calculated using the method outlined in Chapter four (from field data collected in volcanic terrains) are sufficiently weak to allow the development of pronounced instability in both LEM and three-dimensional finite difference modelling. These strengths however, represent a maximum value. Studies of volcanic rock mass strengths, such as presented within this thesis and those of Thomas *et al.* (2004b) and Okubo (2004) tend possibly to overestimate the strength of the materials. This is because these studies include the rock mass as a whole, and make no assumptions about failure on embedded planes of weakness such as joints or fractures (Moon *et. al.*, 2005). Since it is the natural behaviour of a slope to achieve a zero gradient, any slope will take the path of least resistance to failure. Embedded planes of weakness offer such a route, and the method of construction of any volcanic edifice suggests that these weaknesses will always be present within a volcano. The likelihood of failure arising from the effects of internally elevated pore fluid pressures is therefore possibly greater than that modelled within this thesis as there will be regions of the volcanic rock mass weaker than any considered during the course of this investigation.

7.2 The role of internal pressurisation

This project laid the groundwork and examined the theory behind instability generated through increases in deep-sourced pore fluid (gas) pressure. The numerical modelling (both 2D and 3D) validated this theory using ideal circumstances and uniform strength properties. However, the analogue modelling suggested a more complicated relationship, and the assessment of volcanic lithologies using rock mass classification schemes suggested that volcanic rock mass strength, while inherently weak, is not uniform within a volcano (Figs. 4.7 and 4.13). It is difficult to directly compare the three methods used to reach this conclusion (analogue sand-pile modelling, 2D LEM and 3D finite difference modelling) as the results of each method are presented in very different ways. The analogue modelling resulted in physical deformation of the model but provided no

numerical index of stability, and as discussed in Section 6.4.1, 2D LEM provided an explicit solution while the $FLAC^{3D}$ numerical method did not and is dependent on user interpretation. However, if the results are compared from a morphological perspective they all appear similar. All display a deep, arcuate mode of failure with both the analogue and finite difference modelling indicating large, concave collapse scars similar to those seen in nature (e.g. Mount St. Helens (Voight, 2000)). While there is a broad morphological similarity, there are variations between the types of modelling with regard to the volumes of potential failure. These differences are purely a result of the three dissimilar methods used and do not offer any insight into possible fundamental differences in the role of internal pressurisation. For example, as discussed in Section 6.4.1 the 2D LEM do not account for the lateral resistant forces acting on the assumed planar 2D failure wedge. Therefore the failure wedge is able to move more freely than it would be in a fully 3D model. As a result, the predicted potential critical failure surfaces suggested by the LEM are slightly deeper than those predicted in the $FLAC^{3D}$ modelling. However, the role of internal pore fluid pressurisation is identical in both cases.

The specific mechanisms of generating and increasing pore fluid (gas) pressures were not directly under investigation during the course of this project. However, assuming that a significant build up of such pressures (10–20 MPa) is feasible, it has been shown that deep-sourced internal pore fluid pressure accumulation can indeed be influential in generating deep-seated volcanic instability. This has profound implications. While large-scale sector collapse is now recognised as part of the natural cycle of volcano growth, the processes responsible may vary considerably (Chapter two). However, at all *active* volcanoes there will be one constant. This is the production of gas, either in the form of exsolved magmatic volatiles water vapour from the de-hydration of hydrothermal systems. For most volcanoes it is likely that both are at work. Having shown that the increase of pore fluid pressures from a deep source can decrease the stability of a volcanic edifice, it appears reasonable that this process may drive an edifice to a state of criticality such that it becomes particularly susceptible to internal or external perturbations. This underlying mechanism for generating instability will be present at all volcanoes at some stage during their evolution.

The results presented within this thesis make it unlikely that the initiation of large-scale flank collapse is caused solely from the effects of increased internal pore fluid pressures, as the pore

pressures required appear unfeasibly large. One exception would be a drastically weakened rock mass. Estimates of the critical pressures required for wholesale failure from the results of both LEM and three-dimensional finite difference modelling suggested values *at least* in excess of 20 MPa. Although theoretically the build up of pore fluid (gas) pressures is limitless, providing that the gas source remains active and is supplying the same volume of pore space, these required pressures are unlikely to be reached. At pressures approaching and in excess of 20 MPa the tensile strength of the surrounding volcanic country rock will almost certainly be exceeded. This will lead to fracture nucleation, propagation, an increase in volume and ultimately a loss of pressure, especially if the fracture network breaches the surface. This effectively short circuits the internal pressurisation effect, and it is therefore proposed that the role of internal pore fluid (gas) pressure is one of *destabilisation* rather than a full-scale triggering of a collapse event.

Both the numerical methods used in this thesis were constructed in such a manner as to allow for the significant build up of deep pore fluid pressures in a concentrated area. In nature however, this may not be the case, and will depend on three main factors:

1.   The sustained or rapid high-volume generation of volcanic gases from a deep source.

2.   The ability for these gases to accumulate along pathways or in regions of pore space within the edifice to increase the internal pressure.

3.   The presence of a low permeability region that inhibits the migration and expansion of gas and allows substantial pressure build up.

Given that a source of gas is fundamental to the generation of internally sourced pore fluid pressure increases, edifice permeability is most crucial to the theory being tested here. If the permeability of the rock around the gas source is low enough, extremely high pore pressures can develop independent of distinct permeability barriers. In this case however, the probable outcome is massive local fracturing of the rock mass, a sudden increase in permeability and rapid drop in pressure. If the permeability is too high then it would be impossible to generate high pore pressure and as noted by an associate (C. Davies, pers. comm. 2002) "*It would be like trying to pressurise a tea bag by blowing into it*". The case of high permeability is particularly problematic. The work presented in Chapter four highlighted the ubiquitous presence of fractures in volcanic rocks; this

suggests a high permeability and indicates that it may be unlikely for the significant build up of pore fluid pressures. However, even within a fracture network many kilometres long with gas actively flowing through it to the surface, the pressure will *not* be insignificant. If the gas supply rate is large enough at depth, even with a connected flow pathway to the surface, the effect may not significantly decrease pressures at deep levels. This is exemplified by the fact that fumarole fields can be sustained at supersonic speeds for many years. The simple analogue sand-pile models demonstrated that even small changes within the structure of an entirely granular material are enough for high fluid pressures to be generated. A volcanic edifice is a vastly more complex structure offering many more ways in which permeability can be reduced, leading to increases in pore fluid pressures.

7.3 Internal pressurisation and other factors contributing to instability

The results of the *FLAC^{3D}* modelling indicated that the initial stress state (prior to any increases in pore fluid pressures) of a volcanic edifice dictates how the effects of increases in pore fluid pressures manifest. As outlined in Section 2.6 there are many factors at work inside and around volcanoes that act to destabilise and hence alter the stress field within the edifice. With the exception of the points discussed in detail below (Sections 8.3.1 and 8.3.2), from the work conducted as part of this thesis it is not possible to comment on the relevant importance of each process/condition. However, as increases in pore fluid pressures act to reduce the effective stress acting on *any* potential failure surface (where elevated pressures are present) the apparent strength of *each* destabilising factor discussed in Section 2.6 would be magnified by any increase in pore fluid pressures. Thus, for any volcano where there is a capability of generating internally elevated pore fluid pressure, increases the destabilising effect of any pre-existing weaknesses *will* be exaggerated by increases in pore fluid pressure.

The analogue, LEM and finite-difference modelling all assumed *deep* sources of pore pressure. So, what can not be commented on with certainty in light of the results of the modelling work conducted in this project is the event of forceful and *shallow* magma intrusion acting as a trigger. A similar response is expected as a result of increasing pore fluid pressures through direct separation of gas from the magma. However, the effect is anticipated to be both more pronounced and rapid. This is because the confining stresses at higher levels within the edifice are significantly reduced, meaning

that the effective stress would also be much easier to reduce. A pronounced effect relating to thermal pore fluid pressure increases would also be expected as the temperature difference between the intruded magma and pre-intrusion pore fluids would be relatively large. In addition, ground deformation related to the shallow intrusion may also locally reduce flank stability. It is therefore considered that internally elevated pore fluid pressures would have an even greater effect when generated from a shallow source. However, the listed effects of such a shallow magma intrusion are quite likely to be severe enough to cause some form of eruption, shortcutting any potential collapse events.

Three of the conditions discussed in Section 2.6 were specifically examined in the $FLAC^{3D}$ modelling: the presence of a weak, deformable substrate; over-steepened slopes and the effect of a pronounced regional gradient. The importance of these three conditions is discussed in Sections 7.3.1 and 7.3.2.

7.3.1 The effect of changing edifice slope angles

The differences in the frequency and size of collapse events at composite and shield-like volcanoes have been discussed in Chapter two. They are of interest here as the results of the three-dimensional finite difference modelling suggest that as with geologic observations, composite volcanoes tend to have smaller but more frequent collapse events, e.g. Mt. Augustine (Siebert *at al.*, 1995) and Stromboli (Apuani *et al.*, 2005). Figures 6.15a and 6.15d show the factor of safety for the normal geometry and the steep geometry at 20 MPa. Even though the pressure source is defined as deep, almost the entire upper cone in the steep model geometry shows a significant reduction in stability when compared to the model state with no simulated pore fluid pressures. This effect is also to a greater degree than the destabilising effect exhibited in the normal geometry models. However, in the steep model geometry, a smaller total volume of the edifice is shown to suffer substantial reductions in the factor of safety. Increasing the pore fluid pressures from a deep source has the consequence of almost completely destabilising the steep upper cone in the steep model geometry and, in the tilted weak and steep model geometry has reduced the factor of safety to a value approaching unity. This indicates that small volume collapses on the upper flanks of steep sided composite volcanoes may be fairly regular (geologically speaking) occurrences.

On the other hand, increasing the pore fluid pressures from a deep source in the normal model geometry produced a wide spread, but less dramatic reduction in stability. Even though the destabilising effect is less pronounced in the near surface regions it follows that if conditions within the volcanic rock mass are favourable, and an appropriate triggering event occurred, the potential exists for massive flank collapse on a scale *much* larger than that of the steep model geometry. This is because the volume of material above the potential failure surface is much greater (Fig 6.16a). This would be analogous to the massive but less frequent flank collapses of the giant oceanic shield volcanoes e.g. Hawaii (Garcia, 1996; Okubo, 2004), Reunion Island and James Ross Island, Antarctica (Oehler et. al., 2004).

By modelling the effects of increasing volcanic pore fluid pressures and changing the model geometries, is appears, strong correlations can be made with observations of volcanic collapse in nature.

7.3.2 The effects of regional gradients and weak foundations

Many authors have cited regional gradients and/or weak foundations as important factors in the generation of volcanic instability (e.g. van Wyk de Vries and Francis, 1997; Wooller *et al.*, 2004; Acocella, 2005). The three-dimensional finite difference modelling also suggests that the role of the sub-volcanic edifice geology is important. From the results of the three-dimensional numerical models, it becomes clear that the presence of a weak foundation significantly heightens the effect of increasing the pore pressures (Figs 6.11b-6.15b), more so then any other perturbations to the basic normal model geometry. The most striking effect of increasing pore pressures in all three-dimensional models developed in this thesis was to cause deformation of the edifice through a period of inflation/spreading. For weak foundations, this deformation occurs both more efficiently and to a greater extent. As a result, instability is greater compared to models with the same overall shape but resting on strong foundations (Fig. 6.15 a and b).

Within the *FLAC^{3D}* modelling the effect of the regional gradient was as expected, to impart an asymmetry to the results of an otherwise symmetrical model. The destabilising effect of increases in the pore fluid pressure was amplified in the down slope direction. This is an effect of the regional

gradient causing an additional downslope gravity-driven instability within the edifice. The superimposed effect of the additional gravity-driven instability appears to have more of an effect at lower pore fluid pressures. This can be seen from comparing Figures 6.13e and 6.15e. The asymmetry in the distribution of the destabilised areas is much more pronounced at 5 MPa (Fig. 6.13e) compared to 20 MPa (Fig 6.15e). The reason for this is because at higher induced pore fluid pressures, the destabilising effect as a result of the elevated pressures is far greater than the gravity-driven effect. The gravity-driven effect is therefore masked by the overall level of instability caused by the high pore fluid pressures.

Unfortunately this interpretation can not be conclusively backed up by the analogue modelling. While the effect of substrate angle was modelled, with the exception of the steepest angle considered, it appeared to have little effect. All the sand pile models resting on a substrate angle of 23° (the steepest angle modelled) experienced some form of lateral failure (Table 5.2), with models resting on slope angles less than this appearing to behave independently of the substrate geometry. This does imply a tentative agreement with the results of the $FLAC^{3D}$ modelling that steeper substrate angles impart a greater probability of failure in response to internal pore fluid pressure increases. However, the fact that there is no apparent increase in the probability of failure within the analogue sand-pile models over the substrate angle range of $5 - 16^o$ precludes this relationship being clear-cut.

The relationship between regional gradients, weak foundations and the edifice is a significant one; it is unlikely to find a volcano resting on a perfectly horizontal sub-stratum and consisting of entirely "fresh", non-altered rock. Instead most will be resting upon relatively weak and inclined foundations, including the possible low strength horizons such as marine substratums, hyaloclastites or volcaniclastic deltas of oceanic hot-spot volcanoes (Oehler *et. al.*, 2004). This indicates the role of the sub-volcanic basement is especially important, and worthy of future in-depth research.

7.3.3 Enhancement of triggering mechanisms

As discussed in Section 3.4 internal pore fluid pressurisation was considered a prime mechanism for driving a volcanic edifice towards a critical state, in which it may be particularly susceptible to large-scale, deep-seated collapse events. The results of the modelling work conducted as part of this thesis unequivocally confirm this assumption.

In each of the model geometries examined in *FLAC^{3D}*, for each pressure increase, the overall stability of the model was reduced. This destabilising effect imparted its greatest strength deep within the edifice, decreasing in magnitude radially away from the pressure source. Any of the triggering mechanisms discussed in Section 2.6 (Table 2.2) would therefore be enhanced deep within the edifice due to the already reduced stability. In particular external (possibly remote) seismic triggers may play a pivotal role in the triggering of large scale volcanic flank collapse promoted by elevated pore fluid pressures. This is because a seismogenic event external to the edifice would have little relative effect on the stress field within the volcano, meaning that any destabilising effect caused by the event would be additional to those being already experienced. This differs from possible endogenic triggering events. While it is stated at the start of this section that the effects of internally elevated pore fluid pressures are concluded to enhance all triggers, they would do so to different extents. In contrast to external triggers, an endogenic triggering event such as dyke intrusion, which has been suggested by numerous authors, e.g. Iverson (1995) and Voight and Elsworth (1997), would both fundamentally alter the stress field within the edifice and possibly change its physical geometry (i.e. inflation/faulting). These changes may reduce the pre-existing destabilising effect of elevated pore fluid pressures, hence diminishing its additional effect. The heightened state of instability due to deep sourced pore fluid pressure increases was demonstrated by anecdotal evidence from the analogue modelling. Experiment No. 23 (Table 5.2) suffered instantaneous and volumetric collapse in response to a sharp tap on the model substrate. This is analogous to the expected response of a volcanic edifice in a critical state due to increased pore fluid pressures being subjected to a large external earthquake.

7.4 The threat of internally elevated pore fluid pressures at a real volcano

Although no individual volcano has been specifically modelled in this thesis it is a useful exercise to apply the results to a particular edifice in order to demonstrate the potential vulnerability of volcanic edifices to the threat of internally elevated pore fluid pressures. The results are therefore applied to the island of Tenerife, specifically the Teide-Pico Viejo complex that currently occupies the Las Cañadas caldera depression. Tenerife was chosen as it has well documented history of lateral collapse, (Navarro and Coello, 1989; Cantagrel *et al.*, 1999; Ablay and Hürlimann, 2000; Hürlimann *et al.*, 1999; 2001) and it was shown in Chapter four that the strength of the volcanic rock masses on the island are sufficiently weak as to permit the possibility of failure influenced in part, by internal pore fluid pressure increases.

The Teide-Pico Viejo complex is affected by all three of the destabilising factors discussed in detail in Section 7.3. The complex suffers from high slope angles; the possibility of a weak hydrothermally altered core; it is underlain by weak, easily deformable debris avalanche deposits to the north and is in part built directly over the dipping north flank of the island. A geomorphological analysis of Tenerife conducted by Hürlimann *et al.,* (2004) demonstrated slope angles for the Teide-Pico Viejo complex in the range of $20^{o} - 30^{o}$ degrees with angles locally in the region of $30^{o} - 40^{o}$. The same analysis also characterised the northern part of the island above an altitude of 500 m as having a relatively uniform slope angle of about 11° continuing up to (and hence interpreted here as beneath) the Teide-Pico Viejo complex. This certainly demonstrates high slope angles and a dipping substratum beneath the Teide-Pico Viejo complex, and suggests that any destabilising effects imparted by these conditions should be experienced. The northern part of the island is also in part, constructed of at least three extensive breccias interpreted as debris avalanche deposits (Cantagrel *et al.*, 1999). These breccias are up to 200 – 300 m thick and consist of fragmented volcanic material within a clay rich matrix (Navarro and Coello, 1989), and would provide a substratum similar in nature to the weak substratum modelled in $FLAC^{3D}$; a similar destabilising effect in therefore also interpreted. In addition to the presence of these easily deformable layers a shallow hydrothermal system is interpreted for Tenerife (Araña *et al.*, 2000; Almendros *et al.*, 2007). This hydrothermal system could possibly encompass some of the Teide-Pico Viejo complex and may contain large proportions of clay minerals. If this is the case it may act as a weak core

(e.g. Cecchi *et al.*, 2005) and would cause a similar destabilising effect as a weak, easily deformable substratum. From the location of the current Teide-Pico Viejo complex it is also the author's interpretation that any volcanic spreading would be severely restricted in the southern direction due to the presence of the Las Cañadas caldera wall. This inability to undergo efficient spreading would compound any other destabilising effects.

It is apparent from the factors discussed above that the Teide-Pico Viejo complex is subjected to a number of conditions that promote structural instability. It is ominous then that the potential exists for further reduction in stability due to the effect of internally sourced pore fluid pressure increases. During April - May 2004 a series volcano-tectonic (VT) earthquakes were recorded at three seismic antennas deployed within the Las Cañadas caldera (Almendros et al., 2007). These VT events were interpreted as a response to an injection of basaltic magma at a depth of below 14 km under the north-west flank of the island (Almendros et al., 2007). Upward-migrating volatiles exsolved from the intruded magma were interpreted to produce lubrication of fractures at *shallow* levels within the edifice resulting in the onset of period of sustained volcanic tremor recorded on the 18th May 2004 (Almendros et al., 2007), approximately 40 – 50 days after the initial magmatic intrusion. This demonstrates the ability of deep magmatic intrusion to generate gas that is (a) able to propagate the entire way to the surface and (b) impart a significant mechanical effect at distances far from the source. It also raises the possibility that if the migratory pathways of the gas become impeded, or in the case of an overall higher gas flux (resulting from a larger intrusion or a shallower intrusion causing the retrograde boiling of the shallow hydrothermal system) that sufficient pore fluid pressures may be generated to threaten the possibility of whole-scale flank collapse of the edifice.

7.5 Main conclusions

From the work presented within this thesis the following conclusions are drawn:

1. Through the use of geomechanical classification schemes the constituent parts of a volcano can be considered as an equivalent continuum i.e. a rock mass.

2. Provided the intact strength of a rock is well constrained through laboratory testing, it is possible to estimate the strength parameters of a volcano through use of an empirical

relationship involving the RMR system, and that these strengths are far weaker than those of the intact rock.

3. Deep sourced, internal pore fluid (gas) pressure increases can play a significant role in destabilising a volcano flank.

4. The Analogue sand-pile models demonstrated that even small differences in the hydraulic properties of an edifice can dictate how it responds to internal pressurisation.

5. Increases in internal pore fluid (gas) pressure is unlikely to be the sole contributor to wholesale collapse of a volcanic flank unless pressures in excess of 20 MPa are able to be generated.

6. If a volcano is *substantially* weakened (hydrothermal alteration or other rock mass disturbance), internal pressurisation *may* trigger a collapse event.

7. The effects of regional slope and underlying substrate can impact adversely on the overall stability of a volcano. The latter provides a potential feedback mechanism that can aid in the process of volcanic spreading.

8. *FLAC^{3D}*, combined with routine geotechnical rock mass classification provides a robust working methodology for investigating volcano instability.

7.6 Further work

The 3D numerical results are very encouraging and help lay the foundation for further more detailed work. The next upgrade of *FLAC^{3D}* (version 3.0) will bring yet more computational sophistication to help model the processes that govern volcano instability. Version 3.0 runs approximately 10 -20 % faster than pervious versions of *FLAC^{3D}* and the inclusion of a Hoek-Brown constitutive model means that model solve times will be greatly reduced, allowing more complex models to be examined.

The next step is to create the three-dimensional models in *FLAC³D* using additional real world data. There are three particular areas of the three-dimensional models presented in Section 7.3 that could benefit from the inclusion of real world data:

1. Geometry: the use of digital elevation models as the basis of the finite-difference grid, allowing image-based computer modelling of specific volcanoes.

2. Mechanical: the inclusion of detailed geotechnical and hydraulic properties of the rock mass comprising an individual volcano in true spatial orientation.

3. Planetary Geology: The transposition to the study of volcano instability on other planets.

Topographic data can be introduced through the use of digital elevation models. More and more data of this kind is becoming readily available and the inclusion of real world topography would greatly enhance any use that this type of work may have in hazard assessment.

The use of hydraulic properties *requires* attention, as without reliable estimates of the hydraulic properties of a volcano's interior there can be no further development of the internal gas pressure hypothesis. This point was discussed briefly in Chapter three, and is deserving of a fuller discussion here. To date, very few quantitative studies of the engineering properties of volcanic rocks have been conducted (e.g. Schultz, 1995, Thomas *et al.*, 2004b, Okubo, 2004, Moon *et al.*, 2005), with even fewer studies relating to the hydraulic properties of a volcanic rock mass existing in the literature (e.g. Llewellin *et al.*, 2005; Vinciguerra *et al.*, 2005b; Gonnermann *et al.*, 2007). Even where this data does exist, it is subject to many assumptions, and rarely offers a complete picture of all the variables (Moon *et. al.*, 2005). In addition to a requirement of better understanding of the physical (strength and hydraulic) properties of a volcanic rock mass, the distribution and interaction of its constituent parts also needs greater in-depth study, as these interactions may play a pivotal role in the development of elevated pore fluid pressures.

A key assumption of this thesis is that degassing is considered to be pervasive throughout the edifice. While this assumption has shown that it is theoretically possible to generate an enhanced degree of instability from internally generated pore pressure increases, the case of a uniform pressure increase within the edifice is probably unrealistic. This is due in no small part to the

variability of the permeability and porosity of volcanic rocks. Gonnermann *et al.*, (2007) suggested a very large range in permeability, implying that complex outgassing behaviour of magmatic systems should be expected in nature and that it would be improbable to have uniform hydraulic properties throughout the edifice. In addition, the geometry of any enhanced pressure field will rely on the geometry and position of the gas source (be it a body of magma and/or an active hydrothermal system), the geometry and nature of any possible gas conduits that may channelise flow to the surface, and the distribution of any reduced permeability barriers such as regions of the rock mass containing a high proportion of clay minerals. These issues can only be addressed through detailed field mapping, laboratory testing of volcanic rocks, and both field and laboratory monitoring and modelling of volcanic degassing.

The inclusion of either real world topography or accurate hydraulic properties into the three-dimensional models will have a profound effect on the understanding of the processes that govern volcano instability. Further thought also needs to be given to the relative importance of magmatic gas-sourced pressurisation and hydrothermal system contributions. Reid (2004) has shown that the contribution from hydrothermal systems alone potentially threatens the mechanical stability of volcano edifices. This effect must, at a very minimum, be amplified by the consideration of the additional destabilising effect caused by magmatic gas-sourced elevations in pore fluid pressures. However, the additional effect of the two contributions to pore fluid pressure increases may be limited, as in theory they could act on varying time scales. Direct magmatic gas-sourced pressurisation would have an immediate effect as new pore fluids are being generated and introduced to an already pressurised system. The hydrothermal system contribution relies more on the heating of pre-existing pore fluids, which would not raise the pore fluid pressure so rapidly. Depending on the hydraulic properties of the volcanic rock mass the peak effect of the two identified contributions may not coincide. As the hydrothermal system contribution is also highly dependent on temperature, the depth of the system may also play an important role. This is because if the system is too far from the surface the effect may not reach high enough levels (due to cooling) to cause a threat to stability. Conversely, once magmatic gases are exsolved (regardless of depth) and enter the country rock, they continue imparting a pressure on any pore space they occupy until they escape to the atmosphere.

A planetary perspective can be achieved simply through changing the variables with $FLAC^{3D}$, namely the value for gravity. Instability has been identified on other planets (McGuire *et al.*, 1996) and the methodology outlined in this thesis has the ability to study it further.

An important role in volcanic studies is to better understand the behaviour of a volcano in order to predict its future eruptions and help save the lives of any people that may be affected by that event. This study provides the basis for such work concerned with the predicting of failure volumes leading to the prediction of down slope routing and hence hazard analyses of volcanic flank collapse events. Although the three-dimensional models presented in this thesis are essentially simple symmetrical cones that were used to test the validity of the theory, the potential exists to generate much more complicated geometries. This is particularly true considering the latest addition to the $FLAC^{3D}$ program suite. 3D-Shop, a geometry modelling and automatic meshing option for $FLAC^{3D}$ allows the latest version of $FLAC^{3D}$ to use real world topography to generate the finite difference grid. This combined with detailed mapping of any particular volcano and the use of geophysics to interpret the internal structure allows the potential for a new level of realism. By employing the techniques used with in this thesis with the new powers of mesh generation, the ability to accurately predict regions of potential instability and also the potential volumes of a collapse could become routine, providing of course that the relevant data is available.

It is on this point that the use of $FLAC^{3D}$ as a *monitoring* tool falls short. The time and cost involved with the generation of an accurate real topography mesh and the derivation of accurate model properties rules this technique out for day to day monitoring. For a high level of realism in the model geometry a very large mesh must be generated, and the solve time associated with such a large model grid would also compound the incompatibility of this technique with assessing daily changes. Therein lays the benefit of the simplified 2D approach, for which calculations can be completed in a matter of minutes to a few hours depending on their complexity. However, if large and obvious changes occur to a volcanic flank, providing the user is proficient in the use of the $FLAC^{3D}$ programming language (FISH) and failure is not considered imminent (on the time scale of less than 24 hours). It would be relatively straight forward to modify specific regions of the finite difference grid to reflect observed changes in topography and to assign regions within the grid different properties based on surface observations as to the quality of the rock mass and

geophysics as to internal structure changes. These modifications can also be made to pre-existing, saved simulations, hence preserving the stress state and previous regions of instability identified for the original model.

Predicting future collapse however, is a different story. Regardless of other circumstances failure will occur in the weakest part of the volcano. Provided the data used within the *FLAC^3D* model is sufficiently accurate this technique should readily and *automatically* identify these potential areas of instability. In addition, using the outlined 3D methods the *actual* geometry of any potential failure surface and the associated volume of that potential failure may also be predicted. This is beneficial to any hazard assessment of a volcano as the volume of a collapse has implications for the effects of the associated debris avalanche.

It is also routine to monitor the gas flux of a volcano, particularly when it is threatening to erupt. As a result valuable information about the rates and volumes of magma gas-sourced internal pore fluids could be gained on a regular basis. This could lead to more accurate modelling of the depth and size of magma bodies required to generate enough "gas" to significantly raise pore fluid pressures. This is of particular interest to the author. The scope of this project is enormous and although within this thesis substantial ground work has been clearly laid down, only the surface has been scratched. The potential for increases in internal pore fluid (gas) pressure to generate deep seated instability has been established in theory. The next step is to model a real world volcano using real world data and see if the hypothesis holds true in nature.

Appendices

Appendix A – Previous publications

Appendix A contains publications summarising research results undertaken during this study.

Volcanic rock-mass properties from Snowdonia and Tenerife: implications for volcano edifice strength

MARK E. THOMAS[1], NICK PETFORD[1] & EDWARD N. BROMHEAD[2]

[1]*School of Earth Science and Geography, Centre for Earth and Environmental Science Research, Kingston University, Penrhyn Road, Kingston upon Thames KT1 2EE, UK (e-mail: markthomas@kingston.ac. uk)*
[2]*School of Engineering, Kingston University, Penrhyn Road, Kingston upon Thames KT1 2EE, UK*

Abstract: Although volcano instability is increasingly recognized as a societal hazard, numerical data on the relevant mechanical properties remain sparse. We report new field data on the rock-mass properties of volcanic materials from Snowdonia (North Wales, UK) and Tenerife (Canary Islands). Using rock types that range in composition from phonolite to rhyolite, we summarize a method for estimating the overall strength of a volcanic edifice based on the rock-mass rating index (RMR) and the Hoek–Brown criterion. We show that the average rock-mass compressive (σ_{cm}) and cohesive (c) strengths decrease exponentially with RMR according to $\sigma_{cm} = 0.652^{(0.0559RMR)}$ and $c = 0.035^{(0.0669RMR)}$, respectively, and appear insensitive to both initial magma composition and relative age. This exponential relationship provides a new predictive tool for directly estimating rock-mass strength from the RMR. Our analysis further predicts a marked reduction of up to 96% in the rock-mass compressive strength relative to the intact rock value based on laboratory tests and that, overall, the combined results from both study areas yield cohesive strength values from 4.8 to 0.44 MPa. Estimated values of rock-mass angle of friction range from 28° to $c.$ 38°. Recent modifications to the Hoek–Brown criterion, in particular the inclusion of the disturbance factor D, suggest that even these low values of rock-mass strength and cohesion may be optimistic, and the true values of rock parameters relevant for accurate predictions of volcano edifice strength may be up to 30% weaker still.

Keywords: rock failure, rock mechanics, volcanic hazard, geotechnics.

A growing number of studies over the last decade have helped raise awareness of the life- and property-threatening hazards that result from volcano instability (e.g. Tilling 1995; McGuire *et al.* 1996; Siebert 1996; McGuire 1998; Thomas *et al.* 2004). However, although improved models of the processes leading to volcano instability have helped increase our understanding of events that can lead to catastrophic edifice failure, data on the physical properties, in particular the strength and cohesion of volcanic rock masses crucial for informed modelling of the collapse process, remain sparse. At its most basic level, a volcanic edifice is made up from discrete layers of different rock types cut through on a range of scales by pervasive and penetrative discontinuities including faults, fractures and contact surfaces (Fig. 1), making it difficult to assign an overall strength. Characterization of the rock mass can be further hindered by long time gaps in volcanic activity that result in the development of residual soils (Hürlimann *et al.* 2001), and hydrothermal alteration, where the rock is chemically altered primarily to clay minerals (Crowely & Zimbeman 1997; Reid *et al.* 2001). Both residual soil and hydrothermally altered material will cause a decrease in the strength properties of an edifice relative to its unaltered state. However, it is our intention to show that even without these degrading effects, a volcanic rock mass, and by implication the edifice itself, is an inherently weak structure when compared with the intact strength of its constituent rocks.

This paper summarizes an approach for estimating the strength characteristics of a volcano based on well-known techniques used in rock-mass classification at the outcrop scale and larger. We begin by reviewing the various classification schemes, and show how field data on volcanic rocks, combined with relevant Mohr failure envelopes, can be used to make estimates of important material variables including rock-mass strength, rock-mass cohe-sion and instantaneous angle of friction. We finish by considering the implications of a new term in the Hoek Brown criterion that relates the degree of rock face disturbance (D) to the rock-mass rating (RMR). A provisional sensitivity analysis suggests that although the degree to which D affects a typical volcanic slope is unknown, a value > 0.5 will significantly affect the strength of the rock mass.

Rock-mass classification

Classification schemes such as the RMR form the basis of an empirical approach to estimating strength criteria and other rock-mass properties. Widely used in engineering, they have found applications in the stability analysis of tunnels, slopes, founda-tions and mines, and most recently, volcanic systems. At outcrop, a rock mass is an aggregate material consisting of intact material, associated discontinuities (such as bedding planes, faults, joints and solution surfaces) and any areas of alteration. The concept of a rock mass and associated classification schemes are powerful tools for estimating strength criteria on a large (decimetre) scale. Although several rock-mass classification schemes exist, the most widely used is the RMR system of Bieniawski (1976, 1989), and this is the scheme used for this study. Other classification schemes, including the geological strength index (GSI) of Hoek *et al.* (1992) and Hoek (1994), are discussed in a later section.

The RMR system

The RMR system uses five main parameters to classify the rock mass (Table 1), including the strength of the intact rock, the rock quality designation (RQD) of Deere & Deere (1988), the spacing
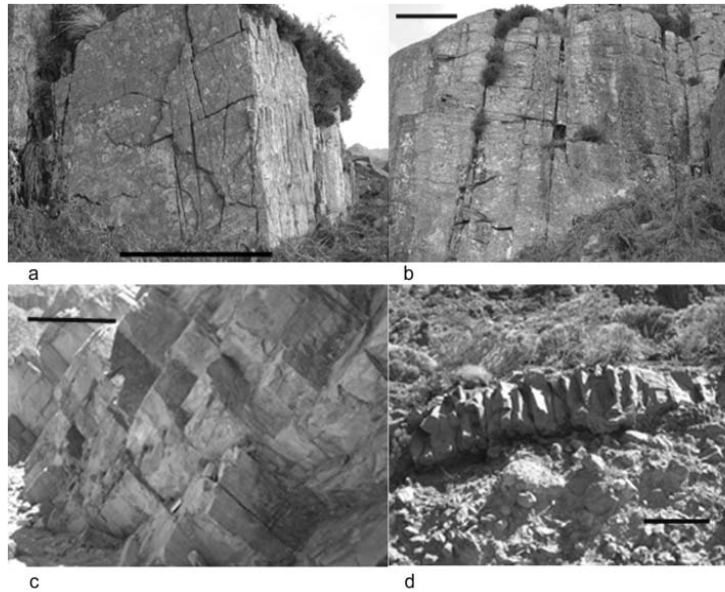
Fig. 1. Photographs from field locations showing the fractured nature of the rock mass: (a, b) Snowdonia (Wales, UK); (c, d) Tenerife. (d) shows a dense lava flow overlying a loose, poorly sorted debris deposit of pyroclastic material, which has been partially altered to a soil. If the weight on top of the weak layer is increased by successive flows, this unstable conformation of a stronger rock overlying a much weaker one is a prime site for the initiation of a future failure surface. In all photographs the black bar represents 1 m.

of discontinuities, the condition of the discontinuities and the groundwater conditions (Schultz 1995, 1996). By their nature, all rock masses are discontinuous, and a volcanic edifice is no different. Therefore to estimate the strength of an edifice it is necessary to first divide it into similar regions that can be assessed using Table 1. These descriptive classification schemes can be used to make predictions about the mechanical properties of the rock mass if used in conjunction with relevant empirical expressions. A particularly powerful combination involves an integration of the RMR and the Hoek–Brown criterion (Hoek & Brown 1980; Hoek 1983), devised to assess rock-mass strength (see below). For example, Schultz (1995, 1996) used RMR data in this way to show that the rock-mass compressive strength of basalt is up to 80% weaker than its intact compressive strength as measured under laboratory conditions. This result has important implications for volcano edifice strength, and is developed more fully in later sections using RMR data collected in this study.

Data collection

The RMR data presented here were collected from two field sites in Snowdonia (North Wales, UK) and Tenerife (Canary Islands). In total, five rock types were examined from a total of 42 field localities. Lithotypes sampled range in composition from alkali basalt to rhyolite (Table 2). With the exception of several microgranite samples from Snowdonia, the rock masses examined were exclusively volcanic in origin, and comprised a mixture of lava flows, dykes and airfall tuffs. Although a granitic rock is unlikely to be found on most volcanic slopes it is included in this study to demonstrate the potential weakness of all igneous rock masses. The volume of rock mass examined in each locality varied between locations, with surface areas ranging from 6 to 180 m². The Snowdonia volcanic province is mainly Ordovician in age (e.g. Owen 1979) whereas the units examined on Tenerife are generally < 4 Ma old and in some cases historical (Carracedo & Day 2002). The extensive time gap between the two field locations, one ancient and the other

geologically young, allowed us to assess the degree to which the gross age of the rock mass (climactic influences excluded) may have influenced the rock-mass strength.

At each locality the RMR was calculated according to the rating system detailed in Table 1. To gain a comprehensive overview of the rock-mass condition and characteristics, the RMR was calculated both horizontally and vertically for each segment of the examined rock mass. The horizontal and vertical RMR values were then averaged to give one RMR value for that region. This was done with the aim of producing an overall estimate of rock-mass strength rather than an estimate that may favour one particular orientation. A summary of the RMR values calculated for each rock type can be found in Tables 2 and 3. For simplicity, we have used the averaged RMR as determined for each rock-mass segment in this study. However, we accept that it may not be realistic to assign a single value, and that a range of RMR values may be more appropriate. We further caution that any stability analysis carried out with strength estimates determined by following the method presented in this paper should use the corresponding range of strength estimates in all calculations.

Estimating rock-mass strength

Hoek Brown criterion

Hoek & Brown (1980, 1988) proposed a novel method for estimating rock-mass strength that makes use of the RMR classification. The Hoek–Brown method, widely used by geotechnical engineers to predict rock-fracture behaviour at the outcrop scale, has recently found application in the strength assessment of volcanic rock masses (Voight 2000). The general empirical criterion for rock-mass strength proposed by Hoek & Brown (1980) is defined by the relationship between the principal stresses at failure:

$$\sigma_1 = \sigma_3 + (m\sigma_c\sigma_3 + s\sigma_c)^{1/2} \qquad (1)$$

VOLCANO ROCK-MASS PROPERTIES   941

Table 1. *The RMR classification parameters and their ratings (shaded), after Bieniawski (1989)*

Strength of intact rock	Uniaxial compressive strength, MPa	> 250	100–250	50–100	25–50	5–25	1–5	< 1
1.	Rating	15	12	7	4	2	1	0
	RQD, %	90–100		75–90		50–75	25–50	< 25
2.	Rating	20		17		13	8	3
	Spacing of discontinuities, m	> 2		0.6–2		0.2–0.6	0.06–0.2	< 0.06
3.	Rating	20		15		10	8	5
	Condition of discontinuities	Very rough, Discontinuous, No separation, Unweathered		Rough walls, separation < 0.1 mm, Slightly weathered		Slightly rough, separation < 1 mm, Highly weathered	Slickenslides or Gouge < 5 mm thick or continuous separation 1–5 mm	Soft Gouge > 5 mm thick Or Separation > 5 mm continuous, decomposed wall rock
4.	Rating	30		25		20	10	0
Ground Water	General conditions	Completely dry		Damp		Wet	Dripping	Flowing
5.	Rating	15		10		7	4	0

This table has been customized from the chart of Bieniawski (1989) to show only the methods used in this paper. RMR − 1 + 2 + 3 + 4 + 5 and ≤100.

Table 2. *A summary of the rock-mass properties obtained from volcanic rocks in the Snowdonia volcanic group and from Tenerife*

Property	Snowdonia			Tenerife	
	Rhyolite	Tuff	Microgranite	Basalt	Phonolite
RMR	52–74	47–74	57–79	48–60	38–60
Laboratory compressive strength (MPa)*	175	150	250	150	175
Rock-mass compressive strength (MPa)	12–41	7–35	23–78	8–16	6–19
Rock-mass tensile strength (MPa)	−0.29 to −1.5	−0.18 to −1.4	−0.3 to −1.55	−0.2 to −0.5	−0.1 to −0.5

*Values taken from Brown (1981).

Table 3. *A summary of the Mohr–Coulomb properties of the rock-mass obtained from volcanic rocks in the Snowdonia volcanic group and from Tenerife*

Property	Snowdonia			Tenerife	
	Rhyolite	Tuff	Microgranite	Basalt	Phonolite
RMR	52–74	47–74	57–79	48–60	38–60
Laboratory compressive strength (MPa)*	175	150	250	150	175
Rock-mass cohesive strength (MPa)	1.16–4.84	0.74–4.28	1.16–6.75	0.79–1.72	0.44–1.84
Rock-mass angle of friction (degrees)	31.3–38.1	27.8–36.1	41.2–49.4	28.1–31.8	28–34.9

*Values taken from Brown (1981).

where σ_1 and σ_3 are the major and minor principal stresses respectively at failure, σ_c is the uniaxial compressive strength of the intact rock, and m and s are empirical constants dependent on rock type and available from published sources (e.g. Hoek 1983; Hoek & Brown 1988). In this paper, standard values of σ_c determined from laboratory studies were taken from the reference library within the Rocscience program RocLab, but can also be obtained from numerous published sources (e.g. Brown 1981). For a given rock mass (Hoek & Brown 1988), the constants m and s are related to the RMR as follows:

$$m = m_i \exp[(RMR - 100)/28] \quad (2)$$

and

$$s = \exp[(RMR - 100)/9] \quad (3)$$

where m_i is the value for the intact rock. The special cases of unconfined compressive strength σ_{cm} and uniaxial tensile strength σ_{tm} for a rock mass can be found by putting $\sigma_3 = 0$ and $\sigma_1 = 0$ respectively into equation (1). Thus

$$\sigma_{cm} = (s\sigma_c)^{1/2} \quad (4)$$

and

$$\sigma_{tm} = \frac{\sigma_c}{2}[m - (m^2 + 4s)^{1/2}]. \qquad (5)$$

Results

Using the Hoek Brown criterion to estimate the strength characteristics of rock masses from Snowdonia (North Wales) and Tenerife (Tables 2 and 3) we find compressive strength reductions of up to 96% in the rock mass (σ_{cm}) relative to intact laboratory tested samples (σ_c). Table 2 also lists rock-mass

tensile strength obtained directly from the Hoek Brown equations. Figure 2 shows plots of rock-mass strength against RMR for the rock masses from Snowdonia and Tenerife. From Figure 2, it can be seen that the compressive and cohesive strength of the rock types examined in this study decreases exponentially with RMR according to

$$\sigma_{cm} = 0.652^{(0.0559RMR)} \qquad (6)$$

$$c_i = 0.035^{(0.0669RMR)} \qquad (7)$$

and appears largely insensitive to both the initial magma composition (basaltic or rhyolitic), and relative ages of the rock masses tested. This apparent exponential decrease suggests that relatively small changes in rock-mass properties will significantly affect edifice strength. This insensitivity to both rock composition and age suggests that these exponential relationships may be useful in providing quick and relatively accurate estimates of rock-mass strength directly from the RMR (Fig. 2). In Figure 2a, where the data for rock-mass compressive strength are plotted alongside the fitted exponential curve, the mean error between the actual value and that predicted by the exponential fit is 13% with a standard deviation of 9.6. However, if the imprecision of the RMR classification scheme is taken into account, this error falls to within an acceptable range, and provides a valid method of estimating, to a first approximation, rock-mass strength directly from the RMR. We note that this tentative exponential relationship also holds for tensile and rock strengths.
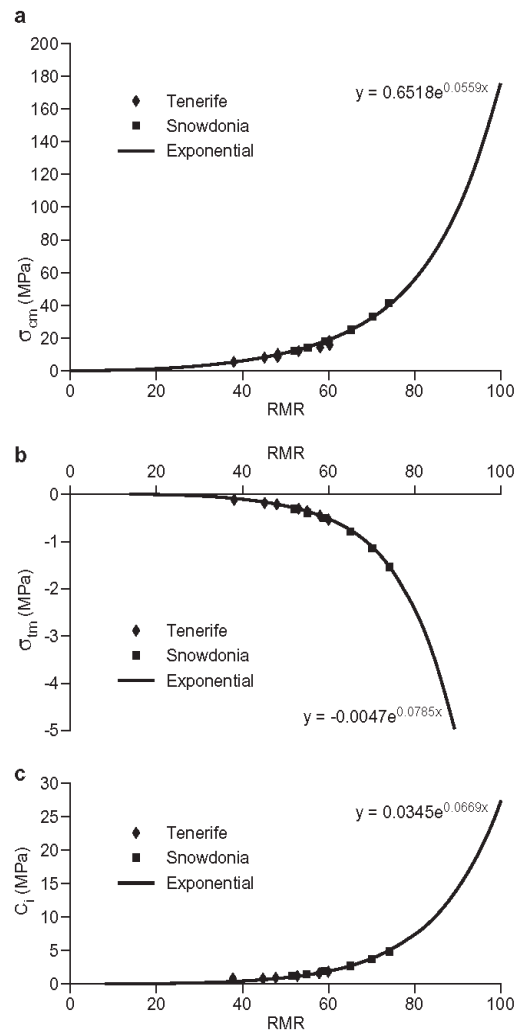
Mohr–Coulomb criterion

As it is the aim to use the estimated rock-mass strength properties in edifice stability studies, and most geotechnical software is still written in terms of Mohr Coulomb criterion, it is necessary to determine an estimated angle of friction and cohesive strength for the rock mass. A graphical means of representing stress relationships was discovered by Culmann (1866) and later developed in detail by Mohr (1882), which led to the implementation of a graphical method (the Mohr stress circle). Uniaxial tension, unconfined axial (uniaxial) compression, or confined (triaxial) compression may affect failure of intact cylindrical rock specimens. Typical examples of effective stress circles for these types of failure are shown in Figure 3. The envelope to the stress circles at failure (Mohr failure envelope) corresponding to the empirical failure criterion defined in equation (1) was derived by Bray (Hoek 1983) and is given by

Fig. 2. Dependence of rock-mass compressive (**a**), tensile (**b**) and cohesive (**c**) strength on RMR for lavas (basalt, phonolite and rhyolite) from Snowdonia and Tenerife. An exponential best-fit curve has the form $\sigma_{cm} = 0.652^{(0.0559RMR)}$. Similar predictive relationships also hold true for the rock-mass tensile and cohesive strengths.
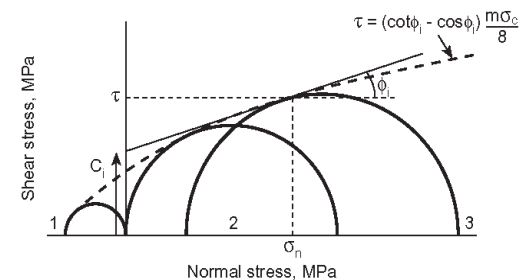

Fig. 3. Typical failure circles for rock and the Bray strength envelope (Hoek 1983): 1, uniaxial tension; 2, unconfined axial (uniaxial) compression; 3, confined (triaxial) compression. Also shown are the instantaneous values of angle of friction (ϕ_i) and cohesion (c_i).

$$\tau = (\cot\phi_i - \cos\phi_i)\frac{m\sigma_c}{8} \qquad (8)$$

where τ is the shear stress at failure, ϕ_i is the instantaneous friction angle at given values of τ and σ, i.e. the inclination of the tangent to the Mohr failure envelope at the point (σ_n, τ). The value of the instantaneous friction angle ϕ_i is given by

$$\phi_1 = \tan^{-1}[4h\cos^2(30° + \frac{1}{3}\sin^{-1}h^{-3/2}) - 1]^{-1/2} \qquad (9)$$

where

$$h = 1 + \frac{16(m\sigma + s)}{3m^2} \qquad (10)$$

at any given value of σ. Mohr failure envelopes for intact rhyolite and a rhyolitic rock mass are compared in Figure 4. As expected, the intact material is stronger than the jointed rock mass. Shear stress tending to cause failure across a plane is resisted by the cohesion of the material and a constant times the normal stress (σ_n) across the plane. This is expressed in the Mohr Coulomb equation for shear strength:

$$\tau = c + \mu\sigma_n \qquad (11)$$

where μ is the coefficient of friction:

$$\mu = \tan\phi. \qquad (12)$$

However, rather than being constants for jointed rock masses, c and ϕ both vary with stress level (Hoek & Brown 1980). It is thus convenient to calculate the instantaneous values for cohesion (c_i) using the instantaneous friction angle defined in equation (7). Thus equation (11) can be rewritten as

$$c_i = \tau - \sigma_n \tan\phi_i. \qquad (13)$$

Figure 5 shows a Mohr failure envelope (equation (8)) for a rhyolitic rock mass from Snowdonia, along with a plot showing the instantaneous friction angle (equation (9)) and instantaneous
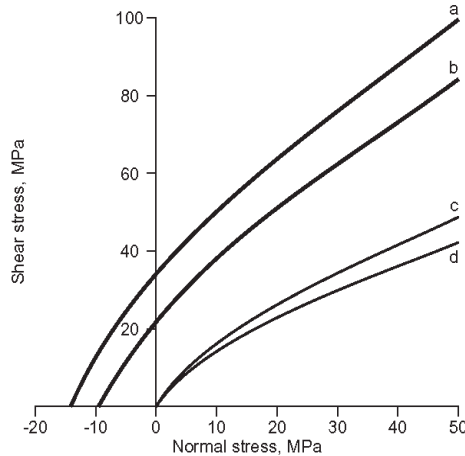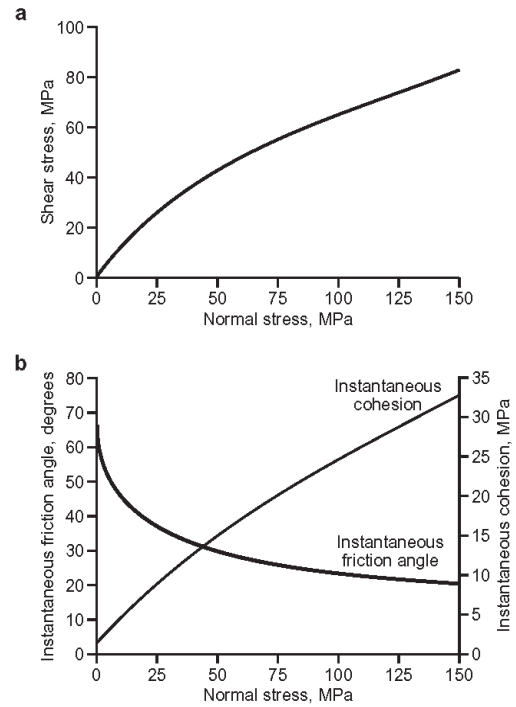
Fig. 5. (a) Mohr failure envelope for a rhyolite rock mass from Snowdonia; (b) plot showing the instantaneous friction angle and instantaneous cohesion.

cohesion (equation (13)). It can be seen that at low values of normal stress, the angle of friction is high and the cohesion is low. As the normal stress is increased, however, this relationship is reversed, suggesting an increase in cohesion but a decreasing angle of friction at progressive deeper parts of the edifice interior. This may be an important factor in determining the shape of a failure surface within a volcanic edifice, and could be a simple explanation for why non-volcanic slope failures tend to be shallow and steep, in that they lack any additional thermal and mechanical pore pressures that may precede volcanic slope failures. Although c and ϕ will vary with stress level, it is useful to fit a straight-line Mohr Coulomb relationship to the failure envelope, as it gives a good approximation of the rock-mass angle of friction and provides an upper limit of cohesive strength (Hoek *et al.* 2002). This is done not by fitting the 'best-fit' tangent to the Mohr failure envelope, which can lead to an overestimate of the cohesive strength, but by fitting a linear Mohr Coulomb relationship (equation (11)) by a least-squares method (Fig. 6) (Hoek *et al.* 2002). As stated above, the value of cohesive strength produced from this method provides an upper limit, and it is prudent to reduce it to 75% of this value to serve any practical purpose.

A more convenient way to gain an estimate of the cohesive strength of the rock mass is to set $\sigma_n = 0$ in equation (13). Thus the cohesion becomes equal to the shear stress, and it can be read directly from the Mohr failure envelope as the intercept on the shear strength axis. The angle of friction and cohesive

Fig. 4. Mohr failure envelopes for a typical intact rhyolite and a rhyolitic rock mass using relevant values from Hoek & Brown (1981). Intact: $m_i = 16$, $s = 1$, $\sigma_c = 225$MPa (curve a); curve b is as curve a, but $\sigma_c = 150$MPa. Rock mass: $m = 2.68$, $s = 0.0039$, $\sigma_c = 225$MPa (curve c); curve d is as curve c, but $\sigma_c = 150$MPa. The Hoek–Brown constants m and s were determined from equations (2) and (3) using an RMR of 50.
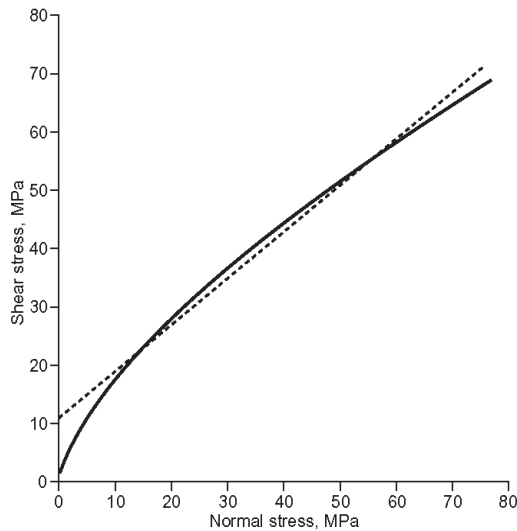
M. E. THOMAS *ET AL.*

Fig. 6. Representative plot showing a straight-line Mohr–Coulomb fit to a Mohr failure envelope obtained using a least-squares method.

strength of rock masses from Snowdonia and Tenerife determined using this method are listed in Table 3.

Discussion

Implications for volcano edifice strength

Our estimates of rock-mass strength compare favourably with previous estimates by, for example, Jaeger & Cook (1979), Voight *et al.* (1983), Schultz (1995, 1996) and Watters *et al.* (2000). Jaeger & Cook (1979) and Voight *et al.* (1983) gave wholesale estimates of edifice cohesive strength in the region of 1 MPa. Watters *et al.* (2000) presented data from mainly altered rock masses, and as expected their values of cohesive strength (0.08 0.4 MPa) are slightly lower than those presented here. Schultz (1995, 1996) reported estimated cohesive strength values of basaltic rock masses of 0.6 6 MPa. Taking the averages of data given in Table 3, the basaltic rock masses from Tenerife have an average cohesion of 1.3 MPa, which compares well with the data of Schultz (1995, 1996). The average overall cohesion for the Tenerife and the Snowdonia rock masses of 1.30 and 1.37 MPa, respectively, also agree well with previous estimates using an approach similar to that outlined above. The overall edifice cohesive strength is also useful in predicting the rock-mass response to failure, i.e. whether it will disaggregate or remain mostly a coherent block. As shown by Watters *et al.* (2000), failure is more likely to develop at sites where discontinuities contain secondary clay or gauge material, rather than along barren joints with no infilling. The same applies to sites of hydrothermal alteration. However, some forms of hydrothermal alteration, in particular silicification, generally produce a stronger and more elastic rock mass (Watters *et al.* 2000). Future work incorporating the GSI (see below) will allow the effects of alteration in the rock mass to be taken into account.

A new approach to the Hoek–Brown failure criterion

Recently Hoek *et al.* (2002) published an update to the Hoek Brown failure criterion. The revised version differs from the method defined previously in two important ways. The first is the replacement of the RMR by a new term, the geological strength index (GSI). The GSI (introduced by Hoek *et al.* (1992) and later refined by Marinos & Hoek (2000)) is designed to take into account the fact that the RMR has proved inadequate in estimating the failure criteria of some very weak rock masses. It should be noted, however, that for a GSI > 25, the RMR and GSI are essentially interchangeable, and thus this problem is not relevant in this study where RMR values are > 38. However, a second variable introduced by Hoek *et al.* (2002), called the disturbance factor (D), may be highly significant in the classification of non-altered volcanic rock masses. The disturbance factor originated from experience in the design of slopes in large mines, where the classical Hoek Brown criterion often proved over-optimistic in estimating rock-mass properties. The value of D is a qualitative measure of the degree of disturbance to which the rock mass has been subjected, and varies from zero (no disturbance) to unity (for the most disrupted). Despite its relevance to the problem in hand, at present it is far from clear how best to characterize a volcanic rock mass in terms of D. In mines and engineering works, the effects of heavy blasting damage, along with stress relief owing to the removal of overburden, result in disturbance of the rock mass. In the case of a volcanic slope, it is easy to visualize a relatively high disturbance factor caused by analogous natural events such as eruptions and landslips. The variable D affects the Hoek Brown constants m and s (equations (2) and (3)) so that

$$m = m_i \exp[(RMR - 100)/(28 - 14D)] \qquad (14)$$

and

$$s = \exp[RMR - 100)/(9 - 3D)]. \qquad (15)$$

The influence of the disturbance factor on rock-mass strength can be large. This is shown in Figure 7, where a Mohr failure envelope with the instantaneous angle of friction and cohesive strength for a rock mass is plotted ($\sigma_c = 150\text{MPa}$ and $m_i = 15$, RMR = 65), for two end-member cases $D = 0$ and $D = 1$. As seen in Figure 7, $D = 1$ results in a decrease in rock-mass cohesive strength of up to 30%. A comparison of the Mohr Coulomb criterion calculated with and without D for the volcanic rock masses examined in this study is shown in Table 4. Both angle of friction and cohesive strength are reduced significantly where $D = 1$, in some cases by up to 50%. Clearly, the idea of defining a disturbance factor for volcanic rocks is deserving of in-depth study. Work aimed at producing estimates for the value of D for a volcano slope is currently under way.

Conclusions

We have proposed a method to assess the strength of a volcanic rock mass using field observations and the Hoek Brown failure criterion. Our results suggest that in general, the rock masses of a volcanic edifice can be very weak, with cohesive strengths less than 1 MPa and rock-mass angles of friction varying from 28° to *c.* 38°. The rock-mass strength of crystalline volcanic material examined in this study also appears largely insensitive to initial magma composition and age. Our data suggest that the measured RMR and strength characteristics of unaltered volcanic rock are related through an exponential dependence that can provide a good first approximation of compressive and cohesive rock-mass
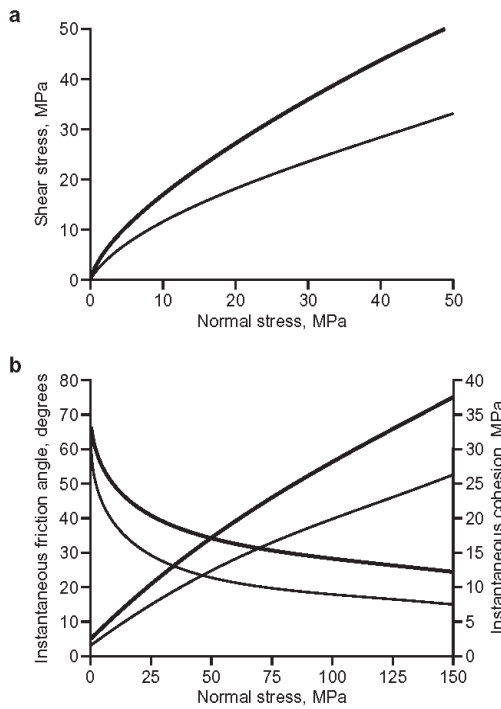
a

b

Fig. 7. (**a**) Mohr failure envelope and (**b**) instantaneous friction angle and instantaneous cohesive strength, for a rock mass where $\sigma_c = 150\text{MPa}$, $m_i = 15$, RMR = 65 and $D = 0$ (bold line) or $D = 1$ (fine line).

strength. The exponential relationship between the RMR and the rock-mass strength characteristics suggests that small changes in the condition of the rock mass may have a large impact on the rock-mass strength. This emphasizes the need for detailed mapping at any potentially hazardous volcano, because, if conditions are concurrent, failure will occur in the weakest area of the edifice regardless of how strong the overall rock mass is. The sensitivity of the mechanical properties of the rock mass to the disturbance factor (D) in the revised Hoek Brown criterion identifies it as an important new variable that should be used in future field assessments of volcano edifice strength.

References

BIENIAWSKI, Z.T. 1976. Rock mass classification in rock engineering. In: BIENIAWSKI, Z.T. (ed.) Exploration for Rock Engineering, Proceedings of the Symposium. Balkema, Cape Town, 1, 97–106.

BIENIAWSKI, Z.T. 1989. Engineering Rock Mass Classifications. Wiley, New York.

BROWN, E.T. (ED.) 1981. Rock Characterisation, Testing and Monitoring—ISRM Suggested Methods. Pergamon, Oxford.

CARRACEDO, J.C. & DAY, S. 2002. Classic Geology in Europe 4, Canary Islands. Terra, Harpenden, Herts, England.

CULMANN, C. 1866. Die Graphische Statik. Institute for Structural Design, Stuttgart.

CROWELY, J.K. & ZIMBEMAN, D.R. 1997. Mapping hydrothermally altered rocks on Mount Rainier, Washington, with Airborne Visible/Infrared Imaging Spectrometer (AVIRS) data. Geology, 25(6), 559–562.

DEERE, D.U. & DEERE, D.W. 1988. The RQD index in practice. In: KIRKDALE, L. (ed.) Proceedings of the Symposium on Rock Classification for Engineering Purposes, Cincinnati. ASTM Special Technical Publication, 984, 91–101.

HOEK, E. 1983. Strength of jointed rock masses, 23rd Rankine Lecture. Géotechnique, 33(3), 187–223.

HOEK, E. 1994. Strength of rock and rock masses. ISRM News Journal, 2, 4–16.

HOEK, E. & BROWN, E.T. 1980. Empirical strength criterion for rock masses. Journal of the Geotechnical Engineering Division, ASCE, 106, 1013–1035.

HOEK, E. & BROWN, E.T. 1988. The Hoek–Brown failure criterion—a 1988 update. In: CURRAN, J.H. (ed.) Proceedings of the 15th Canadian Rock Mechanics Symposium, University of Toronto, 31–38.

HOEK, E., WOOD, D. & SHAH, S. 1992. A modified Hoek–Brown criterion for jointed rock masses. In: HUDSON, J.A. (ed.) Proceedings on Rock Characterisation, Symposium of the International Society of Rock Mechanics: Eurock '92. British Geotechnical Society, London, 209–214.

HOEK, E., CARRANZA-TORRES, C.T. & CORKUM, B. 2002. Hoek–Brown failure criterion—2002 edition. In: CURRAN, J.H. (ed.) Proceedings of the North American Rock Mechanics Society, Toronto. University of Toronto Press, Toronto, 1, 267–273.

HÜRLIMANN, M., LEDESMA, A. & MARTI, J. 2001. Characterisation of a volcanic residual soil and its implications for large landslide phenomena: application to Tenerife, Canary Islands. Engineering Geology, 59, 115–132.

JAEGER, J.C. & COOK, N.G.W. 1979. Fundamentals of Rock Mechanics. Chapman and Hall, New York.

MARINOS, P. & HOEK, E. 2000. GSI—a geologically friendly tool for rock mass strength estimation. In: Proceedings of GeoEng 2000 Conference, Melbourne. Technomic Publishing, Melbourne, 1422–1440.

McGUIRE, W.J. 1998. Volcanic hazards and their mitigation. In: MAUND, J.G. & EDDLESTON, M. (eds) Geohazards in Engineering Geology. Engineering Geology Special Publications, Geological Society, London, 15, 79–95.

McGUIRE, W.J., JONES, A.P. & NEUBERG, J. (EDS) 1996. Volcano Instability on the Earth and other Planets. Geological Society, London, Special Publications, 110.

MOHR, O. 1882. Ueber die Darstellung des Spannungszustandes und des Deformationszustandes eines Korperelementes und uber die Anwendung derdelben in der Festigkeitslehre. Civilengenieur, 28, 113–156.

OWEN, T.R. 1979. The Geology of Snowdonia and Llyn: an Outline and Field Guide. Adam Hilger, Bristol.

REID, M.E., SISSON, T.W. & DIANNE, L.B. 2001. Volcano collapse promoted by hydrothermal alteration and edifice shape, Mount Rainier, Washington. Geology, 29(9), 779–782.

SCHULTZ, R.A. 1995. Limits on strength and deformation properties of jointed basaltic rock masses. Rock Mechanics and Rock Engineering, 28(1), 1–15.

SCHULTZ, R.A. 1996. Relative scale and the strength and deformability of rock masses. Journal of Structural Geology, 18(9), 1139–1349.

Table 4. A comparison of the Mohr–Coulomb criterion produced with and without the consideration of the disturbance factor from the Snowdonia volcanic group and Tenerife

Property	Snowdonia			Tenerife	
	Rhyolite	Tuff	Microgranite	Basalt	Phonolite
Rock-mass cohesive strength (MPa) ($D = 0$)	1.16–4.84	0.74–4.28	1.16–6.75	0.79–1.72	0.44–1.84
Rock-mass angle of friction (degrees) ($D = 0$)	31.3–38.1	27.8–36.1	41.2–49.4	28.1–31.8	28–34.9
Rock-mass cohesive strength (MPa) ($D = 1$)	0.31–2.59	0.21–2.29	0.57–4.08	0.23–0.66	0.1–0.71
Rock-mass angle of friction (degrees) ($D = 1$)	16.8–30.1	14.2–28.2	29.7–43.3	14.7–20.3	12.6–22.9

946   M. E. THOMAS *ET AL.*

SIEBERT, L. 1996. Hazards of very large volcanic debris avalanches and associated eruptive phenomena. *In:* SCARPA, R. & TILLING, R.I. (eds) *Monitoring and Mitigation of Volcano Hazards.* Springer, Berlin, 541–572.

THOMAS, M.E., PETFORD, N. & BROMHEAD, E.N. 2004. The effect of internal gas pressurisation on volcanic edifice stability: evolution towards a critical state. *Terra Nova,* **16**, 312–317.

TILLING, R.I. 1995. The role of monitoring in forecasting volcanic events. *In:* McGUIRE, W.J., KILBURN, C.R.J. & MURRAY, J.B. (eds) *Monitoring Active Volcanoes.* University College London Press, London, 369–402.

VOIGHT, B. 2000. Structural stability of andersite volcanoes and lava domes.

Philosophical Transactions of the Royal Society of London, Series A, **358**, 1663–1703.

VOIGHT, B., JANDA, R.J., GLICKEN, H. & DOUGLASS, P.M. 1983. Nature and mechanics of the Mt. St. Helens rockslide–avalanche of 18th May 1980. *Géotechique,* **33**, 243–273.

WATTERS, R.J., ZIMBELMAN, D.R., BOWMAN, S.D. & CROWLEY, J.K. 2000. Rock mass strength assessment and significance to edifice stability, Mt. Rainier and Mt. Hood, Cascade Range volcanoes. *Pure and Applied Geophysics,* **157**, 957–976.
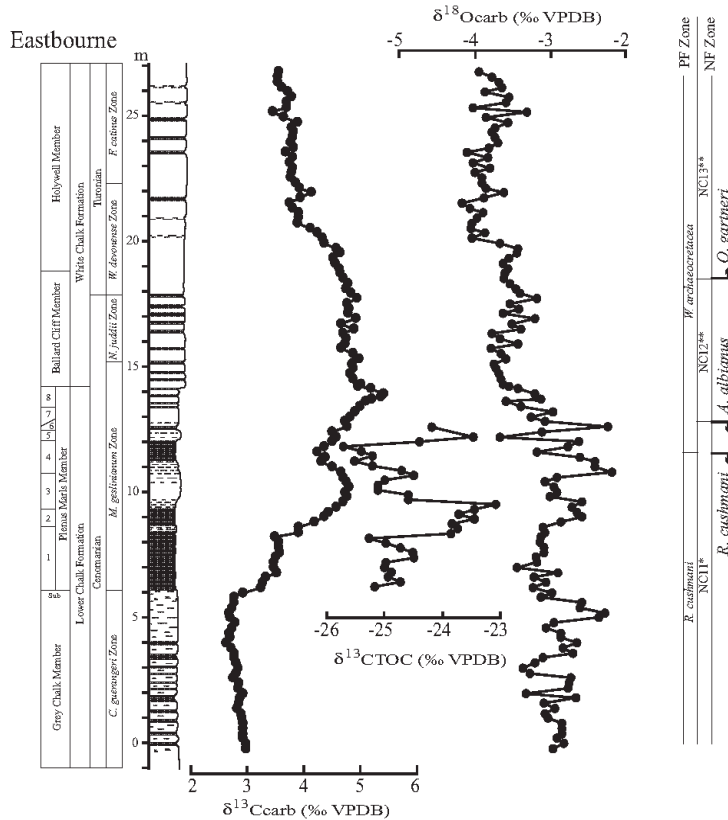
Errata

Carbon-isotope stratigraphy recorded by the Cenomanian–Turonian Oceanic Anoxic Event: correlation and implications based on three key localities

Volume 161, Part 4, p.713

H. TSIKOS, H. C. JENKYNS, B. WALSWORTH-BELL, M. R. PETRIZZO, A. FORSTER, S. KOLONIC, E. ERBA, I. PREMOLI SILVA, M. BAAS, T. WAGNER & J. S. SINNINGHE DAMSTÉ

The carbon-isotope values for organic carbon from the Eastbourne section in Figure 2 were inadvertently plotted incorrectly. The correct figure is reproduced left.

Microbial silicification in Iodine Pool, Waimangu geothermal area, North Island, New Zealand: implications for recognition and identification of ancient silicified microbes

Volume 161, Part 6, p. 985

B. JONES, K. O. KONHAUSER, R. W. RENAUT & R. S. WHEELER

The last sentence of the caption for Figure 2 should have been deleted in the proof-correction process. It relates to an older version of the figure.

Volcanic rock-mass strength properties from Snowdonia and Tenerife: implications for volcanic edifice strength

Volume 161, Part 6, pp. 940 and 941

M. E. THOMAS, N. PETFORD & E. N. BROMHEAD

Equations 1 and 4 should read as follows

$$\sigma_1 = \sigma_3 + \left(m\sigma_c\sigma_3 + s\sigma_c^2\right)^{1/2} \qquad (1)$$

$$\sigma_{cm} = \left(s\sigma_c^2\right)^{1/2} \qquad (4)$$

In the original paper, the σ_c function is missing the squared operator in both equations.

Grenvillian massif-type anothosites in the Sierras Pampeanas

Volume 162, Part 1, p. 9

C. CASQUET, R. J. PANKHURST, C. W. RAPELA, C. GALINDO, J. DAHLQUIST, E. BALDO, J. SAAVEDRA, J. M. GONZáLEZ CASADO & C. M. FANNING

The year is wrong in the catchline at the top of the page, it should be 2005

The effect of internal gas pressurization on volcanic edifice stability: evolution towards a critical state

Mark E. Thomas,[1] Nick Petford[1] and Edward N. Bromhead[2]

[1]School of Earth Science and Geography, and [2]School of Engineering, Kingston University, Kingston KT1 2EE, UK

ABSTRACT

Results from simple physical and numerical models investigating the effects of increased internal pore-fluid pressures of a Mohr–Coulomb volcanic edifice are presented. Physical experiments make use of a heap built from angular sand on top of a stiff substrate of variable angle, with the provision for injection of internal fluid (gas) pressures into the base. The resulting failure geometries arising from internal pressurization of the model appear similar to some natural examples of sector collapse. Two-dimensional limit equilibrium models analysing

42 500 possible failure surfaces were run with internal pressures (P_0) in the range 5–35 MPa, and show that the potential critical failure surface migrates to increasingly deeper levels with increasing internal pressure. Although internal pressurization alone is unlikely to reduce the factor of safety (F_S) below unity, the edifice is driven towards a state of criticality that will render in susceptible to any internal or external perturbations.

Terra Nova, 16, 312–317, 2004

Introduction

Studies during the last two decades have raised awareness of the life- and property-threatening hazards resulting from volcano instability (e.g. Tilling, 1995; McGuire et al., 1996; Siebert, 1996; Wolfe and Hoblitt, 1996; McGuire, 1998). Much new interest arose following the climactic May 1980 eruption of Mount St Helens, caused by a massive landslide on the volcano's northern flank.

Geotechnical engineers and geologists studying landslides are familiar with fluid pressurization by water, and its modifying effects on the shear strength of soils and rocks (e.g. Voight, 1978; Bromhead, 1986). Ordinarily, this pressurization is by groundwater of meteoric origin, and is rarely artesian, being hydrostatic and related to a groundwater level within the slope. Groundwater bodies created by infiltration from the surface lead to shallow landsliding and thus slopes that are stable against deeper-seated modes of failure (e.g. Bromhead, 1995). Recently, Voight and Elsworth (2000) have proposed a novel, highly non-linear instability mechanism for the hazardous collapse of lava domes in which dome failure is instigated by gas overpressure. As a first step towards understanding

Correspondence: Mark E. Thomas, School of Earth Science and Geography, Kingston University, Kingston KT1 2EE, UK. Tel.: +44 (0)20 85742000 ext. 61011; e-mail: markthomas@kingston.ac.uk

edifice failure at a basic level, we have modelled a destabilizing mechanism involving gas pressurization (e.g. Gerlach et al., 1996) that affects the entire interior of the edifice and the external expression of which is a deep-seated failure mode (landslip), which might be the cause of catastrophic eruption. Our model thus differs from other recent studies of volcano instability (e.g. Reid et al., 2001), in which the effects of internal fluid pressures are ignored and collapse is driven purely by gravity acting on regions of weak (hydrothermally altered) rock.

Initial results of an ongoing programme of physical and numerical modelling designed to examine in detail the role of internal (fluid) pressurization in promoting failure in conical structures (heaps) are described. Using simple scaling arguments, it is shown that a volcanic edifice may be regarded as a heap of (Mohr–Coulomb) granular material and that the failure surface resulting from internal (gas) pressurization is deep seated. Rock mass field data show that the edifice is likely to be weak, and using values of natural examples from Snowdonia, Tenerife (Thomas et al., 2004) and work published by Voight et al. (1983), we simulate the change in the factor of safety as a function of internal pressurization. We show that this important but largely unquantified processes may in some circumstances play a major role driving the volcanic edifice towards a critical state (e.g. Hill et al., 2002).

Current models of edifice failure

A number of models have been proposed to explain structural failure and collapse of a volcanic edifice in both fast and slow modes, in response to one or more internal or external triggers. Commonly cited examples include magma chamber replenishment, dyke emplacement and volcanogenic earthquakes (typically M > 5 close to or directly beneath a volcano) and intense rainfall (e.g. Elsworth and Voight, 1995; McGuire, 1998). In addition to the well-documented triggers, hydrothermal activity is recognized to play an important role in weakening the rock mass and rendering it more susceptible to mechanically induced structural failure (e.g. van Wyk de Vries et al., 2000; Reid et al., 2001). Despite this, some important questions remain. For example, major volcanic eruptions are also frequently preceded by emission of large quantities of volcanic gases in conjunction with vigorous fumerole activity, or steam generated by heating of groundwater (e.g. Pyle et al., 1996; Gerlach et al., 1996; Mouginis-Mark et al., 2000). However, although the emission of volcanic gasses and their compositions are routinely monitored, the mechanical effects of the gas phase on the shear strength and structural integrity of the edifice have been mostly overlooked. Gas sources include deep magma reservoirs and the progressive dehydration of the volcano's hydrothermal system (Tilling, 1995). Another factor is the process of

volcanic spreading (Borgia, 1994; Merle and Borgia, 1996), but sector collapse events are thought only to occur if spreading is not efficient (Borgia *et al.*, 2000), and therefore no further consideration is given to this mode of destabilization.

Edifice strength

The strength of an edifice is a property that requires careful consideration in volcano stability simulations. Indeed, the concept of edifice strength becomes critical when considering internal fluid pressurization, as the use of unrealistically high-strength parameters raises the nonsensical idea of a 'floating' volcano, in which the edifice is so strong that the internal pressure can counteract its weight without failing. The structure then becomes neutrally buoyant. Although uniaxial laboratory tests on fresh intact basalt will yield a compressive strength of 100 350 MPa (Schultz, 1995, 1996), a volcanic edifice is not simply intact rock but is cut through by a range of discontinuities, including faults, fractures and layering defined by discrete lava flows. Field approximations of the rock mass strength of crystalline volcanic material are surprisingly low, with cohesion values ranging from 300 kPa to 3.2 MPa (Voight *et al.*, 1983; Schultz, 1995, 1996; Watters *et al.*, 2000; Thomas *et al.*, 2004).

Internal pressurization

Pressurization from within the edifice is known to happen at all active volcanoes. It is well recognized that recorded gas emissions are generally more than the amount predicted from petrological studies of the crystal content of the erupted products (de Hoog *et al.*, 2001), suggesting the magma de-gases within the edifice. There is also the additional factor of dehydration (boiling) of active hydrothermal systems during a volcanic eruption producing elevated gas pressures. Robertson *et al.* (1998) and Sparks (1997) give estimates of values for internal system pressurization for parts of a volcanic system. Robertson *et al.* (1998) showed that a minimum pressurization of 27.5 MPa was required to explain the locations of the largest ballistics produced by the 1996 eruption of Soufriere Hills Volcano,

Montserrat; Sparks (1997) suggested typical excess pressures of 5 20 MPa. Sparks (1997) also suggested maximum theoretical excess pressures of close to 50 MPa, although due to permeable flow within the edifice, these theoretical pressures are rarely reached. These values are not a homogeneous pressure present throughout the edifice, but are presented here to demonstrate values of local pressure that have been measured or interpreted within a volcanic edifice.

Physical modelling

Initial experiments have been carried out with a simple uniform cone constructed of air-dried angular (sharp) sand, with provision for internal pressurization by gas (compressed air) at a controlled rate pumped through the base (Fig. 1a). Angular sand was used because of its higher internal angle of friction and repose compared with other types of granular material. The cone was created by raining particles from above and rested upon a stiff substrate of variable angle. The models were run with substrate angles of 5 20°. Using scaling arguments (below) and following the Buckingham Π theorem (Middleton and Wilcock, 1994), the controlling parameters for a conical heap of sand are given in Table 1. From Table 1 we can see that there are five variables minus three dimensions equal to two independent

Table 1 Geometric and mechanical variables for a conical heap of sand

Variable	Definition	Dimensions
c	cohesion	kN m^{-2}
ϕ	friction angle	–
H	height	m
α	slope angle	–
γ	unit weight	kN m^{-3}

dimensionless products, the stability number N and a non-named group Φ:

$$N - \frac{c}{\gamma H} \quad \text{and} \quad \Phi - \frac{\tan \phi}{\tan \alpha} \quad (1, 2)$$

A model perfectly represents the prototype if the two dimensionless groups are the same for both. The Φ parameter is matched if the ratio of the friction angles and the slope angles are the same. Estimates of the angle of friction for a volcanic pile suggested by other authors (Jaeger and Cook, 1979; Voight *et al.*, 1983; Watters and Delahaut, 1995) match closely the 38° friction angle of the sand used. Thus a model volcanic edifice needs the same slopes as its prototype.

For a 2000-m-high volcanic cone, taking c to be 1 MPa (1000 kN m^{-2}), and γ to be 25 kN m^{-3}, Eq. (1) gives a stability number (N) of 0.02. To achieve this stability number for a 0.2-m-high pile of sand ($\gamma - 20$ kN m^{-3}), substituting these values again into Eq. (1) $c - 0.08$ kN m^{-2} (80 Pa), which is practically unmeas-
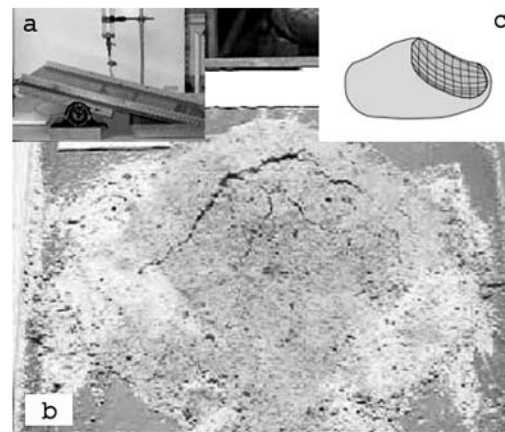

Fig. 1 Sandpile model with air pressurization: (a) experimental set-up, (b) surface expression of failure surface and (c) diagrammatic representation of the failure surface.

urable in the laboratory. Capillary tensions in air-dried sand would probably exceed this equivalent (Schellart, 2000). Hard though it may be to believe, a heap of sand on the laboratory workbench does truly represent a perfectly scaled model of a large volcanic edifice.

The fluid pressures scale on the basis of the maximum pressure (u), H and γ through the pore pressure ratio r:

$$r = u/\gamma H \qquad (3)$$

This is also a linear scaling, so the reduced size of the physical model is realistic. What does not scale linearly is the rate dependency of the collapse mechanism, and the propagation of fluid pressures throughout the edifice. Theses effects must be scaled on the basis of a time factor, which depends on rock mass permeability, fluid–rock relative compressibility, unit weight of the pore fluid and some critical size parameter termed drainage path length raised to the power 2. Modelling rate effects is outside the scope of this paper, except in a qualitative sense.

Numerical modelling

Numerical analysis into the effects of gas pressurization was carried out using two-dimensional limit equilibrium models. Limit equilibrium models use the most widely expressed index of stability, the factor of safety (F_S), which for a potential failure surface is defined as the ratio of shear strength to shear stress:

$$F_s = \int_L s / \int_L \tau \qquad (4)$$

where s is the shear strength, τ is the shear stress and the integration takes place along the length (L) of the failure surface. Numerical calculations were conducted using an in-house slope stability analysis package following the iterative method of Bishop (1955). This form of stability analysis is commonplace in geotechnical engineering and merits no further discussion. Factors of safety of 1 or less imply instability. Ordinarily, analysis is conducted on a plane section through a slope about a centre of rotation, and two-dimensional methods of analysis usually give satisfactory results for simple cases. This approach was used by Voight and

Elsworth (2000) as a general geometry for their limit equilibrium analysis of shallow flank and deep-seated edifice failure. Although our analysis is restricted to two dimensions, three-dimensional methods have been developed and applied to, *inter alia*, non-uniform surface topography and loading, which arguably is closer to the case represented by an unstable volcanic edifice.

The physical values used in our calculations are those defined previously by Voight *et al.* (1983) for the Mt St Helens edifice: cohesion (c, 1000 kPa (1 MPa)), angle of friction (ϕ, 40°) and unit weight (W, 24 kN m^{-3}), with a pore pressure ratio (u) of 0.3. These values were used as they are in the middle of the range of values presented by Schultz (1995, 1996), Thomas *et al.* (2004), Voight *et al.* (1983) and Watters *et al.* (2000).

Results

Physical modelling

The effects of internally pressurizing a sandpile model described above are shown in Fig. 1(b,c). Viewed from above, an arcuate crack is clearly visible traversing the summit and flanks of the pile. Several smaller radial cracks are also evident. This style of deformation was typical of the response of the pile to internal pressurization. A sketch (Fig. 1c) of the internal geometry of the slip surface after the failed portion had been removed confirms its deep-seated nature. Unsurprisingly the effect of increasing the angle of the base resulted in larger volume failures with a shorter time to failure from the onset of pressurizing the model. A key observation is that the surface expression and geometry of the failure surfaces (Fig. 2) are similar to those observed at Mount St Helens (Donnadieu *et al.*, 2001), Mount Etna (Tibaldi and Groppelli, 2002) and La Palma (Day *et al.*, 1999). Detailed morphological comparisons have not been conducted, and the similarities are purely in physical appearance.

Numerical modelling

Numerical results obtained from limit equilibrium modelling independent

from the physical models are shown in Figs 3 and 4. Calculations were set up to take into account the effects of: (1) no source of internal fluid pressurization (dry), (2) internal fluid pressurization produced by ground water infiltration only (wet) and (3) an edifice with a source of internal gas pressurization plus groundwater infiltration (wet plus internal).

A total of 42 500 possible failure surfaces were analysed during each simulation. For both cases, two model geometries were used (Fig. 4) to represent the volcano edifice, a uniform cone and one (more realistic) with topography similar to the pre-1980 eruption Mount Helens. In this paper there is no attempt to model Mount St Helens and it is only the topography that is used in the numerical models. Results of both experiments are summarized in Table 2. The internally pressurized area was defined as 75% of the volume of the defined edifice topography and the pressure was set at 100% at the pressure boundary (Fig. 4) and 0 at the 75% limit, with a linear distribution of pressure between the two boundary conditions.

Figure 3 shows a plot of factor of safety (F_S) against depth (km) calculated for a simple uniform cone for a range of internal pressures from 5 to 35 MPa. For both model types, a potential shallow instability is always present (Fig. 3). However, the end effect of increasing pressure is to (1) drive the potential critical failure surface deeper into the interior of the edifice and (2) decrease the factor of safety for that potential failure surface.

Considering a simple cone, an internal pressure of 25 MPa, a value close to the estimates of Robertson *et al.* (1998), displaces the potential critical failure surface from a shallow potential instability to depth of 3.2 km from the centre of rotation (Fig. 3). Further increasing the pressure to 35 MPa lowers the F_S to below unity and makes the slope unstable without any additional factors being considered.

The effect of driving the potential critical failure surface deeper within the cone is that the volume above the critical failure surface is increased substantially relative to external pressurization by groundwater infiltration (Fig. 4). Should the volcanic edifice fail, then the potential volume of
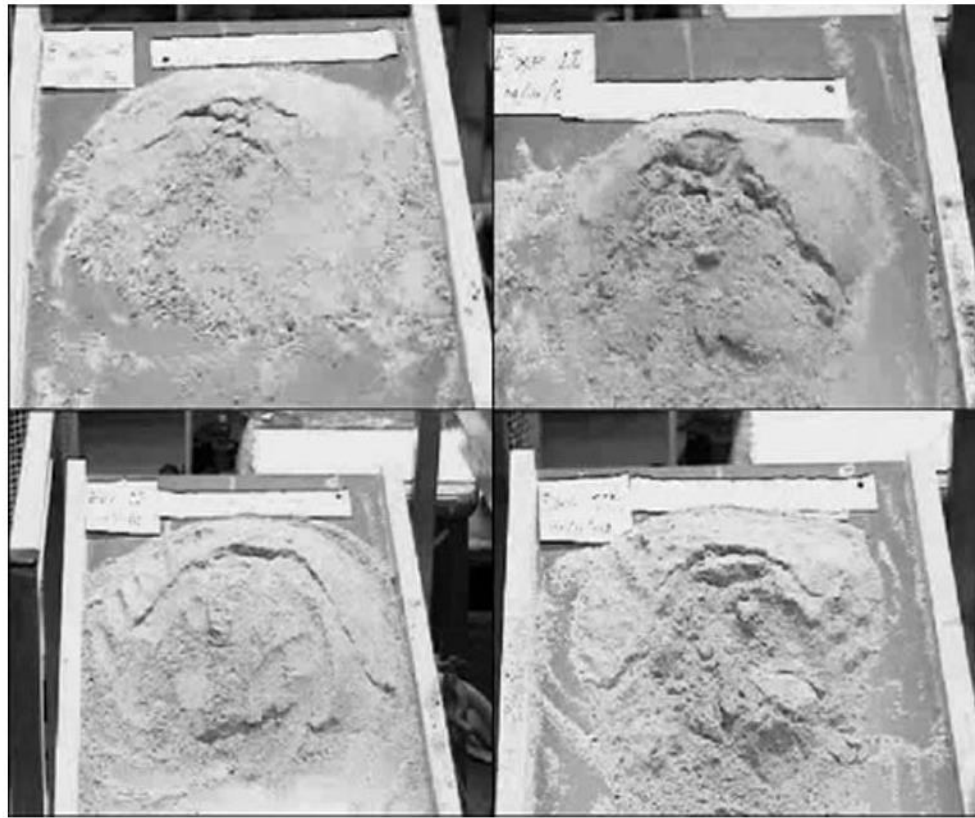
Fig. 2 Digital video stills showing the surface expressions of failure surfaces in the sand-pile models. All these images are from models conducted on 5° slopes.
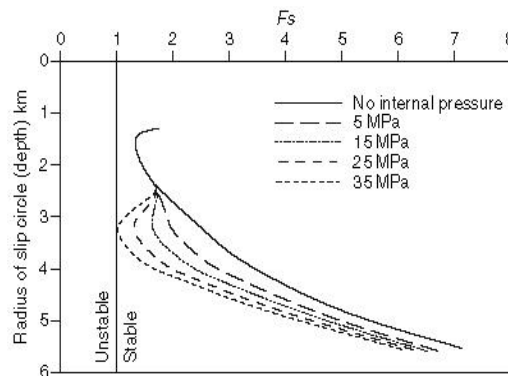

Fig. 3 Plot of factor of safety (F_S) against depth for a uniform cone, calculated at increasing internal pressure. Note that the shallow instability is still present in all cases, but instead of steadily increasing with depth as in the curve at no internal pressurization, F_S starts to decrease at depth when considering increasing internal pressure, until at an internal pressure of 25 MPa, the critical failure surface is no longer shallow, but is located at 3.2 km depth. (Note that all depths are taken from the slip circles to centre of rotation and are not measurements below ground level.)

material liberated during failure will be far greater.

Discussion

Our numerical results and scaling analysis suggest that internal fluid pressurization may be significant in promoting deep-level instabilities within a volcanic edifice. It is fully accepted that the physical models may be an oversimplification of the problem and we acknowledge that internal pressurization is unlikely to be the sole cause of catastrophic edifice collapse. It may nevertheless contribute significantly to the growing number of recognized mechanisms that complicate collapse predictions (e.g. Reid *et al.*, 2001). In particular, it provides a mechanism for driving the edifice close to its critical state (Hill *et al.*, 2002).
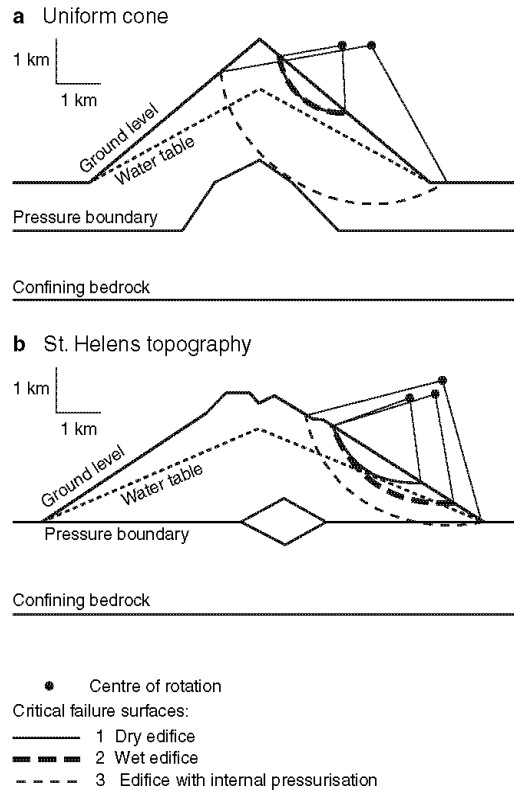
Fig. 4 Potential critical failure surfaces for a uniform cone (a), and an edifice with pre-1980 Mount St Helens like topography (b), potential failure surfaces for a 'dry' edifice, a 'wet' edifice and a 'wet' edifice plus internal gas pressurization are shown. Results are summarized in Table 2.

Table 2 Factor of safety (F_S) for the potential critical failure surfaces in Fig. 4 from the limit equilibrium modelling (numbers refer to pressurization regimes outlined in the text)

Uniform cone		St Helens topography	
1 Dry	1.73	1 Dry	1.99
2 Wet	1.32	2 Wet	1.53
3 Wet plus Internal	1.30	3 Wet plus Internal	1.33

Internal gas pressurization is a phenomenon that must happen to some extent in all active volcanoes, as the recorded gas emissions are generally more than the amount predicted from petrological studies of the crystal content of the erupted products (de Hoog *et al.*, 2001; Wallace, 2001). This suggests the magma has a gas-rich phase at depth. This, coupled with magma de-gassing at shallower levels, could lead to excess upward-propagating pore pressures. In addition, dehydration (boiling) of active hydrothermal systems during magma emplacement leads to considerable elevated pore pressures (Reid, 2004). Once a volcanic system has reached a critical state, collapse my be initiated by any previously studied triggers (Dieterich, 1988; Iverson, 1995; McGuire *et al.*, 1996; Voight and Elsworth, 1997). Indeed, if the edifice has been sufficiently weakened by hydrothermal alteration, internal pressurization may itself bring about the onset of collapse.

References

Bishop, A.W., 1955. The use of the slip circle in the stability analysis of slopes. *Geotechnique*, **5**, 1–17.
Borgia, A., 1994. Dynamic basis for volcanic spreading, *J. Geophys. Res.*, **99** (B9), 17791–17804.
Borgia, A., Delaney, P.T. and Denlinger, R.P., 2000. Spreading volcanoes. *Ann. Rev. Earth Planet. Sci.*, **28**, 539–570.
Bromhead, E.N., 1986. Pore water pressure manipulation in computerised slope stability analysis. In: *Proceedings, Midland Geotechnical Society Conference on Computer Applications in Geotechnical Engineering*, pp. 175–184. Midland Geotechnical Society, Birmingham.
Bromhead, E.N., 1995. *Water and Landslides*, pp. 42–56. Royal Academy of Engineering, London.
Day, S., Carracedo, J.C., Guillou, H. and Gravestock, P., 1999. Recent evolution of the Cumbre Vieja volcano, La Palma, Canary Islands: volcanic roft zone reconfiguration as a precursor to volcano flank instability. *J. Volcanol. Geotherm. Res.*, **94**, 135–167.
Dieterich, J.H., 1988. Growth and persistence of Hawaiian volcanic rift zones. *J. Geophys. Res.*, **93** (B5), 4258–4270.
Donnadieu, F., Merle, O. and Besson, J., 2001. Volcanic edifice stability during cryptodome intrusion. *Bull. Volcanol.*, **63**, 61–72.
Elsworth, D. and Voight, B., 1995. Dike intrusion as a trigger for large earthquakes and the failure of volcano flanks. *J. Geophys. Res.*, **100** (B4), 6005–6024.
Gerlach, T.M., Westrich, H.R. and Symonds, R.B., 1996. Preeruption vapour in magma of the climactic Mt. Pinatubo eruption: source of giant stratospheric sulphur dioxide cloud. In: *Fire and Mud: Eruptions and Lahars of Mt. Pinatubo, Philippines* (C. G. Newhall and R. S. Punongbyan, eds), pp. 415–433. University of Washington Press.
Hill, D.P., Pollitz, F. and Newhall, C., 2002. Earthquake–volcano interactions. *Physics Today*, **November**, 41–47.
de Hoog, J.C.M., Koetsier, G.W., Bronto, S., Sriwana, T. and van Bergen, M.J., 2001. Sulfur and chlorine degassing from primitive arc magmas: temporal changes during the 1982–83 eruptions of Galunggung (West Java, Indonesia). *J. Volcanol. Geotherm. Res.*, **108**, 55–83.

Iverson, R.M., 1995. Can magma-injection and groundwater forces cause massive landslides on Hawaiian volcanoes? *J. Volcanol. Geotherm. Res.*, **66**, 295–308.

Jaeger, J.C. and Cook, N.G.W., 1979. *Fundamentals of Rock Mechanics*, 3rd edn. Chapman & Hall, New York.

McGuire, W.J., Jones, A.P. and Neuberg, J. (eds) 1996. Volcano Instability on the Earth and Other Planets. *Geological Society Special Publication*, **110**.

McGuire, W.J., 1998. Volcanic hazards and their mitigation. In: *Geohazards in Engineering Geology* (J. G. Maund and M. Eddleston). *Spec. Publ. Geol. Soc. Lond.*, **15**, 79–95.

Merle, O. and Borgia, A., 1996. Scaled experiments of volcanic spreading. *J. Geophys. Res.*, **101** (B6), 13805–13817.

Middleton, G.V. and Wilcock, P.P., 1994. *Mechanics in the Earth and Environmental Sciences*. Cambridge University Press, Cambridge, pp. 74–83.

Mouginis-Mark, P.J., Crisp, J.A. and Fink, J.H., 2000. Remote Sensing of Active Volcanism. *Geophysical Monograph Series*, **116**.

Pyle, D.M., Beattie, P.D. and Bluth, G.J.S., 1996. Sulphur emission to the stratosphere from explosive volcanic eruptions. *Bull. Volcanol.*, **57**, 663–671.

Reid, M.E., 2004. Massive collapse of volcano edifices triggered by hydrothermal pressurization. *Geology*, **32**, 373–376.

Reid, M.E., Sisson, T.W.B. and Brien, D.L., 2001. Volcano collapse produced by hydrothermal alteration and edifice shape, Mt. Rainier, Washington. *Geology*, **29**, 779–782.

Robertson, R., Cole, P., Sparks, R.J.S., Harford, C., Lejeune, A.M., McGuire, W.J., Miller, A.D., Murphy, M.D., Norton, G., Stevens, N.F. and Young, S.R., 1998. The explosive eruption of Soufrirer Hills Volcano, Montserrat, West Indies, 17 September, 1996. *Geophys. Res. Lett.*, **25**, 3429–3432.

Schellart, W.P., 2000. Shear test results for cohesion and friction coefficients for different granular materials: scaling implications for their usage in analogue modelling. *Tectonophysics*, **324**, 1–16.

Schultz, R.A., 1995. Limits on strength and deformation properties of jointed basaltic rock masses. *Rock Mechanics Rock Engineering*, **28**, 1–15.

Schultz, R.A., 1996. Relative scale and the strength and deformability of rock masses. *J. Struct. Geol.*, **18**, 1139–1149.

Siebert, L., 1996. Hazards of very large volcanic debris avalanches and associated eruptive phenomena. In: *Monitoring and Mitigation of Volcano Hazards* (R. Scarpa and R. I. Tilling, eds), pp. 541–572. Springer-Verlag, Berlin.

Sparks, R.S.J., 1997. Causes and consequences of pressurisation in lava dome eruptions. *Earth Planet. Sci. Lett.*, **150**, 177–189.

Thomas, M.E., Petford, N. and Bromhead, E.N., 2004. Volcanic rock-mass properties from Snowdonia and Tenerife: implications for volcano edifice strength. *J. Geol. Soc. Lond.*, in press.

Tibaldi, A. and Groppelli, G., 2002. Volcano-tectonic activity along structures of the unstable NE flank of Mt. Etna (Italy) and their possible origin. *J. Volcanol. Geotherm. Res.*, **115**, 277–302.

Tilling, R.I., 1995. The role of monitoring in forecasting volcanic events. In: *Monitoring Active Volcanoes* (W. J. McGuire, C. R. J. Kilburn and J. B. Murray, eds), pp. 369–402. University College London Press, London.

Voight, B. (ed.) 1978. *Rockslides and Avalanches. 1. Natural Phenomena.* Elsevier, Amsterdam.

Voight, B. and Elsworth, D., 1997. Failure of volcano slopes. *Geotechnique*, **47**, 1–31.

Voight, B. and Elsworth, D., 2000. Stability of gas-pressurised lava-domes. *Geophys. Res. Lett.*, **27**, 1–4.

Voight, B., Janda, R.J., Glicken, H. and Douglass, P.M., 1983. Nature and mechanics of the Mt. St. Helens rock-slide-avalanche of 18th May 1980. *Geotechique*, **33**, 243–227.

Wallace, P.J., 2001. Volcanic SO_2 emissions and the abundance and distribution of exsolved gas in magma bodies. *J. Volcanol. Geotherm. Res.*, **108**, 85–106.

Watters, R.J. and Delahaut, D., 1995. Effect of argillic alteration on rock mass stability. In: *Clay and Shale Slope Instability, Review of Engineering Geology*, Vol. X (W.C. Haneburg and S.A. Anderson, eds), pp. 139–150. Geological Society of America, Boulder, CO.

Watters, R.J., Zimbelman, D.R., Bowman, S.D. and Crowley, J.K., 2000. Rock mass strength assessment and significance to edifice stability, Mt. Rainier and Mt. Hood, Cascade Range volcanoes. *Pure Appl. Geophys.*, **157**, 957–976.

Wolfe, E.W. and Hoblitt, R.P., 1996. Overview of the eruptions. In: *Fire and Mud: Eruptions and Lahars of Mt. Pinatubo, Philippines* (C. G. Newhall, and R. S. Punongbyan, eds), pp. 3–20. University of Washington Press.

van Wyk de Vries, B., Kerle, N. and Petley, D., 2000. Sector collapse forming at Casita volcano, Nicaragua. *Geology*, **28**, 167–170.

Appendix B – Brief history of the Hoek-Brown criterion

The Hoek-Brown failure criterion is integral to understanding and implementing the term "*rock mass strength*". The criterion has been through many alterations and enhancements on its way to the current form. Possibly the best summary of the failure criterion exists as a short article included within the Rocscience program RocLab. RocLab is a piece of software for determining rock mass strength parameters, based on the generalised Hoek-Brown failure criterion and is freely available at the time of writing from the Rocscience website. What follows is a summation of this article, which was prepared by Evert Hoek on 10th June 2002.

1980   Hoek E and Brown E.T. 1980. *Underground Excavations in Rock*. London: Institution of mining and Metallurgy 527 p.

Hoek E and Brown E.T. 1980. Empirical strength criterion for rock masses*. Journal of the Geotechnical Engineering Division, ASCE*, **106**(GT9), 1013-1035.

The original failure criterion was developed during the preparation of the book *Underground Excavations in Rock* (Hoek E. and Brown E.T. 1980). The criterion was required in order to provide input information for the design of underground excavations. Since at the time no suitable methods for estimating rock mass strength appeared to be available, the efforts were focussed on developing a dimensionless equation that could be scaled in relation to geological information. The origin of the Hoek-Brown equation was neither new nor unique, an identical equation has been in use for describing the failure of concrete as early as 1936. The significant contribution that Hoek and Brown made was to link the equation to geological observations in the form of Bieniawski's Rock Mass Rating. Hoek and Brown were quick to realise that the criterion would have no practical use unless the parameters could be estimated by simple geological observations in the field. Since Bieniawski's RMR had been published in 1974 and had gained popularity with the rock mechanics community, it was decided to use this as the basic vehicle for geological input, rather than developing a new classification for this purpose.

The original criterion was conceived for use under the confined conditions surrounding underground excavations, and possessed a bias towards hard rock. It was based on the assumption that translation and rotation of individual rock pieces, separated by numerous joint surfaces, control rock mass failure. Failure of the intact rock was assumed to play no significant role in the overall failure process and it was assumed that the joint pattern was 'chaotic' so that there are no preferred failure directions and the rock mass can be treated as isotropic.

1983   Hoek, E. 1983. Strength of jointed rock masses, 23rd. Rankine Lecture. *Géotechnique*, **33**(3), 187-2223.

In 1983 Hoek published what can be considered the most important of all the amendments/updates to the criterion. One of the issues that had been troublesome throughout the development of the criterion has been the relationship between the Hoek-Brown Criterion with the non-linear

parameters *m* and *s,* and the Mohr-Coulomb criterion, with the parameters c and ϕ. As most analyses of soil and rock mechanics are carried out in terms of c and ϕ, practically all software for soil and rock mechanics is also written in terms of the Mohr-Coulomb criterion and it was necessary to define the relationship between *m* and *s,* and *c* and ϕ in order to allow the criterion to be used to provide input for this software. Dr John W. Bray developed an exact theoretical solution to this problem and this solution was first published in Hoek's 1982 Rankine lecture (Hoek, 1983). This publication also expanded on some of the concepts published by Hoek and Brown in 1980 and it represents the most comprehensive discussion on the original Hoek-Brown criterion to date.

1988   Hoek E. and Brown E.T. 1988. The Hoek-Brown failure criterion – a 1988 update. In: Curran J.H. (ed.) *Proceedings of the 15th Canadian Rock Mechanics Symposium*. Toronto, Civil Engineering Department, University of Toronto. 31 – 38.

By 1988 the criterion was being widely used for a variety of rock engineering problems, including slope stability analyses. This posed a new set of problems as the original criterion was developed for the confined conditions surrounding underground excavations and it was recognised that it gave optimistic results near surfaces in slopes. Consequently, in 1988, the idea of undisturbed and disturbed masses was introduced to provide a method for downgrading the properties of near surface rock masses.

1992   Hoek E., Wood D. and Shas S. 1992. A modified Hoek-Brown criterion for jointed rock masses. In: Hudson J.A. (ed.), *Proceedings of the Rock Characterisation Symposium. International Society of Rock Mechanics: Eurock '92*, London, 209 – 214

The use of the Hoek-Brown criterion had now become widespread and, because of the lack of suitable alternatives, it was now being used on very poor quality rock masses. These rock masses differed greatly from the tightly interlocking hard rock mass model used in the development of the original criterion. In particular it was felt that the finite tensile strength being predicted by the original criterion was far too optimistic and that it needed to be revised. A new revised criterion continuing a new parameter, *a*, that provided a means of changing the curvature of the failure envelope particularly at low stress levels was proposed. This change essentially forced the modified Hoek-Brown criterion to produce zero tensile strength.

1993   Hoek E. 1994. Strength of rock and rock masses. *ISRM News Journal*, **2**(2), 4 – 6

1994   Hoek E., Kaiser P.K. and Bawden W.F. 1995. *Support of underground excavations in hard rock*. Rotterdam, Balkema

It soon became evident that the modified criterion was too conservative when used for better quality rock masses and a 'generalised' failure criterion was proposed in these two publications. The generalised criterion incorporated both the original and the modified criteria, with a 'switch' at a RMR value of 25. Hence, for excellent to fair quality rock masses the original criterion was used while for poor and worse rock masses, the modified criterion was used.

These publications also gave the first introduction of the concept of the Geological Strength Index (GSI) as a replacement for Bieniawski's RMR. It had become increasing obvious that the RMR is difficult to apply to very poor quality rock masses (RMR < 25) and also that the relationship between RMR and m and s is no longer linear in these very low ranges. Feed back coming from field personnel also indicated that a system based more heavily on fundamental geological observations and less on numerical parameters was needed.

The idea of undisturbed and disturbed rock masses was dropped and it was left to the user to decide which GSI/RMR value best described the various rock types exposed. The original disturbance parameters were derived by simply reducing the strength by one row in the classification table. It was felt that this was too arbitrary and it was decided that it would be preferable to allow the user to decide what sort of disturbance is involved and to allow the user to make their own judgement on how much to reduce the GSI/RMR to account for the strength loss.

1997   Hoek E. and Brown E.T. 1997. Practical estimates of rock mass strength. *International Journal of Rock Mechanics and mining Sciences*. **34**(8) 1165 –1186

This 1997 paper is the most comprehensive paper published on the criterion and it incorporates all of the refinements described previously. In addition, it introduced a simple way of estimating the equivalent Mohr Coulomb cohesion and friction angle. In this method the Hoek-Brown criterion is used to generate a series of values relating axial strength to confining pressure (or shear stress to normal stress) and theses are treated as the results of a hypothetical large scale in situ triaxial or shear test. A linear regression method is used to find the average slope and intercept and these are then transformed into a cohesive strength c and friction angle ϕ.

2000   Marinos P. and Hoek E. 2000. GSI: A geologically friendly tool for rock mass strength estimation. In: *Proceedings of the international Conference on Geotechnical and Geological engineering (Geo Eng 2000).* Melbourne, Technomic Publishing Company. 1422 -1440

2001   Marinos P. and Hoek E. 2001. Estimating the geotechnical properties of heterogeneous rock masses such as flysch. Bulletin of Engineering, Geology and the Environment. **60**, 85 – 92

These papers add considerably more geology to the Hoek-Brown failure criterion than was available previously. In particular the properties of very weak rock masses were addressed in detail for the first time. In these papers a new GIS chart is introduced for weak rock masses.

2002   Hoek E. Carranza-Torres C.T. and Corkum B. 2002. Hoek-Brown failure criterion – 2002 edition. In: Proceedings of the North American Rock Mechanics Society. Toronto.

The long running issue of the relationship between the Hoek-Brown failure criterion and Mohr-Coulomb criteria is addressed in this paper. An 'exact' method for calculating the cohesive strength and angle of friction is presented and appropriate stress ranges for tunnels and slopes are given. A rock mass damage criterion is introduced to account for the strength reduction due to

stress relaxation and blast damage in slope stability. It was with these latest developments in the Hoek-Brown criterion that the program "RocLab" was developed and at the time of writing was available for downloading, freely over the Internet.

Appendix C – ISRM suggested method for Point Load Strength testing

Rock samples in the form of either core (*diametral and axial tests*), cut blocks (*block tests*) or irregular lumps (*irregular lump test*) can be used (Anon, 1985). Once the field samples have been acquired, little or no sample preparation is required. All the tests conducted during this project were on irregular lumps (Fig. C.1), and all references to the Point Load Strength test will be made from the point of view of the irregular lump test from this point forward. The samples are broken by application of a concentrated load though a pair of spherically truncated, conical platens (Fig. C.2a). As such, the testing machine (Fig. C.2b) consists of a loading system, a system form measuring the load P required to break the sample and a system for measuring the distance D between the two platen contact points.

Testing was carried out in accordance with the International Society of Rock Mechanics suggested method (Anon, 1985) and immediately prior to testing the Point Load Strength testing machine was fully calibrated by Controls (UK). Only a brief outline of the procedure is described here. For a full description of the test the reader is directed to Anon, 1985. Rock lumps of the shape and size shown in Fig. C.1 are suitable for the irregular lump tests. The ratio D/W should be between 0.3 and 1.0, preferably as close to 1.0 as possible. The distance L should be at least 0.5W. If the field samples collected were not in accordance with these sizes they were trimmed by saw before testing. For all locations 10 samples were retrieved and tested. The samples are inserted in the testing machine and the platens are closed to make contact with the smallest dimension of the lump sample. The load is then steadily increased such that failure occurs within 10 – 60 seconds, and the failure load P is recorded.

The uncorrected Point Load Strength I_s, is calculated as:

$$I_s = \frac{P}{D_e^2}$$

(Equation C.1)

where D_e is the equivalent core diameter (Fig. C.1), which for the irregular lump test is given by:

$$D_e^2 = \frac{4A}{\pi}$$

(Equation C.2)

and

$A = WD$ = minimum cross sectional area of a plane through the platen contact points (Fig. C.1).

I_s varies as a function of D_e, so a size correction is applied to obtain a point load strength for the sample location, from which there were 10 individual samples tested. The size-corrected Point Load Strength Index, $I_{s(50)}$, Is defined as the value of I_s that would have been recorded by a test on a core with a diameter of 50 mm. $I_{s(50)}$ can be obtained by multiplying I_s by the size correction factor F:

$$I_{s(50)} = F \times I_s \qquad \text{(Equation C.3)}$$

where

$$F = \left(D_e / 50\right)^{0.45} \qquad \text{(Equation C.4)}$$

Mean values of $I_{s(50)}$ are always to be used, and are calculated by omitting the two highest and lowest values from the 10 or more valid tests, and calculating the mean of the remaining values. If there are significantly lower valid tests, only the highest and lowest values are omitted. All the data presented in Table 5.6 were calculated using this method.
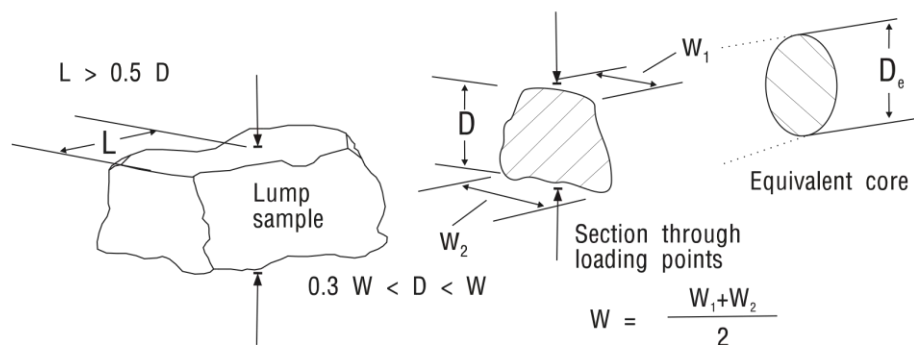
Figure C.1: **(Top)** Type examples of the irregular lumps used in the point load strength testing for all five localities listed in table 5.6. Samples, left to right, are from localities 2-1, 3-1, 3-2, 3-3 and 4-1. **(Bottom)** The characteristics which all lump samples must satisfy in order to produce valid tests, and the variables required to be measures in order to produce a size-corrected Point Load Strength Index. (Modified from Anon, 1985)

Figure C.2: (a) Schematic representation of the ideal shape of the two platen contact points on the point load strength test machine. (b) Full view of the point load strength testing machine with a lump sample between the platen contact points.

Appendix D – Rock mass strength data

The Following is a directory of what can be found on the Appendix CD:

D.1 RMR and GSI Field Data

Microsoft© Excel worksheets used for the calculation of the rock mass compressive and tensile strengths from both field data collected in Snowdonia and Tenerife and published RMR values (Okubo, 2004). Appendix D.1 also includes worksheets used to calculate the RQD and two comparison worksheets that include the data from every locality, one of which removes the influence of any anomalous results.

D.2 Mohr Circle Data

Microsoft© Excel worksheets used for the plotting of Mohr circles and ultimately the determination of a rock mass cohesive strength from both field data collected in Snowdonia and Tenerife and published RMR values (Okubo, 2004). Appendix D.2 also includes a comparison worksheet that includes the data form all localities.

D.3 Point Load Strength Data

Microsoft© Excel worksheets used for the determination of the rock point load strength and estimates of intact compressive and tensile strengths from field data collected in Tenerife.

Appendix E – Limit equilibrium calculations

The Following is a directory of what can be found on the Appendix CD:

E.1 In House Slope Stability Code

The code used to carry out the two-dimensional limit equilibrium modelling

E.2 Model Data Files

Data files used for the two-dimensional limit equilibrium modelling including the simple uniform cone in the states of:

1. Dry

2. Wet

3. At all pressure states (5 – 35 MPa)

A realistic edifice shape similar to pre-eruption Mount St. Helens in the sates of:

1. Dry

2. Wet

3. Pressurised at 10 MPa

E.3 Model Results

Both the raw results (.res files) and the results imported into Microsoft© Excel worksheets for convenience of manipulating the data.

E.4 Original LEM Output

Original Corel© Draw graphics that are exported from the LEM modelling program, these graphics were edited for the convenience of the reader before they were inserted into the text of the thesis.

Appendix F – *FLAC^{3D}*

The Following is a directory of what can be found on the Appendix CD:

F.1 Model Data Files

Data files for all five model geometries:

1. Normal

2. Steep

3. Tilted

4. Weak

5. Tilted, weak and steep

F.2 Fish Functions

Fish functions used to manipulate the modelling process:

1. tilt.fis: a function used to introduce a regional gradient

2. strengthstressratio_null.fis: a function used to calculate the factor of safety

F.3 Model Results

The raw results for all model geometries at all pressure states:

1. Normal

2. Steep

3. Tilted

4. Weak

5. Tilted, weak and steep
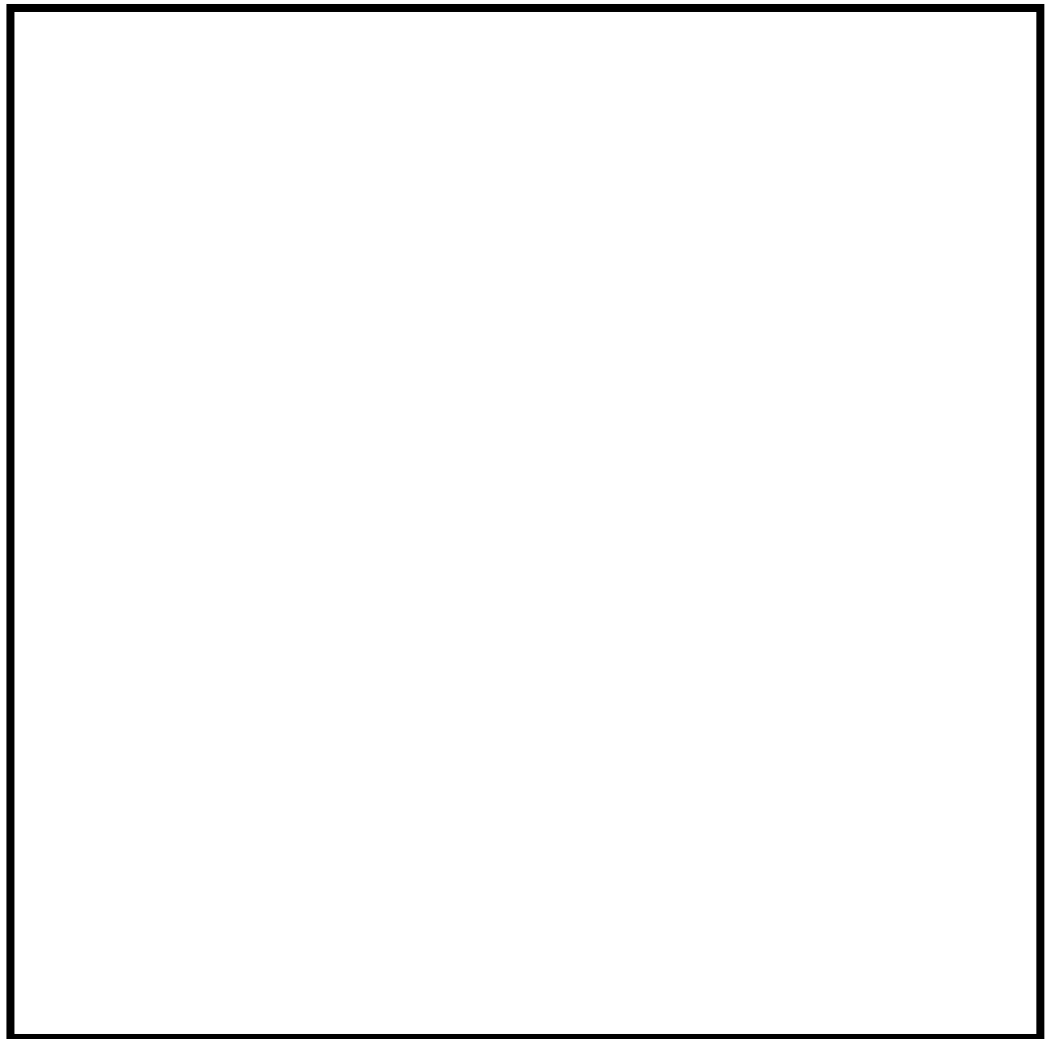
Reference List

Ablay, G., and Hürlimann, M., 2000. Evolution of the north flank of Tenerife by recurrent giant landslides, *Journal of Volcanology and Geothermal Research*, 103, 135-159

Ablay, G., and Kearey, P., 2000. Gravity constraints on the structure and volcanic evolution of Tenerife, Canary Islands, *Journal of Geophysical Research,* 105, 5783-5796

Acocella, A., 2005, Modes of sector collapse of volcanic cones: Insights from analogue experiments, *Journal of Geophysical Research*, 110 (B02205), doi:10.1029/2004JB003166

Almendros, J., Ibanez, J.M., Carmona E. and Zandomeneghi D., 2007. Array analyses of volcanic earthquakes and tremor recorded at Las Cañadas caldera (Tenerife Island, Spain) during the 2004 seismic activation of Teide volcano. *Journal of Volcanology and Geothermal Research,* 160, 285-299

Ancochea, E., Fuster, J.M., Ibarrola, E., Cendrero A., Coello, J., Hernan, F., Cantagrel, J.M. and Jamond, C., 1990. Volcanic evolution of the island of Tenerife (Canary Islands) in the light of new K-Ar data, *Journal of Volcanology and Geothermal Research,* 44, 321-249

Anonymous, 1985. Suggested method for determining point load strength: International society of rock mechanics commission on testing methods, *International Journal of Rock Mechanics and Mining Science,* 22*,* 51-60

Apuani, T., Corazzato, C., Cancelli, A. and Tibaldi, A., 2005. Stability of a collapsing volcano (Stromboli, Italy): Limit equilibrium analysis and numerical modelling, *Journal of Volcanology and Geothermal Research*, 144, 192-210

Araña, V., Camacho, A.G., Garcia, A., Mantesinos, F.G., Blanco, I. and Vieira, R., 2000. internal structure of Tenerife (Canary Islands) based on gravity, aeromagnetic and volcanological data. *Journal of Volcanology and Geothermal Research*, 104, 43-64

Baldi. P. Fabris. M. Marsella. M.. and Monticelli. R., 2005. Monitoring the morphological evolution of the Scaria del Fuoco during the 2002-2003 Stromboli eruption using multi-temporal photogrammetry. *Photogrammetry and Remote Sensing,* 59, 199-211

Beget, J.E. and Kienle, J., 1992. Cyclic formation of debris avalanches at Mt. Augustine volcano, Alaska. *Nature*, 356, 701-704

Bieniawski, Z.T. 1973. Engineering classifications of jointed rock masses. *Transactions of the South African Institute of Civil Engineering*, 15, 335-344

Bieniawski, Z.T. 1976. Rock mass classification in rock engineering. *In*, Bieniawski Z.T. (Ed.), *Exploration for Rock Engineering, Proceedings of the Symposium*. Cape Town: Balkema, 97-106

Bieniawski, Z.T., 1978. Determining rock mass deformability - experience from case histories, *International Journal of Rock Mechanics and Mining Sciences,* 15, 237-247

Bieniawski, Z.T. 1989. *Engineering Rock Mass Classifications*, New York: Wiley

Bieniawski, Z.T., 1993, Classification of rock masses for engineering, *In*: Hudson J. A., Hoe (Eds.), *Comprehensive Rock Engineering, Vol. 3*. New York: Pergamon, 553-573

Bishop, A.W., 1954, the use of the slip circle in the stability analysis of slopes, *Geotechnique, 5,* 1-17

Blong, A.W. 1984, *Volcanic Hazards*, Australia, Academic Press

Bonforte, A., and Puglisi, G., 2003, Magma uprising and flank dynamics on Mount Etna volcano, studied using GPS data (1994-1995). *Journal of Geophysical Research,* 108 (B3), doi:10.1029/2002JB001845

Borgia, A., 1994. Dynamic basis for volcanic spreading, *Journal of Geophysical Research,* 99 (B9), 17791-17804

Borgia, A., Delaney, P.T., Denlinger, R.P., 2000, Spreading volcanoes, *Annual Review of Earth and Planetary Sciences,* 28, 539 – 70

Bromhead, E.N., 1986. Pore water pressure manipulation in computerised slope stability analysis, *In*: *Proceedings, Midland Geotechnical Society Conference on Computer Applications in Geotechnical Engineering*. 175-184

Bromhead, E.N., 1995. Water and landslides. *Royal Academy Engineering, IDNDR Special Publication*, 42-56

Brown, E.T., 1981 (Ed.). *International Society for Rock Mechanics, Rock characterisation, testing and monitoring - ISRM suggested methods*. Oxford: Pergamon

Bryan, S.E., Marti, J. and Cas, R.A.F., 1998. Stratigraphy of the Bandas del Sur Formation: an extracaldera record of Quaternary phonolitic explosive eruptions from the Las Cañadas edifice, Tenerife (Canary Islands). *Geological Magazine*, 135, 605-636

Bryan, S.E., Marti, J. and Lesson, M., 2002 Petrology and Geochemistry of the Bandas del Sur Formation, Las Cañadas Edifice, Tenerife (Canary Islands). *Journal of Petrology*, 43, 10, 1815-1856

Candela, P.A., 1991. Physics of aqueous phase evolution in plutonic environments. *American Mineralogist,* 76, 1081-1091

Cantagrel, J.M, Arnaud, N.O., Ancochea, E., Fuster, J.M. and Huertas, M.J., 1999. Repeated debris avalanches on Tenerife and genesis of Las Cañadas caldera wall (Canary Islands), *Geology, 27*, 739-742

Carracedo, J.C., 1994. The Canary Islands: an example of structural control on the growth of large oceanic island volcanoes. *Journal of Volcanology and Geothermal Research,* 60, 225-241

Carracedo, J.C., Day, S.J., Guillou, H. and Torrado, F.J., 1999. Giant Quaternary landslides in the evolution of La Palma and El Hierro, Canary Islands. *Journal of Volcanology and Geothermal Research,* 94, 169-190

Carracedo, J.C., Day, S.. 2002. *Classic Geology in Europe 4, Canary Islands*. Hertfordshire, UK: Terra Publishing

Cecchi, E., van Wyk de Vries, B. and Lavest, J., 2005. Flank spreading and collapse of weak-cored volcanoes, *Bulletin of Volcanology*, 67, 72-91 doi:10.1007/s00445-004-0369-3.

Centro Nacional de Prevencion de Desastres., 2005 [online]. Available from: http://www.cenapred.unam.mx/en [Accessed 12 May 2006].

Chen, C.F., 2000. *Soil engineering: Testing, design and remediation*, Boca Raton, Florida, USA: CRC press

Chouet, B., Dawson, P. and Arciniega-Ceballos, A. 2005. Source mechanism of Vulcanian degassing at Popocatepetl Volcano, Mexico, determined from wave form inversions of very long period signals, *Journal of Geophysical Research*, 110 (B07301), doi:10.1029/2004JB003524

Cobold, P.R. and Castro, L., 1999. Fluid pressure and effective stress in sandbox models, *Tectonophysics,* 301, 1-19

Costa, J.E., 1984. Physical geomorphology of debris flows. *In*: Costa J.E. and Fleischer P.J. (Eds.), *Development and Applications in Geomorphology*. New York, Springer Berlin Heidelberg, 263-317

Crandell, D.R., 1989. Gigantic debris-avalanche of Pleistocene age from ancestral Mount Shasta volcano, California, and debris-avalanche hazard zonation. *Bulletin of the US Geological Survey*, 1861

Crandell, D.R. and Hoblitt, R.P., 1986. Lateral blasts at Mount St. Helens and hazard zonation, *Bulletin of Volcanology,* 48, 27-37

Crowely, J.K., Zimbelman, D.R., 1997. Mapping hydrothermally altered rocks on Mount Rainier, Washington, with Airborne Visible/Infrared Imaging Spectrometer (AVIRS) data, *Geology,* 25 (6), 559-562

Culmann, C. 1866. *Die Graphische Statik*, Zurich

Davidson, J., Turner, S., Handley, H., Macpherson, C. and Dosseto, A., 2007. Amphibole "sponge" in arc crust? *Geology*, 35, 791-794

Day, S.J., Carracedo, J.C., Guillou, H., 1997. Age and geometry of an aborted rift flank collapse: the San Andres fault system, El Hierro, Canary Islands, *Geological Magazine,* 134, 523-537

Day, S.J., Carracedo, J.C., Guillou, H., Gravestock, P., 1999. Recent evolution of the Cumbre Vieja volcano, La Palma, Canary Islands: volcanic rift zone reconfiguration as a precursor to volcano flank instability, *Journal of Volcanology and Geothermal Research*., 94, 135-167

Deere, D.U. and Deere, D.W. 1988. The RQD index in practice. *In*: Kirkdale L., (Ed.) *Proceedings of Symposium on Rock Classification for engineering purposes*, *1998 Cincinnati*. Philadelphia: ASTM Special Technical Publication 984, 91-101

Delaney, P.T., 1982. Rapid intrusion of magma into wet rock: Groundwater flow due to pore pressure increases, *Journal of Geophysical Research,* 87*,* 7739-7756

Donnadieu, F., and Merle, O., 1998. Experiments on the indentation process during cryptodome intrusions: New insights into Mount St. Helens deformation, *Geology,* 26 (1), 79-82

Donnadieu, F., Merle, O., and Besson, J., 2001. Volcanic edifice stability during cryptodome intrusion. *Bulletin of Volcanology*, 63, 61-72

Druitt, T.H., and Kokelaar, B.P., (Eds.) 2002. *The Eruption of Soufriére Hills Volcano, Montserrat, from 1995 to 1999*. Geological Society, London, Memoirs, 21

Duff, P.McL.D., and Smith A.J., 1992. *Geology of England & Wales.* London: The Geological Society, London

Dzurisin, D., Vallance J.W., Gerlach, T.M., Moran, S.C. and Malone, S.D., 2005. Mount St. Helens reawakens, *Eos*, 86, (3) 25-29

Edmonds, M., Oppenheimer, C., Pyle, D.M., Herd, R.A. and Thompson, G., 2003. SO_2 emissions from Soufriere Hills Volcano and their relationship to conduit permeability, hydrothermal interaction and degassing regime. *Journal of Volcanology and Geothermal research, 124,* 23-43

Eichelberger, J.C., 1995. Silicic volcanism: ascent of viscous magmas from crustal reservoirs. *Annual Review of Earth and Planetary Science*, 23, 41-63

Elsworth, D., Voight, B., 1995. Dike intrusion as a trigger for large earthquakes and the failure of volcanic flanks, *Journal of Geophysical Research,* 100 (B4), 6005-6024

Elsworth, D., Voight, B., 1996. Evolution of volcano flank instability triggered by dyke intrusion. *In*: McGuire, W.J., Jones, A.P., and Neuberg, J., (Eds), 1996. *Volcano instability on the Earth and other planets.* London: Geological Society London Special Publication, 110, 45-53

Elsworth, D. and Day, S. 1999. Flank collapse triggered by intrusion: the Canarian and Cape Verde Archipelagos, *Journal of Volcanology and Geothermal research,* 94, 323-340

Endo, E., Malone, S.D., Noson, L.L and Weaver, C.S., 1981. Locations, magnitudes and statistics of the March 20-May 18 earthquake sequence. *Professional paper of the U.S. Geological Survey*, 1250, 90-108

Firth, I.R., Watters, R.J. and Bowman, S.D., 2000. Modelling of volcano edifice and flank stability and implications for hazard zonation. *In:* Girard, Liebman*,* Breeds and Doe (Eds.), *Pacific Rocks 2000.* Rotterdam: Balkema, 491- 496

Frank, D. 1995, Surficial extend and conceptual model of hydrothermal system at Mount Rainier, Washington, *Journal of Volcanology and Geothermal research,* 65, 51-80.

Franklin, J.A., Broch, E. and Walton, G., 1972. Logging the mechanical character of rock, *Transactions of the Institute of Mining and Metallurgy,* 80, A1-A9.

Fairbridge, R.W. 1950. Landslide patterns on oceanic volcanoes and Atolls, *Geographical Journal,* 115, 82-88

Garcia, O.M., 1996. Turbidites from slope failure on Hawaiian volcanoes, *In*: McGuire, W.J., Jones, A.P., and Neuberg, J., (Eds), 1996. *Volcano instability on the Earth and other planets.* London: Geological Society London Special Publication, 110, 281-294

Gerlach, T.M. and Graeber, E.J., 1985. Volatile budget of Kilauea Volcano. *Nature*, 313, 273-277.

Gerlach, T.M., Westrich, H.R., and Symonds, R.B., 1996. Pre-eruption vapour in magma of the climactic Mount Pinatubo eruption: source of giant stratospheric sulphur dioxide cloud, *In*: Newhall, C.G. and Punongbyan, R.S., (Eds.), *Fire and Mud: Eruptions and Lahars of Mount Pinatubo, Philippines.* Washington: University of Washington Press, 415-433

Gibbons, W. and Young T.P., 1999. Mid-Caradoc magmatism in central Llŷn, rhyolite petrogenesis, and the evolution of the Snowdonia volcanic corridor in NW Wales. *Journal of the Geological Society London*, 156, 301-316

Glicken, H., 1982. Criteria for identification of large volcanic debris avalanches (abstract), *Eos*, 63, 1141

Gorshkov, G.S., 1959. Gigantic eruption of the volcano Bezymia, *Bulletin of Volcanology*, 21, 77-109

Gorshkov, G.S., 1963. Directed volcanic blasts, *Bulletin of Volcanology,* 26, 83-88

Gonnermann, H.M., Manga, M., 2007. The fluid mechanics inside a volcano, *Annual Review of Fluid Mechanics*, 39, 321-356

Grove, T.L., 2000. Origin of magmas. In: Sigurdsson H. (Ed), 2000. *Encyclopaedia of Volcanoes.* San Diego: Academic Press. 133-147

Hill, D.P., Pollitz, F., Newhall, C., Earthquake-Volcano interactions, *Physics Today, November* 2002, 41-47

Hoek, E., 1983. Strength of jointed rock masses, 23rd. Rankine Lecture, *Geotechnique, 33*, 3, 187-223

Hoek, E. 1994. Strength of rock and rock masses, *ISRM News Journal*, 2, 4-16

Hoek, E and Brown, E.T. 1980. *Underground Excavations in Rock*. London: Institution of Mining and Metallurgy.

Hoek, E., Brown, E.T., 1980. Empirical strength criterion for rock masses, *Journal of the Geotechnical Engineering Division – ASCE*, 106, 1013-35

Hoek, E. and Brown, E.T. 1988. The Hoek-Brown failure criterion – a 1988 update. In, Curran J.H. (Ed.) *Proc. 15th Canadian Rock Mech. Symposium, 1998 Toronto*. Toronto: University of Toronto Press, 31-38

Hoek, E., Wood, D. and Shah, S. 1992. A modified Hoek-Brown criterion for jointed rock masses. *In*: Hudson J.A. (Ed.), *Proc. Rock Characterisation, Symposium of International Society of Rock Mechanics.: Eurock '92*, 1992 London. London, 209-214

Hoek, E., Kaiser, P.K. and Bawden, W.F., 1995. *Support of underground excavations in hard rock.* Rotterdam: Balkema

Hoek, E., Brown, E.T., 1997. Practical estimates of rock mass strength, *International Journal of Rock Mechanics and Mining Science,* 34 (8), 1165-86

Hoek, E., Carranza-Torres, C. T. and Corkum, B. 2002. Hoek-Brown failure criterion – 2002 edition. *In*: *Proceedings of the North American Rock Mechanics Society*, *2002 Toronto*

Howells, M.F., Leveridge, B.E., and Reedman, A.J., 1981. *Snowdonia*. London: Unwin Paperbacks*.*

Hürlimann, M., Turon E. and Marti, J., 1999. Large landslides triggered by caldera collapse events in Tenerife, Canary Islands, *Physics and Chemistry of the Earth (A),* 24 (10), 921-924

Hürlimann, M., Ledesma, A., and Marti, J., 2001. Characterisation of a volcanic residual soil and it's implications for large landslide phenomena: application to Tenerife, Canary Islands, *Engineering Geology,* 59, 115-132

Hürlimann, M., Marti, J., and Ledesma, A., 2004. Morphological and geological aspects related to large slope failures on oceanic islands. The huge La Orotava landslides on Tenerife, Canary Islands, *Geomorphology*, 62, 143-158

Hurwitz, S., Geoff, F., Janik, C.J., Evans, W.C., Counce, D.A., Sorey, M.L. and Ingebritsen, E. 2003. Mixing of magmatic volatiles with ground water and interaction with basalt on the summit of Kilauea Volcano, Hawaii. *Journal of Geophysical Research,* 108, doi:10.1029/2001JB001594

Hutton, D.H.W., 1988. Strike-slip terranes and a model for the evolution of the British and Irish Caledonides. *Geological Magazine*, 124, 405-425

Iverson, R.M., 1995. Can magma-injection and groundwater forces cause massive landslides on Hawaiian volcanoes? *Journal of Volcanology and Geothermal research*, 66, 295-308.

Jakob, M., 2005. A size classification for debris flows. *Engineering Geology*, 79, 151-161

Jander, R.J., Scott, K.M., Nolan, K.M. and Martinson, H.A., 1981. Lahar movement, effects, and deposits. *In*: Lipman, P.W. and Mullineaux, D.R., (Eds.), 1981. *The 1980 eruption of Mount St. Helens, Washington*. US Geological Survey Professional Paper, 1250, 461-478

Jaupart, C., 1998. Gas loss from magma through conduit walls, *In*: Gillbert, J.S. and Sparks, R.J.S. (Eds), 1996. *The Physics of Explosive Eruptions*. London: Geological Society London Special Publication, *145*, 73-90

Jaupart, C. and Allegre, C.J. 1991. Gas content, eruption rate and instabilities of eruption regimes in silicic volcanoes. *Earth and Planetary Science Letters*, 102, 413-429

Jaeger, J.C. and Cook, N.G.W. 1979. *Fundamentals of Rock Mechanics, 3rd edition*. New York: Chapman and Hall

Jorden, R. and Kieffer, H.H., 1981. Topographic changes at Mount St. Helens: large scale photogrammetry and digital terrain models. *Professional paper of the U.S. Geological Survey*, 1250, 135-141

Kerle, N., van Wyk de Vries, B., 2000. The 1998 debris avalanche at Casita volcano, Nicaragua – investigation of structural deformation as the cause of slope instability using remote sensing, *Journal of Volcanology and Geothermal research*, 105, 49-63

Kokelaar, P. 1988. Tectonic controls of Ordovician arc and marginal basin volcanism in Wales. *Journal of the Geological Society London*, 145, 759-755

Komorowski, J.C., Navarro, C., Cortes C. and Siebe, C., 1994. The unique tendency for the recurrent collapse of Colima volcano (*Mexico*): the challenge of reconciling geologic evidence with C^{14} chronology, implications for hazard assessment. *In*: *Proceedings of the International Conference on Volcano Instability on the Earth and Other Planets, London*. London: The Geological Society of London

Krantz, R.W., 1991. Measurements of friction coefficients and cohesion for faulting and fault reactivation in laboratory models using sand and sand mixtures. *Tectonophysics,* 188, 203-207

Lopez, D.L., Williams, S.N., 1993. Catastrophic volcano collapse: Relation to hydrothermal processes. *Science,* 260, 1794-96

Lipman, P.W., Normark, W.R., Moore, J.G., Wilson, J.B. and Gutmacher, C.E., 1988. The giant submarine Aika debris slide, Mauna Loa, Hawaii, *Journal of Geophysical Research*, 93, 4279-4299

Lister, J.R., 1990. Buoyancy-driven fluid fracture: The effects of material toughness and of low-viscosity precursors, *Journal of Fluid Mechanics,* 210, 263-280

Lister, J.R., and Kerr, R.C., 1991. Fluid-mechanical models of crack propagation and their application to magma transport in dykes, *Journal of Geophysical Research,* 96*,* 10049-10077*.*

Llewellin, E.W., Blower, J.D. and Mantle, M.D., 2005. Gas Flow in Volcanic Rocks: Lattice-Boltzmann Simulations of Porosity-Permeability Relationships, *Eos Trans. AGU, 86(52), Fall Meeting*. Abstract V34B-02, 2005

Malone, S.D., Endo, E., Weaver, C.S. and Ramey, J.W., 1981. Seismic monitoring fro eruption prediction, *Professional paper of the U.S. Geological Survey*, 1250, 803-813

Maps of Mexico. Available from: http://www.maps-of-mexico.com/puebla-state-mexico/puebla-state-mexico-map-main.shtml [Accessed 18 May 2006]

Marinos, P. and Hoek, E. 2000. GSI – A geologically friendly tool for rock mass strength estimation. *In*: *Proceedings of GeoEng 2000 Conference, 2000 Melbourne*. Technomic Publishing Company. 1422 -1440

Marinos, P. and Hoek, E. 2001. Estimating the geotechnical properties of heterogeneous rock masses such as flysch. *Bulletin of Engineering, Geology and the Environment.* 60, 85 –92.

Marsh, B.D., 2000. Magma Chambers. In: Sigurdsson H. (Ed), 2000. *Encyclopaedia of Volcanoes.* San Diego: Academic Press. 191-206

Marti, J. and Cundall, P.A., 1982, Mixed discretization procedure for accurate solution of plasticity problems, *International Journal of Numerical Methods and Analysis methods in Geomechanics,* 6, 129-139

McGuire, W.J., 1995. Volcanic landslides and related phenomena. *In*: *Landslides Hazard Mitigation – with particular reference to developing countries.* London: The Royal Academy of Engineering, 83-95

McGuire, W.J., 1996. Volcano instability: a review of contemporary themes. *In*: McGuire, W.J., Jones, A.P., and Neuberg, J., (Eds), 1996. *Volcano instability on the Earth and other planets*. London: Geological Society London Special Publication, 110

McGuire, W.J., 2003. Volcano instability and lateral collapse, *Revista*, 1, 33-45

McGuire, W.J., Murray J.B., Pullen A.D. and Saunders S.J., 1991. Ground deformation monitoring at Mount Etna: evidence fro dyke emplacement and slope stability. *Journal of the Geological Society London,* 148, 577-583

McGuire, W.J., Jones, A.P. and Neuberg, J., (Eds), 1996. *Volcano instability on the Earth and other planets*. London: Geological Society London Special Publication, 110.

McGuire, W.J., Howarth, R.J., Firth, C.R., Solow, A.R., Pullen, D., Saunders, S.J., Stewart I.S, S., Vita-Finzi, C., 1997, Correlation between rate of sea-level change and frequency of explosive volcanism in the Mediterranean, *Nature,* 389, 473-476

Melekestsev, I.V. and Braitseva, O.A., 1984. Gigantic rockslide avalanches on volcanoes, *Volcanology and Seismology*, 4, 14-23.

Merle, O. and Borgia, A. 1996. Scaled experiments of volcanic spreading, *Journal of Geophysical Research,* 101 (B6), 13805-13817

Merle, O. and Lénat, J.F. 2003. Hybrid collapse mechanism at Piton de la Fournaise volcano, Reunion Island, Indian Ocean. *Journal of Geophysical Research,* 108(B3), 2166, doi:10.1029/2002JB002014

Middleton, G.V. and Wilcock, P.P., 1994. *Mechanics in the Earth and Environmental Sciences.* Cambridge: Cambridge University Press

Mohr, O. 1882. Ueber die Darstellung des Spannungszustandes und des Deformationszustandes eines Korperelementes und uber die Anwendung derdelben in der Festigkeitslehre, *Civilengenieur, 28*, 113-156

Moon, V., Bradshaw, J., Smith, R. and de Lange, W., 2005. Geotechnical characterisation of stratocones crater wall sequences, White Island Volcano, New Zealand. *Engineering Geology*, 81, 146-178

Moore, J.G., 1964. Giant submarine landslides on the Hawaiian ridge, *U.S. Geological Survey Professional Paper,* 501-D, D95-D98

Moore, J.G., Normark W.R. and Holcomb, R.T. 1994. Giant Hawaiian landslides of the Hawaiian ridge. *Annual Review of Earth and Planetary Sciences, 22,* 119-144

Murase, T. and McBirney, A.R., 1973. Properties of some common igneous rocks and their melts and high temperatures, *Geological Society of America Bulletin*, 84, 3563-3592

Murray, J.B. and Voight, B., 1996. Slope stability and eruption prediction on the eastern flank of Mount Etna. *In*: McGuire, W.J., Jones, A.P., and Neuberg, J., (Eds), 1996. *Volcano instability on the Earth and other planets.* London: Geological Society London Special Publication, 110, 111-114

Navarro, J.M. and Coello, J., 1989. Depressions originated by landslide processes in Tenerife. *In*: *European Science Foundation Meeting on Canarian Volcanism*: Cabildo insular de Lanzarote, Abstract, 150-152

Newhall, C.G. and Self, S., 1982. The Volcanic Explosivity Index (VEI): an estimate of explosive magnitude for historical volcanism. *Journal of Geophysical Research,* 87, 1231-1238

Oehler, J., van Wyk de Vries, B., and Labazuy, P. 2004. Landslides and spreading of oceanic hot-spot and arc shield volcanoes on Low Strength Layers (LSLs): an analogue modeling approach, *Journal of Volcanology and Geothermal Research*, doi:10.1016j.jvolgeores.2004.11.023

Okada, H., 1983. Comparative study of earthquake swarms associated with major volcanic activities. *In*: Shimozuru, D. and Yokoyama, I. (Eds), 1983. *Arc volcanism: physics and tectonics.* Tokyo: Terra Science, 43-61

Okubo, C.H., 2004. Rock mass strength and slope stability of the Hilina slump, Kilauea Volcano, Hawaii. *Journal of Volcanology and Geothermal research,* 128, 43-76

Oppenheimer, C, Pyle, D & Barclay, J. (Eds.), 2003. *Volcanic Degassing.* London: Geological Society Special Publication, 213

Owen, T.R. 1979. *The Geology of Snowdonia and Llyn: An outline and field guide.* Bristol: Adam Hilger Ltd.

Perfit, M.R. and Davidson, J.P., 2000. Plate tectonics and volcanism. In: Sigurdsson H. (Ed), 2000. *Encyclopaedia of Volcanoes.* San Diego: Academic Press. 89-114

Pritchard, M.E., and Simons, M., 2004, Surveying volcanic arcs with satellite radar interferometry: the Central Andes, Kamchatka, and beyond, *GSA Today,* 14, 4-11

Ridley, W.I. 1971. The origin of some collapse structures in the Canary Islands, *Geological Magazine,* 108, 6, 477-484

Reid, M.E., 1994a. A pore pressure diffusion model for estimating landslide-inducing rainfall. *Journal of Geology,* 102, 709-717

Reid, M.E., 1994b. Transient thermal pressurisation in hydrothermal systems: a cause of large-scale collapse of volcanoes? Geological Society of America Bulletin, 26, 376-385

Reid, M.E. 1995. Destabilizing hydrothermal pressurization in volcanoes: *IUGG XXI general assembly, Boulder, Colorado, USA. Abstract.* A464.

Reid, M.E., 2004, Massive collapse of volcano edifices triggered by hydrothermal pressurization, *Geology*, 32, 5, 373-376

Reid, M. E., Christian, S. B., Brien, D. L., 2000. Gravitational stability of three-dimensional stratovolcano edifices. *Journal of Geophysical Research 105* (B3), 6043-56

Reid, M.E., Sisson, T.W., Dianne, L.B., 2001. Volcano collapse promoted by hydrothermal alteration and edifice shape, Mount Rainier, Washington, *Geology,* 29 (9), 779-782

Richards, J.P. and Villeneuve, M., 2001. The Llullaillaco volcano, northwest Argentina: construction by Pleistocene volcanism and destruction by sector collapse. *Journal of Volcanology and Geothermal Research,* 105, 77-105

Rintoul, M.D. and Torquato, S., 1997. Precise determination of the critical threshold and exponents in a three-dimensional percolation model. *Journal of Physics A: Mathematical and General*, 30, L585-L592

Robertson, R., Cole, P., Sparks, R.J.S., Harford, C., Lejeune, A.M., McGuire, W.J., Miller, A. D, Murphy, M.D, Norton, G., Stevens, N.F. and Young, S.R., 1998. The explosive eruption of Soufriere Hills Volcano, Montserrat, West Indies, 17 September, 1996, *Geophysical Research Letters, 25* (18), 3429-3432

Roche, O., van Wyk de Vries, B. and Druitt, T.H., 2001. Sub-surface structures and collapse mechanisms of summit pit craters, *Journal of Volcanology and Geothermal Research,* 105, 1-18

Russo, G., Gilberti, G. and Sartoris, G., 1996. The influence of regional stress on the mechanical stability of volcanoes. *In*: McGuire, W.J., Jones, A.P., and Neuberg, J., (Eds), 1996. *Volcano instability on the Earth and other planets.* London: Geological Society London Special Publication, *110*, 65-75

Rust, D. and Neri, M., 1996. The boundaries of large-scale collapse on the flanks of Mount Etna, Sicily. *In*: McGuire, W.J., Jones, A.P., and Neuberg, J., (Eds), 1996. *Volcano instability on the Earth and other planets.* London: Geological Society London Special Publication, *110*, 193-208

Schellart, W.P., 2000. Shear test results for cohesion and friction coefficients for different granular materials: scaling implications for their usage in analogue modelling, *Tectonophysics, 324*, 1-16

Schultz, R. A., 1995. Limits on strength and deformation properties of jointed basaltic rock masses, *Rock Mechanics and Rock Engineering,* 28, 1, 1-15.

Schultz, R.A., 1996. Relative scale and the strength and deformability of rock masses. *Journal of Structural Geology,* 18 (9), 1139-49

Siebert, L. 1984. large volcanic debris avalanches: characteristics of source areas, deposits, and associated eruptions. *Journal of Volcanology and Geothermal Research*, 22, 163-197

Siebert, L. 1992. Volcano hazards – threats from debris avalanches, *Nature*, 356 (6371), 658-659

Siebert, L., Glicken, H., and Ui, T., 1987. Volcanic hazards from Bezymianny - and Bandi-type eruptions, *Bulletin of Volcanology,* 49, 435-459

Siebert, L., Beget J.E., Glicken H., 1995. The 1883 and late -prehistoric eruptions of Augustine volcano, Alaska, *Journal of Volcanology and Geothermal Research*, 66, 367-395

Simkin, T. and Siebert, L., 2000. Earth's volcanoes and eruptions: An overview. In: Sigurdsson H. (Ed), 2000. *Encyclopaedia of Volcanoes.* San Diego: Academic Press. 249-261

Smith, M.S. and Shepherd, J.B. 1996. Tsunamigenic landslides at Kick 'em Jenny. In: McGuire, W.J., Jones, A.P., and Neuberg, J., (Eds), 1996. *Volcano instability on the Earth and other planets*. London: Geological Society Special Publication, *110*. 115-124

Sparks, R.S.J., 1994. Causes and consequences of pressurisation in lava dome eruptions, *Earth and Planetary Science Letters,* 150, 177-189

Sparks, R.S.J., 2003. Dynamics of Magma Degassing, In: Oppenheimer, C, Pyle, D & Barclay, J. (Eds.), 2003. *Volcanic Degassing.* London: *Geological Society Special Publication*, *213*, 5-22

Spera, F.J., 2000. Physical properties of magma. In: Sigurdsson H. (Ed), 2000. *Encyclopaedia of Volcanoes.* San Diego: Academic Press. 171-190

Terzaghi, K., 1943. *Theoretical Soil Mechanics*. New York: John Wiley and Sons

Terzaghi, K., 1960. *From Theory to Practice in Soil Mechanics*. New York: John Wiley and Sons

Thomas, M.E., Petford, N. and Bromhead, E.N., 2004a. The effect of internal gas pressurisation on volcanic edifice stability: evolution towards a critical state, *Terra Nova,* 16, 312-317

Thomas, M.E., Petford, N. and Bromhead, E.N., 2004b. Volcanic rock-mass properties from Snowdonia and Tenerife: implications for volcano edifice strength. *Journal of the Geological Society London,* 161, 1-8

Thorpe, R.S., Leat, P.T., Mann, A.C., Howells, M.F., Reedman, A.J. and Campbell, S.D.G., 1993. Magmatic evolution of the Ordovician Snowdon Volcanic Centre, North Wales (UK). *Journal of Petrology*, 34, 4, 711-741

Tibaldi, A., 2001. Multiple sector collapses at Stromboli volcano, Italy: how they work, *Bulletin of Volcanology*, 63, 112-125

Tibaldi, A., 2004. Major changes in volcano behaviour after a sector collapse: insights from Stromboli, Italy, *Terra Nova,* 16, 2-8

Tibaldi, A. and Groppelli, G., 2002. Volcano-tectonic activity along structures of the unstable NE flank of Mount Etna (Italy) and their possible origin, *Journal of Volcanology and Geothermal Research,* 115, 277-302

Topinka, L., 1980. Mount St. Helens photographs (Fig. 1.3) [online]. Available from: http://vulcan.wr.usgs.gov/Volcanoes/MSH/SlideSet/ljt_slideset.html [Accessed 18 May 2006].

Ui, T., 1985. Debris avalanche deposits associated with volcanic activity. *Proceedings of the IVth International Conference workshop on Landslides*, *1985 Tokyo*. 405-410

van Wyk de Vries, B. and Borgia, A., 1996. The role of basement in volcano deformation. In: McGuire, W.J., Jones, A.P., and Neuberg, J., (Eds), 1996. *Volcano instability on the Earth and other planets.* London: Geological Society Special Publication, *110*, 95-110

van Wyk de Vries, B. and Francis, P.W., 1997. Catastrophic collapse at stratovolcanoes induced by gradual volcano spreading, *Nature,* 387, 387-390

van Wyk de Vries, B., Kerle N. and Petley D. 2000. Sector collapse forming at Casita volcano, Nicaragua, *Geology,* 28, 2, 167-170

Vidal, N. and Merle, O., 2000. Reactivation of basement faults beneath volcanoes: a new model of flank collapse, *Journal of Volcanology and Geothermal Research*, 99, 9-26.

Vinciguerra, S., Elsworth, D. and Malone, S., 2005a. The 1980 pressure response and flank failure of Mount St. Helens (USA) inferred from seismic scaling exponents. *Journal of Volcanology and Geothermal Research,* 144, 155-168

Vinciguerra, S., Trovato, C., Meredith, P.G. and Benson, P.M., 2005b. Relating seismic velocities, thermal cracking and permeability in Mt. Etna and Iceland basalts. *International Journal of Rock Mechanics and Mining Sciences*, 42, 900-910.

Voight, B., (Ed.), 1978. *Rockslides and avalanches. 1. Natural Phenomena.* Amsterdam: Elsevier.

Voight, B., 1981. Time scale for the first movements of the May 18 eruption. *Professional paper of the U.S. Geological Survey*, 1250, 69-86

Voight, B., 2000. Structural stability of andesite volcanoes and lava domes, *Philosophical Transactions of the Royal Society of London Series A, mathematical, physical and engineering sciences,* 1770, 1663-1703

Voight, B., Glicken, H., Janda, R.J. and Douglass, P.M., 1981. Catastrophic rock-slide avalanche of May 18. *Professional paper of the U.S. Geological Survey*, 1250, 347-378

Voight, B., Janda, R.J., Glicken, H. and Douglass, P.M., 1983. Nature and mechanics of the Mount St. Helens rockslide-avalanche of 18th May 1980, *Geotechnique,* 33, 243-273.

Voight, B., and Elsworth, D., 1997. Failure of volcano slopes, *Geotechnique,* 47, 1-31

Voight B. and Elsworth D., 2000, Instability and collapse of hazardous gas-pressured lava domes, *Geophysical Research Letters,* 27, 1, 1-4

Walker, G.P.L., 1984. Downsag calderas, ring faults, caldera sizes, and incremental caldera growth. *Journal of Geophysical Research,* 89, 8407-8416

Wallace, P.J., 2001, Volcanic SO^2 emissions and the abundance and distribution of exsolved gas in magma bodies. *Journal of Volcanology and Geothermal Research*, 108, 85-106

Wallace, P.J., Anderson Jr, A.T., Davis, A.M., 1995. Quantification of pre-eruptive exsolved gas contents is silicic magmas. *Nature*, 377, 612-616

Wallace, P.J., Carn, S.A.R., William, I., Bluth, G.J.S. and Gerlach, T.M., 2003. Integrating petrologic and remote sensing perspectives on magmatic volatiles and volcanic degassing. *Eos, Transactions of the American Geophysical Union*, 84, 446-447

Walter, T.R., and Troll, V.R., 2003. Experiments on rift zone evolution in unstable volcanic edifices. *Journal of Volcanology and Geothermal Research,* 127, 107-120

Watters, R.J., and Delahaut, D., 1995. Effect of argillic alteration on rock mass stability, *In*: Haneburg, W.C., and Anderson, S.A., (Eds.), *Clay and Shale Slope Instability, Review of Engineering Geology*, *Volume X*: Boulder, Colorado: Geological Society of America, 139-150

Watters, R.J., Zimbelman, D.R, Bowman, S.D., Crowley, J.K., 2000. Rock mass strength assessment and significance to edifice stability, Mount Rainier and Mount Hood, Cascade Range volcanoes, *Pure and Applied Geophysics,* 157, 957-976

Watts, A.B. and Masson, D.G., 1995. A giant landslide on the north flank of Tenerife, Canary Islands, *Journal of Geophysical Research, 102, 20325-20342*

Weaver, P.P.E., Rothwell, R.G., Ebbing, J., Gunn, D.E. and Hunter P.M., 1992. Correlation, frequency of emplacement and source directions of megaturbidites on the Madeira abyssal plain. *Marine Geology,* 109, 1-20

Wadge, G. and Isaacs, M. C., 1987. *Volcanic Hazards from Soufriére Hills Volcano, Montserrat, West Indies.* A Report to the Government of Montserrat and the Pan Caribbean Disaster Preparedness and Prevention Project. Department of Geography, University of Reading, UK.

Williams, D, Ramsay, J.G, 1968. Geology of some classic British areas: Snowdonia, *Geologists' Association Guides: No.28*, Geologists' Association

Wilson, L. and Head, III J.W., 2003. Deep generation of magmatic gases on the Moon and implications for pyroclastic eruptions. *Geophysical Research Letters,* 30 (12), 1605, doi:10.1029/2002GL016082

Woodcock, N. and Strachan, R. 2000. *Geological History of Britain and Ireland*. Oxford: Blackwell Science Ltd.

Wooller, L., van Wyk de Vries, B., Murray, J.B., Rymer, H. and Meyer, S., 2004. Volcano spreading controlled by dipping substrata, *Geology,* 30 (7), 573-576

Young, R.W. and Bryant, E.A., 1992. Catastrophic wave erosion on the south-eastern coast of Australia: impact of the Lanai tsunamis ca. 105 KA? *Geology,* 20, 199-202